

ISBN 90-393-4110-9

Phase Behavior of Charged Colloids and the Effect of External Fields Antti-Pekka Hynninen 2005

Phase Behavior of Charged Colloids and the Effect of External Fields

Antti-Pekka Hynninen

Invitation to attend
the public defense
of my dissertation

Phase Behavior of Charged Colloids and the Effect of External Fields

on Tuesday
6th of December 2005
at 10:30 am
in the Academiegebouw
(Domplein 29, Utrecht)

After the promotion
there will be a reception

Antti-Pekka Hynninen
a.p.hynninen@phys.uu.nl
+31 6 135 31950

Paranimfs

Teemu Heinilehto
theinile@uiah.fi

Mirjam Leunissen
m.e.leunissen@phys.uu.nl

Phase Behavior of Charged Colloids
and the Effect of External Fields

Phase Behavior of Charged Colloids and the Effect of External Fields

Fasegedrag van geladen colloïden en het effect van externe velden

(met een samenvatting in het Nederlands)

Proefschrift

ter verkrijging van de graad van doctor aan de Universiteit Utrecht
op gezag van de Rector Magnificus, Prof. Dr. W. H. Gispen, in gevolge
het besluit van het College voor Promoties in het openbaar te verdedigen
op dinsdag 6 december 2005 des ochtends te 10:30 uur

door

Antti-Pekka Hynninen

geboren op 21 december 1977 te Oulu, Finland

Promotor: Prof. Dr. A. van Blaaderen
Soft Condensed Matter Group, Debye Institute,
Department of Physics and Astronomy,
Faculty of Science, Utrecht University

Co-promotor: Dr. M. Dijkstra
Soft Condensed Matter Group, Debye Institute,
Department of Physics and Astronomy,
Faculty of Science, Utrecht University



This work is part of the research programme of the “Stichting voor Fundamenteel Onderzoek der Materie (FOM)”, which is financially supported by the “Nederlandse Organisatie voor Wetenschappelijk Onderzoek (NWO)”.

A digital version of this thesis is available at <http://www.colloid.nl>
ISBN: 90-393-4110-9

Contents

1	Introduction	1
1.1	Spherical Charged Colloids	2
1.1.1	<i>Primitive Model</i>	3
1.1.2	<i>The DLVO Theory</i>	3
1.1.3	<i>Like-Charge Attraction</i>	6
1.1.4	<i>The Restricted Primitive Model</i>	8
1.2	Colloids in External Fields	8
1.3	Computer Simulations	9
1.3.1	<i>Monte Carlo Simulation Method</i>	10
1.4	Scope of This Thesis	11
2	Phase Behavior of Charged Colloids within the Yukawa Model	15
2.1	Introduction	16
2.2	Model	17
2.3	Methods	17
2.3.1	<i>Helmholtz Free Energy of Solid Phases</i>	18
2.3.2	<i>Helmholtz Free Energy of Fluid Phases</i>	20
2.3.3	<i>Gibbs-Duhem Integration</i>	20
2.3.4	<i>Mapping Between Point Yukawa and Hard-Core Yukawa Models</i>	21
2.4	Results	22
2.4.1	<i>Technical Details</i>	27
2.5	Conclusions	29
3	Effect of Density-Dependent Truncation on the Phase Behavior of Charged Colloids	31
3.1	Introduction	32
3.2	Model and Methods	33
3.3	Results	34
3.4	Conclusions	38
4	Effect of Three-Body Interactions on the Phase Behavior of Charged Colloids	41
4.1	Introduction	42
4.2	Model	43
4.3	Methods	45
4.4	Results	47
4.5	Conclusions	51
5	Melting Line of Charged Colloids from Primitive Model Simulations	53
5.1	Introduction	54
5.2	Simulation Method	55
5.2.1	<i>Highly Asymmetric Primitive Model</i>	55
5.2.2	<i>Hard-Core Repulsive Yukawa Model</i>	58
5.3	Results	60

5.3.1	<i>Effect of Lattice Discretization</i>	60
5.3.2	<i>Charge Distribution and Structure</i>	62
5.3.3	<i>Melting Line</i>	66
5.4	Conclusions	68
6	Critical Point of Asymmetric Electrolyte Mixtures	71
6.1	Introduction	72
6.2	Model and Methods	73
6.3	Results	77
6.4	Conclusions	86
7	Crystal Structures of Oppositely Charged Colloids with Size Ratio 0.31	89
7.1	Introduction	90
7.2	Methods	90
7.3	Results	91
7.4	Conclusions	97
8	Phase Behavior of Oppositely Charged Particles	99
8.1	Introduction	100
8.2	Interactions Between Oppositely Charged Colloids	100
8.3	Phase Diagrams of Oppositely Charged Particles	102
8.4	NaCl-CsCl Zero-Pressure Phase Diagram	107
8.5	Conclusions	108
9	Phase Behavior of Dipolar Hard and Soft Spheres	111
9.1	Introduction	112
9.2	Model and Methods	112
9.3	Results	115
9.3.1	<i>Phase Diagrams</i>	115
9.3.2	<i>Stability of the Bco Phase</i>	119
9.3.3	<i>Multipole Moment Expansion</i>	121
9.3.4	<i>Dipolar Fluid Phase</i>	123
9.4	Conclusions	124
9.5	Ewald Sums	125
10	Sedimentation of Charged Colloids: Entropic Lift and Charge Separation	129
10.1	Introduction	130
10.2	Theory	131
10.3	Simulation Method	132
10.4	Results	133
10.5	Conclusions	136
	References	137
	Summary	146
	Samenvatting	148

Acknowledgements	151
Curriculum vitae	153
List of publications	154

1

Introduction

Colloids are particles with a size in the nano- to micrometer range that are dispersed in a solvent, and that due to collisions from the solvent molecules, undergo Brownian motion [1]. As colloids are much larger than molecules and much smaller than macroscopic objects, they possess peculiar thermodynamic, rheological, and optical properties. Examples of colloids can be found in almost every aspect of life. In biology, red blood cells, bacteria, and viruses, are all in the colloidal regime. Colloids are used in paint, food (e.g., mayonnaise, butter, and milk), and make-up products as stabilizers that keep the structure of the product unchanged. Magnetic colloids can be found in state-of-the-art bridges where they act as cable dampers [2]. The most familiar of the optical properties is the scattering of light. Colloids arranged on a regular crystal lattice act as a three-dimensional diffraction grating that splits white light into its components. In nature, beautiful examples of this are the colors of peacock feathers, butterfly wings, and gem opals. Optical properties of colloids also have industrial applications as photonic crystals, which can be built from colloids by utilizing their ability to self-organize.

The tunability of the interactions, size, shape, and composition have made colloids an important model system for atoms and molecules as they, like atoms and molecules, have a well-defined thermodynamic temperature and manifest many of the same phenomena, but are easier to study due to their greater size and longer timescales. For example, laser confocal microscopy enables real-time and real-space studies of colloids in three dimensions on a single particle level. This makes it possible to perform detailed studies of, e.g., crystal nucleation and growth [3], glass transition [4], and solid-solid transitions [5]. The tunability of the interactions can be achieved in many ways. For example, in charged colloidal suspensions, the colloid pair potential can be tuned from a soft long-range repulsive to essentially hard-sphere like [3, 4, 6–10] by adding salt. In a binary mixture of two species of colloids, added salt can even reverse the charge on one of the species, resulting in oppositely charged colloids [11]. On the other hand, in uncharged colloidal suspensions, addition of polymer gives rise to a short-range depletion attraction [12]. Also non-spherically symmetric interactions can be realized. A dipole-dipole interaction between colloids can be achieved either by using specially prepared ferromagnetic particles [13, 14], or by exposing the colloids to an external electric [3] or magnetic field [15]. Employing two such external fields gives rise to even more complex interactions [16].

Colloids with a well-characterized size, shape, and interactions, are a perfect subject for computer simulations. Computer simulations, which are typically quicker, easier, and cheaper to perform than experiments, have become indispensable for predicting the behavior of colloids and explaining the experimental

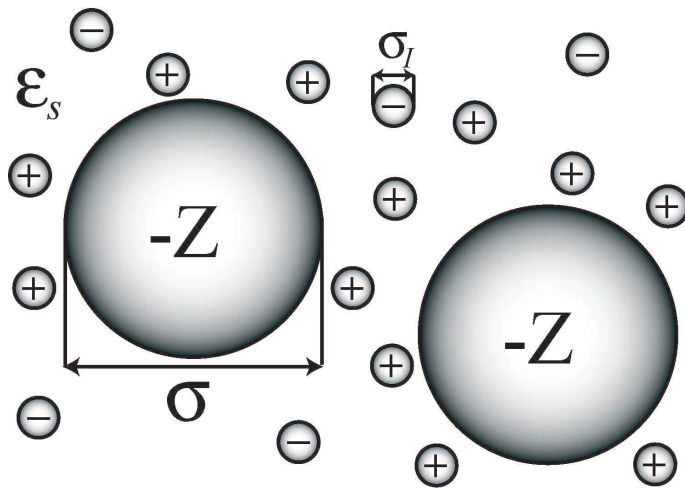


Figure 1.1: Illustration of the primitive model that includes colloids with diameter σ and charge $-Ze$, and co- and counterions with diameter σ_l and charges $-e$ and $+e$, respectively, in a solvent characterized by the dielectric constant ϵ_s .

results. Some examples of this can be found in the research described in this thesis.

The rest of this chapter is organized as follows. In Section 1.1, we give an introduction to charged colloids, present the theoretical models that are used to describe them, and discuss the anomalous behavior where like-charged colloids attract each other. In Section 1.2, we present examples of external fields that can be used to manipulate colloids. In Section 1.3, we give a brief introduction to computer simulations and especially to the Monte Carlo method. We finish in Section 1.4, where the layout of the rest of the thesis is given.

1.1 Spherical Charged Colloids

In most cases when a colloid is dispersed in a solvent, the surface of the colloid acquires a net charge due to dissociation of chemical groups at the surface. For simplicity, we assume that the surface charge is homogeneous, although in reality the charge is most likely concentrated on charge centers. The ions that are released from the surface are called *counterions* as they carry a charge that is opposite to the colloid charge. In addition to the counterions, most solvents also contain a certain concentration of dissociated *coions* and counterions. For example, water in room temperature contains 10^{-7}M of H^+ and OH^- ions. The total excess amount of co- and counterions is called “added salt” or just simply “salt”. The salt concentration can be lowered by deionizing the solvent and increased by adding a salt solution. Because the counterions undergo thermal motion but are still attracted to the colloids electrostatically, they build up a layer of opposite charge around each colloid. Thus, we obtain what is called an *electric double layer* where the first layer is the colloid surface charge and the second is the cloud of counterions surrounding the colloid surface.

This section is divided into four subsections. In Section 1.1.1, we present the so-called primitive model, where the co- and counterions are taken into account explicitly. In Section 1.1.2, we discuss the DLVO theory that is standardly used to

describe charged colloids and where the co- and counterions are integrated out. Section 1.1.3 deals with the possibility to have attraction between like-charged colloids - a topic that has caught a lot of attention during the recent years. In Section 1.1.4, we introduce the restricted primitive model (RPM) that is used to model strongly coupled electrolytes, and its colloidal analog where the particles interact via screened Coulomb potentials.

1.1.1 Primitive Model

A detailed theoretical description of charged colloidal suspensions is given by the so-called *primitive model*, which is illustrated in Fig. 1.1. In this model, the colloids are charged spheres with diameter σ and charge $-Ze$, the co- and counterions are charged spheres with diameter σ_I and charges $-e$ and e , respectively. The solvent is treated as a uniform continuum with dielectric constant ϵ_s and temperature T . The interactions between all the species are taken into account via the Coulomb potential given by

$$\frac{u(r)}{k_B T} = \begin{cases} \frac{Z_i Z_j \lambda_B}{r} & \text{for } r \geq \sigma_{ij} \\ \infty & \text{for } r < \sigma_{ij}. \end{cases} \quad (1.1)$$

where $\lambda_B = e^2 / \epsilon_s k_B T$ is the Bjerrum length, Z_i and Z_j are the charge numbers ($-Z$ or ± 1) of particles i and j , and σ_{ij} is the hard-core distance between them: For colloid-colloid interaction $\sigma_{ij} = \sigma$, for colloid-microion interaction $\sigma_{ij} = (\sigma + \sigma_I)/2$, and for microion-microion interaction $\sigma_{ij} = \sigma_I$.

Although the primitive model is typically considered to capture most of the features of real charged colloidal suspensions, it is clearly a simplification. For example, systems that include hydrodynamic effects can not be studied with the primitive model due to the simple treatment of the solvent. The main problem in using the primitive model is the difficulty of obtaining accurate predictions. In computer simulations of charged colloids, for example, simulations at the primitive model level typically become too demanding at $Z > 100$ due to the great number of counterions that have to be included to neutralize the colloid charge*. Therefore, much of our understanding of charged colloids have come from studying simpler models where the co- and counterions are coarse-grained out. The most famous of these models is the DLVO theory, which is described in the following section.

1.1.2 The DLVO Theory

As mentioned above, the presence of counterions builds up an electric double layer around each colloid. The most important feature of the double layer is that it provides a repulsive interaction between two charged colloids. Without such repulsive interaction, colloids would aggregate due to London-van der Waals attractions. This charge stabilization mechanism was first introduced in the 1940s by Derjaguin and Landau [17], and independently by Verwey and Overbeek [18].

*A simulation with $N = 100$ colloids with charge $Z = 100$ requires 10 000 counterions.

The DLVO theory, which bears the names of its inventors, assumes a single spherical colloid with charge $-Ze$ and diameter σ suspended in a continuum solvent with dielectric constant ϵ_s and temperature T . The solvent contains point-like ($\sigma_I = 0$) co- and counterions, whose density far from the colloid is $2\rho_s$. In the DLVO theory, the co- and counterion densities are given by the Boltzmann distribution and written as

$$\begin{aligned}\rho_-(r) &= \rho_s \exp[\Phi(r)] & (\text{coion}), \\ \rho_+(r) &= \rho_s \exp[-\Phi(r)] & (\text{counterion}),\end{aligned}\tag{1.2}$$

where $\Phi(r) = e\phi(r)/k_B T$ is the dimensionless electric potential at distance r from the colloid center. Next, the Boltzmann distributions (1.2) are combined with the Poisson equation to give the Poisson-Boltzmann (PB) equation

$$\nabla^2 \Phi(r) = -\kappa^2 \sinh[-\Phi(r)],\tag{1.3}$$

which is subject to boundary conditions

$$\begin{aligned}\Phi(r) &= 0 & \text{for } r \rightarrow \infty \\ \mathbf{n} \cdot \nabla \Phi(r) &= \frac{4\lambda_B Z}{\sigma^2} & \text{for } r = \sigma/2,\end{aligned}\tag{1.4}$$

where $\kappa = \sqrt{8\pi\lambda_B\rho_s}$ is the inverse Debye screening length and \mathbf{n} is a unit vector normal to the particle surface. For spherical particles, the PB equation (1.3) has to be linearized in order to solve it analytically. The result of the linearization is

$$\nabla^2 \Phi(r) = \kappa^2 \Phi(r).\tag{1.5}$$

The solution of the linearized PB equation (1.5) with the boundary conditions (1.4) reads

$$\Phi(r) = -\frac{Z\lambda_B}{\sigma} \frac{\exp(\kappa\sigma/2)}{1 + \kappa\sigma/2} \frac{\exp(-\kappa r)}{r/\sigma}.\tag{1.6}$$

One readily checks from Eq. (1.6) that the linearization is acceptable provided that

$\max |\Phi(r)| = |\Phi(\sigma/2)| \ll 1$ or if the constant proportional to $\kappa\sigma$ is ignored, $\Phi(\sigma/2) \propto Z\lambda_B/\sigma \ll 1$. That is, the linearization is permissible for low Z and/or for low λ_B/σ . Eq. (1.6) shows that the electric potential surrounding a colloid is given by a Coulomb potential which is screened by a factor $\exp(-\kappa r)$. In Fig. 1.2, we plot an example of the co- and counterion densities, $\rho_-(r)$ and $\rho_+(r)$, using Eqs. (1.2) and (1.6) for a system with $Z = 100$, $\lambda_B = 0.005\sigma$, and $\kappa\sigma = 2$ and 4. As Fig. 1.2 shows, the counterion density in the double layer is highest close to the colloid and it decays towards the bulk value ρ_s at large r . Figure 1.2 also shows the thickness of the double layer: The double layer is thin for high inverse screening length ($\kappa\sigma = 4$) corresponding to high salt concentration, and thick for low inverse screening length ($\kappa\sigma = 2$) corresponding to low salt concentration.

The pair potential between two charged colloids can be derived from the electric potential in Eq. (1.6) by assuming that the two double layers do not disturb

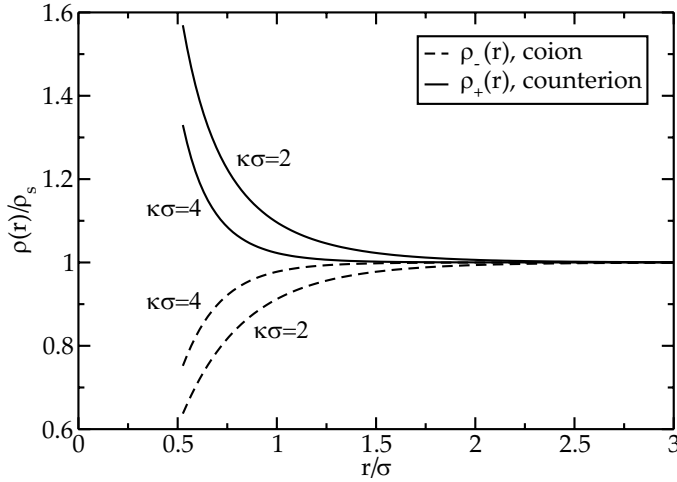


Figure 1.2: Co- and counterion densities, $\rho_-(r)$ and $\rho_+(r)$ (in units of the reservoir salt density ρ_s), as a function of distance r from the colloid center for a system with $Z = 100$, $\lambda_B = 0.005\sigma$, and $\kappa\sigma = 2$ and 4.

each other. The result is a screened Coulomb (or repulsive Yukawa) potential given by

$$\frac{u(r)}{k_B T} = \begin{cases} \frac{Z^2 \lambda_B}{(1 + \kappa\sigma/2)^2} \frac{\exp[-\kappa(r - \sigma)]}{r} & \text{for } r \geq \sigma \\ \infty & \text{for } r < \sigma, \end{cases} \quad (1.7)$$

where we have included a hard-core repulsion that makes sure that the colloids do not overlap, and neglected the London-van der Waals attractions. The London-van der Waals attractions can be neglected if the refractive indices of the colloids and the solvent are matched or if Z is so high that the colloid-colloid pair interaction is dominated by the repulsive term and therefore, the colloids never come close enough to feel the attractive forces. In this thesis, we always assume that at least one of the above conditions is fulfilled and neglect the London-van der Waals forces. As can be seen from Eq. (1.7), the screening length κ determines the range of the pair interaction analogously to the thickness of the double layer: At high salt concentration, κ is large and the repulsion is short-ranged, while at low salt concentration, κ is small and the repulsion is long-ranged. Therefore, the interactions between charged colloids can be tuned by the amount of added salt. Due to its simplicity and accuracy, the DLVO potential (1.7) has become the most-used model for spherical charged colloids. It correctly predicts the experimental phase diagram of charged colloids with stable fluid, body-centered-cubic (bcc), and face-centered-cubic (fcc) phases [8, 9, 19–21].

The DLVO theory is routinely used outside its original range of applicability. For example, in the case of highly charged colloids, where the linearization of the PB equation can not be justified close to the colloid surface, it is customary to use a renormalized charge $Z_{\text{eff}} < Z$ that takes into account the non-linear effects arising close to the surface [22]. Another example is the use of the DLVO theory at high colloid densities or low salt concentrations, where the nearby double layers overlap and the assumption of pairwise additivity becomes suspect.

1.1.3 Like-Charge Attraction

An important parameter characterizing a system of charged colloids is the microion-microion electrostatic coupling at the length scale of the colloids (see e.g. Ref. [23] for a similar definition),

$$\Gamma = \frac{\lambda_B}{\sigma}. \quad (1.8)$$

Parameter Γ describes the importance of electrostatic correlations and we distinguish two extreme cases: (i) strong coupling where $\Gamma \gg 1$ and (ii) weak coupling where $\Gamma \ll 1$. Experimentally, the weak coupling region corresponds to μm size particles in aqueous solvent with monovalent salt, while the strong coupling region corresponds to small colloids (e.g. charged micelles) with a diameter in the nanometer range or larger colloids with multivalent salt. At weak coupling, the linearization of the PB equation is justified and the system can be described using the DLVO theory. At strong coupling, however, the DLVO theory breaks down and counterions condense on the colloid surface such that the double layer thickness is in the order of the counterion diameter. In this limit, a short-range attraction between like-charged colloids has been shown to exist experimentally [24, 25], theoretically [26, 27], and by simulations [28–32]. This like-charge attraction originates from spatial correlations between counterions associated with different colloids. At short colloid-colloid separations, the attractive electrostatic correlation dominates over the repulsive double layer interaction. Like-charge attraction has been shown to give rise to a gas-liquid phase coexistence [31], and the location of the gas-liquid critical point is known fairly accurately for $Z \leq 10$ from Monte Carlo simulations [33–36], while for $10 < Z \leq 80$ the location of the critical point can be roughly estimated using a scaling formula [37]. It is very important to bear in mind that like-charge attraction is well-established only in the case of strong coupling. As we will see in the following, at weak coupling, the possibility of like-charge attraction has been proposed, but there is still no consensus whether it exists or not.

The debate over like-charge attraction at weak coupling was initiated by a variety of unexplained phenomena that has been reported in experiments of charge-stabilized colloidal suspensions with monovalent salt at room temperature. Without exception these phenomena were all observed at low salt concentrations, and they include a broad gas-solid coexistence [38, 39], a gas-liquid condensation [40, 41], large stable ‘voids’ [42, 43], and anomalously long-lived dense clusters [44]. A long-range attraction would account naturally for these phenomena, but is inconsistent with the long-accepted repulsive DLVO potential. The disagreement with the experiments and the DLVO theory gave rise to a number of theoretical models that tried to explain the experimental observations. These theories include: attractive pair interactions [45, 46], volume terms [47–49], and many-body interactions [50]. While the attractive pair interactions suggested by Sogami and Ise [45, 46] are not widely accepted by the colloid community [51], volume theories and many-body interactions have been better received.

The idea behind many-body interactions is that the effective pair potential description fails at low salt concentration where the nearby double layers overlap

giving rise to three- and higher-body interactions. Russ et al. [50] studied the two- and three-body interactions of charged colloids by expanding the effective Hamiltonian H_N of N colloidal particles into effective n -body interactions Ω_n as

$$H_N = N\Omega_1 + \sum_{i<j}^N \Omega_2(i,j) + \sum_{i<j<k}^N \Omega_3(i,j,k) + \sum_{i<j<k<l}^N \Omega_4(i,j,k,l) + \dots \quad (1.9)$$

The authors calculated the one-body (Ω_1), two-body (Ω_2), and three-body (Ω_3) potentials by solving the non-linear PB equation numerically for fixed configurations of one, two, and three colloids. They found that the two-body potential Ω_2 is repulsive and in agreement with the DLVO theory, whereas the three-body potential Ω_3 is always attractive. An attractive three-body potential has also been obtained from primitive model simulations [52, 53]. The first indirect experimental observation of many-body interactions was done by Brunner et al. [54, 55], who studied a highly charged colloidal suspension confined in two dimensions. The authors measured radial distribution functions at different colloid densities and inverted them to obtain the corresponding effective pair potentials. At short distances, the pair potentials were repulsive, as expected according to the DLVO theory. At greater distances, however, a density-dependent “truncation” was observed: The pair potential was much less repulsive than expected on the basis of the DLVO theory. The density dependence of the pair potential signals that the underlying Hamiltonian contains many-body terms. Since then, the density-dependent truncation has been observed also in three-dimensional suspensions [56–58] and can be understood in terms of a many-body shielding effect [54, 55, 58]. The first direct experimental measurement of many-body interactions was done by the same group using optical tweezers [59]. The authors found an attractive three-body potential in agreement with the calculations of Russ et al. [50]. The subsequent experiments and numerical calculations have established the existence of many-body interactions [60, 61].

The first volume theory aimed at explaining the aforementioned unexplained experiments was devised by van Roij and Hansen [62]. After the first volume theory, many others followed. The essence of all volume theories is that the effective Hamiltonian of a system of charged colloids includes, in addition to the normal two-body term, a density dependent volume term that is independent of the colloid coordinates. The density dependence of the volume term traces back to the linearization of the Poisson-Boltzmann equation, where the many-body interactions are projected onto an effective one- and two-body Hamiltonian. Thus, volume terms and many-body interactions are just the two sides of the same coin. In general, volume theories predict gas-liquid and fluid-solid coexistence in the parameter range of realistic charged colloidal suspensions and would therefore seem to explain the experimental observations. However, there are several weak points in volume theories. First, at the moment there is no consensus on which theory is correct. Second, improving a theory can make the phase coexistence disappear [63, 64]. Third, none of the theories have been confirmed using primitive model computer simulations.

1.1.4 The Restricted Primitive Model

An important special case of the primitive model is obtained when one considers solely the electrolyte part, i.e., co- and counterions without colloids. In this case, the primitive model reduces to what is called “restrictive primitive model” (RPM), because it is *restricted* in a sense that all particles have the same size and the same magnitude of charge. The RPM is widely used to model electrolytes and ionic liquids, and in the past the phase behavior of the RPM has been studied extensively. By now, it is known that the RPM exhibits a gas-liquid phase separation and the location of the critical point is known to high accuracy [65]. Also the global phase diagram, consisting of fluid, CsCl (or bcc), tetragonal, and fcc disordered phases [66–68], has been constructed. Related to the RPM is a system of oppositely charged *screened* Coulomb particles. The interest in this system has started only very recently, when it became possible to realize it experimentally using oppositely charged colloids that form stable crystal structures instead of aggregates [11, 69].

1.2 Colloids in External Fields

An intriguing feature of colloids is the possibility to use external fields to manipulate their interactions, structure, and dynamics [70]. Examples of external fields include confinement, gravity, temperature, shear flow, optical tweezers, and external electric or magnetic fields. A full description of all these external fields would be outside the scope of this thesis, and therefore, in the following, we will restrict our discussion to gravity, optical tweezers, and external electric or magnetic fields.

Gravity is the most common external field acting on colloids as it is present even in the most meticulously density-matched samples and can only be truly eliminated by performing the experiments in space [71]. Gravity makes non density-matched colloids sediment giving rise to an equilibrium sedimentation profile. If the density of colloids is low enough, the sedimentation profile is given by the well-known barometric height-distribution

$$\rho(z) = \rho_0 \exp\left(-\frac{z}{L}\right), \quad (1.10)$$

where $L = k_B T / mg$ is the gravitational length in terms of the gravitational acceleration g and the buoyant mass of the colloids m , and ρ_0 is the number density at the bottom ($z = 0$). In the case of hard-sphere colloids, sedimentation profiles have been used to check the hard-sphere equation of state experimentally [72–74]. In charged colloids at low salt concentration, gravity (or a centrifugal force) has been recently shown to give rise to sedimentation profiles that are greatly inflated compared to the barometric profile (1.10) [75–77]. More precisely, colloids are lifted against gravity such that their sedimentation profile is given by

$$\rho(z) = \rho_0 \exp\left(-\frac{z}{(Z+1)L}\right), \quad (1.11)$$

which is highly non-barometric for $Z \gg 1$. A simple mean-field theory has been proposed to explain this phenomenon [78], offering the following qualitative picture. The colloids are pulled towards the bottom by gravity. Due to electrostatic attractions, the colloids also pull counterions with them. However, this leads to a highly nonhomogeneous density distribution of counterions, which is very unfavorable to the entropy of the counterions. Therefore, a compromise is made: the colloid sedimentation profile is inflated, which allows the counterions to be distributed more homogeneously and at the same time guarantees low electrostatic energy. The inflated sedimentation profiles are due to an electric field, which is caused by a macroscopic charge separation arising from the redistribution of charge. Note that this phenomenon only occurs in deionized samples. At high salt concentration, the coions accompany the counterions at all heights, making the counterion distribution more homogeneous and thus suppressing the entropic need for redistribution.

Optical tweezers are laser-optical traps where a highly focused laser beam can catch and hold a colloidal particle. By scanning a line with an optical tweezer, it is possible to confine two or more colloids on a line. This method has been used, for example, to measure three-body interactions between charged colloids [59] (see Section 1.1.3). Furthermore, by time sharing optical traps it is possible to trap hundreds of colloids in an array [79]. Using a binary mixture of core-shell colloidal particles, selective optical trapping can be used to create small two- or three-dimensional clusters of colloids of one type, without affecting a concentrated dispersion of the other type [79]. As the geometry and size of the cluster can be readily manipulated, it can be used as a nucleus in studies of crystal nucleation [80]. Crystallization can also be induced by optical gradient forces, which trap assemblies of colloids without manipulating them on a single particle level [81]. This method is similar to the “dielectrophoretic bottle” where an electric field gradient is used to increase the local concentration of colloids [82].

In an external electric or magnetic field, colloids whose dielectric constant or magnetic susceptibility is different from that of the solvent, acquire a (electric or magnetic) dipole moment parallel to the field. The colloid pair potential is governed by the dipole-dipole interaction, whose strength can be tuned by the magnitude of the field. Such suspensions are called electrorheological (ER) and magnetorheological (MR) fluids and they are used in industrial applications as dampers [2], hydraulic valves, clutches, brakes [83], and displays [84]. An important feature of ER/MR fluids is their ability to crystalize above a certain critical field strength [85]. The high-field crystal structure is body-centered-tetragonal (bct) [86], but at lower field strengths, also other structures are possible [3]. The tunability of the crystal structure via an external field makes ER/MR suspensions appealing for photonic applications [3, 87, 88].

1.3 Computer Simulations

In this section, we describe computer simulations, which are used in this thesis as a tool to study charged colloids. The origin of computer simulations dates back to the 1950s, when the first computers were built during and after the Second

World War. The early computer simulations were met with great skepticism and regarded “useless” by many scientists who wanted to preserve the *status quo* of theory and experiments with no computers in between that might mess things up. Since then, however, computer simulations have proven immensely useful in testing theoretical results, as they can be used to calculate numerically exact results in systems that are too difficult to study theoretically without resorting to approximations. A good example of such a system is the liquid phase. In order to test liquid state theories, good experimental results are required. Before the introduction of computer simulations, liquids were studied by large assemblies of macroscopic spheres, e.g., ball bearings and rubber balls [89]. This method is obviously very time consuming, the effect of gravity can not be ruled out, and the choice in particle pair interaction is quite limited. Although the early mechanical simulations of liquids proved to be quite realistic, one certainly would prefer to perform the simulation using a mathematical, rather than a physical, model. Therefore, it is not surprising that the liquid equation of state was one of the first problems tackled with computer simulations [90]. Computer simulations are more than a mere extension of theory, they can also be used as a tool to find new phenomena. A classical example of this is hard-sphere freezing. Before the introduction of computer simulations, it was not known if particles without attractive forces can form a solid phase. This issue was solved by Alder and Wainwright [91] and Wood and Jacobson [92], who showed that hard spheres undergo a first-order freezing transition. In modern materials research, one of the common applications of simulations is to predict the properties of existing materials but also materials which do not yet exist and have been designed by computer simulations.

1.3.1 Monte Carlo Simulation Method

The early work of Metropolis et al. [90] on the liquid equation of state also gave birth to what is now known as the *Metropolis Monte Carlo* method. The name refers to the famous casino in Monaco and describes the repetitive use of randomness analogous to the activities conducted at a casino. The Monte Carlo method had been proposed before by Mayer and Ulam to evaluate multidimensional integrals by sampling them using a random, rather than a regular, array of points. An example of such an integral is the statistical mechanical average of quantity A in a three-dimensional system with N particles and interaction potential U , given by

$$\langle A \rangle = \frac{\int A(\mathbf{r}^N) \exp[-U(\mathbf{r}^N)/k_B T] d\mathbf{r}^N}{\int \exp[-U(\mathbf{r}^N)/k_B T] d\mathbf{r}^N}. \quad (1.12)$$

A simple Monte Carlo method of evaluating the integrals in Eq. (1.12) would amount to placing N particles in a random configuration, evaluating $U(\mathbf{r}^N)$ and giving this configuration weight $\exp[-U(\mathbf{r}^N)/k_B T]$, and repeating the procedure. For any non-trivial system at high density, however, such method would be inefficient because of the high probability of choosing configurations that have a very small weight $\exp[-U(\mathbf{r}^N)/k_B T]$. The ingenious idea of Metropolis et al. was to pick the configurations with probability $\exp[-U(\mathbf{r}^N)/k_B T]$ and weigh

them evenly, instead of picking random configurations evenly and then weighting them with $\exp[-U(\mathbf{r}^N)/k_B T]$, as was done before. This can be achieved by the following procedure. We start from any configuration of N particles and displace a random particle i at \mathbf{r}_i by a random amount $\Delta\mathbf{r}$ to a new position $\mathbf{r}_i + \Delta\mathbf{r}$. We then calculate the change in energy, ΔU , due to the displacement. If $\Delta U < 0$, the energy is lowered and we accept the displacement. If $\Delta U > 0$, we accept the displacement with a probability $\exp(-\Delta U/k_B T)$ by drawing a random number p between 0 and 1 and comparing it with $\exp(-\Delta U/k_B T)$: If $p < \exp(-\Delta U/k_B T)$, the displacement is accepted, otherwise, the displacement is rejected and the particle is returned to its original position. It can be shown that this procedure produces a Markov chain of configurations that are all picked according to the probability $\exp[-U(\mathbf{r}^N)/k_B T]$. The ensemble average of A can now be calculated from the unweighted average

$$\langle A \rangle = \frac{\sum_{k=1}^M A_k}{M}, \quad (1.13)$$

where A_k is the value of A after the k th trial move and M is the total amount of trial moves. In the rest of this thesis, “Monte Carlo” (or MC) always refers to the Metropolis Monte Carlo.

Due to its simplicity and effectiveness, now, over fifty years later, the original Metropolis displacement move is still by far the most used Monte Carlo move, especially in molecular simulations. The displacement move is typically the one which is used to perform simulations in the canonical ensemble where the number of particles, volume, and temperature are fixed. However, the Monte Carlo method is by no means limited to the canonical ensemble [93]. By introducing volume moves, it is possible to perform simulations in the constant pressure ensemble. On the other hand, the grand canonical ensemble, where the chemical potential is fixed, can be simulated by carrying out particle insertion and removal moves. In many applications, Monte Carlo moves can be made more efficient by using cluster move techniques [93].

1.4 Scope of This Thesis

The purpose of this thesis is to study the phase behavior of spherical charge-stabilized colloids and the effect of external fields using computer simulations. We use Monte Carlo simulations in all chapters, except in the last one where Molecular Dynamics is used. This thesis can be divided into four parts.

Part I, consisting of Chapters 2, 3, 4, and 5, deals with the phase diagram of charged colloids. In Chapter 2, we study the phase diagram of charged colloids described by the DLVO potential (1.7). Although the phase diagram of “point Yukawa” particles that interact via the DLVO potential (1.7) without a hard-core is known from earlier studies [19], no systematic study on the effect of the hard-core on the phase behavior has been performed. In order to study this effect, we calculated four phase diagrams for hard-core Yukawa particles at different colloid-colloid contact potentials and compared the results with the corresponding point Yukawa phase diagrams. In Chapters 3 and 4, we discuss two

attempts of amending the DLVO description to include many-body interactions: (i) density-dependent truncation and (ii) three-body interactions. While the existence of both phenomena have been confirmed experimentally and numerically, much less is known about their influence on the phase behavior. Therefore, in Chapter 3, we study the effect the density-dependent truncation of the phase diagram of charged colloids, and in Chapter 4, we do the same for the three-body interactions. In Chapter 5, we use the primitive model to study the melting line of charged colloids. As we are interested in potential many-body effects, the simulations are performed using the same parameter as in Chapter 4. The primitive model simulations are done by confining the colloids and the microions on a fine lattice. Lattice effects on the physical properties of the system are checked. We estimate the fluid-solid melting line and compare the result with the melting line of particles interacting via the Yukawa potential. We also take a look at the structure of the electric double layer and the radial distribution function of colloids close to the fluid-solid transition, and discuss the mapping between the primitive and Yukawa models.

In Part II, contained in Chapter 6, we use the primitive model and grand canonical Monte Carlo simulations to study colloids with charges $Z = 3$ and 10 at strong electrostatic coupling (where $\Gamma \gg 1$). As discussed in Section 1.1.3, at strong coupling charged colloids undergo a gas-liquid phase separation. Our purpose is to study the effect of added salt (co- and counterions) on the gas-liquid critical point by calculating the critical point loci that connects the colloid rich state (no salt) with the pure salt state (no colloids). In Chapter 6, a slightly different terminology is used than in the rest of the thesis. This is done in order to be consistent with the existing literature on electrolytes. Accordingly, we refer to colloids as “macroions” and call charged colloidal suspensions “asymmetric electrolyte mixtures”.

Part III, consisting of Chapters 7 and 8, deals with oppositely charged colloids. This research is motivated by the recently introduced experimental system of oppositely charged colloids that form equilibrium crystal structures. In Chapter 7, we predict crystal structures for a mixture of large and small oppositely charged colloids with size ratio 0.31. The predictions are done for small-large stoichiometries from 1 to 8 using an interactive Monte Carlo method based on simulated annealing. Employing the discovered structures in Madelung energy calculations, we construct a ground-state phase diagram and compare the results with experimental observations. In Chapter 8, we study the phase behavior of equal-size oppositely charged colloids using Monte Carlo simulations and make comparison with experimental observations. In the simulations, two systems are considered: (i) the restricted primitive model (RPM) and (ii) a system of screened Coulomb particles. The use of screened Coulomb potentials to model oppositely charged colloids is justified by calculating the effective pair interaction from primitive model simulations. We construct the phase diagrams of both the RPM and screened Coulomb particles, and compare them with each other and with experimental results. We also study the zero-pressure phase diagram of screened Coulomb particles with charge asymmetry.

Finally, in Part IV, which consists of Chapters 9 and 10, we study charged colloids in external fields. The focus of Chapter 9 is on the phase diagram of colloids

in an external electric or magnetic field. As mentioned in Section 1.2, the external field induces a fixed dipole moment on the particles giving rise to a dipole-dipole interaction. Two cases are considered: (i) colloids without charge (or dipolar hard spheres) and (ii) colloids with charge (or dipolar soft spheres). The colloids are modelled as particles with a fixed dipole moment and the charge repulsion is taken into account using the DLVO theory. The phase diagrams are constructed from Helmholtz free energies calculated by Monte Carlo simulations. We make a comparison with an experimental phase diagram that has been measured for charged colloids in an external electric field. We also study the stability of the fluid phase with respect to a gas-liquid phase separation, and discuss the validity of the dipole approximation by performing exact calculations using a multipole moment expansion method. In Chapter 10, we use the primitive model and Molecular Dynamics simulations to study charged colloids in gravity. As mentioned in Section 1.2, the equilibrium sedimentation profile of charged colloids is inflated due to an entropic lift from the counterions. This effect is captured in the simple mean-field theory presented in Ref. [78]. Our purpose is to check the validity of the theory by calculating sedimentation profiles for colloids with charges $Z = 5$ and 10 , and check the effect of added salt by adding a constant amount of co- and counterions into the system.

2

Phase Behavior of Charged Colloids within the Yukawa Model

ABSTRACT

We determine the phase behavior of charged colloids interacting via a hard-core repulsive Yukawa (or screened Coulomb) potential as predicted by the DLVO theory. We study the effect of the hard-core diameter of the colloids on the phase behavior of Yukawa particles by comparing our phase diagrams with those of point Yukawa particles. We show that, for sufficiently high contact values of the pair potential ($\epsilon \geq 20$), the fluid-face-centered-cubic (fcc) at high screening, the fluid-body-centered-cubic (bcc), and the bcc-fcc coexistence for packing fractions $\eta \lesssim 0.5$, are well-described by the phase boundaries of point Yukawa particles by employing a mapping of the point Yukawa system onto a hard-core Yukawa system. While the bcc-fcc coexistence is well-described by the point Yukawa limit for $\eta < 0.5$, we find a deviation at higher η as the hard-core repulsion favors the fcc solid for $\eta \geq 0.5$, independent of the screening. Consequently, a second triple point appears in the phase diagram in the weak screening regime. In addition, we find that all phase coexistence regions are narrow, i.e., the density jump between the coexisting phases is small.

2.1 Introduction

Particles whose interactions are described by the repulsive Yukawa (screened Coulomb) pair potential can be used to model various physical systems including elementary particles, small, charged “dust” grains observed in plasma environments, and suspensions of charge-stabilized colloids. Our interest lies especially in the phase behavior of the last example, i.e., colloids. In what follows, since there is no danger of misinterpretation, we refer to “repulsive Yukawa potential” simply as “Yukawa potential”.

The phase diagram of point Yukawa particles is known from earlier studies [19, 21]. However, much less is known about the phase behavior of hard-core Yukawa particles. Intuitively, two limiting cases for the effect of the hard-core can be considered: (i) In the limit of highly charged colloids or low density of colloids (or both), the particles hardly ever come sufficiently close to each other and therefore the effect of the hard-core diameter is minimal. (ii) In the other extreme of low charge or high density (or both), the hard-core interaction should play a large role. However, in order to make a more precise analysis, we decide to study the phase behavior of hard-core Yukawa particles systematically.

Phase diagrams of hard-core Yukawa particles have been studied earlier in Refs. [94, 95]. These earlier studies have inspired our work in many ways: Not only do we use similar methods, but we also directly utilize the data given in them. In Ref. [95], a full phase diagram was presented for one contact value $\epsilon = 8$ and also a comparison with point Yukawa particle results was made. We extend this study by calculating phase diagrams for several values of ϵ and perform a mapping between the hard-core Yukawa and the point Yukawa systems. Our main conclusion is that the phase diagram of hard-core Yukawa particles can be obtained for any sufficiently high contact value ($\epsilon \geq 20$) by mapping the well-known phase boundaries of the point Yukawa system onto those of the hard-core Yukawa system, and using that the hard-core repulsion favors the fcc phase over the bcc phase at $\eta > 0.5$.

The remainder of this chapter is organized as follows. In Section 2.2 we present the model. Section 2.3 describes the methods and is divided into four subsections: Sections 2.3.1 and 2.3.2 detail the thermodynamic integration method that is used to calculate Helmholtz free energies, Section 2.3.3 presents the Gibbs-Duhem integration method for tracing coexistence curves, and Section 2.3.4 shows the mapping of a point Yukawa phase diagram on a hard-core Yukawa phase diagram. In Section 2.4, we present the results, compare them to earlier results of point Yukawa particles, and give technical details regarding the calculations. Finally, in Section 2.5, we conclude.

2.2 Model

In our model, the colloids interact via a hard-core repulsive Yukawa potential, given by

$$\frac{u(r)}{k_B T} = \begin{cases} \epsilon \frac{\exp[-\kappa\sigma(r/\sigma - 1)]}{r/\sigma} & r > \sigma \\ \infty & r < \sigma, \end{cases} \quad (2.1)$$

where ϵ is the value of the pair potential at contact per $k_B T$, κ is the inverse Debye screening length and σ is the hard-core diameter. The contact value is given by

$$\epsilon = \frac{Z^2}{(1 + \kappa\sigma/2)^2} \frac{\lambda_B}{\sigma}, \quad (2.2)$$

where Z is the charge of the colloids and $\lambda_B = e^2/\epsilon_s k_B T$ is the Bjerrum length of the solvent with dielectric constant ϵ_s (see Section 1.1.2). The total potential energy of N particles is given by the sum over all pairs as

$$U(\mathbf{r}^N) = \sum_{i < j}^N u(r_{ij}). \quad (2.3)$$

In this study, we take ϵ , $\kappa\sigma$, and η as independent variables, and calculate the phase behavior in the three dimensional space spanned by them. This choice is made for the sake of simplicity. In experimental charge-stabilized colloidal suspensions, all these variables depend on each other. Experimental parameters can be mapped on our phase diagrams by estimating the effective screening length $\kappa\sigma$ and contact value ϵ . Note that, in our phase diagrams, two phases in coexistence have equal pressure, chemical potential, $\kappa\sigma$, and ϵ , but different η .

2.3 Methods

The Monte Carlo (MC) simulations were carried out in a cubic box (with few exceptions) and with periodic boundary conditions. The cut-off radius of the potential was always chosen to be half of the box length and a continuous distribution of particles beyond the cut-off was assumed [93]. In the limit of weak screening $\kappa\sigma \ll 1$, the use of cut-offs in the potential is inaccurate as the range of the potential is larger than half of the box length. This problem can be fixed by using Ewald summation adapted for Yukawa interactions [96] or by applying the method elaborated in Ref. [97], where spline functions are used to approximate the effective interactions that result from taking into account all image particles. However, in the current case, it is sufficient to limit ourselves to $\kappa\sigma \geq 2.0$, where the effects of the finite cut-off remain small or can be eliminated by moderate increase of the system size.

Our purpose is to use a combination of Helmholtz free energy calculations and the so-called Gibbs-Duhem integration method to trace out the phase diagram of

the hard-core Yukawa particles. We will give the details of these methods in Sections 2.3.1, 2.3.2, and 2.3.3. Note that, similar methods were used in Refs. [94, 95] to study the phase diagram of hard-core Yukawa particles. The phase diagram consists of stable regions of fluid, bcc, and fcc phases that are bounded by coexistence regions between any two phases. Therefore, the determination of the phase diagram reduces to the calculation of the coexistence lines. Points on the coexistence line can be determined by calculating, for each phase, the Helmholtz free energy per volume as a function of density and using the common tangent construction to obtain the densities of the coexisting phases. In principle, this could be repeated for every point to obtain a smooth coexistence line. However, this would be computationally very demanding and, as it turns out, not even necessary. This is because, once one point on the coexistence line is known, the rest of the line can be calculated by using the Gibbs-Duhem integration, without performing additional free energy calculations.

2.3.1 Helmholtz Free Energy of Solid Phases

The Helmholtz free energy of the solid phases is calculated using the Frenkel-Ladd method [93, 98]. In this method, one starts from an Einstein crystal where the particles are tied to their ideal lattice positions by harmonic springs. Then, the springs are slowly removed and one recovers the original interactions. The auxiliary potential energy function that includes the harmonic springs is given by

$$U_\lambda(\mathbf{r}^N) = U(\mathbf{r}^N) + k_B T \lambda \alpha \sum_{i=1}^N (\mathbf{r}_i - \mathbf{r}_{0,i})^2 / \sigma^2, \quad (2.4)$$

where $\mathbf{r}_{0,i}$ is the lattice position of particle i , α is a dimensionless spring constant, and $\lambda \in [0, 1]$ is a coupling parameter. At $\lambda = 0$, we recover the system of interest, while at $\lambda = 1$, once the spring constant α is chosen large enough, the particles do not “feel” each other and the system reduces to an Einstein crystal with Madelung energy $U(\mathbf{r}_0^N)$ (the potential energy of a crystal with all particles at their lattice positions). The Helmholtz free energy is obtained from [93, 98, 99]

$$F(N, V, T) = F_{\text{Ein}}^{\text{CM}}(N, V, T, \alpha) + F_{\text{CM}}(N, V, T) - k_B T \int_0^1 d\lambda \left\langle \alpha \sum_{i=1}^N (\mathbf{r}_i - \mathbf{r}_{0,i})^2 / \sigma^2 \right\rangle_\lambda^{\text{CM}}, \quad (2.5)$$

where the ensemble average $\langle \dots \rangle_\lambda^{\text{CM}}$ is calculated with a Boltzmann factor $\exp(-U_\lambda/k_B T)$ for a crystal with a fixed center of mass. In Eq. (2.5), the free energy of an Einstein crystal with fixed center of mass is given by

$$F_{\text{Ein}}^{\text{CM}}(N, V, T, \alpha) = U(\mathbf{r}_0^N) + \frac{3(N-1)}{2} k_B T \ln \left(\frac{\alpha \Lambda^2}{\pi \sigma^2} \right), \quad (2.6)$$

where Λ is de Broglie wavelength, and the term

$$F_{\text{CM}}(N, V, T) = k_B T \ln \left(\frac{\Lambda^3}{V N^{1/2}} \right), \quad (2.7)$$

corrects for the fixed center of mass. As noted in Ref. [93], it is useful to rewrite the integral in Eq. (2.5) as

$$\int_{\ln c}^{\ln(\alpha+c)} (\lambda\alpha + c) \left\langle \sum_{i=1}^N (\mathbf{r}_i - \mathbf{r}_{0,i})^2 / \sigma^2 \right\rangle_{\lambda}^{\text{CM}} d[\ln(\lambda\alpha + c)], \quad (2.8)$$

where

$$c = \frac{1}{\left\langle \sum_{i=1}^N (\mathbf{r}_i - \mathbf{r}_{0,i})^2 / \sigma^2 \right\rangle_0^{\text{CM}}}. \quad (2.9)$$

Another option for the auxiliary potential energy function in Eq. (2.4) is to write it as

$$U_{\lambda}(\mathbf{r}^N) = U_{\text{HS}}(\mathbf{r}^N) + (1 - \lambda)U(\mathbf{r}^N) + k_B T \lambda \alpha \sum_{i=1}^N (\mathbf{r}_i - \mathbf{r}_{0,i})^2 / \sigma^2. \quad (2.10)$$

In this case, the potential energy term $U(\mathbf{r}^N)$ vanishes at $\lambda = 1$ and the system interacts via a hard-core potential $U_{\text{HS}}(\mathbf{r}^N)$ plus harmonic springs. The Helmholtz free energy is now obtained from

$$F(N, V, T) = F_{\text{Ein}}^{\text{CM}}(N, V, T, \alpha) + F_{\text{CM}}(N, V, T) - \int_0^1 d\lambda \left\langle k_B T \alpha \sum_{i=1}^N (\mathbf{r}_i - \mathbf{r}_{0,i})^2 / \sigma^2 - U(\mathbf{r}^N) \right\rangle_{\lambda}^{\text{CM}}, \quad (2.11)$$

where the free energy of the Einstein crystal is given without the Madelung energy term as

$$F_{\text{Ein}}^{\text{CM}}(N, V, T, \alpha) = \frac{3(N-1)}{2} k_B T \ln \left(\frac{\alpha \Lambda^2}{\pi \sigma^2} \right). \quad (2.12)$$

The integrals in Eqs. (2.8) and (2.11) can be calculated numerically using a Gauss-Legendre quadrature [100]. If used correctly, the two methods in Eqs. (2.5) and (2.11), give the same result. The method in Eq. (2.5) has the advantage that the integral can be written as in Eq.(2.8), which often yields a more slowly varying integrand than the one in Eq. (2.11). On the other hand, in order to reach the Einstein crystal limit, the method in Eq. (2.5) requires 100-2000 times higher α than the method in Eq. (2.11). Most free energy calculations in this thesis are done using Eq. (2.5).

Finally, we like to point out that the solid free energy has a system-size dependence that scales as N^{-1} . It is possible to remove this finite size effect by performing free energy calculations for increasing values of N and extrapolating to the $N \rightarrow \infty$ limit [93, 99]. According to our experience, the $1/N$ system-size dependence affects the phase behavior primarily in cases where the system is close to a hard-sphere system, i.e., when forces other than the hard-core repulsion are weak. In such cases, the system-size correction has a big effect especially on the fluid-solid phase coexistence because the fluid free energy calculation does not suffer from a similar system-size dependence.

2.3.2 Helmholtz Free Energy of Fluid Phases

The Helmholtz free energy of a fluid phase can be calculated using the Kirkwood's coupling parameter method [93, 101]. To this end, we introduce an auxiliary potential energy function

$$U_\lambda(\mathbf{r}^N) = U_{\text{HS}}(\mathbf{r}^N) + \lambda U(\mathbf{r}^N), \quad (2.13)$$

where $\lambda \in [0, 1]$ is a coupling parameter. At $\lambda = 1$, we recover the system of interest, while at $\lambda = 0$, the system reduces to a hard-sphere fluid. The Helmholtz free energy is given by

$$F(N, V, T) = F_{\text{HS}}(N, V, T) + \int_0^1 \langle U(\mathbf{r}^N) \rangle_\lambda d\lambda, \quad (2.14)$$

where F_{HS} is the free energy of hard-sphere fluid, which is obtained from the Speedy equation of state [102] or from the more simple Carnahan-Starling expression [103] given by

$$\frac{F_{\text{HS}}(N, V, T)}{Nk_B T} = \ln \left(\frac{N\Lambda^3}{V} \right) - 1 + \frac{\eta(4 - 3\eta)}{(1 - \eta)^2} + \frac{\ln(2\pi N)}{2N}. \quad (2.15)$$

Again, the numerical integration in Eq. (2.14) can be performed using a Gauss-Legendre quadrature [100].

2.3.3 Gibbs-Duhem Integration

In this section, we briefly describe the Gibbs-Duhem method first proposed by Kofke [104, 105]. More details can be found from the original articles or from Ref. [93]. In the current application, we are interested in calculating phase coexistence lines in the $(\eta, \kappa\sigma)$ plane for a fixed ϵ . In this case, the Gibbs-Duhem method amounts to integrating

$$dp = - \frac{\langle U' / Nk_B T \rangle_1 - \langle U' / Nk_B T \rangle_2}{\langle V / N\sigma^3 \rangle_1 - \langle V / N\sigma^3 \rangle_2} d(\kappa\sigma), \quad (2.16)$$

(for the derivation see Ref. [95]) from a known starting point $(p, \kappa\sigma)$. Note that the two phases in coexistence have the same p, ϵ and $\kappa\sigma$ but different η . In Eq. (2.16), $p = P\sigma^3 / k_B T$ is the dimensionless pressure, $\langle \dots \rangle_i$ denotes an ensemble average of the i th phase ($i = 1, 2$) and U' is the partial derivative of the total potential energy with respect to $\kappa\sigma$.

In practice Eq. (2.16) is integrated as follows. The differentials dp and $d(\kappa\sigma)$ are replaced by finite differences Δp and $\Delta(\kappa\sigma)$. Starting from a known coexistence point with p and $\kappa\sigma$, MC simulations are performed for both phases in the NPT -ensemble to calculate the ensemble averages in Eq. (2.16). This gives us a prediction for the slope of the coexistence line in the $(p, \kappa\sigma)$ plane. Changing $\kappa\sigma$ to $\kappa\sigma + \Delta(\kappa\sigma)$ we perform MC simulations for both phases at pressure $p + \Delta p$, as predicted by Eq. (2.16), and calculate again the ensemble averages in Eq. (2.16). Continuing in this manner gives us a series of points $\{p_j, (\kappa\sigma)_j\}$ that lie on the coexistence line. At each point, the packing fractions of the two phases can be

determined from $\eta_i = \frac{\pi}{6}\sigma^3 N / \langle V \rangle_i$, where $\langle V \rangle_i$ is obtained from the *NPT* simulation.

The practical limitation of this method is that there is no inherent mechanism that guarantees that we stay on the coexistence line. In other words, during the integration of Eq. (2.16), numerical errors may accumulate to yield large deviations from the actual coexistence line. This problem can be avoided by employing a more sophisticated version of the method by Meijer and El Azhar, where additional free energy calculations are used to fix the estimates of the coexisting points [94]. However, instead of implementing the method of Meijer and El Azhar, we decided to check the stability of the Gibbs-Duhem integration by performing separate free energy calculations at a couple of points along the coexistence line. The difference between the results from the free energy and Gibbs-Duhem integration gives us an idea of the total numerical error accumulated.

2.3.4 Mapping Between Point Yukawa and Hard-Core Yukawa Models

In order to compare our results for hard-core Yukawa particles to the earlier results obtained for point Yukawa particles [19, 21], we need to define a mapping between the two systems. A natural choice for this mapping is to equate the two Yukawa potentials outside the hard-core. However, since the results for the point Yukawa particle phase diagrams are typically presented in different units than those for the hard-core Yukawa particles, we have to explain the situation a little further.

In the case of point Yukawa particles, the relevant length scale is the characteristic interparticle separation $a = \rho^{-1/3}$. Once a is chosen as the length scale, the pair potential can be written as

$$\frac{u(r)}{k_B T} = U_0 \frac{\exp(-\lambda r/a)}{r/a}, \quad (2.17)$$

where U_0 is a constant prefactor in units of $k_B T$ and λ is the inverse screening length in units of a . While the phase space of hard-core Yukawa particles is three dimensional (ϵ , $\kappa\sigma$, and η), only two independent variables exist in the case of point Yukawa particles; since a is chosen as the length scale, there is no need for a density axis. We are therefore left with a two dimensional phase space consisting of the prefactor U_0 and the inverse screening length λ . By setting the two pair potentials in Eqs. (2.1) and (2.17) equal at $r > \sigma$, we obtain

$$\begin{aligned} \kappa &= \lambda/a \\ e^{\kappa\sigma} \sigma \epsilon &= U_0 a. \end{aligned} \quad (2.18)$$

The first line of Eq. (2.18) results from setting the exponential decays of the two pair potentials equal and the second from the equality of the prefactors. Using the fact that $a = (6\eta/\pi)^{-1/3}\sigma$, we can rewrite Eq. (2.18) as

$$\begin{aligned} U_0 &= e^{\kappa\sigma} \epsilon (6\eta/\pi)^{1/3} \\ \lambda &= \kappa\sigma (6\eta/\pi)^{-1/3}. \end{aligned} \quad (2.19)$$

Eq. (2.19) can be used to map a phase diagram of hard-core Yukawa particles onto a phase diagram of point Yukawa particles, and vice versa.

As mentioned above, the phase diagram of point Yukawa particles can be given in terms of the inverse screening length λ and the prefactor U_0 . This is what we call the (λ, U_0) representation. Another representation of the point Yukawa phase diagram is the (λ, \tilde{T}) , where

$$\tilde{T} = \left[\frac{2}{3} \lambda^2 U_0 u_M(\lambda) \right]^{-1} \quad (2.20)$$

is the dimensionless temperature and where $u_M(\lambda)$ is the Madelung energy of an fcc crystal per particle per U_0 [19, 21]. The (λ, \tilde{T}) representation is convenient since it leads to phase boundaries that are almost straight lines. Hamaguchi et al. [21] gave the results for the fluid-bcc and fluid-fcc melting lines, and the bcc-fcc phase boundary as polynomial fits in the (λ, \tilde{T}) plane. Here, we give the fits of Hamaguchi et al. for the phase boundaries of point Yukawa particles in the (λ, U_0) plane, as this representation does not require the calculation of the Madelung energy $u_M(\lambda)$. The fluid-bcc phase boundary is well fitted by

$$\begin{aligned} \ln(U_0) &= 4.670 - 0.04171\lambda \\ &+ 0.1329\lambda^2 - 0.01043\lambda^3 \\ &+ 4.343 \times 10^{-4}\lambda^4 - 6.924 \times 10^{-6}\lambda^5, \\ &\text{for } 0 \leq \lambda \leq 12, \end{aligned} \quad (2.21)$$

while the fit of the bcc-fcc phase boundary is given by

$$\begin{aligned} \ln(U_0) &= 97.65106 - 150.469699\lambda + 106.626405\lambda^2 \\ &- 41.67136\lambda^3 + 9.639931\lambda^4 - 1.3150249\lambda^5 \\ &+ 0.09784811\lambda^6 - 0.00306396\lambda^7, \\ &\text{for } 1.85 \leq \lambda \leq 6.8. \end{aligned} \quad (2.22)$$

Together with Eq. (2.19), the fits in Eqs. (2.21) and (2.22) enable us to map the phase diagram of point Yukawa particles onto any hard-core Yukawa system.

2.4 Results

Using the methods described in Section 2.3, we study the phase behavior of hard-core Yukawa particles, whose interactions are described by the pair potential given by Eq. (2.1). The phase diagrams are calculated for fixed contact values ϵ and they are given in the $(\eta, 1/\kappa\sigma)$ representation. We calculate the phase diagram for four contact values, $\epsilon = 8, 20, 39,$ and 81 , and the results are given in Figs. 2.1, 2.2, 2.3, and 2.4, respectively. In all four phase diagrams, the gray areas bounded by the solid lines give the coexistence regions (tie lines are horizontal), while the dashed lines give the point Yukawa phase boundaries of Hamaguchi et al. [21] that are plotted using the mapping presented in Section 2.3.4. This section is organized in two parts: first we present the results; second we give technical details regarding the calculations.

Let us first describe the structure of the phase diagrams in Figs. 2.1-2.4. The phase diagrams start from the hard-sphere limit at $1/\kappa\sigma = 0$ with coexisting

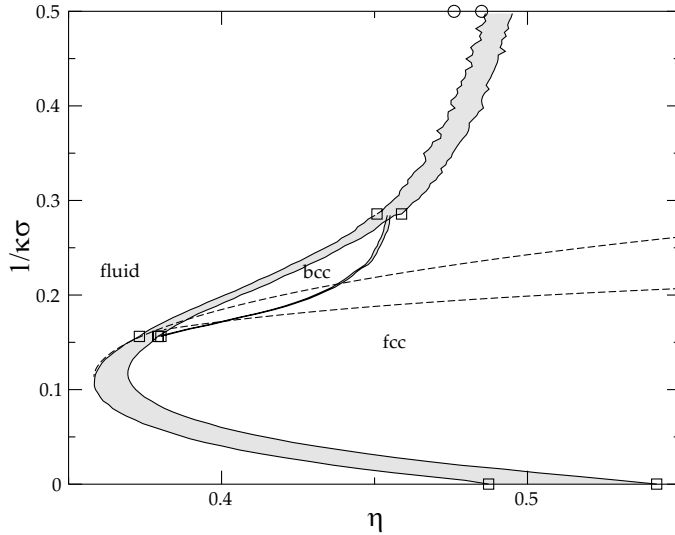


Figure 2.1: The phase diagram of hard-core Yukawa particles with $\epsilon = 8$ presented in the (η , Debye screening length $1/\kappa\sigma$) plane. The lower part of the diagram ($1/\kappa\sigma = 0$) is high salt regime and the upper part ($1/\kappa\sigma = 0.5$) is low salt regime. The solid lines are coexistence lines obtained from Gibbs-Duhem integration and the gray areas denote the coexistence regions, where tie lines are horizontal. We find a stable fluid phase at low η , a stable face-centered-cubic (fcc) solid at high η , and in between a stable body-centered-cubic (bcc) solid. The dashed lines are the phase boundaries of point Yukawa particles by Hamaguchi et al. [21]. The squares (\square) mark the starting points for Gibbs-Duhem integration and the circles (\circ) are control points from free energy calculations.

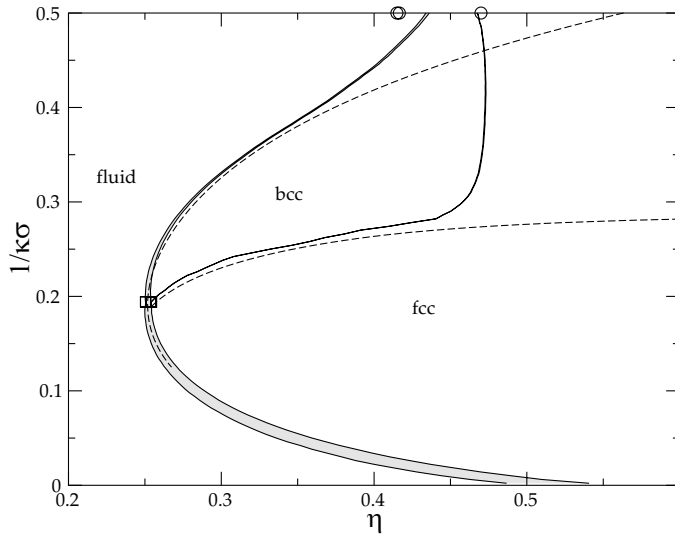


Figure 2.2: The phase diagram of hard-core Yukawa particles with $\epsilon = 20$ presented in the (η , $1/\kappa\sigma$) plane. The symbols and lines are the same as in Fig. 2.1. Note the difference in the η scale compared to Figs. 2.1, 2.3, and 2.4.

fluid and fcc phases at packing fractions $\eta = 0.491$ and $\eta = 0.543$, respectively. As the softness and the range of the interactions increase with increasing screening length $1/\kappa\sigma$, the fluid-fcc coexistence becomes thinner and moves to lower packing fractions, in agreement with Ref. [106]. A further increase of $1/\kappa\sigma$ takes us to a fluid-bcc-fcc triple point. Here the softness and the range of the interactions are so pronounced that at lower packing fractions it is more favorable to form a bcc crystal than an fcc crystal.

Increasing $1/\kappa\sigma$ from the triple point, two phase coexistence lines originate, namely the fluid-bcc and the bcc-fcc. While the fluid-bcc coexistence line is relatively slowly varying, the bcc-fcc line moves quickly to higher packing fraction,

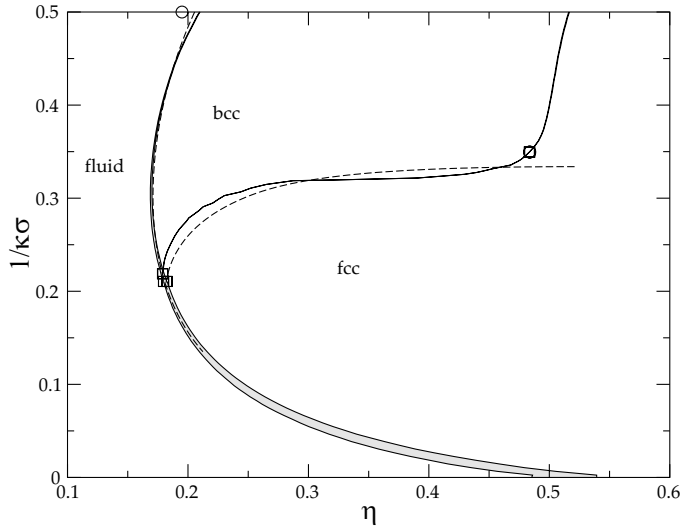


Figure 2.3: The phase diagram of hard-core Yukawa particles with $\epsilon = 39$ presented in the $(\eta, 1/\kappa\sigma)$ plane. The symbols and lines are the same as in Fig. 2.1. Note the difference in the η scale compared to Figs. 2.1, 2.2, and 2.4.

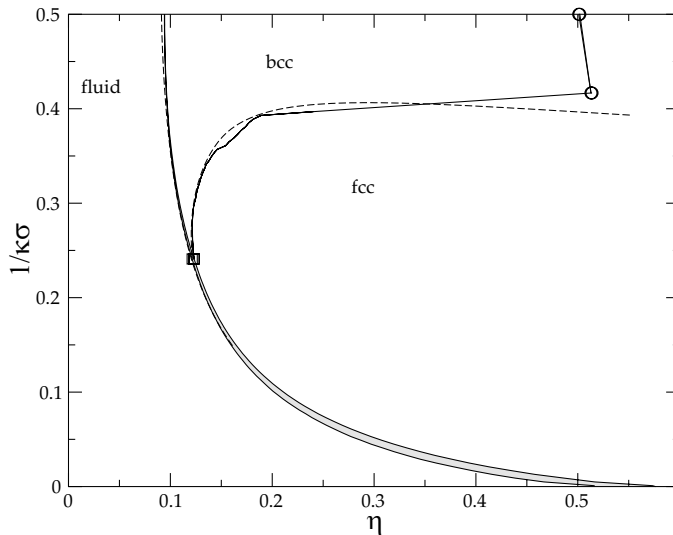


Figure 2.4: The phase diagram of hard-core Yukawa particles with $\epsilon = 81$ presented in the $(\eta, 1/\kappa\sigma)$ plane. The symbols and lines are the same as in Fig. 2.1. Note the difference in the η scale compared to Figs. 2.1, 2.2, and 2.3.

producing a broad region of stable bcc phase. This is especially true for $\epsilon = 20, 39,$ and 81 (Figs. 2.2-2.4), and we can see that the steepness of this “shoot-up” behavior becomes more pronounced with large ϵ . After the shoot-up, at higher values of $1/\kappa\sigma$, the bcc-fcc coexistence line turns and behaves more or less as a straight vertical line at $\eta \approx 0.5$. At high $1/\kappa\sigma$, the fluid-bcc coexistence line turns to higher packing fractions, i.e., here the fluid phase becomes more favorable with respect to the bcc phase. This is because at high $1/\kappa\sigma$, where the range of interactions becomes longer than the average interparticle spacing in the crystal, both the fluid and the bcc phase have a similar energetic contribution to the free energy, and thus the fluid phase wins since it has larger entropy.

It is worthwhile to note that in all the phase diagrams in Figs. 2.1-2.4, both the fluid-bcc and the bcc-fcc coexistence regions are very narrow, or in other words, the density difference between the two coexisting phases is small. In particular the bcc-fcc coexistence region is extremely narrow: the largest density jump

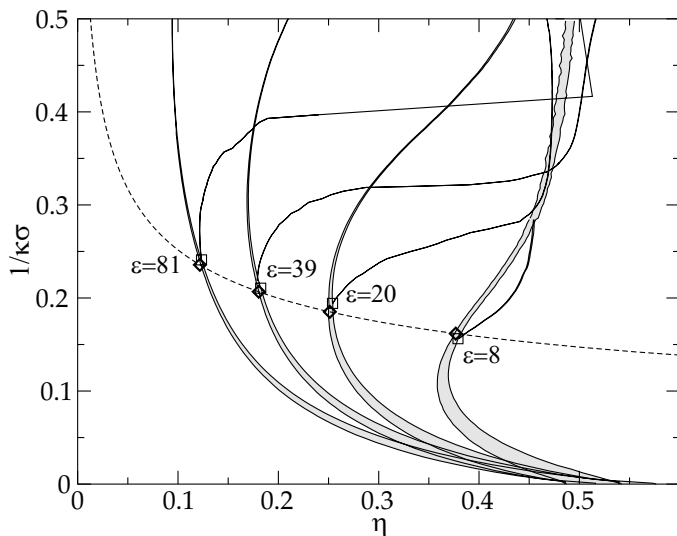


Figure 2.5: The phase diagrams of Figs. 2.1-2.4 plotted in one figure. The dashed line gives the line of triple points for point Yukawa particles [21], the diamonds (\diamond) highlight the triple points at $\epsilon = 8, 20, 39,$ and $81,$ and the squares (\square) mark the position of the triple points used in our calculations.

between the bcc and the fcc phases is at $\epsilon=8$, where it is less than 0.3%.* Therefore, it is surprising that some experiments on charge stabilized colloids report on (broad) bcc-fcc coexistence, i.e., they are able to have measurement points well inside the bcc-fcc coexistence region [9, 10].

In the case of the lowest contact value $\epsilon = 8$ (Fig. 2.1), the bcc region ends at another triple point around $1/\kappa\sigma = 0.28$. The presence of a second triple point for hard-core Yukawa particles was already found in Ref. [95], where the phase diagram for $\epsilon = 8$ was presented. The tendency of the bcc region to close up can also be seen in the phase diagram for $\epsilon = 20$ (Fig. 2.2), where the fluid-bcc and the bcc-fcc coexistence lines turn towards each other at around $1/\kappa\sigma = 0.5$. Note also that this tendency moves to higher $1/\kappa\sigma$ with increasing contact value ϵ . Based on our results, we expect another triple point for all ϵ at high values of $1/\kappa\sigma$, although our calculations could only reach it at $\epsilon = 8$. We also predict that with increasing ϵ , this other triple point escapes very quickly to high values of $1/\kappa\sigma$, where numerical calculations are difficult to carry out.

Figure 2.5 summarizes the results from Figs. 2.1-2.4 by plotting all the phase diagrams in one figure. As can be seen from Fig. 2.5, the low $1/\kappa\sigma$ triple point moves to lower η and higher $1/\kappa\sigma$ with increasing contact value ϵ . Another observation is that the region of stable bcc phase broadens mainly because the fluid-bcc coexistence line moves to lower packing fractions, while the bcc-fcc coexistence line moves only slightly to higher η and seems to saturate around $\eta \gtrsim 0.5$. The dashed line connecting the triple points in Fig. 2.5 is discussed later.

Now, we turn our attention to the comparison of our results on hard-core Yukawa particles with those obtained for point Yukawa particles by Hamaguchi et al. [21]. Note that the calculations of Hamaguchi et al. did not include the determination of phase coexistence regions. Therefore, in the case of point Yukawa particles only phase boundaries are considered. In Figs. 2.1-2.4 these phase boundaries are plotted with dashed lines. Figures 2.1-2.4 show that the phase bound-

*To put this in context, note that the density jump for the fluid-fcc coexistence of the hard spheres is around 10%.

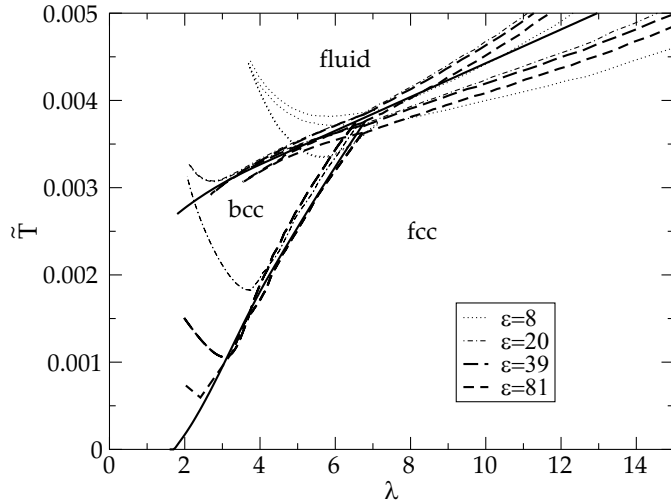


Figure 2.6: The phase diagram in the (λ, \tilde{T}) representation. The solid lines are point Yukawa results of Hamaguchi et al. [21] and the rest of the lines are our hard-core Yukawa results $\epsilon = 8, 20, 39,$ and 81 using the mapping discussed in the text. For clarity, the coexistence regions of the hard-core Yukawa results are left unfilled and only the coexistence lines are drawn.

aries of hard-core Yukawa particles approach those of the point Yukawa particles with increasing ϵ . This is because at high values of ϵ , the particles hardly ever get close enough to feel the hard-core interaction. High ϵ corresponds to highly charged colloids, see Eq. (2.2). The deviation between the point and hard-core Yukawa results is particularly pronounced for $\epsilon = 8$, see Fig. 2.1. For the phase diagrams with higher values of ϵ , the description with point Yukawa particles improves. Especially, the fluid-fcc line at high $1/\kappa\sigma$, the fluid-bcc line, and the beginning of the bcc-fcc line, are well predicted by the point Yukawa picture. However, the vertical rise of the bcc-fcc line at high $1/\kappa\sigma$ is completely missing in the point Yukawa phase diagram. Instead, the bcc region is predicted to become indefinitely broad in the point Yukawa system, and hence the second triple point is absent. Thus, the closing of the bcc region by a second triple point is caused solely by the presence of the hard-core.

Next, we make a small excursion to study the position of the low $1/\kappa\sigma$ triple point. In the case of point Yukawa particles, the position of the triple point is at $\lambda^{\text{tp}} = 6.90$ and $U_0^{\text{tp}} = 3474$ [21]. We can map this point to any hard-core Yukawa system by using Eq. (2.19). More specifically, we can solve the triple point $\kappa\sigma$ for a fixed ϵ from

$$\kappa\sigma e^{\kappa\sigma} = U_0^{\text{tp}} \lambda^{\text{tp}} / \epsilon \quad (2.23)$$

and use the second line of Eq. (2.19) to obtain η . The resulting line of triple points is denoted by the dashed line in Fig. 2.5, where the diamonds highlight the triple points at $\epsilon = 8, 20, 39,$ and 81 , and the squares give the triple points used in our calculations. We see that the agreement between the two results (the squares and the diamonds) does not depend much on the value of ϵ and therefore we can conclude that the position of the lower triple point is given quite precisely by the point Yukawa results.

It is also instructive to map our hard-core Yukawa phase diagrams in the (λ, U_0) and (λ, \tilde{T}) representations. These representations are typically used to draw the phase diagram of point Yukawa particles. The mapping is given by Eq. (2.19) and (2.20). The phase diagram in the (λ, \tilde{T}) representation is shown in Fig. 2.6,

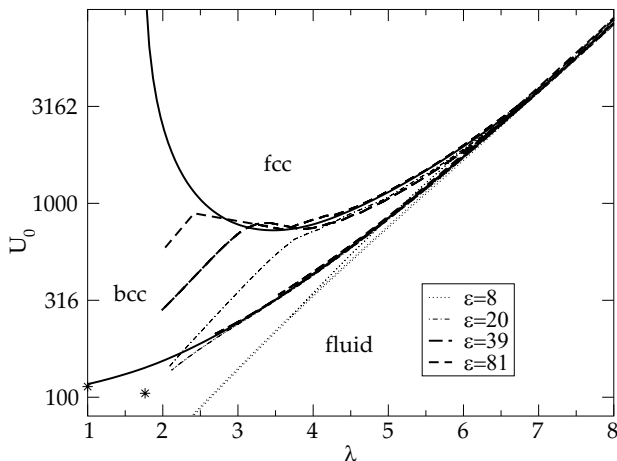


Figure 2.7: The phase diagrams in the (λ, U_0) representation plotted in linear-log scale. The lines are the same as in Fig. 2.6 and the stars (*) mark the approximate positions of the triple points for $\epsilon = 20$ and 39 , obtained by extrapolation.

where the solid lines are the point Yukawa results of Hamaguchi et al. [21] and the other lines are our hard-core Yukawa results. In Fig. 2.6, the effects due to the hard-core interaction are minimal in the regions where the phase lines with different ϵ fall on top of each other and on top of the point Yukawa phase lines. This is especially true near the low $1/\kappa\sigma$ triple point region, located at $\lambda^{\text{tp}} = 6.90$ and $\tilde{T}^{\text{tp}} = 0.0038$ [21]. Moving from this triple point to larger values of λ , corresponding to decrease of $1/\kappa\sigma$, we see that the point Yukawa fluid-fcc phase boundary stays between the fluid-fcc coexistence regions of the hard-core Yukawa results. Note that, the fluid-fcc phase coexistence region looks very broad in this representation and that the tie lines are no longer horizontal. Moving away from the triple point along the fluid-bcc or the bcc-fcc line, we see that deviations from the point Yukawa limit appear sooner for smaller ϵ .

In Fig. 2.7, we show the phase diagram in the (λ, U_0) representation plotted in linear-log scale. In this representation, the bcc-fcc and the fluid-fcc coexistence lines from our hard-core Yukawa calculations are almost linear. This inspired us to estimate the position of the high $1/\kappa\sigma$ triple point for $\epsilon = 20$ and $\epsilon = 39$ by simply extrapolating the coexistence lines and calculating the intercept point. The resulting approximate triple points are plotted in Fig. 2.7 with stars. After converting to the $(\eta, \kappa\sigma)$ plane using Eq. (2.19), they read $\eta = 0.47$ and $\kappa\sigma = 1.7$ for $\epsilon = 20$, and $\eta = 0.57$ and $\kappa\sigma = 1.0$ for $\epsilon = 39$.

2.4.1 Technical Details

The final part of this section is devoted to technical details about the phase diagram calculations and on error estimates. The phase diagram for $\epsilon = 8$ shown in Fig. 2.1 was already in Ref. [95] and serves also as a check for the methods used. In order to obtain the phase diagram in Fig. 2.1, four Gibbs-Duhem integrations were started from the three positions given in Ref. [95]: one from the hard-sphere limit corresponding to $p = 11.5541$, $1/\kappa\sigma = 0.0001$ ($\kappa\sigma = 10000.0$), $\eta_{\text{fluid}} = 0.491$, and $\eta_{\text{fcc}} = 0.543$, two from the lower triple point with $p = 20.70$, $1/\kappa\sigma \approx 0.156$ ($\kappa\sigma = 6.4$, Eq. (2.23) predicts $\kappa\sigma = 6.18$), $\eta_{\text{fluid}} = 0.373$, $\eta_{\text{bcc}} = 0.379$, and $\eta_{\text{fcc}} = 0.380$, and one from the higher triple point with $p = 44.1$, $1/\kappa\sigma \approx 0.286$ ($\kappa\sigma = 3.5$), $\eta_{\text{fluid}} = 0.453$, and $\eta_{\text{fcc}} = 0.460$. In all the Gibbs-Duhem integrations, the number of parti-

cles was $N_{\text{fluid}} = 256$, $N_{\text{bcc}} = 250$, and $N_{\text{fcc}} = 256$, and the step size was $\Delta(\kappa\sigma)^{-1} = 0.004$. The thermodynamic averages needed in Eq. (2.16) were calculated by performing 10 000 *NPT* MC steps (trial moves per particle or attempt to change the volume) both for the equilibration and for the production runs. When calculating the bcc-fcc coexistence, 30 000 steps were used.

The accuracy of the Gibbs-Duhem integration can be checked by measuring how the end points of the integration match with the results of free energy calculations. In order to know the fluid-fcc coexistence at $1/\kappa\sigma = 0.5$, free energy calculations were performed with system size $N_{\text{fluid}} = N_{\text{fcc}} = 500$. Here and in all subsequent free energy calculations, 10 000 *NVT* MC steps for the equilibration and measurement runs were taken in order to calculate the ensemble averages and 10 integration points were used in the Gauss-Legendre quadrature. In Fig. 2.1, the resulting fluid-fcc coexistence points are marked with circles. Figure 2.1 shows that the fluid-bcc, bcc-fcc, and low $1/\kappa\sigma$ fluid-fcc coexistence lines end up at the correct triple points. Therefore, we expect that the errors in the corresponding Gibbs-Duhem integrations are small. However, at $1/\kappa\sigma = 0.5$ the fluid-fcc coexistence points ($\eta_{\text{fluid}} = 0.486$ and $\eta_{\text{fcc}} = 0.495$) do not correspond exactly to the free energy results ($\eta_{\text{fluid}} = 0.476$ and $\eta_{\text{fcc}} = 0.485$), although the error is only about 1%. To check if the error is due to the difference in the system size, we redid the free energy calculation with the same system size as used in the Gibbs-Duhem integration, $N_{\text{fluid}} = N_{\text{fcc}} = 256$. This resulted in fluid-fcc coexistence with $\eta_{\text{fluid}} = 0.469$ and $\eta_{\text{fcc}} = 0.477$, leading to an error of slightly less than 2% with respect to the Gibbs-Duhem integration result. Furthermore, since the result with the same system size does not correspond to the end point of the Gibbs-Duhem integration, we can conclude that the error is most likely due to an error in the position of the second triple point at $1/\kappa\sigma \approx 0.286$.

In the other phase diagrams with $\epsilon = 20, 39$, and 81 , the location of the triple point, and hence the starting point of the Gibbs-Duhem integration, was obtained from Fig. 5 of Ref. [95]. Note that, while Fig. 5 of Ref. [95] gives only the pressure at the triple point, the packing fraction can be determined by performing an *NPT* MC simulation. For the phase diagram with $\epsilon = 20$ in Fig. 2.2, three Gibbs-Duhem integrations were started from $p = 15.0$, $1/\kappa\sigma \approx 0.194$ ($\kappa\sigma = 5.15$, while Eq. (2.23) predicts $\kappa\sigma = 5.40$) with $\eta_{\text{fluid}} = 0.250$, $\eta_{\text{bcc}} = 0.2540$, and $\eta_{\text{fcc}} = 0.2543$. The same system sizes, number of MC steps, and $\Delta(\kappa\sigma)^{-1}$ were used as in the phase diagram with $\epsilon = 8$. The two check points at $1/\kappa\sigma = 0.5$, the fluid-bcc and the bcc-fcc coexistence points, were obtained using free energy calculations with system sizes $N_{\text{fluid}} = N_{\text{bcc}} = 686$ and $N_{\text{fcc}} = 864$. As can be seen, the accuracy of the Gibbs-Duhem integration is good for the bcc-fcc coexistence line (error 1%) while the fluid-bcc line is slightly off (error 2%).

In the phase diagram with $\epsilon = 39$, in Fig. 2.3, the triple point is at $p = 10.516$, $1/\kappa\sigma \approx 0.211$ ($\kappa\sigma = 4.75$, Eq. (2.23) predicts $\kappa\sigma = 4.84$) with $\eta_{\text{fluid}} = 0.1797$, $\eta_{\text{bcc}} = 0.1824$, and $\eta_{\text{fcc}} = 0.1827$. Again the same system sizes, number of MC steps, and $\Delta(\kappa\sigma)^{-1}$ were used in the Gibbs-Duhem integration as for $\epsilon = 8$ and 20 . For the bcc-fcc phase coexistence line, the Gibbs-Duhem integration was stable until $1/\kappa\sigma \approx 0.32$. At higher values of $1/\kappa\sigma$, we found large fluctuations in η , denoting the breakdown of the Gibbs-Duhem integration. Only mild damping of the fluctuations was observed when the Gibbs-Duhem integration was re-

peated with a smaller step-size $\Delta(\kappa\sigma)^{-1} = 0.001$ (and with 15 000 MC steps). In order to resolve the bcc-fcc coexistence line above $1/\kappa\sigma = 0.32$, a new starting point was determined by free energy calculations at $1/\kappa\sigma \approx 0.35$ ($\kappa\sigma = 2.86$). The free energy calculations were performed for systems with $N_{\text{bcc}} = 700$ and $N_{\text{fcc}} = 768$ particles. The system size was increased in order to minimize the effect of the finite cut-off length. Note that with the new system sizes the simulation box is not cubic but close to it. The resulting bcc - and fcc packing fractions are $\eta_{\text{bcc}} = 0.4835$, $\eta_{\text{fcc}} = 0.4837$ with pressure $p = 240.318$. From this new coexistence point, using the larger system sizes, two Gibbs-Duhem integrations were performed: towards lower $1/\kappa\sigma$ (with $\Delta(\kappa\sigma)^{-1} = 0.002$) and towards higher $1/\kappa\sigma$ (with $\Delta(\kappa\sigma)^{-1} = 0.006$). The number of MC steps for both Gibbs-Duhem integrations was 20 000. For the Gibbs-Duhem integration going down in $1/\kappa\sigma$, again large fluctuations were seen near $1/\kappa\sigma = 0.32$. In order to obtain a continuous phase diagram we connected the stable parts of the two Gibbs-Duhem integrations. Free energy calculations were performed at $1/\kappa\sigma = 0.5$ for the fluid-bcc coexistence point ($N_{\text{fluid}} = N_{\text{bcc}} = 432$) and as can be seen the accuracy of the Gibbs-Duhem integration is adequate (error $< 2\%$).

In the phase diagram for $\epsilon = 81$, shown in Fig. 2.4, the location of the triple point is at $p = 7.242$ and $1/\kappa\sigma \approx 0.241$ ($\kappa\sigma = 4.15$, Eq. (2.23) predicts $\kappa\sigma = 4.24$) with $\eta_{\text{fluid}} = 0.1214$, $\eta_{\text{bcc}} = 0.1232$, and $\eta_{\text{fcc}} = 0.1234$. The same number of MC steps and $\Delta(\kappa\sigma)^{-1}$ were used as previously. Again, as for $\epsilon = 39$, the calculation of the bcc-fcc coexistence line was hindered because of a breakdown of the Gibbs-Duhem integration that this time occurred close to $1/\kappa\sigma = 0.4$. We noticed that above $1/\kappa\sigma = 0.4$, in order to get rid of the effect of the finite cut-off, the system size should be increased dramatically. Therefore, instead of performing Gibbs-Duhem integrations with very large system sizes, we used free energy calculations at two points, at $1/\kappa\sigma \approx 0.42$ ($\kappa\sigma = 2.4$) and at $1/\kappa\sigma = 0.5$, and connected the two points in order to get an estimate of the bcc-fcc coexistence line. The free energy calculation at $1/\kappa\sigma \approx 0.42$ was done with the same parameters as for $\epsilon = 39$, except that the system size for the bcc was increased to $N_{\text{bcc}} = 800$ (resulting in an almost cubic simulation box). At $1/\kappa\sigma = 0.5$, the system sizes were further increased to $N_{\text{bcc}} = 1024$ (cubic box) and $N_{\text{fcc}} = 972$ (almost cubic box).

2.5 Conclusions

We have determined the phase diagram of charged colloids, where the interactions are given within the DLVO theory by hard-core repulsive Yukawa pair potential. The phase diagrams were obtained using Monte Carlo simulations by a combination of Helmholtz free energy calculations and the Gibbs-Duhem integration method. We compared the phase diagrams with those of point Yukawa particles by mapping both systems onto each other. We showed that the difference between the phase behaviors of the hard-core Yukawa and point Yukawa particles reduces upon increasing the contact value ϵ , as might be expected. By comparing the phase diagrams in more detail, we determined the influence of the hard sphere interaction. We found that the fluid-bcc coexistence line is well predicted by the point Yukawa phase diagram, while at low screening length

(high $1/\kappa\sigma$) bcc-fcc coexistence line deviates. The reason for the difference in the bcc-fcc coexistence line is that at $\eta \gtrsim 0.5$, the hard-core repulsion favors the fcc phase. The behavior of the bcc-fcc coexistence line for hard-core Yukawa particles gives rise to a second triple point at low screening (high $1/\kappa\sigma$), something that is missing in the phase diagram of point Yukawa particles. It was observed that with increasing ϵ , the second triple point escapes quickly to low screening, where, with the methods used in this study, the calculations are difficult to carry out. Because of this, our calculations reached the second triple point only for the lowest contact value ϵ , for two other values of ϵ we estimated its position by extrapolation.

Our calculations explicitly included the determination of the phase coexistence regions. We observed that all of the coexistence regions are very small, i.e., the difference between the densities of the coexisting phases is small. This was seen to be the case especially for the bcc-fcc coexistence. It was also observed that the coexistence regions become smaller with increasing contact value ϵ . Therefore, one might expect that the coexistence regions of highly charged colloids would be unmeasurably narrow. However, this is in contrast with the experimental observations in Refs. [8–10] that report (relatively broad) fcc-bcc coexistence.

In conclusion, we show that the phase diagram of hard-core repulsive Yukawa particles can be obtained for any sufficiently high contact value ϵ^\dagger by mapping the well-known phase boundaries of the point Yukawa particles given by the fits (2.21) and (2.22) onto those of the hard-core repulsive Yukawa system using Eq. (2.19), and bearing in mind that the stable bcc region is bounded by a bcc-fcc coexistence at $\eta \approx 0.5$.

[†] $\epsilon = 20$ or higher, corresponding to charge $Z > 100$ for colloids with diameter $\sigma = 100$ nm suspended in water

3

Effect of Density-Dependent Truncation on the Phase Behavior of Charged Colloids

ABSTRACT

We study the phase behavior of charged colloids described by hard-core repulsive Yukawa particles where the repulsion is set to zero at distances larger than a density dependent cut-off distance. Earlier studies based on experiments and computer simulations in colloidal suspensions have shown that the *effective* colloid-colloid pair interaction that takes into account many-body effects resembles closely this truncated Yukawa potential. We calculate a phase diagram for the truncated Yukawa system by combining Helmholtz free energy calculations and the Gibbs-Duhem integration method. Compared to the non-truncated Yukawa system, we observe (i) a radical reduction of the stability of the body-centered-cubic (bcc) phase, (ii) a wider fluid region due to instability of the face-centered-cubic (fcc) phase and a re-entrant fluid phase, and (iii) hardly any shift of the fcc melting line when compared with the bcc melting line for the full Yukawa potential for sufficiently high salt concentrations. We compare our results with earlier results on the truncated Yukawa potential and with results from simulations where the full many-body Poisson-Boltzmann problem is solved.

3.1 Introduction

As was discussed in Chapter 1, the DLVO theory [17, 18] predicts that the effective pair interaction between two isolated charged colloidal spheres consists of a hard-core repulsion due to the finite size of the colloids and Yukawa (screened Coulomb) repulsion with the screening length given by the Debye length κ^{-1} of the electrolyte. The screening length κ^{-1} defines the thickness of the double layer of opposite charge surrounding each colloid. One speaks of a high-salt (low-salt) regime when the double layer around the colloid is thin (expanded).

In the regime of high-salt and/or low colloid volume fraction, where there is little overlap of more than two double layers, pairwise additivity is often assumed and the effective colloidal interactions are well described by the hard-core repulsive Yukawa model. However, in the opposite limit of low-salt and (relatively) high colloid volume fraction, the double layers of more than two colloids overlap considerably and there is no guarantee that the assumption of pairwise additivity should work. Instead, the total potential energy of the system is expected to be a sum of many-body (pair, triplet and so on) potentials of the colloids. By now it has been established both experimentally [54, 55] and by computer simulations [50, 56–58] that these many-body interactions between the colloids do exist, and that they manifest themselves as an enhanced decay in the effective colloid pair potential at distances larger than the typical pair separation. Qualitatively this effect can be understood as follows. For a pair of colloids at distances greater than the typical pair separation (at that density ρ), it is likely that there is a third particle between the pair. The effect of the third particle is to screen the repulsion between the pair of colloids, as shown by explicit numerical calculations [50]. The simplest way to incorporate this many-body screening to the colloid pair potential is to state that after a certain distance the colloids do not feel each other anymore and therefore the pair force is set to zero [56–58]. The distance at which the potential is truncated, the so-called cut-off distance, depends on the average separation of colloids, i.e., it is proportional to $\rho^{-1/3}$. This takes us to a simple model for the effective colloid pair potential, which has the usual hard-core Yukawa form at distances smaller than the cut-off distance, but is set to zero at colloid separations exceeding the cut-off distance. We use this so-called truncated hard-core Yukawa interaction as our effective colloid pair potential and we study the resulting phase behavior.

The motivation for our study is to find out what are the implications of the truncation to the phase behavior of Yukawa particles. In previous works on the phase diagram of the truncated Yukawa system, Dobnikar et al. [56–58] used the Lindemann criterion [107] to estimate the solid-liquid phase boundaries. This method, however, is not suitable for studying the relative stability of bcc and fcc crystal structures or phase coexistence. Therefore, we were motivated to calculate the “exact” phase behavior of truncated Yukawa system using a combination of Helmholtz free energy calculations and Gibbs-Duhem integration. Our findings are in agreement with the results of Dobnikar et al. [56–58] who found that the truncation promotes a fluid phase. This means that parts of the phase diagram that show a stable crystal phase (bcc or fcc) for the full Yukawa potential, are replaced by a fluid, when the potential is truncated. This observation

is also supported by Brownian dynamics (BD) simulations where the Poisson-Boltzmann (PB) equation is solved numerically “on the fly” for each colloid configuration during the BD simulation, i.e., it includes all the effective many-body interactions [56–58]. These PB-BD simulations are regarded here as the simulations that have the “correct” effective many-body interactions and thus give the “true” phase behavior, while the truncated Yukawa model tries to explain the results only with an effective density-dependent pair interaction that incorporates some of the many-body interactions. The current study makes the phase diagram of truncated Yukawa particles somewhat more precise: We show that the re-entrance of the fluid phase suggested in [56–58] does indeed exist. More importantly, we demonstrate the instability of the bcc phase with respect to the fcc phase. Destabilization of the bcc phase is also found in Chapter 4, where we will investigate the effect of three-body interactions on the phase diagram of charged colloids as a first order correction to pairwise additivity.

This chapter is organized as follows. In Section 3.2, we present the model and briefly discuss the methods used to calculate the phase diagram. In Section 3.3, we present the results and make comparisons with the results of Dobnikar et al. [56–58]. Finally, in Section 3.4 we conclude.

3.2 Model and Methods

Our model consists of particles interacting with a pairwise repulsive hard-core Yukawa potential that is truncated at a distance which depends on the average distance between the particles. More specifically, our pair potential is given by

$$\frac{u(r)}{k_B T} = \begin{cases} \infty & r < \sigma \\ \epsilon \frac{\exp[-\kappa\sigma(r/\sigma - 1)]}{r/\sigma} & \sigma \leq r < x\rho^{-1/3} \\ 0 & r \geq x\rho^{-1/3}, \end{cases} \quad (3.1)$$

where ϵ is the value of the pair potential at contact per $k_B T$, κ is the inverse Debye screening length, σ is the hard-core diameter, ρ is the number density of particles, and x is a dimensionless constant. In Eq. (3.1), $x\rho^{-1/3}$ is the cut-off distance, where $\rho^{-1/3}$ describes the average distance between particles and x is a prefactor that can be used to tune the cut. For example, in a crystal phase x determines how many nearest neighbor particles are included before the potential is truncated. We use $x = 1.5$, which gives a potential that is for the fcc truncated between the first and the second nearest neighbors and for the bcc between the second and the third. With this value for x , both fcc and bcc have approximately equal number of neighbor interactions: 12 for fcc and 14 for bcc.

A subtle difference between our model for the cut-potential in Eq. (3.1) and the one used by Dobnikar et al. [56–58] is that we truncate the pair potential, while they truncate the force. Our motivation to truncate the potential instead of the force stems from the experiments [54, 55], which suggest truncation in the pair potential. In the case of truncation with a smooth decay to zero, i.e., the one proposed by the experiments [54, 55], truncation of force and potential yield the same pair potential. However, in the case of non-smooth truncation, there are two

differences between a truncated pair potential, and a pair potential obtained by integrating the truncated force (called force-truncated potential in what follows): (i) Truncated potential has a step to zero at the cut-off distance, while the force-truncated potential does not, and (ii) the truncated potential has a fixed contact value ϵ , while the contact value of the force-truncated potential depends on the density. While the effect of (i) on the phase diagram is not known and would require further studies, the effect of (ii) was studied and found to be small.

Our goal is to calculate the phase diagram of a system in which the particles interact with (3.1) for fixed contact value $\epsilon = 81$. The phase diagram consists of stable regions of fluid, bcc, and fcc phases that are bounded by coexistence regions between two phases. Therefore, the determination of the phase diagram reduces to the calculation of the coexistence lines. We use a combination of Helmholtz free energy calculations and the so-called Gibbs-Duhem integration method to trace out the coexistence lines. In this method, Helmholtz free energy calculations are used to obtain a single phase coexistence point, from which Gibbs-Duhem integration are started to trace out the rest of the coexistence line. The same methods were used in Chapter 2 to study phase diagram of hard-core Yukawa particles. The details can be found from Sections 2.3.1, 2.3.2, and 2.3.3. *NPT*- and *NVT* Monte Carlo (MC) simulations needed in the Gibbs-Duhem integration and free energy calculations were carried out in a cubic box with periodic boundary conditions. The number of particles used in the simulations was $N = 256$ for the fluid and the fcc phase, and $N = 250$ for the bcc phase.

The results of Dobnikar et al. [56–58] were given in the so-called (λ, \tilde{T}) representation, while our results are given in (packing fraction η , Debye screening length $1/\kappa\sigma$) representation. Therefore, in order to compare the two results, we use the mapping presented in Section 2.3.4. In Chapter 2, it was shown that for sufficiently high ϵ , the phase boundaries are well-described by those of point Yukawa particles by employing this mapping.

3.3 Results

In Fig. 3.1, we show the phase diagram of particles whose interactions are described by Eq. (3.1) with contact value $\epsilon = 81$ and with $x = 1.5$ in the (packing fraction η , Debye screening length $1/\kappa\sigma$) representation. The solid lines in Fig. 3.1 give the coexistence lines obtained from the Gibbs-Duhem integrations, which were started from the phase equilibria points marked by the squares. These, and the other phase equilibria points marked by the circles, are calculated using the common tangent construction on free energy data obtained from separate Helmholtz free energy calculations. See Table 3.1 for numerical values of the phase equilibria points. The coexistence regions are shaded, while the tie-lines are horizontal. The dotted lines with labels $2k_B T$, $5k_B T$, and $10k_B T$ denote the regions where the potential at the cut-off distance is equal to the respective value. This means, for example, that at the right hand side of the line labelled with $2k_B T$, the value of the potential at the cut-off is larger than $2k_B T$. For comparison we plot the phase diagram of the non-truncated Yukawa system from Chapter 2 (the dashed lines). The phases for the non-truncated and truncated Yukawa systems

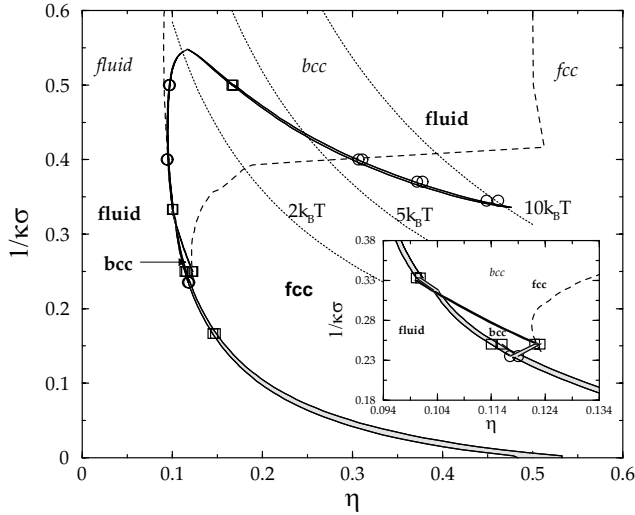


Figure 3.1: The phase diagram for a system in which the particles interact via a hard-core repulsive Yukawa pair potential (3.1) with $\epsilon = 81$ and cut-off $x = 1.5$ presented in the (packing fraction η , Debye screening length $1/\kappa\sigma$) plane. The low part of the diagram ($1/\kappa\sigma = 0$) is high salt regime and the upper part ($1/\kappa\sigma = 0.6$) is low salt regime. The solid lines are the coexistence lines obtained by the Gibbs-Duhem integration and the gray areas denote the coexistence regions with horizontal tie lines. The dashed lines are the phase boundaries of the hard-core Yukawa particles without truncation from Chapter 2 and the dotted lines with labels $2k_B T$, $5k_B T$, and $10k_B T$ denote the regions where the potential at the cut-off distance is equal to the respective value. The labels “fluid”, “bcc”, and “fcc” printed in *italic* are for the phase diagram of non-truncated Yukawa particles and the labels printed in **bold** are for the phase diagram of truncated Yukawa particles. The squares mark the starting points for the Gibbs-Duhem integration and the circles are check-up points for the coexistence, both of which are obtained using free energy calculations. The inset shows a close up of the bcc pocket.

are labelled with *italic* and **bold**, respectively. The inset in Fig. 3.1 shows a close up of the bcc pocket.

The phase diagram in Fig. 3.1 starts from the hard-sphere fluid-fcc coexistence at $1/\kappa\sigma = 0$ ($\kappa\sigma = \infty$). As the softness and the range of the interactions increase ($1/\kappa\sigma$ increases), the fluid-fcc coexistence becomes narrower and moves to lower packing fractions, until a fluid-bcc-fcc triple point is reached at $1/\kappa\sigma \approx 0.24$. Below the triple point ($1/\kappa\sigma < 0.24$), the truncated and non-truncated potential give basically the same result for the fluid-fcc coexistence lines. The reason for this is that in this regime where $\kappa\sigma$ is high (and density low), the pair potential is close to zero at the cut-off distance. Above the triple point ($1/\kappa\sigma > 0.24$), important deviation between the results of the truncated and non-truncated potential emerge: While the system with Yukawa interactions has a large bcc pocket (the region bounded by the dashed lines), only a small region of bcc is seen in the truncated Yukawa system. This region is concentrated close to the fluid-bcc-fcc triple point at $1/\kappa\sigma \approx 0.24$. The instability of the bcc phase is due to the short-range nature of the truncated potential: bcc is the stable phase in systems that have soft long-ranged interactions. This is why we expect that when the cut is made more dramatic, i.e., x is made smaller, the stability of the bcc phase is reduced even further. Conversely, with a less dramatic cut, i.e., with a larger x , more bcc phase is expected to be present. Indeed, preliminary free energy calculations with

$1/\kappa\sigma$	$P\sigma^3/k_B T$	η_1	η_2	Phases
0.167	5.94	0.145	0.148	fluid-fcc
0.235	-	0.118	0.119	fluid-fcc
0.250	6.29	0.114	0.116	fluid-bcc
0.250	7.53	0.122	0.123	bcc-fcc
0.333	7.31	0.100	0.101	fluid-fcc
0.345	-	0.450	0.460	fcc-fluid
0.370	-	0.372	0.378	fcc-fluid
0.400	-	0.094	0.095	fluid-fcc
0.400	-	0.307	0.311	fcc-fluid
0.500	-	0.097	0.098	fluid-fcc
0.500	37.62	0.166	0.169	fcc-fluid

Table 3.1: The phase coexistence points of Fig. 3.1 (the squares and circles) obtained from free energy calculations. $P\sigma^3/k_B T$ gives the dimensionless pressure, and η_1 and η_2 give the packing fractions of the two phases at coexistence. The pressure is only given at coexistence points from which Gibbs-Duhem integration was started (the squares in Fig. 3.1).

$x = 1.77$ showed a stable bcc phase at $1/\kappa\sigma = 0.4$. Note that, the destabilization of the bcc phase is also found in Chapter 4, where we investigate the effect of three-body interactions on the phase diagram of charged colloids. It is also worth mentioning that the fluid-fcc phase boundary above the second triple point follows closely the fluid-bcc phase boundary of the non-truncated Yukawa system. Thus, the sole effect of the truncation on the melting line at low η is that the bcc phase is replaced by the fcc phase.

Another effect of the truncation seen in Fig. 3.1 is the re-entrance of the fluid phase above $1/\kappa\sigma = 0.35$ at higher η , i.e., one observes a sequence of fluid, fcc, and again a fluid phase, with increasing colloid volume fraction. Re-entrance is not seen in Yukawa systems (see e.g. Chapter 2 and Refs. [19, 21, 94, 95]) but has been observed in an earlier study on truncated Yukawa system [56–58]. Although not studied here further, we expect that, because of the hard-core interaction, the fluid phase will freeze again to the fcc phase at high enough packing fractions, around $\eta \approx 0.5$. The reason why this re-freezing transition was not studied here is that the description using the truncated potential fails to represent any physically relevant system when the cut becomes too large. From Fig. 3.1 we see that at re-freezing the cut would be more than $10k_B T$.

In the low salt regime in Fig. 3.1, from around $1/\kappa\sigma = 0.4$ upwards, one sees that the fluid-solid phase boundaries with and without truncation deviate from each other (the difference between the dashed and the solid line); system with truncation has more fluid phase. Moreover, at $1/\kappa\sigma \approx 0.55$ the fluid-fcc and the re-entrant fcc-fluid phase coexistence lines join, implying that above this point only the fluid phase is stable.

In Fig. 3.2 we compare our results with the truncated point Yukawa system of Dobnikar et al. [56–58]: The filled and open diamonds connected with long-dashed lines mark the fcc and bcc melting lines for a truncated point Yukawa system with $x = 1.5$. Before analyzing Fig. 3.2 further, we wish to make a few remarks on the Lindemann criterion, which was employed in [56–58]. The Lindemann criterion states that at the melting line the root mean square displacements of the particles about their equilibrium positions in the crystal phase is a univer-

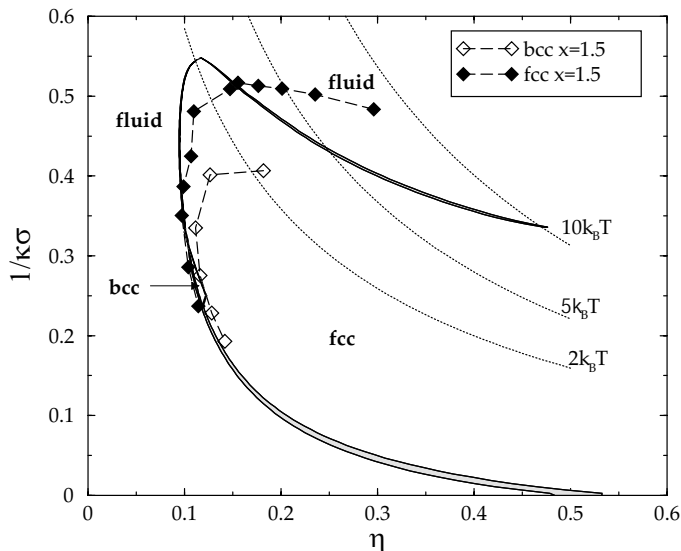


Figure 3.2: The phase diagram for a system in which the particles interact via a hard-core repulsive Yukawa pair potential (3.1) with $\epsilon = 81$ and cut-off $x = 1.5$ presented in the (packing fraction η , Debye screening length $1/\kappa\sigma$) plane. The low part of the diagram ($1/\kappa\sigma = 0$) is the high salt regime and the upper part ($1/\kappa\sigma = 0.6$) is the low salt regime. The solid lines are coexistence lines obtained by using the Gibbs-Duhem integration and the gray areas denote the coexistence regions with horizontal tie lines. The filled and open diamonds connected with long-dashed lines are, respectively, the fcc and the bcc melting lines for a truncated point Yukawa system with $x = 1.5$ from [56–58]. The dotted lines with labels $2k_B T$, $5k_B T$, and $10k_B T$ denote the regions where the potential at the cut-off distance is equal to the respective value.

sal fraction of the interparticle distance a , often taken to be 0.19 [107]. The solid phase should always be the stable phase immediately at the melting line. Simulation started from a *metastable* solid phase melts at lower temperatures or higher packing fractions than the stable solid phase [19]. Figure 3.2 shows that the truncated Yukawa bcc melting line of Dobnikar et al. [56–58] is at higher packing fraction than the fcc melting line for all $1/\kappa\sigma$, indicating that the bcc phase is always metastable with respect to the fcc phase at the solid-fluid phase boundary. The agreement of the fcc melting line with our fluid-fcc phase coexistence line is reasonable but gets worse with increasing $1/\kappa\sigma$. In particular, the prediction of the re-entrant fcc-fluid phase boundary clearly deviates from our result. The method used by Dobnikar et al. [56–58] is based on the Lindemann criterion, which is not accurate enough to find the tiny pocket of stable bcc phase at the melting line. It is tempting to relate the bcc melting line with the bcc-fcc phase boundary as was, although very implicitly, done in Refs. [56–58]. However, to our knowledge, it has never been tested that a universal behavior of the root mean square displacement hold at the solid-solid phase boundaries similar to that at the melting line, as stated by the Lindemann criterion. Comparing the bcc melting line obtained from the Lindemann criterion with our “exact” phase diagram, we indeed see that this line can not be associated with any of our phase boundaries.

In Fig. 3.3 we show results from Fig. 3.2 combined with the PB-BD results of Dobnikar et al. [56–58] in the (λ, \tilde{T}) representation. The open circles and full squares denote the melting points obtained from the PB-BD simulations while the (thin) solid lines give our results. The thick solid lines show the fluid-solid and the bcc-fcc phase boundaries of point Yukawa particles without truncation [21]. Please note that according to these non-truncated point Yukawa results,

the triangle formed by the thick lines has a stable bcc phase. From Fig. 3.3 we find that in our results the bcc phase is replaced by fcc, while the PB-BD results indicate that bcc phase gets substituted by fluid. The only agreement between our results and the PB-BD results is that both show more fluid phase than what is found when no truncation is used. Because of the lack of data, it can not be said if the re-entrance, seen in the truncated Yukawa results, would appear in PB-BD simulations. Keeping in mind that the fcc melting line is obtained from the Lindemann criterion for fluid-solid transitions, it is rather surprising that it follows so accurately the bcc-fcc line of the full Yukawa system. However, as already mentioned before and shown to be incorrect for the truncated Yukawa system, we should be very cautious in using the Lindemann criterion to predict any phase boundaries other than the fluid-solid one.

Finally, we would like to discuss some problems that arise when comparing the many-body PB-BD simulation results with results obtained using a pairwise Yukawa potential. The PB-BD simulation melting points of reference [56–58] were determined for several values of κ^{-1} by varying the charge Z at a *single* packing fraction $\eta = 0.03$. Once the melting point Z and κ^{-1} were known, the effective charge Z_{eff} and screening length κ_{eff}^{-1} were estimated. These effective values of Z and κ^{-1} are needed in order to make comparison with systems interacting with a pairwise Yukawa potential. As long as the hard-core does not play a role, and this is to be expected at $\eta = 0.03$, it is then possible to plot the results in the (λ, \tilde{T}) representation using the effective charge Z_{eff} and screening length κ_{eff}^{-1} , as was done in [56–58]. In order to re-plot our truncated Yukawa results from Fig. 3.2 in the (λ, \tilde{T}) plane, we employ the mapping that was presented in Section 2.3.4 and which is only valid when the hard-core does not play an important role. The effect of the hard-core on the phase behavior of the Yukawa system was studied earlier in Chapter 2. There it was found that for $\epsilon = 81$, the hard-core interaction leads to deviations in the phase behavior only at high packing fractions, around $\eta = 0.5$. In Fig. 3.2, only the very end of the re-entrant fcc-fluid phase coexistence line reaches such high packing fractions that one might expect deviations from the point-Yukawa system. Therefore, our results can be plotted in the (λ, \tilde{T}) plane. If the PB-BD simulation would be repeated at a different volume fraction than η , possibly a different phase diagram in the (λ, \tilde{T}) plane would be obtained. This is because the effective charge Z_{eff} and screening length κ_{eff}^{-1} depend on η . However, the pairwise Yukawa results, both ours and those from reference [56–58], can still be compared with the PB-BD results in the (λ, \tilde{T}) plane.

3.4 Conclusions

The phase diagram of a system where the particles interact with the truncated hard-core repulsive Yukawa potential of Eq. (3.1) was studied with contact value $\epsilon = 81$ and cut-prefactor $x = 1.5$. We observed (i) a radical reduction of the stability of the bcc phase with respect to the fcc phase, (ii) more fluid phase due to instability of the fcc phase and a re-entrant fluid phase, and (iii) for sufficiently high salt concentrations, hardly any shift of the fcc melting line when compared with the bcc melting line for the full Yukawa potential; i.e., truncation of the po-

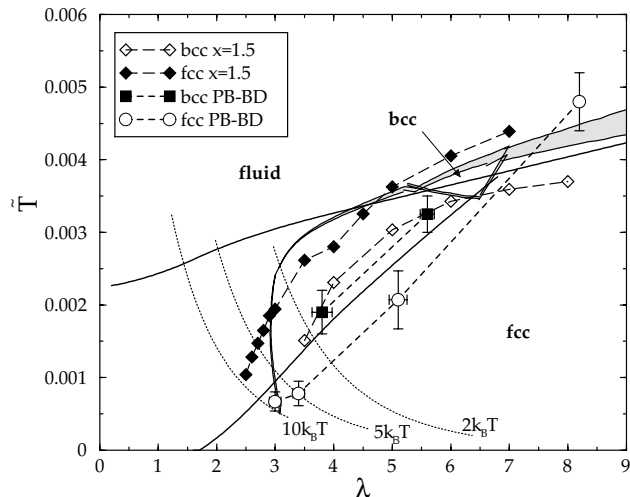


Figure 3.3: The phase diagram in the (λ, \tilde{T}) representation. The thick solid lines are the phase boundaries for point Yukawa particles obtained by Hamaguchi et al. [21] and the (thin) solid lines are the phase boundaries for a system of truncated hard-core Yukawa particles with $\epsilon = 81$ and with cut-off $x = 1.5$. The hard-core Yukawa results are plotted using the mapping given in Section 2.3.4. The filled and open diamonds connected with long-dashed lines are, respectively, the fcc and the bcc melting lines for $x = 1.5$ from [56–58]. The circles and the filled squares with error bars give the melting points of [56–58] for fcc and bcc phases, respectively, obtained from the PB-BD simulations where the full Poisson-Boltzmann equation is solved giving the “exact” effective many-body interaction for the colloids. The dotted lines with labels $2k_B T$, $5k_B T$, and $10k_B T$ denote the regions where the potential at the cut-off distance is equal to the respective value.

tential does not affect the location of the solid-fluid line, but only replaces the bcc phase with fcc at the melting line. Of these observations (ii) has already been confirmed by Dobnikar et al. [56–58] in the truncated point Yukawa system. However, whether the observations (i) and (iii) are supported by their results can not be answered since the Lindemann criterion used in [56–58] is not suited to resolve the relative stability of the bcc and fcc phases. Finally, we like to stress that (i), the instability of the bcc phase, is also seen in Chapter 4 where we will investigate the effect of three-body interactions on the phase diagram of charged colloids.

Only one value of the cut-prefactor, $x = 1.5$, was used in this study. It is natural to expect that if x is made larger all three effects (i), (ii), and (iii) mentioned earlier, will become less pronounced and finally vanish at $x = \infty$. Conversely, with smaller x , we expect that the three effects become more pronounced.

The only agreement with the full Poisson-Boltzmann Brownian dynamics (PB-BD) simulation results is the increased stability of the fluid phase. In order to obtain more quantitative comparison, a different cut prefactor x for fluid, bcc and fcc phases should probably be used. Also, in order to have a pair potential that agrees more with the real effective pair potential, instead of truncating the potential, a smooth decay to zero should be made. As a preliminary result we have seen that adding a smooth truncation alters the phase behavior of the system. For example, it is natural to expect that the bcc phase becomes more stable when introducing a smooth decay. However, playing with the cut and adding a smooth truncation increases the number of parameters considerably, and the real problem

is how to choose these parameters realistically. One way to obtain them would be to perform PB-BD simulations and extract the parameters by fitting to an effective pair potential. Finally, it is worth noting that since we are using a very simplified model to incorporate some of the many-body effects, one might not even expect good agreement with the PB-BD results and, thus, a direct comparison between both approaches is difficult. We also like to mention that it would be highly desirable to have more results on the phase behavior from the full PB-BD simulations in order to be able to make more definite conclusions about the many-body interactions, e.g. when are they important and what is the effect of them on the phase behavior and structure of the colloidal suspension.

Acknowledgements We thank H. H. von Grünberg and J. Dobnikar for providing the numerical data from Ref. [58].

4

Effect of Three-Body Interactions on the Phase Behavior of Charged Colloids

ABSTRACT

We study the effect of attractive three-body interactions on the phase behavior of suspensions of charged colloids at low salt concentration. In our computer simulations, we employ the effective two- and three-body potentials that were obtained from a numerical Poisson-Boltzmann study by Russ et al. [50]. On the basis of free energy calculations, we determine the phase diagram of an aqueous suspension of identical spheres of diameter $\sigma = 32$ nm and charge $Z = 80$ as a function of colloid concentration and salt concentration, both for the purely pairwise additive system and for the system with two- and three-body interactions. The main effect of the effective three-body interactions is a destabilization of the body-centered-cubic (bcc) crystal phase in favor of the face-centered-cubic (fcc) crystal phase. As a consequence, the phase diagram features coexistence of a rather dilute fluid with an almost close-packed fcc phase at low salt concentration, and bcc-fcc coexistence with a big density jump at intermediate salinity. The three-body attractions do not affect the phase behavior at sufficiently high salt concentration; under these conditions the system is well described by the pairwise potential description.

4.1 Introduction

As was mentioned in Chapter 1, the DLVO theory predicts that the effective pair interaction between the colloids consists of a hard-core repulsion due to the finite size of the colloids, screened-Coulomb (Yukawa) repulsion with the screening length given by the Debye length κ^{-1} of the electrolyte, and van der Waals attractions with a typical range of a few nm. The screening length κ^{-1} defines the thickness of the double layer of opposite charge surrounding each colloidal surface. The range κ^{-1} of the screened-Coulomb repulsion is a function of the salt concentration of the electrolyte, the dielectric constant of the solvent, and the temperature. Here we focus on the effect of the salt concentration as this can be tuned over several decades.

As we already discussed in Section 1.1.3, some experimental observations have been published that question the validity of the DLVO theory. Without exception these experiments were done in the low salt regime and they include observations of a broad gas-solid coexistence [38, 39], “voids” of vapor in otherwise homogeneous suspension [42, 43, 108], long-lived dense metastable crystallites [44, 108], even a gas-liquid coexistence [40] (although not without some dispute [41]). A long-range attraction between like-charged spheres would account naturally for these experimental observations, but would be in contradiction with the long-accepted DLVO theory. This discrepancy triggered intense theoretical and experimental activities and vivid debates. For more details on the current state-of-affairs, the reader is referred to review papers [109, 110]. At low salt concentration, of the order of several μM 's, the double layer thickness is of the order of the colloid diameter, i.e., $\kappa^{-1} \geq \sigma$, and pairwise additivity might break down as many-body interactions become important. In some of the theoretical approaches the many-body contributions are captured in so-called volume terms that do not depend on the particle coordinates but on the density of the system [47–49, 62, 111–115]. Alternatively, one captures the many-body effect by many-body potentials, i.e., functions of the colloidal coordinates but *not* of colloid density.

Recent experimental [54, 55, 59, 116] and theoretical [50, 56–58] results support the existence of many-body effects. Both studies show that the pair repulsion is reduced at distances larger than the mean distance between the colloids, due to many-body interactions. The reduction of the repulsion at distances larger than the mean distance between the colloids can be traced back to the shielding effect of the macroions. This is in line with recent explicit numerical calculations within nonlinear Poisson-Boltzmann theory, which show that the pairwise repulsion between two colloids is dramatically reduced when a third colloid is placed in between [50]. This effect results in effective *attractive* three-body interactions between the charged colloidal spheres. At high salt concentrations this effect is not important, since the double layers are small and the Yukawa repulsion has already decayed at the distance between the outermost colloids (two diameters or more). However, at low salt concentrations the double layers are large and a considerable reduction of the repulsion between the outermost colloids is caused by the presence of the third intermediate colloid: pairwise additivity breaks down and many-body interactions become important. Based on numerical calculations,

simple empirical expressions were obtained for the two- and three-body interactions within the nonlinear Poisson-Boltzmann theory, specifically in the nonlinear regime of low salt concentrations and high charges [50]. Moreover, it was shown within a van der Waals-like mean-field theory that the strength of the attractive three-body interaction is large enough to induce gas-liquid phase coexistence.

In this chapter, we use computer simulations to study the effect of attractive three-body interactions on the phase behavior of charge-stabilized colloidal suspensions. We determine the phase diagram using free energy calculations both for an effective one-component system of colloids interacting with two- and three-body interactions, and that of a pairwise system without the three-body interactions. We find that attractive three-body interactions drive most likely a gas-solid transition, instead of a gas-liquid transition that was found previously within the van der Waals-like mean-field theory [50]. Moreover, the presence of three-body attractions also affects the relative stability of fcc and bcc crystals.

The rest of this chapter is organized as follows. In Section 4.2 we present our model, and in Section 4.3 we briefly describe the simulation techniques used. The results are given in Section 4.4, and we make some concluding remarks in Section 4.5.

4.2 Model

Our model for the colloidal suspension consists of N identical spherical colloidal particles with a hard-core diameter σ and a uniformly distributed surface charge of $-Ze$, immersed in a volume V , together with NZ monovalent counterions, and added salt at a bulk (reservoir) concentration of ρ_s . The unit (proton) charge is denoted by e_s . The monovalent positive counterions and negative coions are assumed to be charged point particles. The electrolyte is treated as a structureless continuum characterized by the dielectric constant ϵ . In our approach, the microions are not treated individually, but at the level of their equilibrium density distributions $\rho_{\pm}(\mathbf{r})$ for the positive and negative microions in a fixed configuration of the colloids. Due to large differences in time scales, the microions may be assumed to be in thermodynamic equilibrium for any configuration of the colloids. The inhomogeneous density distributions $\rho_{\pm}(\mathbf{r})$ in the presence of a fixed configuration of colloidal particles can be obtained by solving the nonlinear Poisson-Boltzmann equation. It is convenient to treat the electrolyte grand-canonically, i.e., at fixed chemical potential of salt μ_s . Once $\rho_{\pm}(\mathbf{r})$ have been determined, the effective interactions between the colloids are given by

$$V_{\text{eff}}(\{\mathbf{r}_i\}) = \sum_{i < j}^N u_{\text{HS}}(\mathbf{r}_i, \mathbf{r}_j) + \Omega(\{\mathbf{r}_i\}, N, \mu_s) \quad (4.1)$$

where the center-of-mass coordinates of the colloids are given by \mathbf{r}_i with $i = 1, \dots, N$, $\Omega_N = \Omega(\{\mathbf{r}_i\}, N, \mu_s)$ is the grand potential of the electrolyte in the external field of a fixed configuration of N colloidal particles, and

$$u_{\text{HS}}(\mathbf{r}_i, \mathbf{r}_j) = \begin{cases} 0, & r \geq \sigma \\ \infty, & r < \sigma \end{cases} \quad (4.2)$$

is the non-electrostatic hard-sphere part of the pair potential between colloids i and j . In principle, the effective interactions can be calculated “on the fly” for each colloid configuration in the same spirit as the “ab initio” method of Car and Parrinello for ion-electron systems [117] (Applications for colloidal systems are found in Refs. [118–120]). However, here we adopt a different method based on effective n -body interactions. It can be shown explicitly that Ω_N can be uniquely decomposed into effective n -body interactions $\Omega^{(n)}$ between the colloids [50, 121]:

$$\Omega_N = N\Omega^{(1)} + \sum_{i<j}^N \Omega^{(2)}(\mathbf{r}_i, \mathbf{r}_j) + \sum_{i<j<k}^N \Omega^{(3)}(\mathbf{r}_i, \mathbf{r}_j, \mathbf{r}_k) + \cdots, \quad (4.3)$$

where the ellipsis represents the terms $\Omega^{(n)}$ for $n \geq 4$. The n -body potentials are defined in a system with n colloids with neutralizing counterions in contact with a salt reservoir at chemical potential μ_s . The one-body potential $\Omega^{(1)}$ is actually the grand-potential difference between a sea of salt at μ_s and volume V with and without a single colloid; it can be interpreted as the self-energy of a colloid or the Henry coefficient. The effective pair potential $\Omega^{(2)}(\mathbf{r}_i, \mathbf{r}_j)$ between two colloids is the grand potential difference between a system with volume V containing two colloids at separation $r_{ij} = |\mathbf{r}_i - \mathbf{r}_j|$ and at infinite separation. For $n > 2$, the effective n -body interactions can be defined along the same lines and will depend on the exact coordinates of n colloids. It is worth noting that the mapping of Ω_N onto effective n -body interactions with $n = 1, \dots, N$ is exact. One actually hopes, of course, that the rate of convergence of the expansion is fast and that Ω_N can be approximated by only including n -body potentials of $n = 1, 2, \dots, n^* \ll N$. In many cases, the expansion is truncated at pair potential level, and three- and higher-body interactions are ignored. In Ref. [50], two- and three-body interactions were calculated numerically within Poisson-Boltzmann theory. The effective pair interactions turn out to be purely repulsive and can be fitted by a screened Coulomb potential, consistent with the well-known DLVO result:

$$\frac{\Omega^{(2)}(r)}{k_B T} = A^{(2)} \frac{\lambda_B}{\sigma} \frac{\exp(-\kappa r)}{r/\sigma}, \quad (4.4)$$

Here $A^{(2)}$ is a fitting constant, $\kappa = \sqrt{8\pi\lambda_B\rho_s}$ is the inverse Debye screening length, and $\lambda_B = e^2/\epsilon_s k_B T$ is the Bjerrum length. By contrast, the three-body interactions are purely attractive in all cases considered. More surprisingly, the three-body interaction calculated for many configurations of the three colloids collapsed onto one master curve that can be fitted remarkably well by a Yukawa potential which depends on the sum of the three distances $L = r_{ij} + r_{jk} + r_{ik}$, instead of the three distances separately:

$$\frac{\Omega^{(3)}(L)}{k_B T} = -A^{(3)} \frac{\lambda_B}{\sigma} \frac{\exp(-\gamma L)}{L/\sigma}, \quad (4.5)$$

where the two fit parameters are the decay constant γ and the prefactor $A^{(3)}$. The prefactors $A^{(2)}$ and $A^{(3)}$, as well as the decay length γ , are given in Ref. [50] for

different combinations of the reduced charge $\bar{Z} = Z\lambda_B/\sigma$ and screening length $\kappa\sigma$. These empirical fits for the two- and three-body potentials enable us to perform computer simulations and study the effect of attractive three-body potentials as the lowest-order correction to pairwise additivity.

4.3 Methods

Our purpose is to calculate the Helmholtz free energy of a system with a Hamiltonian that includes a potential energy that is given as a sum of the two- and three-body potential energies of Eqs. (4.4) and (4.5), respectively, and of the hard-core contribution $u_{\text{HS}}(\mathbf{r}_i, \mathbf{r}_j)$. That is, the potential energy function of our Hamiltonian is written as

$$U(\mathbf{r}^N) = \sum_{i<j}^N \left[u_{\text{HS}}(\mathbf{r}_i, \mathbf{r}_j) + \Omega^{(2)}(r_{ij}) \right] + \sum_{i<j<k}^N \Omega^{(3)}(r_{ij} + r_{jk} + r_{ik}). \quad (4.6)$$

Note that the kinetic energy term in the Hamiltonian plays no role in phase stability and can therefore be ignored.

The simulations are performed in a cubic box with periodic boundary conditions and the minimum image convention is used. While the minimum image convention works fine for particle pairs, there is no unique way of applying it to a group of three particles [122]. In order to see this, consider a triangle of particles labelled by i , j , and k . The minimum image convention can only be applied to two sides of the triangle, say to particle j with i and to particle k with i . The distance between particle j and k is then fixed. However, the distance between the closest image of particles j and k with respect to particle i is not necessarily the minimum image distance of j to k . This can easily be shown by defining the x component of the translation vector

$$t_{ij} = [(x_i - x_j)/K]K \quad \text{and} \quad t_{ik} = [(x_i - x_k)/K]K, \quad (4.7)$$

where K is the box length and $[x]$ the closest integer to x . After applying the minimum image convention, the x component of the separation vectors between the three particles are given by

$$\begin{aligned} x_{ij} &= x_i - x_j - t_{ij} \\ x_{ik} &= x_i - x_k - t_{ik} \\ x_{jk} &= x_j - x_k + t_{ij} - t_{ik}, \end{aligned}$$

and similarly for the y and z components. In most cases, x_{jk} is equal to the result given by minimum image convention, where $x_{jk} = x_j - x_k - t_{jk}$. However, for cases where this is not true, one should check if the total side length of the triangle can be minimized by applying the minimum image convention to the other sides of the triangle. In fact, there are at most three possible choices of triangles that have at least two sides with lengths less than half the box length. This is because the minimum image convention can only be applied to two sides of the triangle. However, in order to save CPU time, we have chosen a simpler

minimum image convention. Our minimum image rule for the triplets is best explained and motivated by considering the way the potential energy is calculated: We first take particle i (N choices), we then take particle j , from the set of $N - 1$ particles that are left, and apply the minimum image rule for particle i and j . The two-body potential $\Omega^{(2)}$ is calculated for the pair ij . For each pair ij we take a third particle k from the set of $N - 2$ particles that are left. Since now the distance between i and j is already fixed, we only have two choices for the minimum image of k , i.e., we can take the minimum image of k with respect to i or with respect to j . By choosing the minimum image of k that gives the triangle with the smallest total side length $r_{ij} + r_{jk} + r_{ik}$, we take into account the position of particle k that screens the pair interaction between particles i and j the most.

A consequence of this three-body minimum image convention is that the resulting three-body potential energy $\sum_{i < j < k}^N \Omega^{(3)}(r_{ij} + r_{jk} + r_{ik})$ depends on the order in which the summation is done. This is why the result is not (in all geometries) equal to one sixth of the unrestricted sum $\sum_{i,j,k}^N \Omega^{(3)}(r_{ij} + r_{jk} + r_{ik})$, where all triangles are calculated six times. However, according to our tests, the error is at least five orders of magnitude smaller than the error due to statistical noise. The two-body potential is truncated at a cut-off radius r_c , which is chosen to be equal to the half of the box length. For the three-body potential we choose to truncate the potential when one of the side lengths of the minimum image triangle is greater than r_c (the same method as used in Ref. [122]).

The free energy calculations were done as described in Sections 2.3.1 and 2.3.2. We used 10 points in the Gauss-Legendre quadrature. This number of integration points was tested to be adequate by recalculating some of the results with more (20 or 32) integration points. The number of particles was chosen to be $N = 250$ for the bcc and $N = 256$ for the fcc and the fluid phase. The solid phase free energies were calculated by rewriting the numerical integration as in Eq. (2.8). The value of c given by Eq. (2.9) was evaluated in the beginning of the free energy calculation.

Each evaluation of the integrands in Eqs. (2.5) and (2.14), respectively, consisted of an equilibration run and a sampling run, both with 1000 – 2000 trial moves per particle. For systems interacting with a potential energy given by Eq. 4.6, the evaluation of the three-body interaction scales with N^3 . Our choice of trial moves resulted in MC simulations that took about 36 CPU hours per free energy point on a supercomputer. In order to map out the phase diagram the Helmholtz free energy must be determined for the fluid, bcc, and fcc phase and for many statepoints, i.e., about 10 different packing fractions and about 8 different values of salt concentrations or $\kappa\sigma$, which resulted in approximately one year of CPU time on a supercomputer. For the two-body system the number of trials was often increased to 10 000 per particle. At small values of λ , the data become more noisy and therefore, in order to reach better statistical accuracy, the number of trial moves was doubled for the three integration points with smallest value of λ and for estimation of the parameter c (the $\lambda = 0$ point).

In our free energy calculations, the Madelung energy $U(\mathbf{r}_0^N)$ in Eq. (2.6) was evaluated for a large crystal with 5000 - 20 000 particles. For such system size, the tail correction to the potential energy due to the finite cut-off radius can be ne-

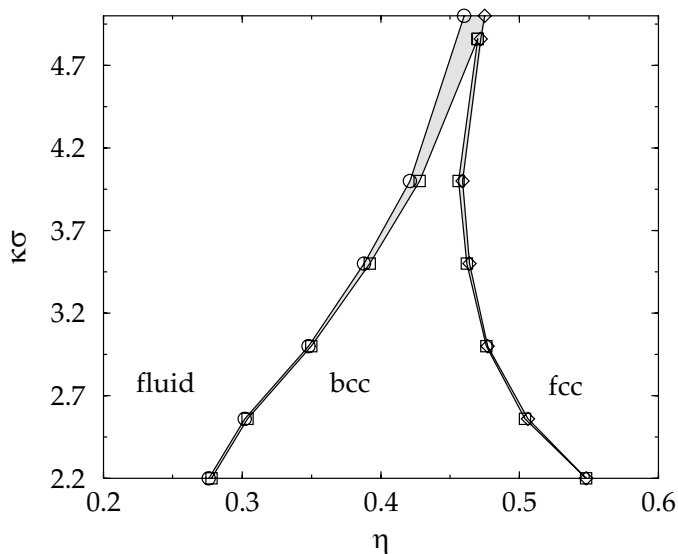


Figure 4.1: The phase diagram for $\bar{Z} = 1.8$ including only the two-body interactions. The gray color represents a coexistence region, while circles (\circ), squares (\square), and diamonds (\diamond) represent the fluid, bcc, and fcc phase boundaries, respectively.

glected. Therefore, no further tail corrections to the potential energy are needed*. Similar treatment is not possible for fluid, and therefore, the fluid free energy calculation inevitably suffers from the finite cut-off radius r_c for the potential energy. For a system with only pair interactions, this problem can be solved by adding a tail contribution to the potential energy, which is approximated by the potential energy due to a continuous distribution of particles beyond the cut-off radius r_c , i.e., by setting $g(r) = 1$ for $r > r_c$ [93]. A similar tail correction for the three-body potential $\Omega^{(3)}$ is not very practical as it requires a numerical integration over a three-dimensional region, and the approximation $g(r) = 1$ is not accurate because some triangles consist of particle pairs with $r < r_c$. Therefore, the fluid tail correction is approximated by setting it equal to the tail correction for an ideal fcc crystal at the same density. The fcc crystal tail correction is calculated as the difference in the Madelung energies of an “infinite” crystal with 5000 - 20 000 particles and a crystal with 256 particles.

4.4 Results

Using the methods described in Section 4.3, we performed free energy calculations for given $\kappa\sigma$ and $\bar{Z} = Z\lambda_B/\sigma$ with the parameters $A^{(2)}$, $A^{(3)}$, and γ taken from Ref. [50]. Common tangent construction was used to determine phase coexistence from the free energy data. We chose the ratio between the Bjerrum length and the colloidal diameter to be $\lambda_B/\sigma = 0.0225$, and focused on calculating the phase behavior for reduced charge $\bar{Z} = 1.8$. This corresponds to a charge $Z = 80$ and, in water at room temperature (for which $\lambda_B = 7.2 \text{ \AA}$), to diameter $\sigma = 32 \text{ nm}$. Phase diagrams are presented in the $\eta - \kappa\sigma$ representation, where $\eta = \pi\sigma^3 N/6V$ is the colloidal packing fraction. Note that κ does *not* depend on η .

In Fig. 4.1, we present the phase diagram for a system including only the two-body interactions, i.e., for the potential energy of Eq. (4.6) where the three-body

*However, the finite cut-off does affect the value of the ensemble average in Eq. (2.5).

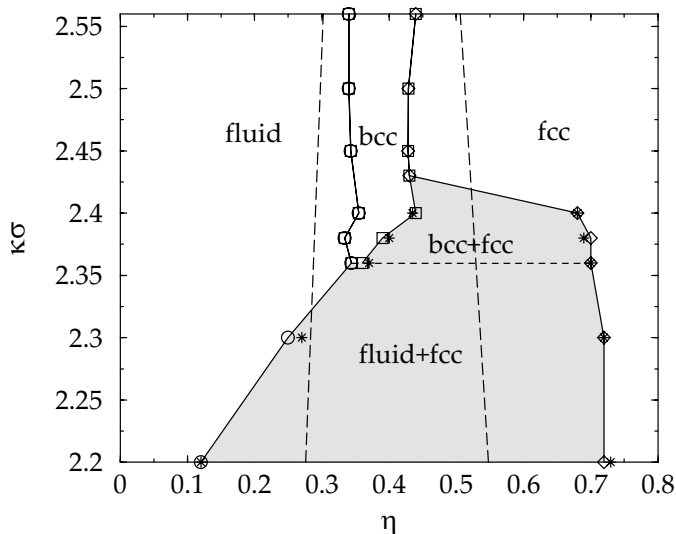


Figure 4.2: The phase diagram for $\bar{Z} = 1.8$ including the two- and three-body interactions. The gray color represents a coexistence region, while circles (\circ), squares (\square), and diamonds (\diamond) represent the fluid, bcc, and fcc phase boundaries, respectively. The stars ($*$) mark the bcc-fcc and the fluid-fcc coexistence points based on Eq. (4.8). The two vertical long-dashed lines represent the fluid-bcc and bcc-fcc phase boundaries of the system with only two-body interactions, see Fig. 4.1. The horizontal dashed line denotes the fluid-bcc-fcc triple point.

term is disregarded. The coexistence regions are colored gray, and tie lines between the coexisting phases are horizontal. The prefactors $A^{(2)}$ for $\kappa\sigma > 2.56$ were obtained by linear extrapolation with respect to $\kappa\sigma$. This is because the data in Ref. [50] only goes up to $\kappa\sigma = 2.56$. As can be seen from Fig. 4.1, the bcc phase is very much favored at low values of $\kappa\sigma$ (low salt), while the bcc regime ends in an upper triple point (position of which is given here only as a rough estimate) at $\kappa\sigma \simeq 4.86$. We compared our fluid-bcc coexistence line with the one given for point-Yukawa particles in Ref. [21], and found them to be in good agreement in the low- $\kappa\sigma$ regime, where the hard-core is not expected to play a role. Note also from Fig. 4.1 that the fluid-bcc and the bcc-fcc coexistence regions shrink when moving to the lower values of $\kappa\sigma$, as expected since the potential becomes softer.

In Fig. 4.2, we present the phase diagram for the same system but now with two- and three-body interactions, i.e., for the full potential in Eq. (4.6). Note the different $\kappa\sigma$ scale in Figs. 4.1 and 4.2. Because the values of the parameters $A^{(2)}$, $A^{(3)}$, and γ are only given in Ref. [50] for $\kappa\sigma = 2.0$ and $\kappa\sigma = 2.56$, linear interpolation with respect to $\kappa\sigma$ was used to get the parameter values at intermediate $\kappa\sigma$. Figure 4.2 shows a very broad fluid-fcc coexistence in the low-salt regime at $\kappa\sigma \lesssim 2.36$, below the fluid-bcc-fcc triple point (denoted by the horizontal dashed line in Fig. 4.2). In the regime $2.36 \lesssim \kappa\sigma \lesssim 2.43$ above the triple point, there is a very narrow fluid-bcc coexistence at $\eta \approx 0.35$, and a rather broad bcc-fcc coexistence at higher η . The density jump of the latter shrinks upon approach of $\kappa\sigma \approx 2.43$, and goes to a negligible value for $\kappa\sigma > 2.43$.

The essentially vertical long-dashed lines in Fig. 4.2 give the fluid-bcc and bcc-fcc phase boundaries of the system where only two-body interactions are present (Fig. 4.1). We observe that the inclusion of the three-body interactions reduces the stability of the bcc phase in the regime $2.36 \lesssim \kappa\sigma \lesssim 2.56$, and closes up the bcc pocket at $\kappa\sigma \approx 2.36$. In the limit of high salt, the phase diagram of the system with the two- and three-body interactions (Fig. 4.2) should converge to the phase diagram of the system with only the two-body interactions (Fig. 4.1). In order to investigate this, we calculated the Madelung energies per particle at $\kappa\sigma = 4.0$

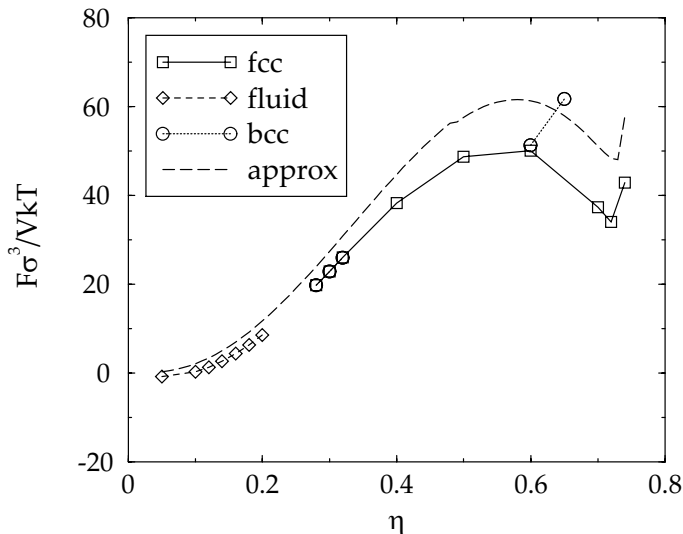


Figure 4.3: Helmholtz free energies per volume for the fluid, bcc, and fcc phases, at $\kappa\sigma = 2.2$. Also shown is the result from the approximate theory of Eq. (4.8).

for both systems, and found them to be very close to each other. Therefore, we expect that at $\kappa\sigma > 4.0$ the phase diagram of Fig. 4.2 reduces to the two-body phase diagram of Fig. 4.1.

In Fig. 4.3, we show the free energy data for $\kappa\sigma = 2.2$, which includes the two- and three-body interactions. A common tangent construction reveals a coexistence between a fluid at packing fraction $\eta \approx 0.12$ and an fcc solid at packing fraction $\eta \approx 0.72$. Because the dip in the fcc free energy at $\eta \approx 0.72$ is very deep, the underlying fluid-bcc coexistence is metastable and the same holds for a possible gas-liquid coexistence. In order to study the source of this dip we made a very simple theoretical approximation for the free energy based on the sum of the Madelung energy (energy term) and the free energy of a hard-sphere system (entropy term) as

$$F_{\text{Approx}}(\eta) = Nu_M(\eta) + \begin{cases} F_{\text{HS}}^{\text{fluid}}(\eta) & \eta \leq 0.49 \\ F_{\text{HS}}^{\text{sol}}(\eta) & \eta > 0.49. \end{cases} \quad (4.8)$$

Here the Madelung energy per particle $u_M(\eta)$ is that of an fcc solid and the free energy of the hard sphere solid $F_{\text{sol}}^{\text{HS}}(\eta)$ is obtained from the equation of state by Hall [123]. In Fig. 4.3, F_{Approx} is plotted with the long-dashed line and, as can be seen, the result is qualitatively the same as the one from the elaborate free energy calculations. This result explains the very broad fluid-fcc coexistence: because of the three-body attraction, at low $\kappa\sigma$ and high densities ($\eta > 0.55$ for $\kappa\sigma = 2.2$) the Madelung energy per particle u_M is a monotonically decreasing function of the density. This produces a lowering of the free energy at high densities, which in Fig. 4.3 can be seen at $\eta \approx 0.6$. At very high densities ($\eta \approx 0.72$ in Fig. 4.3), the free energy shoots up again, because there the hard sphere solid free energy $F_{\text{HS}}^{\text{sol}}$ starts to increase rapidly. Thus the competition between the Madelung energy and the hard sphere free energy, produces a minimum in the fcc free energy curve at high density, and explains the broad fluid-fcc coexistence. As the range of the three-body attraction is reduced at higher values of $\kappa\sigma$ (higher salt concentrations), the minimum becomes less pronounced. At the same time, the coexisting fluid

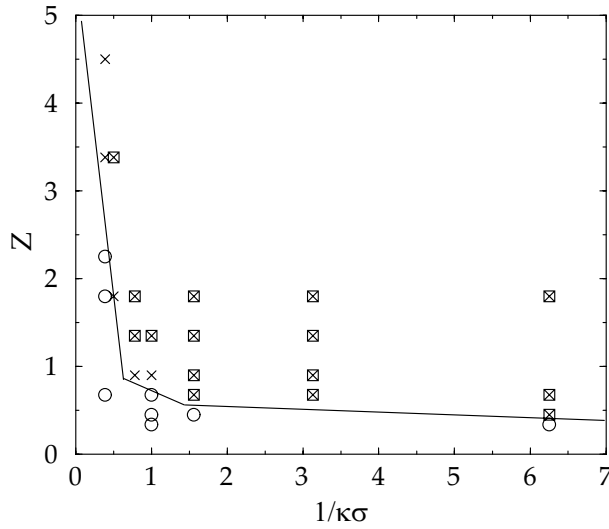


Figure 4.4: Crosses (\times) denote the points $(\bar{Z}, 1/\kappa\sigma)$ where free energy calculations based on Eq. (4.8) predict a gas-solid coexistence, squares (\square) show the points where the van der Waals theory of Ref. [50] predicts a gas-liquid coexistence, and circles (\circ) show the points where a “narrow” fluid-solid coexistence is predicted by our approach and Ref. [50]. The line is our prediction for the crossover from a “broad” gas-solid to a “narrow” fluid-solid coexistence.

phase moves to higher densities. Finally, at $\kappa\sigma \approx 2.36$ the fluid is metastable with respect to the bcc, and the fluid-fcc coexistence is replaced by a broad bcc-fcc coexistence.

The approximation for the free energy given in Eq. (4.8) can be used as a quick tool for mapping out the fluid-fcc and the bcc-fcc coexistence points in the low $\kappa\sigma$ -regime[†]. In Fig. 4.2, the coexistence points obtained from the approximate free energy curves are denoted by stars (*). As can be seen, the results obtained from the approximate method are in good agreement with those from free energy calculations. We also used Eq. (4.8) to check the stability of the gas-liquid critical point, which was predicted for the present system in Ref. [50] on the basis of a simple van der Waals-like theory. For $\bar{Z} = 1.8$ the analysis of Ref. [50] yields a gas-liquid critical point at $\kappa\sigma \simeq 1.8$ and $\eta \simeq 0.4$, i.e., for $\kappa\sigma < 1.8$ there is predicted to be an η -regime where gas and liquid coexist. Comparison with the present phase diagram for $\bar{Z} = 1.8$ in Fig. 4.2 reveals that this predicted critical point is in fact metastable with respect to fluid-fcc coexistence. The same conclusion holds for the critical points that were identified for other values of \bar{Z} and $\kappa\sigma$: Application of Eq.(4.8) reveals that a broad fluid-fcc coexistence is thermodynamically more favorable than a gas-liquid coexistence for all values of \bar{Z} and $\kappa\sigma$ considered. Meaning that a gas-liquid phase separation is always metastable with respect to a gas-solid phase separation. However, the analysis of Ref. [50] is still of use, since the curve in the $(\bar{Z}, 1/\kappa\sigma)$ plane that separates the supercritical from the subcritical regime turns out to be remarkably close to the line that separates a “narrow” fluid-solid regime from a “broad” gas-solid regime (for $\bar{Z} = 1.8$ this would take place at $\kappa\sigma \simeq 2.4$). This is illustrated in Fig. 4.4, where the crosses denote a “broad” gas-solid coexistence based on Eq. (4.8), the squares denote gas-liquid coexistence as predicted in Ref. [50]. The circles denote a “narrow” fluid-solid regime and the line represents our prediction for the crossover from a “narrow” fluid-solid to a “broad” gas-solid regime.

[†]The approximate free energy F_{Approx} in Eq. (4.8) only accounts for the “gross features of the phase diagram”, i.e., either for the broad fluid-fcc or for the broad bcc-fcc phase coexistence. It is unable to predict the phase behavior in the $\kappa\sigma$ -regime where these effects are not seen.

4.5 Conclusions

We performed a computer simulation study of the phase diagram of a suspension of charged colloids at low salt concentration, taking into account effective two- and three-body interactions between the colloids. The effective potentials are taken from an earlier Poisson-Boltzmann study [50], and are such that the pair potential is a DLVO-like screened-Coulomb repulsion [see Eq. (4.4)], whereas the three-body potential is purely attractive [see Eq. (4.5)]. The main effect of the inclusion of three-body interactions is a reduction of the stability of the bcc phase in favor of the fluid and fcc phase or coexistence of the latter two. The three-body attractions induce, at sufficiently low salt concentration, a very broad coexistence region of a dilute fluid with an extremely dense fcc phase, while at intermediate salt concentration, a broad bcc-fcc coexistence regime appears. We also conclude that any gas-liquid coexistence that may occur due to the attractive three-body interactions, is metastable with respect to gas-solid coexistence. This is in line with the results of Ref. [124], where it was shown that many-body attractions have a strong tendency to give rise to gas-solid rather than gas-liquid coexistence. The reduction of the stability of the bcc phase was also seen in Chapter 3, where the many-body interactions were taken into account by truncating the pair-potential at mean colloid separation

Finally, some critical remarks on our results must be made, since they are, at least in the low-salt regime, in disagreement with experimental observations: we are not aware of reports of observations of almost close-packed fcc phases with a dilute gas phase. This suggests that a fully realistic description of charged colloids in this regime requires the inclusion of 4-body and higher-order terms as well, which constitutes a daunting task: not only is the calculation of the n -body potential $\Omega^{(n)}$ for $n \geq 4$ computationally demanding, but including them into an (efficient) Monte Carlo scheme is also far from trivial. A better approach to study many-body interactions is to use methods where they are included implicitly. This can be done for example by using a Poisson-Boltzmann solver [56–58, 120] or the primitive model. In the next chapter, we will present a primitive model study of the system presented in this chapter.

5

Melting Line of Charged Colloids from Primitive Model Simulations

ABSTRACT

We develop an efficient simulation method to study suspensions of charged spherical colloids using the primitive model. In this model, the colloids and the co- and counterions are represented by charged hard spheres, whereas the solvent is treated as a dielectric continuum. In order to speed up the simulations, we restrict the positions of the particles to a cubic lattice, which allows precalculation of the Coulombic interactions at the beginning of the simulation. Moreover, we use multiparticle cluster moves that make the Monte Carlo sampling more efficient. The simulations are performed in the semi-grand canonical ensemble, i.e., the temperature, the volume, the number of colloids, and the chemical potential of the salt (added co- and counterions) are fixed. Employing our method, we study a system consisting of colloids carrying a charge of 80 elementary charges and monovalent co- and counterions. At the colloid densities of our interest, we show that lattice effects are negligible for sufficiently fine lattices. We determine the fluid-solid melting line in a packing fraction η -inverse screening length κ plane, and compare it with the melting line of charged colloids predicted by the Yukawa potential of the DLVO theory. We find qualitative agreement with the Yukawa results, and we do not find any effects of many-body interactions. We discuss the difficulties involved in the mapping between the primitive model and the Yukawa model at high colloid packing fractions ($\eta > 0.2$).

5.1 Introduction

As we discussed in Section 4, there has been a lot of debate whether the DLVO pairwise description is valid at low salt concentrations, where double layers of nearby colloids overlap. Indeed, according to both experiments and numerical calculations [50, 54, 55, 59–61], the effective pair potential description fails at low salt concentration and three- and higher-body interactions become important. What remains to be less clear-cut is the effect of the many-body interactions on the phase behavior of charged colloids. Dobnikar and co-workers [56–58] have studied the melting transition by solving the non-linear Poisson-Boltzmann equation for a multi-colloid system. They found that the effective many-body interactions shift the melting line, extending the fluid range, than expected on the basis of pairwise interactions alone. In Section 4, we studied the effect of attractive three-body interactions on the phase behavior of charged colloids, and found that they give rise to broad fluid-fcc and bcc-fcc coexistence regions. The question remains whether the effective three-body approach, which ignores the effective four- and higher-body terms, is valid at high colloid densities. This question becomes even more important in the light of recent experimental evidence, which suggests that the four-body term is repulsive [61], and is of the same range and magnitude as the attractive three-body interaction. Hence, a substantial fraction of the three-body attraction seems to be cancelled by the four-body repulsion.

In order to resolve this issue, we decided to perform direct simulations of the primitive model, using the same parameters as in Section 4, where three-body interactions are important. To this end, we develop an efficient simulation method for the highly asymmetric primitive model. In the primitive model description, colloids, coions, and counterions are treated as charged hard spheres, while the solvent is treated as a structureless continuum characterized by a dielectric constant ϵ_s . Since the primitive model includes all the charged species explicitly, it also includes all the effective many-body interactions. Employing our simulation method, we determine the fluid-solid transition at various salt concentrations for the primitive model and we compare the results with the predictions of the DLVO theory.

In comparing the primitive model results with the effective Yukawa potential of the DLVO theory, it is important to know how to map the primitive model parameters onto the Yukawa model parameters. At low colloid packing fractions, this mapping can be done quite reliably using the Poisson-Boltzmann cell model [22], see, e.g., Refs. [58, 125]. At high colloid packing fractions η , less is known about the validity of the Yukawa potential [126] and about the way the parameters should be mapped. An example of this can be found in Refs. [118, 119, 127], where highly charged colloidal suspensions were studied using a Car-Parrinello-like *ab initio* method [117]. At high η , it was found that the DLVO theory underestimates the structure, meaning, that the colloids see an effective charge that is *higher* than the real colloidal charge. Supposedly, the reason for this is that at high η , the screening of the Coulomb interactions is reduced because the counterions are excluded by the neighboring colloids [127]. We find evidence of this charge renormalization but we are not able to directly prove the mechanism behind it. We are unable to find a mapping between the primitive model and the Yukawa

model that would work at all packing fractions.

The rest of this chapter is organized as follows. In Section 5.2 we present our simulation method for the highly asymmetric primitive model. In Section 5.3, we discuss our results and we end with some concluding remarks in Section 5.4.

5.2 Simulation Method

5.2.1 Highly Asymmetric Primitive Model

Our system consists of N colloidal hard spheres with a diameter σ , carrying a positive charge $+Ze$, and N_S co- and $ZN + N_S$ counterions with a diameter σ_m and a charge $+e$ and $-e$, respectively. Here e denotes the elementary charge. The particles interact via the pairwise additive Coulombic potential and a hard-core repulsion

$$\frac{U_{ij}(r)}{k_B T} = \begin{cases} \frac{q_i q_j \lambda_B \sigma}{\sigma r} & \text{for } r \geq \frac{1}{2}(\sigma_i + \sigma_j) \\ +\infty & \text{for } r < \frac{1}{2}(\sigma_i + \sigma_j), \end{cases} \quad (5.1)$$

where $\lambda_B = e^2 / \epsilon_s k_B T$ is the Bjerrum length, ϵ_s is the dielectric constant of the solvent, and r is the distance between the ions i and j that have charge numbers q_i and q_j .

Our primitive model Monte Carlo simulations are performed in the semi-grand canonical ensemble, i.e., the volume V , the temperature T , the number of colloids N , and the chemical potential of the salt μ_S are kept constant. The simulations represent a system of colloids in osmotic equilibrium with a salt reservoir at the same chemical potential μ_S . In our simulations, one MC cycle consist of $N(Z + 1) + 2N_S$ attempts to displace a randomly selected particle (a colloid or a microion). Attempts to insert or remove a coion-counterion pairs are performed ten times per MC cycle. We use the standard grand canonical ensemble method for the insertion and removal steps [93].

The simulations are performed in a cubic box with side length L and periodic boundary conditions are applied in all three dimensions. The long range Coulombic interactions are calculated using the Ewald summation method [93, 128] with conducting boundary conditions, 518 Fourier-space vectors, and real-space damping parameter $\alpha = 5$. In order to speed up the simulations, we have used the fine lattice discretization method of Panagiotopoulos and Kumar [129]. In this method, the positions of the particles are restricted to a cubic lattice with lattice spacing a . We introduce a lattice refinement parameter $\xi = \sigma/a$, which gives the number of lattice points per colloid diameter. Continuum is recovered in the limit of $\xi \rightarrow \infty$. Previously, the lattice method has been used to study the criticality of electrolytes and polyelectrolytes, see Section 6 and the references therein. In these systems, the lattice has little impact on the critical behavior once $\xi \geq 3$ [129]. The effect of lattice discretization on hard spheres has been studied in Ref. [130]. The advantage of using a lattice is that it allows a single precalculation of all the Coulombic interactions into a three-dimensional $(L/a) \times (L/a) \times (L/a)$ matrix at the beginning of the simulation. During a simulation, the pair interactions can be determined by a simple table lookup. Figure 5.1 shows the CPU time

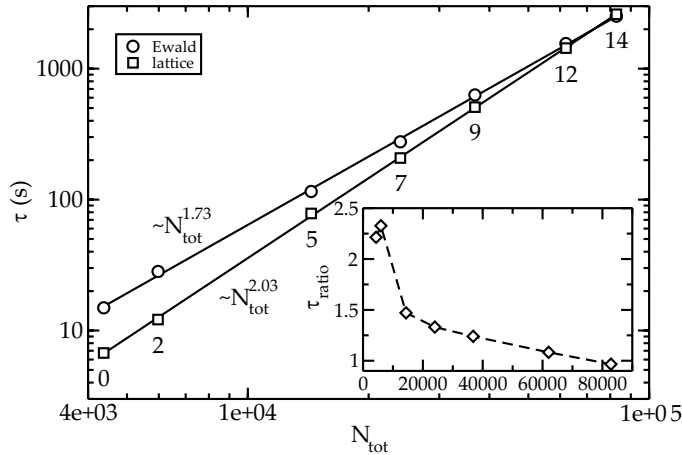


Figure 5.1: CPU time τ vs the total number of charge centers $N_{\text{tot}} = N(Z + 1) + 2N_S$ for a system with $Z = 80$, $\eta = 0.2$, and $\xi = 19$. The circles (\circ) mark the results of the Ewald summation and the squares (\square) mark the results of the lattice method. The annotated numbers show the $\kappa_{\text{id}}\sigma$ values. The full lines are linear fits to the data points. The inset shows the ratio of the Ewald summation and the lattice method CPU times.

τ as a function of the total number of charges $N_{\text{tot}} = N(Z + 1) + 2N_S$ of both the Ewald summation method and the lattice method, and the inset shows the ratio between the two CPU times *. The Ewald parameters were chosen as described in Ref. [93]. The full lines in Fig. 5.1 are linear fits to the data points. From these fits we see that the CPU time of the Ewald summation method scales as $N_{\text{tot}}^{1.73}$ and the CPU time of the lattice method scales as $N_{\text{tot}}^{2.03}$. We note that the lattice method has the expected scaling, while the Ewald summation does not have the ideal $N_{\text{tot}}^{1.5}$ scaling [131]. In the Ewald summation, a slightly non-ideal scaling is obtained because we do not use neighbor lists in the total potential energy calculation, and therefore, the distance between each particle has to be calculated. We are not sure how much better the Ewald summation would perform if neighbor lists were used since the construction and updating of the lists also requires CPU time.

In a system with high density of microions, a simple displacement of a colloid would almost always result in an overlap with at least one of the microions. In order to overcome this problem, we remove the microions that hinder the displacement of the colloid at its new position and reinsert them into the space vacated by the displacement of the colloid. Figure 5.2(a) shows a typical starting configuration. The colloid at its new trial position is denoted by a dashed line and the microions that result in an overlap with the colloid at its new position are filled gray. In our cluster move, the overlapping microions are reflected through the center between the old and the new colloid position (marked P) into the space left empty by the displacement of the colloid. An example of such a reflection is shown in Fig. 5.2(a) by the gray arrow. Figure 5.2(b) shows the end situation, where the colloid and the microions are at their new positions. Cluster moves are performed only in three lattice coordinate directions, which guarantees that each reflected microion has a well defined lattice position. The cluster moves satisfy detailed balance as they are entirely symmetric, i.e., moving a colloid back to its original position returns the microions to their original positions. Our method is similar to the cluster move technique used in Ref. [132]. However, in their ap-

* τ is defined as the time it takes to calculate the total potential energy ten times on a Pentium 4 3GHz CPU.

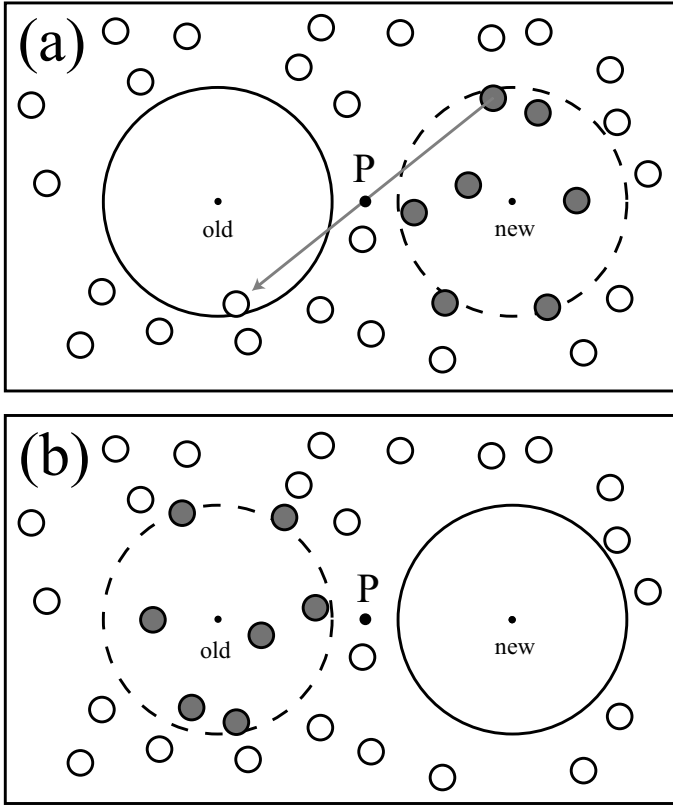


Figure 5.2: The multiparticle cluster move technique: In (a), the colloid is at its old position and the colloid at its new trial position is drawn with a dashed line. The gray microions overlap with the colloid at its new position and are therefore included in the cluster move. The reflection point P is in the middle between the old and the new colloid position. The gray arrow shows an example of a reflection through point P. In (b), the colloid is at its new position and the microions (gray) are reflected to their new positions.

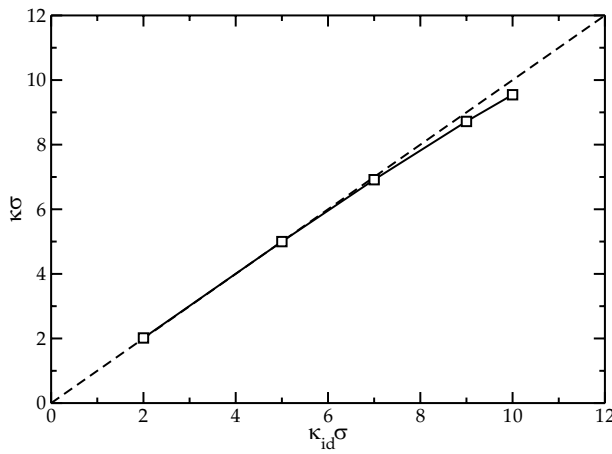


Figure 5.3: The reservoir screening length $\kappa\sigma$ as a function of the ideal reservoir screening length $\kappa_{id}\sigma$. The dashed line gives the ideal gas result, where $\kappa\sigma = \kappa_{id}\sigma$. The error bars are not shown as they are smaller than the symbol sizes. The solid line is a guide to the eye.

proach, also the counterions close to the colloids are added in the cluster move. In our case, these extended cluster moves are not needed as the coupling between the colloid and the counterions is weak.

We define the (inverse) Debye screening length of the reservoir as

$$\kappa\sigma = \sqrt{8\pi\lambda_B\sigma^2\langle\rho_S^{res}\rangle}, \quad (5.2)$$

where $\langle\rho_S^{res}\rangle = \langle N_S \rangle / V$ is the average salt density in the reservoir measured from a simulation with no colloids ($N = 0$) and a fixed μ_S . In the ideal gas approximation, the salt chemical potential μ_S is related to the (ideal) salt reservoir density

ρ_S^{res} through

$$\mu_S = 2k_B T \ln(\rho_S^{res} \sigma^3), \quad (5.3)$$

and one can define an ideal reservoir screening length as

$$\kappa_{id} \sigma = \sqrt{8\pi \lambda_B \sigma^2 \rho_S^{res}}. \quad (5.4)$$

We tested the validity of the ideal gas approximation in Eq. (5.3) by performing simulations of a reservoir system ($N = 0$). The simulations were performed in a box with side length $L = 2.11\sigma$, Bjerrum length $\lambda_B = 0.0225\sigma$, microion diameter $\sigma_m = \sigma/19$, and lattice parameter $\zeta = 38$. For a fixed μ_S , we measured $\langle \rho_S^{res} \rangle$ in a simulation and calculated the reservoir screening length $\kappa\sigma$, using Eq. (5.2). In Fig. 5.3, we plot the reservoir screening length $\kappa\sigma$ as a function of the ideal reservoir screening length $\kappa_{id}\sigma$. The dashed line gives the ideal gas result, where $\kappa\sigma = \kappa_{id}\sigma$. As can be seen from Fig. 5.3, the reservoir screening length $\kappa\sigma$ starts to deviate from the ideal reservoir screening length at $\kappa_{id}\sigma > 6$, but the difference remains small even up to $\kappa_{id}\sigma = 10$, where $\kappa\sigma \approx 9.5$. Therefore, Eqs. (5.3) and (5.4) give a convenient way of approximating $\kappa\sigma$ at a given salt chemical potential μ_S .

In summary, we present an efficient simulation method to study model suspensions of charged colloids using the primitive model. Primitive model simulations cause severe sampling problems as the number of particles involved in the simulations increases with larger charge asymmetry and the convergence slows down due to the high density of microions close to the colloids. The combination of the fine lattice discretization approach and the cluster moves enables us to solve some of the sampling problems. We estimate that the lattice gives a speed up of a factor 2 compared to continuum simulations in the range of parameters where most of our simulations were performed, and the cluster move technique gives a speed up of 10 or more. Therefore, the cluster move technique is considered essential to make the simulations feasible. These methods are a combination of methods used previously. For previous studies on highly charged colloidal suspensions, see, e.g., Refs.[31, 132, 133]. See also a recent review [134] and the references therein. Distinct from previous work, our simulations are performed in the semi-grand canonical ensemble, i.e., the salt chemical potential and, hence, the Debye screening length of the reservoir, are fixed. This facilitates a direct comparison with theoretical predictions. To the best of our knowledge, we are not aware of any simulation study of the primitive model at fixed salt chemical potential in the colloidal regime.

5.2.2 Hard-Core Repulsive Yukawa Model

In addition to the primitive model simulations, we also perform MC simulations of the hard-core Yukawa model. According to the DLVO theory [17, 18], the colloid-colloid pair interaction is given by a repulsive Yukawa potential with a hard-core

$$\frac{u(r)}{k_B T} = \begin{cases} \frac{Z^2 \lambda_B / \sigma}{(1 + \kappa\sigma/2)^2} \frac{\exp[-\kappa(r - \sigma)]}{r/\sigma} & \text{for } r \geq \sigma \\ +\infty & \text{for } r < \sigma. \end{cases} \quad (5.5)$$

Simulations of the continuum hard-core Yukawa model are performed in the canonical ensemble using a cubic box with periodic boundary conditions. The DLVO theory is derived for infinite dilution where $\eta = 0$. At $\eta > 0$, it is customary to replace the reservoir screening length κ in Eq. (5.5) by an effective screening length κ_{eff} . The effective screening length κ_{eff} takes into account that, at a finite colloid density, the screening length in the colloidal suspensions is not simply determined by that of the reservoir (where the colloid density is zero). The reason is that the counterions from other colloids also contribute to the screening length. A simple way to incorporate this extra contribution is to substitute the reservoir charge density $2\langle\rho_S^{\text{res}}\rangle$ in Eq. (5.2) by the average total microion charge density $2\langle\rho_S\rangle + Z\rho$

$$\kappa_{\text{eff}}\sigma = \sqrt{4\pi\lambda_B\sigma^2 (2\langle\rho_S\rangle + Z\rho)}, \quad (5.6)$$

where $\rho = N/V$ is the colloid number density and $\langle\rho_S\rangle = \langle N_S\rangle/V$ is the average salt density measured from a primitive model simulation. We also consider an effective screening length where the excluded volume of the colloids is taken into account (see e.g. Ref. [135])

$$\kappa'_{\text{eff}}\sigma = \sqrt{4\pi\lambda_B\sigma^2 \left(\frac{2\langle\rho_S\rangle}{1-\eta_c} + \frac{Z\rho}{1-\eta_c} \right)}, \quad (5.7)$$

where $\eta_c = \eta(1 + \sigma_m/\sigma)^3$ is the fraction of the volume excluded by the colloids. For highly charged colloids, it is typical to replace the bare charge Z in Eq. (5.5)-(5.7) by a renormalized charge Z_{re} . The renormalized charge Z_{re} takes into account the condensation of counterions on the colloid surface, see e.g. Refs. [22, 126]. As Z_{re} is a sum of the colloid charge Z and the charge in the condensed shell of counterions, it is smaller than the bare charge Z . In the simulations presented in this chapter, charge renormalization is insignificant (see also Section 5.3.3).

At low colloid concentration, there is both numerical and experimental evidence that the Yukawa form (5.5) is valid at high coupling [133], high charge [125, 136], and at high salt concentration [56–58]. At low salt concentrations, one observes a “cut-off” behavior: at large distances the force between a pair of colloids is considerably smaller than expected on the basis of the Yukawa potential [54–58, 137]. Hence, the effective colloid-colloid pair interaction resembles closely a Yukawa potential that has a density dependent truncation. Phase diagrams of such potentials have been studied in Refs. [56–58].

As was mentioned in the introduction, much less is known about the validity of the Yukawa form at high colloid concentrations, even with effective parameters (see, e.g., the discussion in Ref. [126]). In Refs. [118, 119, 127], highly charged colloidal suspensions were studied using an *ab initio* method that can be seen as a classical counterpart of the Car-Parrinello method [117]. It was found that the Yukawa potential is valid at all packing fractions, but that the parameters of the potential do not follow the DLVO theory. At low η , the DLVO theory overestimates the structure, as expected according to the charge renormalization discussed above. At high η , the DLVO theory underestimates the structure, meaning, that the colloids see an effective charge that is *higher* than the bare charge.

The reason for this is that at high η , the screening of the Coulomb interactions is reduced because the counterions are excluded by the neighboring colloids [127]. Therefore, the colloids experience a stronger repulsion than expected based on the DLVO theory. The effect of the excluded volume on the effective pair potential is included by Belloni[138] (see also Ref. [126]) by imposing that the structure factor within an integral equation theory using the mean spherical approximation (MSA) is the same in the effective one component system and the primitive model. According to Ref. [138], the effective charge Z_{eff} can be calculated from

$$Z_{\text{eff}} = ZX(1 + \kappa\sigma/2) \exp(-\kappa\sigma/2), \quad (5.8)$$

where

$$X = \cosh(\kappa\sigma/2) + U \left[\frac{\kappa\sigma}{2} \cosh(\kappa\sigma/2) - \sinh(\kappa\sigma/2) \right], \quad (5.9)$$

and

$$U = \frac{3\eta}{(1-\eta)(\kappa\sigma/2)^3} - \frac{\Gamma\sigma}{\kappa\sigma [1 + \Gamma\sigma/2 + 3\eta/(1-\eta)]}, \quad (5.10)$$

and where Γ can be solved from

$$(\Gamma\sigma)^2 = (\kappa\sigma)^2 + \frac{24\eta\lambda_B/\sigma}{1 + \Gamma\sigma/2 + 3\eta/(1-\eta)}. \quad (5.11)$$

In practice, one solves Eq. (5.11) numerically for a given $\kappa\sigma$, η , and λ_B/σ , and then evaluates Eqs. (5.10), (5.9), and (5.8). The effective charge Z_{eff} , is at high η larger than Z , and at low η equal to Z . Our simulations are in the range where $Z_{\text{eff}} > Z$. The MSA theory is known to fail at low densities [138] (see Ref. [125] for experimental evidence of this). At low densities, we also find that the MSA theory gives a worse description of the interactions than the DLVO theory (see Section 5.3.2).

We determine the melting lines of the primitive and hard-core Yukawa model using the Lindemann criterion [107], which states that a crystal is stable when the root-mean-square (RMS) displacement $\sqrt{\langle u^2 \rangle}$ of the colloids about their equilibrium lattice positions $\{\mathbf{r}_{0,i}\}$ is below 19% of the mean colloid distance $\rho^{-1/3} = \sigma(\pi/6\eta)^{1/3}$, i.e.,

$$\sqrt{\langle u^2 \rangle} \equiv \sqrt{\langle |\mathbf{r}_i - \mathbf{r}_{0,i}|^2 \rangle} < 0.19\sigma \left(\frac{\pi}{6\eta} \right)^{1/3}. \quad (5.12)$$

We define the melting packing fraction η_{melt} as the smallest η for which Eq. (5.12) holds, i.e., where a crystal is still stable.

5.3 Results

5.3.1 Effect of Lattice Discretization

Our system consists of colloids with charge $80e$, and monovalent co- and counterions. We use Bjerrum length $\lambda_B = 0.0225\sigma$ and microion diameter $\sigma_m = \sigma/19 \approx$

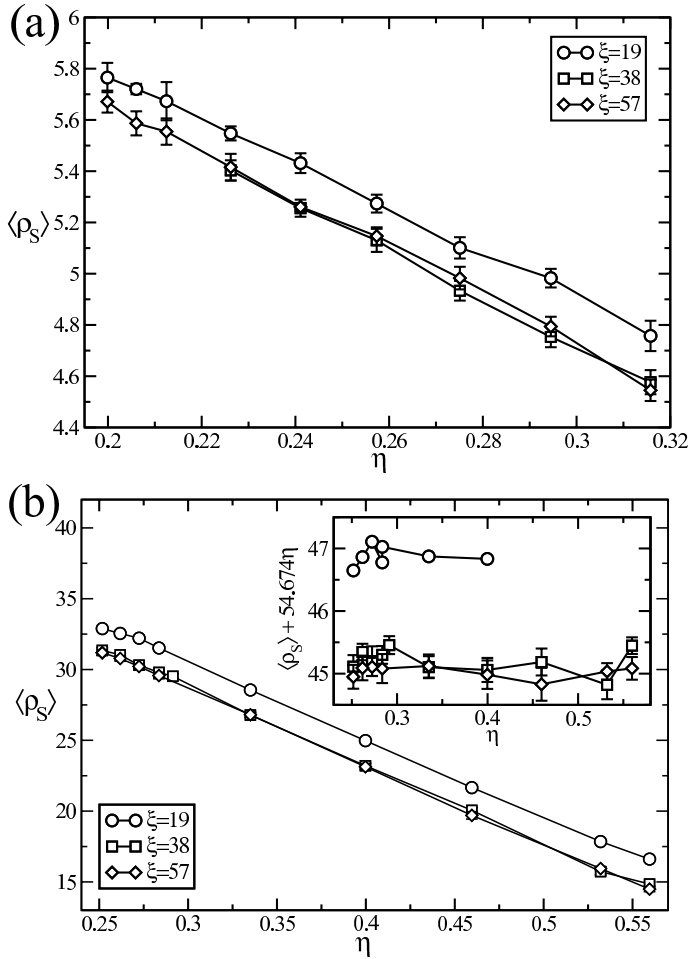


Figure 5.4: The average salt density $\langle \rho_S \rangle$ (in units of σ^{-3}) as a function of the packing fraction η for lattice parameters $\zeta = 19, 38,$ and 57 . $\langle \rho_S \rangle$ in (a) bcc is for a crystal with $N = 54$ colloids and reservoir screening length $\kappa\sigma = 2$. $\langle \rho_S \rangle$ in (b) is for an fcc crystal with $N = 32$ colloids and $\kappa\sigma = 5$. In the inset in (b), we subtract a linear fit from $\langle \rho_S \rangle$ to make the differences more visible. The lines are a guide to the eye.

0.053σ . Typical simulation runs consist of 5000 equilibration cycles (attempts to displace each particle once) and 10 000 production cycles. Statistical errors are estimated from ten block averages using the Student's t-test with 95% confidence.

We study the effect of the lattice discretization on the average salt density $\langle \rho_S \rangle$, the average total potential energy per particle $\langle U \rangle / N$, and the RMS displacement of the colloids $\sqrt{\langle u^2 \rangle}$. The ensemble averages are calculated for lattice discretization parameters $\zeta = 19, 38,$ and 57 , and for two reservoir screening lengths, $\kappa\sigma = 2$ and 5 . For $\kappa\sigma = 2$, the simulations were started from a bcc crystal containing $N = 54$ colloids, and for $\kappa\sigma = 5$, the simulations were started from an fcc crystal with $N = 32$ colloids. Figures 5.4(a) and (b) show $\langle \rho_S \rangle$ as a function of the packing fraction η for screening lengths $\kappa\sigma = 2$ and 5 , respectively. We clearly observe that $\zeta = 38$ and $\zeta = 57$ give results that are equivalent within the statistical accuracy, while $\zeta = 19$ overestimates $\langle \rho_S \rangle$. A similar conclusion can be drawn from the data for $\langle U \rangle / N$ shown in Figs. 5.5(a) and (b): the results for the lattice discretization $\zeta = 38$ and $\zeta = 57$ are again equivalent within the statistical accuracy, while those for $\zeta = 19$ differ systematically. Figures 5.6(a) and (b) show the RMS displacement in units of the mean colloid distance, $\sqrt{\langle u^2 \rangle} / \rho^{-1/3}$, for $\kappa\sigma = 2$ and $\kappa\sigma = 5$, respectively. For $\kappa\sigma = 2$, in Fig. 5.6(a), the effect of the lattice discretization on $\sqrt{\langle u^2 \rangle} / \rho^{-1/3}$ is not clear due to the statistical noise. For $\kappa\sigma = 5$,

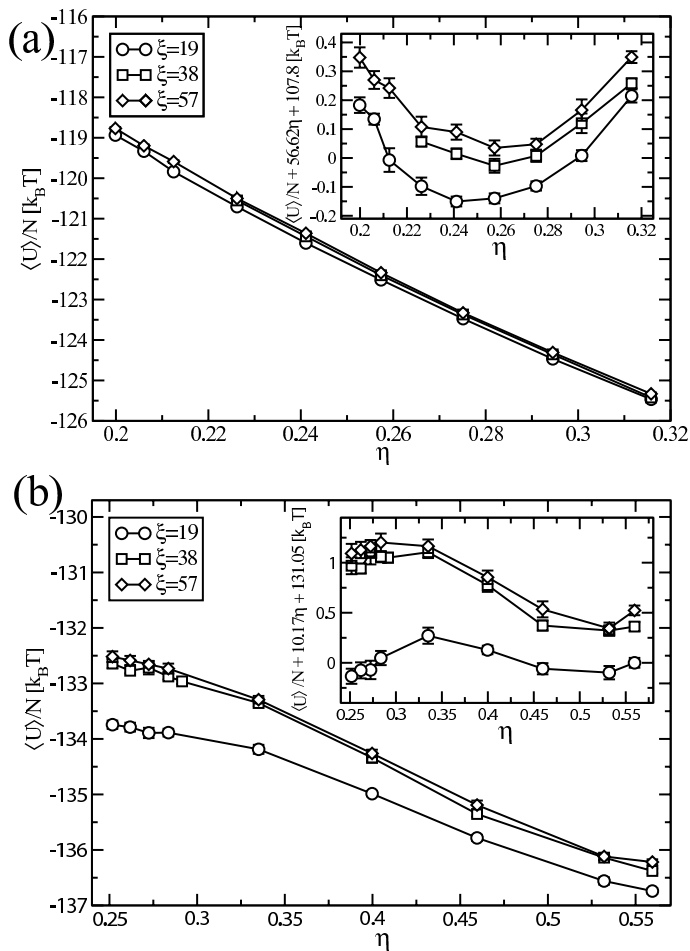


Figure 5.5: The average potential energy per particle $\langle U \rangle / N$ (in units of $k_B T$) as a function of the packing fraction η for lattice parameters $\zeta = 19, 38$, and 57 . $\langle U \rangle / N$ in (a) is for a bcc crystal with $N = 54$ colloids and reservoir screening length $\kappa\sigma = 2$. $\langle U \rangle / N$ in (b) is for an fcc crystal with $N = 32$ colloids and $\kappa\sigma = 5$. In the insets, we subtract a linear fit from $\langle U \rangle / N$ to make the differences more visible. The lines are a guide to the eye.

in Fig. 5.6(b), we clearly see that $\zeta = 19$ overestimates $\sqrt{\langle u^2 \rangle} / \rho^{-1/3}$ compared to the results obtained for $\zeta = 38$ and 57 . Again, we observe that the results for $\zeta = 38$ and 57 are equivalent within the statistical accuracy. To conclude, the lattice discretization $\zeta = 38$ is sufficient to yield results that are independent of ζ , and are similar to the continuum case. We will use $\zeta = 38$ (or in some cases $\zeta = 57$) in all subsequent calculations.

5.3.2 Charge Distribution and Structure

We study the distribution of co- and counter-ions in a bcc crystal with $N = 54$ colloids at packing fraction $\eta = 0.34$ and reservoir screening length $\kappa\sigma = 5$. A snapshot of this system is shown in Fig. 5.7. Since we are interested in the ion distribution in a crystal of colloids, we fix the colloid positions and do MC moves only for the ions. Co- and counterion positions were recorded into 400 frames during 2000 MC cycles. From this data, charge distributions were obtained by averaging the co- and counterion positions on a bcc unit cell that contains one colloid in the center and eight in the corners of a cube. The averages were saved on $60 \times 60 \times 60$ matrices, which were visualized by plotting the 3D constant-density contours with the gOpenMol program [139]. Figures 5.8(a)-(d) show 3D contour plots for (a)-(b) counterion, (c) coion, and (d) charge densities (counterion density

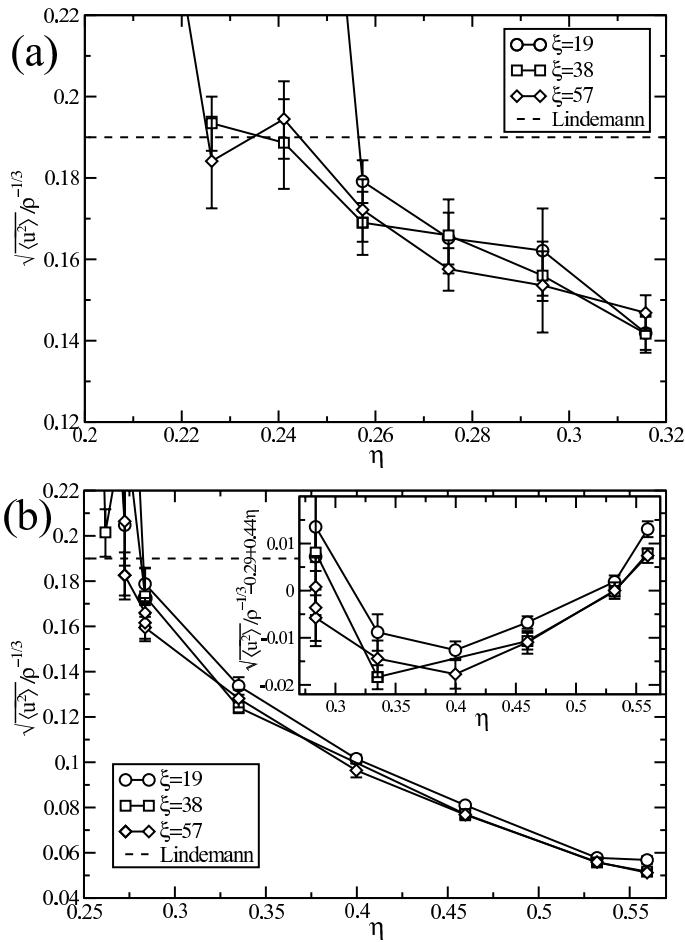


Figure 5.6: The root-mean-square (RMS) displacement $\sqrt{\langle u^2 \rangle}$ in units of the mean colloid distance $\rho^{-1/3}$ as a function of packing fraction η for lattice parameters $\xi = 19, 38,$ and 57 . The RMS displacement in (a) is for a bcc crystal with $N = 54$ colloids and reservoir screening length $\kappa\sigma = 2$. The RMS displacement in (b) is for an fcc crystal with $N = 32$ colloids and $\kappa\sigma = 5$. The dashed line gives the Lindemann criterion. In the inset in (b), we subtract a linear fit from $\sqrt{\langle u^2 \rangle} / \rho^{-1/3}$ to make the differences more visible. The lines are a guide to the eye.

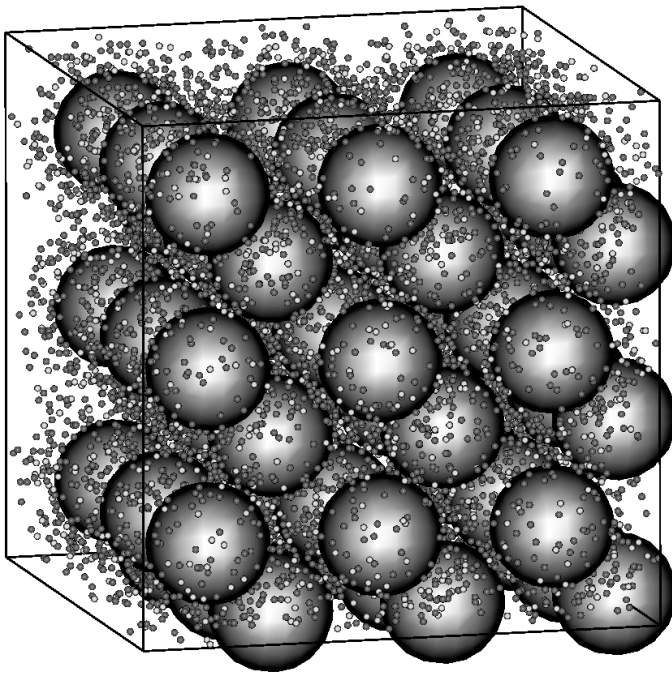


Figure 5.7: A snapshot of a bcc crystal with $N = 54$ colloids at packing fraction $\eta = 0.34$ and reservoir screening length $\kappa\sigma = 5$. The small light spheres are coions and the small dark spheres are counterions. This system was used to calculate the contour plots in Figs. 5.8(a)-(d).

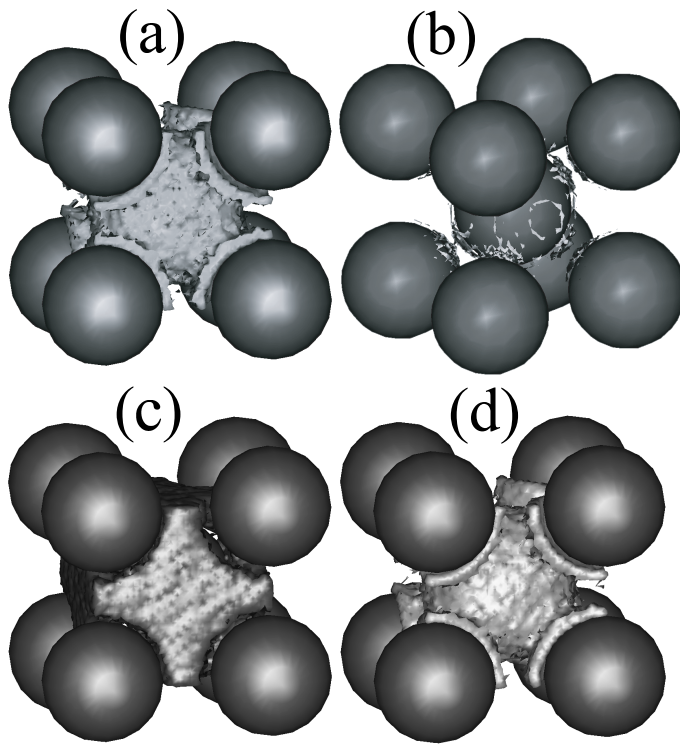


Figure 5.8: Constant-density contour plots for (a)-(b) counterion, (c) coion, and (d) charge density in a bcc unit cell at packing fraction $\eta = 0.34$ and reservoir screening length $\kappa\sigma = 5$. In (a), (c), and (d), the central colloid of the bcc unit cell is covered by the contour plots.

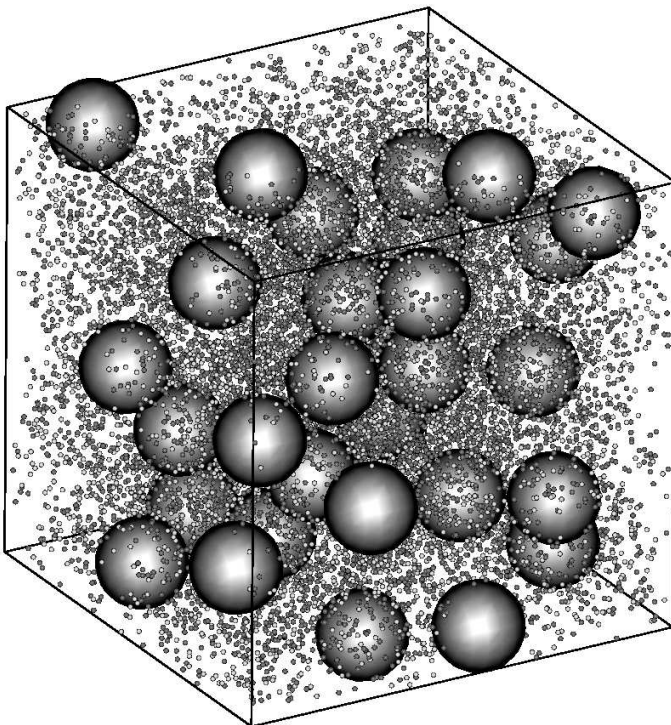


Figure 5.9: A snapshot of fluid phase with $N = 30$ colloids at packing fraction $\eta = 0.11$ and reservoir screening length $\kappa\sigma = 5$. The small light spheres are coions and the small dark spheres are counterions.

minus coion density) in the bcc unit cell. Note that in Figs. 5.8(a), (c), and (d), the central colloid of the bcc unit cell is covered by the contour plots. The counterion contour plot in Fig. 5.8(a) shows that the counterions are distributed in a spherical orbital around each colloid, just like the DLVO theory predicts. Figure 5.8(b) shows a contour plot of counterions, where the constant-density contour is set at a higher counterion density than in Fig. 5.8(a). As can be seen from Fig. 5.8(b), the highest counterion density is on the part of the colloid surface where the nearest neighbors are closest to each other (i.e., between the center colloid and one of the corner colloids). This can be explained by superimposing two spherical orbitals, as is expected based on the DLVO theory. The coion contour plot in Fig. 5.8(c) shows that the coions are distributed in the regions left empty by the colloids, and are depleted from the surfaces of the colloids. The highest density of coions is in the space between next nearest neighbors (i.e., between the colloids in the corners of the unit cell). This region of space is still completely charge neutral, because it contains as many counterions as coions. This can be seen from Fig. 5.8(d), which shows a contour plot of the charge density (counterion density minus coion density). Figure 5.8(d) also shows that the charge distribution is similar in shape to the counterion distribution in Fig. 5.8(a). Figure 5.9 is a snapshot of fluid phase containing $N = 30$ colloids at packing fraction $\eta = 0.11$ and reservoir screening length $\kappa\sigma = 5$.

Figures 5.10(a) and (b) show the colloid-colloid, the colloid-coion, and the colloid-counterion radial distribution functions (RDFs) for two statepoints close to the fluid-bcc melting line. The RDFs in Fig. 5.10(a) are for packing fraction $\eta = 0.206$ and reservoir screening length $\kappa\sigma = 2$, and those in Fig. 5.10(b) are for $\eta = 0.266$ and $\kappa\sigma = 5$. In Fig. 5.10, we also plot the RDFs of Yukawa systems, where the screening length $\kappa_{\text{eff}}\sigma$ is from Eq. (5.6) (the gray dashed and dot-dashed lines) or $\kappa'_{\text{eff}}\sigma$ from Eq. (5.7) (the gray dotted and full lines). We use a constant effective charge $Z_{\text{eff}} = 80$ for the RDFs plotted with the dotted and the dashed lines, and we use the effective charge from the MSA theory, Eq. (5.8), for the RDFs plotted with the full and the dot-dashed lines. We observe that the results with $Z_{\text{eff}} = 80$ always underestimates the structure. The best agreement (the gray full lines) is obtained by using $\kappa'_{\text{eff}}\sigma$ from Eq. (5.7) and Z_{eff} from the MSA theory [Eq. (5.8)], although the result always slightly overestimates the structure. We want to point out that the primitive model RDFs in Figs. 5.10(a) and (b) can be fitted with $Z_{\text{eff}} = 80$ if $\kappa_{\text{eff}}\sigma$ is treated as a fitting parameter. However, from our colloid-colloid RDF data for statepoints in the range $\eta \in [0.03, 0.314]$ and $\kappa\sigma \in [0, 9.5]$, we noticed that at $\eta \gtrsim 0.2$ the fitting was not possible, if $Z_{\text{eff}} = 80$ was used. More specifically, at state points $\kappa\sigma = 2.0$ and $\eta = 0.21$, $\kappa\sigma = 5.0$ and $\eta = 0.27$, $\kappa\sigma = 6.9$ and $\eta = 0.28$, $\kappa\sigma = 8.7$ and $\eta = 0.30$, and $\kappa\sigma = 9.5$ and $\eta = 0.31$, we observed that a higher effective charge was required to make the fitting of the colloid-colloid RDF even qualitative.

In conclusion, our results seem to suggest that, at $\eta > 0.2$, the effective screening length is best described by taking into account the excluded volume of the colloids, as we do in Eq. (5.7), and the effective charge should be chosen larger than the bare charge. At $\eta < 0.2$ we find that the colloid-colloid structure can be described by the DLVO theory, i.e., with $Z_{\text{eff}} = 80$ and $\kappa_{\text{eff}}\sigma$ from Eq. (5.6). At these low densities, we also find that the MSA theory gives in certain cases

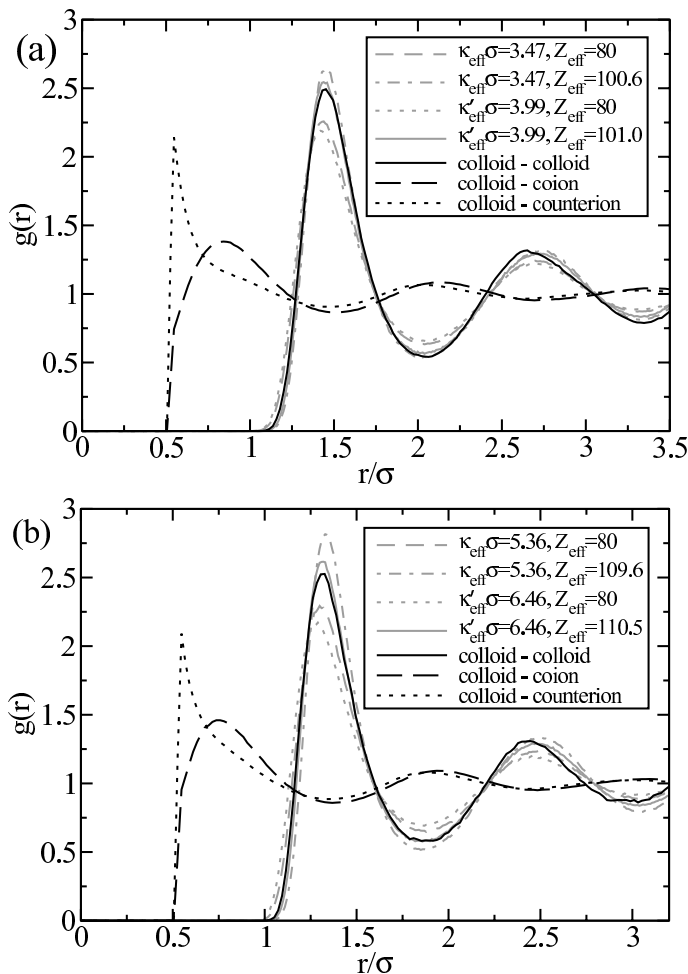


Figure 5.10: Radial distribution functions (RDFs) for a system with $N = 54$ colloids with charge $Z = 80$, close to the fluid-bcc melting line. (a) shows the RDFs for a system at packing fraction $\eta = 0.206$ and reservoir screening length $\kappa\sigma = 2$. (b) shows the RDFs for a system at packing fraction $\eta = 0.266$ and reservoir screening length $\kappa\sigma = 5$. The colloid-colloid RDFs are plotted with the full lines, the colloid-coion with the dashed lines, and the colloid-counterion with the dotted lines. The grey lines give the RDFs of Yukawa systems for four different choices of Yukawa parameters, see text.

a worse description of the structure than the DLVO theory. We emphasize that our results are not meant to validate the MSA theory. We use this theory simply in lack of anything better and acknowledge that it gives only a rough idea of the optimal effective charge.

Note that we have implicitly assumed that the Yukawa form of the pair potential is valid at concentrated colloidal suspensions. This does not need to be so, but we do not have evidence of any other form of the pair potential either.

5.3.3 Melting Line

We determine the melting line for the primitive model at reservoir screening lengths $\kappa\sigma = 0.0, 2.0, 5.0, 6.9, 8.7,$ and 9.5 , using the Lindemann criterion (5.12). The numerical values for the melting points are given in Table 5.1. In Table 5.1, the effective screening lengths $\kappa_{\text{eff}}\sigma$ are calculated using Eq. (5.6) and $\kappa'_{\text{eff}}\sigma$ are calculated using Eq. (5.7). We also give the corresponding effective charges Z_{eff} and Z'_{eff} that are calculated using the MSA theory from Eq. (5.8). We checked that charge renormalization due to condensation is insignificant by calculating Z_{re} at the state points in Table 5.1 using the Poisson-Boltzmann cell model [22]. According to our results, the renormalized charge is $Z_{\text{re}} \approx 79$, i.e., very close to the bare

crystal	η_{melt}	$\kappa_{\text{id}}\sigma$	$\kappa\sigma$	$\kappa_{\text{eff}}\sigma$	Z_{eff}	$\kappa'_{\text{eff}}\sigma$	Z'_{eff}	$\langle\rho_S\rangle\sigma^3$
bcc	0.219	0	0.0	3.08	101.9	3.57	102.3	0.0
bcc	0.257	2	2.0	3.74	107.1	4.48	107.7	5.1
fcc	0.284	5	5.0	5.39	112.0	6.75	116.7	29.8
fcc	0.335	7	6.9	6.55	120.6	8.39	122.4	50.2
fcc	0.350	9	8.7	7.69	124.1	10.00	126.3	77.9
fcc	0.366	10	9.5	8.22	129.3	10.85	129.8	91.5

Table 5.1: Numerical values for the primitive model melting line. η_{melt} is the melting packing fraction according to the Lindemann criterion (5.12), $\kappa_{\text{id}}\sigma$ is the ideal reservoir screening length [see Eq. (5.4)], $\kappa\sigma$ is the reservoir screening length [see Eq. (5.2)], $\kappa_{\text{eff}}\sigma$ and $\kappa'_{\text{eff}}\sigma$ are the effective screening lengths from Eq. (5.6) and Eq. (5.7), respectively, and Z_{eff} and Z'_{eff} are the corresponding effective charges from the MSA theory [Eq. (5.8)], and $\langle\rho_S\rangle\sigma^3$ is the average salt density.

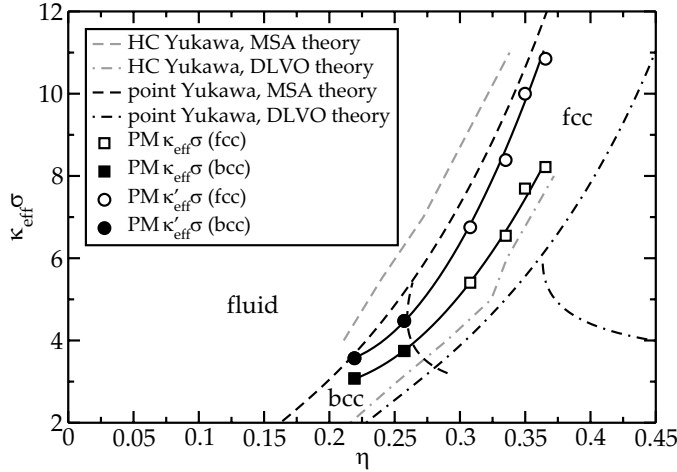


Figure 5.11: Phase diagram of charged colloids with charge $Z = 80$ and Bjerrum length $\lambda_B/\sigma = 0.0225$ in the packing fraction η -effective screening length $\kappa_{\text{eff}}\sigma$ representation. The point Yukawa phase boundaries from Ref. [21] are denoted by the black dashed and the dot-dashed lines and the corresponding hard-core Yukawa melting lines are denoted by the gray lines. The primitive model melting points are denoted by the squares (\square) and the circles (\circ). The filled and the open symbols are the melting points for bcc and fcc crystals, respectively. The full lines are a guide to the eye.

charge.

Figure 5.11 shows the melting line of the primitive model in the η - $\kappa_{\text{eff}}\sigma$ representation. The squares mark the results where the mapping onto the η - $\kappa_{\text{eff}}\sigma$ plane is done using $\kappa_{\text{eff}}\sigma$ from Eq. (5.6), and the circles mark the results where the mapping onto the η - $\kappa_{\text{eff}}\sigma$ plane is done using $\kappa'_{\text{eff}}\sigma$ from Eq. (5.7). The filled symbols denote the melting points of a bcc crystal, while the open symbols denote the melting points of an fcc crystal. For comparison, Fig. 5.11 also shows the phase diagrams of point Yukawa particles (the black dashed and the dot-dashed lines) from Ref. [21], which were mapped onto the η - $\kappa_{\text{eff}}\sigma$ plane by matching the point Yukawa pair potential with the hard-core pair potential at $r > \sigma$ (for details, see Section 2.3.4). In the mapping of the dashed lines, we used the effective charge Z_{eff} from the MSA theory [Eq. (5.8)], and in the mapping of the dot-dashed lines, we used the DLVO theory bare charge $Z_{\text{eff}} = 80$. We also calculated the melting line of hard-core Yukawa particles using the Lindemann criterion. These are plotted by the gray lines, and the effective charges are chosen as in the corresponding point Yukawa phase lines. As can be seen from Fig. 5.11, the primitive model

melting lines are between the Yukawa fluid-solid phase lines, and it is hard to say which mapping of the primitive model and the Yukawa model is the best. Using the DLVO theory, i.e., $\kappa_{\text{eff}}\sigma$ from Eq. (5.6) and $Z_{\text{eff}} = 80$, gives a reasonable agreement between the primitive model results denoted by the squares and the Yukawa fluid-solid line denoted by the dot-dashed line. In this case, the Yukawa model predicts more fluid phase than the primitive model. Using $\kappa'_{\text{eff}}\sigma$ from Eq. (5.7) and Z_{eff} from the MSA theory [Eq. (5.8)] gives a reasonable agreement between the primitive model results denoted by the circles and the Yukawa fluid-solid line denoted by the dashed line. In this case, the Yukawa model predicts less fluid phase than the primitive model. As noted in Section 5.3.2, at $\eta > 0.2$ the agreement of the colloid-colloid RDFs of the primitive model and the Yukawa system is the best in this case. We have also calculated the melting point for a system with $Z = 160$ and no added salt ($\kappa\sigma = 0$). We found $\eta_{\text{melt}} = 0.066 \pm 0.005$ for a bcc crystal with $N = 54$ colloids. At this density, $\kappa_{\text{eff}}\sigma = 2.47$ and $\kappa'_{\text{eff}}\sigma = 2.58$, from Eqs.(5.6) and (5.7), respectively. Using $\kappa_{\text{eff}}\sigma = 2.5$ and $Z_{\text{eff}} = 160$ in the hard-core Yukawa model gives melting at $\eta_{\text{melt}} = 0.071$, in good agreement with the primitive model result. This shows that at low densities, the DLVO theory gives a good description of charged colloids (as long as charge renormalization is not important). We can only conclude that it is not clear how the mapping between the primitive model and the Yukawa model should be done in the packing fraction range $\eta > 0.2$.

In Section 4, we performed simulations of the effective one-component system using a repulsive two-body Yukawa potential and an attractive three-body potential, and we found broad fluid-fcc and bcc-fcc coexistence regions at $\kappa\sigma = 2.2 - 2.45$. Using this effective three-body potential approach, the simulations showed a clear phase separation for state points well inside such a broad two-phase coexistence region. This is in contrast with our primitive model simulations, which do not give any indication of phase separation or broad coexistence regions, when the same parameters are used as in Section 4.

5.4 Conclusions

We develop an efficient simulation method to study suspensions of charged spherical colloids using the primitive model. The combination of a fine lattice discretization approach and cluster moves enables us to speed up sampling. We find the cluster moves essential to make the primitive model simulations feasible in the colloidal regime. These methods are a combination of methods used previously [31, 129, 132–134]. We showed that by increasing the lattice discretization, its effect on the results can be made small in a sense that no change is observed if the lattice is refined further. The crucial difference between our work and earlier work is that we perform the simulations in the semi-grand canonical ensemble, where the volume, the temperature, the number of colloids, and the salt chemical potential are fixed. This allows us to make a direct comparison with experiments but also with various theoretical approaches. For instance, Refs. [77, 140] show a direct comparisons of radial distribution functions measured experimentally using confocal microscopy and those obtained from our primitive model code.

We studied charge distributions in a bcc crystal by plotting contour plots of coion, counterion, and charge (counterion minus coion) densities. The charge distributions were found to be in qualitative agreement with the DLVO theory, which predicts spherical double layers around each colloid.

We determined the fluid-solid melting line of the primitive model for colloidal charge $Z = 80$ using the Lindemann criterion, and compared it with the melting line of colloids described by the effective Yukawa potential of the DLVO theory. We find that the agreement between the primitive model and the Yukawa model depends strongly on the way the mapping between the two systems is performed, i.e., on the choice of the effective screening length and the effective charge. Our results for colloid-colloid RDFs at $\eta > 0.2$ suggest that the effective screening length is best described by taking into account the excluded volume of the colloids, and that the effective charge is higher than the bare charge. According to Refs. [127, 138], this charge renormalization is due to the excluded volume of the colloids that reduces the volume available for the microions and therefore reduces the screening. Thus, the colloids feel a stronger repulsion because their charges are less screened. However, we do not have direct evidence confirming this mechanism. At $\eta < 0.2$, the colloid-colloid structure can be described by using an effective charge equal to the bare charge, i.e., $Z_{\text{eff}} = 80$. We are not aware of a unique way of mapping between the primitive model and the Yukawa model that would work at all packing fractions, except fitting [127]. One possibility is that the Yukawa form of the pair potential breaks down at high densities, but we do not have any definite evidence supporting this. Clearly, more theoretical and computational work is needed to resolve these issues.

Treating the salt grand canonically allows us to make a direct comparison with the results in Section 4, where three-body attraction gave rise to broad fluid-fcc and bcc-fcc coexistence regions. We use the same parameters as in Section 4, but do not find any broad coexistence regions or any other manifestations of many-body interactions. This suggests that the four- and higher-body terms play an essential role in the parameter range considered here; they seem to cancel the effective three-body attraction. Therefore, the effective colloid interactions in colloidal suspensions seem to be better described by an effective pair potential description than by an effective Hamiltonian truncated after the three-body term, as was done in Section 4.

Acknowledgements The lattice Monte Carlo code is based on A. Z. Panagiotopoulos' code. The Poisson-Boltzmann cell model calculations were done using a program by B. Zoetekouw.

6

Critical Point of Asymmetric Electrolyte Mixtures

ABSTRACT

In this chapter, the critical behavior of asymmetric electrolyte mixtures is studied using grand canonical Monte Carlo simulations. The mixtures consist of large multivalent macroions and small monovalent co- and counterions. The system can be viewed as a binary mixture of macroions (with their counterions) and salt (co- and counterion pair). The primitive model description is used, in which the ions are point charges with a hard core and the solvent is treated as a uniform dielectric continuum. The grand canonical simulations are based on insertions and removals of neutral molecules: macroion with its counterions or coion and a counterion. We propose a distance biasing method that enables direct grand canonical simulations up to charge asymmetry of 10:1. We calculated the critical loci that connect the salt-free state, which consists of only macroions and counterions, with the pure salt state using mixed-field finite-size scaling with no pressure mixing. The critical parameters are determined for macroion to counterion charge asymmetries of 2:1, 3:1, and 10:1. Our results suggest that binary electrolyte mixtures are type-I mixtures, where the two components mix continuously.

6.1 Introduction

In recent years, the gas-liquid phase separation of ionic fluids has been the subject of many experimental [141, 142], theoretical [143–148] and simulation studies [33, 35, 149–151]. The simplest and most frequently used model for electrolytes is the primitive model, where the ions are point charges with a hard core and the solvent is taken into account as a uniform dielectric continuum. Panagiotopoulos and co-workers [33, 35, 149] and Yan and de Pablo [34, 152–154] have determined the critical parameters for size- and charge-asymmetric primitive model electrolytes using grand canonical Monte Carlo (GCMC) simulations. A different approach to the problem was taken by Reščič and Linse [36], who estimated the critical parameters for 10:1 charge-asymmetric electrolyte using thermodynamic scaling Monte Carlo.

Most theoretical studies on electrolytes have considered salt-free systems with macroions and counterions, but no coions [32, 132, 155–157]. However, in many real micellar and colloidal systems, salt is always present and often difficult to get rid of. In this chapter, we consider asymmetric electrolyte mixtures that consist of large multivalent macroions and small monovalent co- and counterions (salt). One can view the system as a binary mixture of macroions with their counterions and salt. Our objective is to calculate the critical loci connecting the two extremes: (i) salt-free state with macroions and counterions, and (ii) pure salt state with co- and counterions. The simulations are done for macroion to counterion charge asymmetries of 2:1, 3:1, and 10:1, using the fine-lattice primitive model GCMC method of references [33, 149].

Our GCMC simulations are based on insertions and removals of electroneutral sets of molecules: a macroion with its counterions or a coion and a counterion. The main practical problem in performing the insertion and removal moves is how to choose molecule configurations that have a high probability. This problem is made especially difficult by the fact that the critical point of electrolyte systems is at low reduced temperatures, where the unlike-ion coupling is so high, that the counterions condense on the macroions. At these conditions, the standard grand canonical scheme, where the counterion positions are chosen uniformly, has low probability of acceptance. A popular solution is to use a distance biasing scheme, where counterion positions close to the macroion are favored [158]. In previous studies [33, 149], a distance biasing scheme has been used to calculate critical parameters up to charge asymmetry of 3:1.

Highly charge-asymmetric electrolytes (above 3:1) are particularly demanding to simulate with GCMC methods, because of the high number of counterions in neutral sets of molecules. Each counterion, if not at an energetically favorable position, tends to lower the acceptance of the insertion and removal steps. In order to increase acceptance at high charge asymmetries, Cheong and Panagiotopoulos [35] used a reservoir GCMC method, where molecules are picked from a reservoir held at the same temperature as the GCMC simulation. This way, they were able to try insertions of highly probable molecule configurations. Consequently, they were able to determine critical parameters up to charge asymmetry of 10:1. In order to obey detailed balance in the removal step of the reservoir method, each ion is assigned to a macroion with the Stillinger-Lovett pairing

protocol [35, 159]. The pairing protocol introduces an extra parameter R_c , the maximum allowed distance between a macroion and its counterions. As was noted in Ref. [35], the critical parameters depend (although rather weakly) on R_c .

Our distance biasing scheme is similar to the ones used in previous works [33, 149, 158]. By changing the biasing function such that it takes the macroion valency into account, we are able to simulate 10:1 electrolytes directly. This chapter is organized as follows. In Section 6.2 we describe the model and the methods used in the simulations, in Section 6.3 we present the results, and in Section 6.4 we present the conclusions from our study.

6.2 Model and Methods

We consider a system of N_M macroions with diameter σ_M carrying charge $+Ze$, and N_S co- and $N_- = ZN_M + N_S$ counterions with diameter σ_I carrying charges $+e$ and $-e$, respectively, where e is the proton charge. The particles interact via Coulomb potential plus hard-core repulsion such that

$$U_{ij}(r_{ij}) = \begin{cases} \frac{z_i z_j}{\epsilon_s r_{ij}} & \text{for } r_{ij} \geq \frac{1}{2}(\sigma_i + \sigma_j) \\ +\infty & \text{for } r_{ij} < \frac{1}{2}(\sigma_i + \sigma_j), \end{cases} \quad (6.1)$$

where ϵ_s is the dielectric constant of the solvent, z_i and z_j are the charges of ions i and j , and r_{ij} is the distance between the ions. The size asymmetry between a macro- and microion is described by

$$\delta = \left(\frac{\sigma_M}{\sigma_{MI}} \right) - 1 = 1 - \frac{\sigma_I}{\sigma_{MI}}, \quad (6.2)$$

where $\sigma_{MI} = \frac{1}{2}(\sigma_M + \sigma_I)$ is the macroion-microion collision diameter.

The Monte Carlo simulations are performed in the grand canonical ensemble, where the thermodynamic state of the system is defined by temperature T , volume V , and chemical potentials of the macro- and coions, μ and μ_S , respectively. In the grand canonical ensemble, the number of macroions N_M and coions N_S fluctuate. We use a cubic box of length L with periodic boundary conditions. We work in reduced units with a reduced temperature

$$T^* = \frac{k_B T \epsilon_s \sigma_I}{e^2}. \quad (6.3)$$

We use the microion diameter σ_I to define the reduced temperature T^* because we wish to keep the temperature independent of the size of the macroion. The reduced density is defined as the total volume fraction of the macro- and microions, and reads

$$\phi = \frac{\pi}{6L^3} \left[\sigma_M^3 N_M + \sigma_I^3 (ZN_M + 2N_S) \right]. \quad (6.4)$$

Chemical potentials of the macroions μ^* and the coions μ_S^* are defined such that at the ideal-gas limit

$$\left. \begin{aligned} \frac{\mu^*}{Z+1} &\rightarrow T^* \ln \frac{N_M \sigma_{MI}^3}{V} \\ \frac{\mu_S^*}{2} &\rightarrow T^* \ln \frac{N_S \sigma_{MI}^3}{V} \end{aligned} \right\} \text{for } T^* \rightarrow \infty, \phi \rightarrow 0. \quad (6.5)$$

The reduced pressure is defined in units of the microion diameter σ_I as

$$P^* = \frac{P\sigma_I^3}{k_B T}. \quad (6.6)$$

We again use the microion diameter σ_I to define P^* in order to keep it independent of the macroion size.

Long-range Coulombic interactions are calculated using the Ewald summation method [93, 128] with conducting boundary conditions, 518 Fourier-space vectors, and real-space damping parameter $\kappa = 5$. In order to speed up simulations, we use the fine-lattice discretization method of Panagiotopoulos and Kumar [129]. The advantage of the lattice method is that it allows us to precalculate all the Coulombic interactions in the beginning of the simulation. During the simulation, the pair interactions are determined by a simple table lookup. Denoting the lattice spacing by a , we can define a lattice refinement parameter

$$\xi = \sigma_{MI}/a. \quad (6.7)$$

Continuum is recovered when $\xi \rightarrow \infty$. The presence of salt introduces an additional length scale, the microion diameter σ_I , and, therefore, we introduce a second lattice refinement parameter

$$\xi_I = \sigma_I/a = (1 - \delta)\xi. \quad (6.8)$$

The effect of lattice discretization on the critical behavior of 1:1 systems was studied in Ref. [129], where it was found that the normal vapor-liquid phase coexistence is recovered for $\xi \geq 3$. For $\xi \leq 2$, no vapor-liquid phase coexistence is possible, but instead the system phase separates into a disordered and an antiferromagnetic phase. In order to ensure that the salt in our system has a vapor-liquid phase coexistence, we use microion refinement $\xi_I \geq 3$. For the macroions, we use $\xi \geq 10$, as it is known from an earlier work [160] that the difference between the critical parameters at $\xi = 10$ and $\xi \rightarrow \infty$ is small, about 1% for the temperature and about 4% for the density.

Our GCMC simulations are based on insertions and removals of two types of neutral sets of molecules: (i) a macroion with Z counterions and (ii) a coion with a counterion. As the vapor-liquid phase separation occurs at low reduced temperatures, the counterions have a strong tendency to form clusters around macroions and coions. Therefore, purely random (i.e., uniform) insertions and removals of counterions lead to very low acceptance rates. In order to improve the acceptance, we use a distance biasing scheme. In the distance biasing scheme, counterions are inserted with a biased probability distribution that increases the probability of inserting a counterion close to a macroion or a coion. In the present case, a natural choice for the biased probability distribution is

$$w_{\text{bias}}(r_{ij}) = \begin{cases} \exp\left(\frac{Z_b}{T^*} \frac{1}{r_{ij}}\right) & \text{for } r_{ij} \geq \frac{1}{2}(\sigma_i + \sigma_j) \\ 0 & \text{for } r_{ij} < \frac{1}{2}(\sigma_i + \sigma_j), \end{cases} \quad (6.9)$$

that is the Boltzmann factor of a Coulomb interaction between a positive ion of charge Z_b and a counterion. Note that the probability distribution in Eq. (6.9) is not normalized.

In Eq. (6.9), the “bias charge” Z_b is a free parameter that can be adjusted to obtain maximum acceptance. We use, $Z_b = Z$ for molecules with $Z = 1$ and 3, and $Z_b = 6$ for molecules with $Z = 10$. As we observed, for $Z \approx 10$, it is favorable to choose $Z_b < Z$, in order to account for counterion-counterion repulsion that reduces the effective charge seen by the counterions. For $Z = 10$, optimal Z_b was determined by running a short simulation with different Z_b and choosing the one that gave the highest acceptance. The choice $Z_b = 6$ was also confirmed by fitting the effective macroion-macroion pair potential (obtained from the radial distribution function at low density) with Z_b/r . For $Z = 3$ and 1, we did not try to find an optimal Z_b because $Z_b = Z$ already gave high acceptance. Note that $Z_b = 1$ was used for all Z in previous works [33, 149]. This gives relatively low acceptance for $Z > 1$, although still much higher than without biasing at all.

In the following, we describe in detail the insertion and the removal steps of a macroion; the insertion and removal of a coion are completely analogous. In the insertion step, the trial position of the macroion is chosen uniformly. Counterion positions are chosen according to the probability distribution $w_{\text{bias}}(R_{k_x k_y k_z})$ given by Eq. (6.9), where $R_{k_x k_y k_z}$ is the distance between a macroion center and a lattice site (k_x, k_y, k_z) . In practice, the cumulative probability

$$W_{k_x k_y k_z} = \frac{1}{Q} \sum_{\ell_z=1}^{k_z} \sum_{\ell_y=1}^{k_y} \sum_{\ell_x=1}^{k_x} w_{\text{bias}}(R_{\ell_x \ell_y \ell_z}) \quad (6.10)$$

is precalculated into a three-dimensional $\xi L \times \xi L \times \xi L$ matrix at the beginning of a simulation. In Eq. (6.10),

$$Q = \sum_{\ell_z=1}^{\xi L} \sum_{\ell_y=1}^{\xi L} \sum_{\ell_x=1}^{\xi L} w_{\text{bias}}(R_{\ell_x \ell_y \ell_z}) \quad (6.11)$$

is the appropriate normalization factor, i.e., sum of w_{bias} over all lattice positions $[1, \dots, \xi L; 1, \dots, \xi L; 1, \dots, \xi L]$. In the simulation, we find the lattice site (k_x, k_y, k_z) for the trial position of the counterions by going through the matrix and finding the first lattice site (k_x, k_y, k_z) , for which the cumulative probability $W_{k_x k_y k_z}$ is smaller than a random number drawn from a uniform $[0, 1]$ distribution. We use a binary search algorithm to make the search efficient. This procedure is repeated for each of the Z counterions. Once all the counterion lattice sites are found, the insertion is accepted according to the criteria

$$\text{acc}(N \rightarrow N + 1) = \min \left[1, \left(\frac{V}{N + 1} \right)^{Z+1} \frac{B_{\text{ins}}}{B_{\text{del}}} \exp[(\mu^* - U_{N+1} + U_N)/T^*] \right], \quad (6.12)$$

where U_N and U_{N+1} are the potential energies (in units of $k_B T$) before and after insertion, and

$$\frac{B_{\text{ins}}}{B_{\text{del}}} = \left(\frac{Z}{\xi^3 L^3} \right)^Z \prod_{i=1}^Z \frac{N_- - (i - 1)}{\sum_{j=1, j \neq [k_1, \dots, k_{i-1}]}^{N_-} \exp(Z_b/T^* r_j)} \quad (6.13)$$

is a factor that corrects for the bias, and hence detailed balance is satisfied. In the removal step, a macroion is chosen randomly and the first counterion is chosen according to the probability

$$\frac{\exp(Z_b/T^*r_{k_1})}{\sum_{j=1}^{N_-} \exp(Z_b/T^*r_j)}. \quad (6.14)$$

When choosing the second counterion, the first (k_1) counterion has to be removed from the normalization. Thus, the second counterion is chosen according to the probability

$$\frac{\exp(Z_b/T^*r_{k_2})}{\sum_{j=1, j \neq k_1}^{N_-} \exp(Z_b/T^*r_j)}. \quad (6.15)$$

Continuing in this manner, we have for the Z th counterion

$$\frac{\exp(Z_b/T^*r_{k_Z})}{\sum_{j=1, j \neq [k_1, \dots, k_{Z-1}]}^{N_-} \exp(Z_b/T^*r_j)}. \quad (6.16)$$

When all the Z counterions are chosen, the removal step is accepted according to the criteria

$$\text{acc}(N+1 \rightarrow N) = \min \left[1, \left(\frac{N+1}{V} \right)^{Z+1} \frac{B_{\text{del}}}{B_{\text{ins}}} \exp[(-\mu^* + U_{N+1} - U_N)/T^*] \right]. \quad (6.17)$$

In practice, when choosing the first counterion, we calculate the probability in Eq. (6.14) for every counterion, and then, as in the case of insertion, use a binary search for the cumulative probability. For the second counterion, we simply exclude the first counterion from the cumulative sum and repeat the search.

In addition to the insertion and removal steps, displacement moves are carried out for microions. We noticed that displacement moves help the system to equilibrate. The portion of displacement moves over all the moves was set to 10%.

Simulations consist of equilibration and sampling runs. In a sampling run, a histogram containing the number of macroions N_M , coions N_S , and total energy U is collected. In order to determine the critical point, a simulation is done at a temperature that is close but above the critical temperature. Close to the critical point, systems sample a broad density range, due to critical fluctuations. From the (N_M, N_S, U) histogram, the critical point is determined using a mixed-field finite-scaling method [161] that assumes Ising criticality with no pressure mixing. The effects of pressure mixing on the critical parameters, if any, are expected to be minor, but require substantial additional computational effort [162]. Typically, a single simulation run is not enough to determine the critical point to a desired accuracy, and therefore multiple runs with different macroion chemical potential μ^* are combined using a histogram reweighting technique [163, 164].

μ_S^*	μ_c^*	x_S	$T_c^* \times 10^2$	$\phi_c \times 10^2$	$P_c^* \times 10^3$
$-\infty$	-2.0260(2)	0(0)	4.770(5)	5.7(1)	0.328(4)
$-\infty$	-2.0254(4)	0(0)	4.75(1)	5.8(1) ^a	...
$-\infty$	-2.02557(9)	0(0)	4.752(3)	5.99(6)	0.352(4) ^b
-1.500	-2.0315(4)	0.0496(1)	4.798(8)	5.5(1)	0.308(3)
-1.500	-2.0300(6)	0.0503(6)	4.75(2)	5.91(8)	0.325(2) ^b
-1.300	-2.0684(6)	0.35320(2)	4.733(8)	5.5(1)	0.341(6)
-1.250	-2.1049(6)	0.531(2)	4.708(8)	5.4(2)	0.45(1)
-1.200	-2.1944(5)	0.760(1)	4.70(1)	5.3(2)	0.74(3)
-1.175	-2.3115(1)	0.8868(5)	4.817(8)	5.1(2)	1.20(2)

Table 6.1: Critical parameters for system (a) with charge asymmetry of 2:1 and size asymmetry $\delta = 0.5$. The parameters are for box size $L = 12\sigma_{MI}$, except those marked with ^a and ^b are for box size $L = 15\sigma_{MI}$. Parameters marked with ^a are from Ref. [33]. The numbers in parentheses refer to the statistical uncertainty of the last decimal place shown.

The pressure is given by the relation

$$\frac{P^*V}{\sigma_I^3} = \frac{PV}{k_B T} = \ln \Xi(\mu, \mu_S, V, T) + \text{const}, \quad (6.18)$$

where $\Xi(\mu, \mu_S, V, T)$ is the grand canonical partition function, which can be obtained from the histogram data. In the limit of low density, where the system behaves as an ideal gas, a plot of $\ln \Xi$ vs $(N_M + N_S)$ gives a straight line with unit slope. The “const” in Eq. (6.18) is given by the extrapolation of this line to the limit $N_M + N_S \rightarrow 0$.

6.3 Results

We study four different systems with charge and size asymmetries of: (a) 2:1 and $\delta = 0.5$, (b) 3:1 and $\delta = 0.667$, (c) 10:1 and $\delta = 0.9$, and (d) 10:1 and $\delta = 0.667$. For systems (a)-(c), the size asymmetry was chosen so that a macroion-counterion pair and a coion-counterion pair have an equal Coulomb potential energy at contact. The lattice refinement parameter ξ is set to $\xi = 10$ in systems (a), (b), and (d). According to Eq. (6.8), this gives $\xi_I = 5$ in system (a) and $\xi_I = 3.33$ in systems (b) and (d). In system (c), $\xi = 10$ would give a microion lattice refinement of $\xi_I = 1$. As was mentioned in Section 6.2, only systems with $\xi_I \geq 3$ have a vapor-liquid phase separation. Therefore, in system (c), we use a finer lattice with $\xi = 30$, to make sure that the salt has a vapor-liquid phase separation ($\xi_I = 3$).

In our simulations, we start from a salt-free state with $\mu_S^* = -\infty$ and add salt by increasing μ_S^* in steps. For each step, the critical parameters are determined. We characterize the amount of the added salt by the salt mole fraction, defined as

$$x_S = \frac{N_S}{N_M + N_S}. \quad (6.19)$$

μ_S^*	μ_C^*	x_S	$T_c^* \times 10^2$	$\phi_c \times 10^2$	$P_c^* \times 10^3$
$-\infty$	-2.6672(2)	0(0)	4.488(5)	7.3(2)	0.095(4)
-1.17	-2.7077(9)	0.3710(6)	4.40(2)	7.5(2)	0.120(6)
-1.13	-2.7282(4)	0.4824(9)	4.354(5)	7.5(4)	0.146(3)
-1.12	-2.744(1)	0.5446(9)	4.33(3)	7.3(2)	0.164(7)
-1.07	-2.8294(3)	0.749(2)	4.26(1)	7.3(2)	0.28(1)
-1.07	-2.8305(5)	0.752(2)	4.23(1)	7.41(9)	0.33(2) ^a
-1.05	-2.8855(3)	0.8169(6)	4.270(4)	7.7(1)	0.410(1)
-1.03	-2.9693(6)	0.8818(6)	4.320(2)	7.2(2)	0.590(2)
-1.02	-3.039(1)	0.9157(8)	4.382(4)	6.9(3)	0.77(1)
-1.01	-3.167(2)	0.9535(3)	4.505(0)	6.5(4)	1.0(2)
-1.00	-3.32(1)	0.977(2)	4.62(1)	5.6(5)	1.4(1)

Table 6.2: Critical parameters for system (b) with charge asymmetry of 3:1 and size asymmetry $\delta = 0.667$. The parameters are for box size $L = 12\sigma_{MI}$, except those marked with ^a are for box size $L = 15\sigma_{MI}$. The numbers in parentheses refer to the statistical uncertainty of the last decimal place shown.

μ_S^*	μ_C^*	x_S	$T_c^* \times 10^2$	$\phi_c \times 10^2$	$P_c^* \times 10^6$
$-\infty$	-6.801(1)	0(0)	3.28(1)	15.2(1)	2.444(2)
-1.26	-6.807(1)	0.093(1)	3.28(1)	14.5(5)	1.2(2)
-1.20	-6.818(3)	0.208(4)	3.28(2)	14.3(8)	1.3(3)
-1.10	-6.8784(8)	0.559(7)	3.26(2)	15(1)	1.5(2)
-1.08	-6.9078(1)	0.641(3)	3.24(1)	15(2)	1.7(2)

Table 6.3: Critical parameters for system (c) with charge asymmetry of 10:1 and size asymmetry $\delta = 0.9$. The parameters are for box size $L = 12\sigma_{MI}$. The numbers in parentheses refer to the statistical uncertainty of the last decimal place shown.

μ_S^*	μ_C^*	x_S	$T_c^* \times 10^2$	$\phi_c \times 10^2$	$P_c^* \times 10^3$
$-\infty$	-22.744(2)	0(0)	11.10(1)	11.2(2)	0.101(5)
-1.80	-22.737(6)	0.126(3)	10.89(3)	11.8(3)	0.18(1)
-1.67	-22.732(2)	0.202(2)	10.74(2)	11.9(5)	0.26(2)
-1.53	-22.726(3)	0.30(1)	10.49(3)	13(1)	0.40(4)
-1.33	-22.718(3)	0.48(1)	9.73(2)	15(1)	0.69(1)
-1.33	-22.723(3)	0.50(2)	9.83(2)	12(1)	0.521(9) ^a
-1.30	-22.733(1)	0.535(9)	9.732(5)	13.4(8)	0.683(5) ^a
-1.17	-22.758(5)	0.661(7)	8.61(8)	16(1)	1.2(1)
-1.17	-22.771(2)	0.667(4)	8.79(5)	16.2(7)	1.2(5) ^a
-1.1	-22.8229(4)	0.755(2)	7.99(7)	15(1)	1.3(1) ^a

Table 6.4: Critical parameters for system (d) with charge asymmetry of 10:1 and size asymmetry $\delta = 0.667$. The parameters are for box size $L = 12\sigma_{MI}$, except those marked with ^a are for box size $L = 10\sigma_{MI}$. The numbers in parentheses refer to the statistical uncertainty of the last decimal place shown.

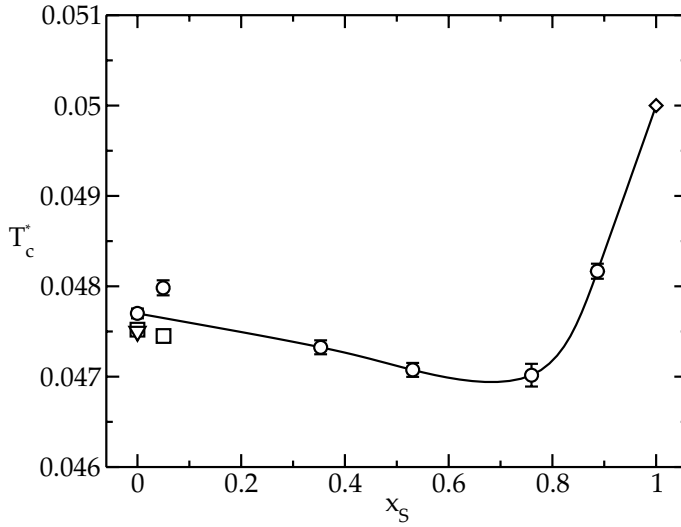


Figure 6.1: Critical temperature T_c^* of system (a) with charge asymmetry of 2:1 and size asymmetry $\delta = 0.5$, as a function of the salt mole fraction x_S . The points marked with the circles (\circ) are for box size $L = 12\sigma_{MI}$, while those marked with the squares (\square) and triangles (∇) are for box size $L = 15\sigma_{MI}$. The line is a guide to the eye. The pure salt critical temperature at $x_S = 1$ (\diamond) is from Ref. [129] and salt-free critical temperature at $x_S = 0$ (∇) is from Ref. [33] ($L = 15\sigma_{MI}$). Error bars smaller than the symbol size are not drawn.

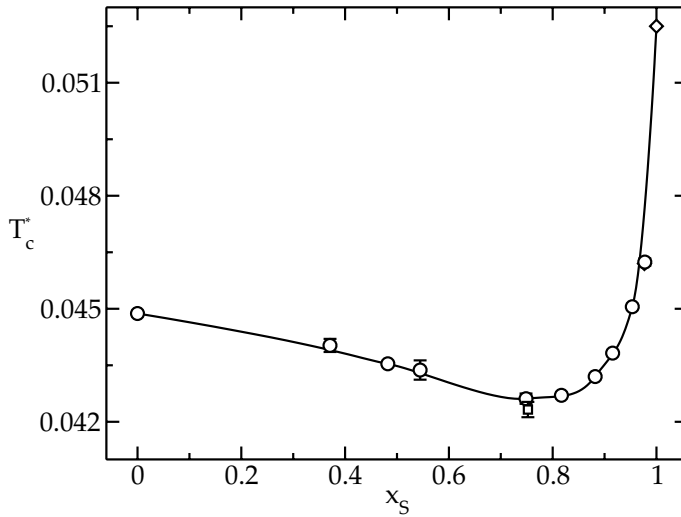


Figure 6.2: Critical temperature T_c^* of system (b) with charge asymmetry of 3:1 and size asymmetry $\delta = 0.667$, as a function of the salt mole fraction x_S . The points marked with the circles (\circ) are for box size $L = 12\sigma_{MI}$ and the point marked with the square (\square) is for box size $L = 15\sigma_{MI}$. The line is a guide to the eye. The pure salt critical temperature at $x_S = 1$ (\diamond) is from Ref. [129]. Error bars smaller than the symbol size are not drawn.

With this definition, $x_S = 0$ corresponds to a salt-free state and $x_S = 1$ corresponds to a pure salt state. Our results are listed in Tables 6.1-6.4. Unless otherwise indicated, the parameters are for box size $L = 12\sigma_{MI}$. Error estimates are calculated from (two to four) independent runs at different temperatures using the Student's t -test with 90% confidence interval.

Figures 6.1-6.4 show the critical temperature T_c^* as a function of the salt mole fraction x_S . The pure salt critical temperature is taken from Ref. [129]: we use $\zeta = 5$ results for system (a), whose ions are on a lattice with $\zeta_I = 5$, and $\zeta = 3$ results for systems (b)-(d), whose ions are on a lattice with $\zeta_I = 3.33$. As can be seen from Figs. 6.1-6.3, in systems (a)-(c), where the pure salt has a higher critical temperature than the salt-free state, $T_c^*(x_S)$ is not monotonic, but goes through a minimum (at $x_S \approx 0.6 - 0.8$). In system (c), we did not reach high enough salt fractions to locate the minimum explicitly, but as the inset in Fig. 6.3 shows, T_c^* is decreasing with increasing x_S . Therefore, we expect there to be a minimum. We have extrapolated lines from our data to pure salt to indicate the expected qual-

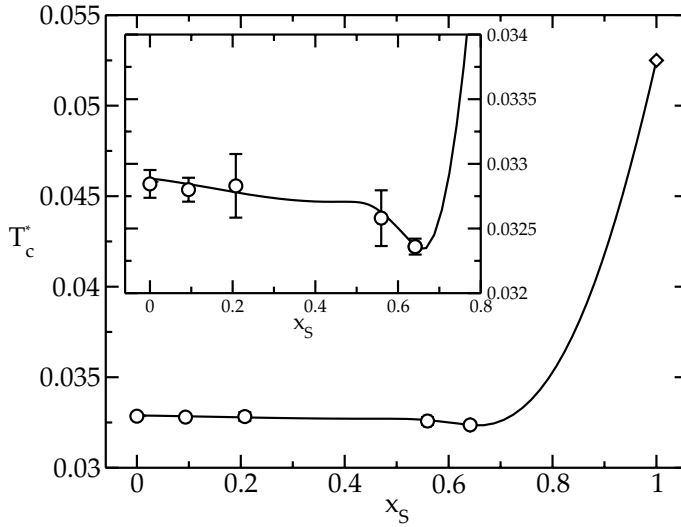


Figure 6.3: Critical temperature T_c^* of system (c) with charge asymmetry of 10:1 and size asymmetry $\delta = 0.9$, as a function of the salt mole fraction x_S (\circ). The results are for box size $L = 12\sigma_{MI}$. The line is a guide to the eye. The pure salt critical temperature at $x_S = 1$ (\diamond) is from Ref. [129]. Error bars smaller than the symbol size are not drawn.

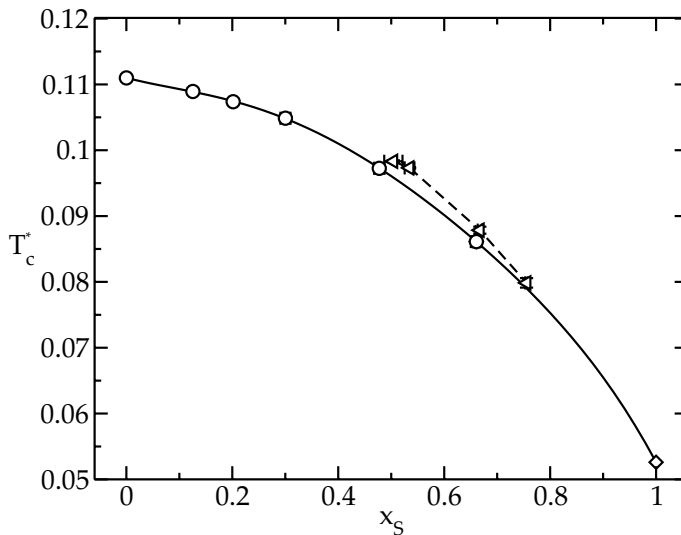


Figure 6.4: Critical temperature T_c^* of system (d) with charge asymmetry of 10:1 and size asymmetry $\delta = 0.667$, as a function of the salt mole fraction x_S . The points marked with the circles (\circ) are for box size $L = 12\sigma_{MI}$ and those marked with the triangles (\triangleleft) are for box size $L = 10\sigma_{MI}$. The lines are guides to the eye. The pure salt critical temperature at $x_S = 1$ (\diamond) is from Ref. [129]. Error bars smaller than the symbol size are not drawn.

itative behavior of T_c^* over the complete composition range. This extrapolation is, of course, only approximate - it would take significantly more computational resources than those available to us to enable calculations for systems with large amounts of salt because of the difficulty in sampling macroion insertions and removals.

In Figs. 6.1-6.3, the decrease in the critical temperature at $x_S < 0.8$ can be explained by a more general result, which states that external disturbances, such as walls, added components, etc., lower the critical temperature [165]. At $x_S > 0.8$, the critical temperature increases to reach the pure salt critical point. In contrast, in system (d), where pure salt has a lower critical temperature than the salt-free state, $T_c^*(x_S)$ decreases monotonically, see Fig. 6.4.

In Figs. 6.5-6.8, we plot the critical volume fraction ϕ_c as a function of the salt mole fraction x_S . In systems (a)-(c), ϕ_c is more or less a constant for $0 < x_S < 0.9$, and at $x_S > 0.9$, ϕ_c starts to decrease rapidly towards the pure salt critical point. In the 10:1 systems [(c) and (d)], we were not able to calculate critical

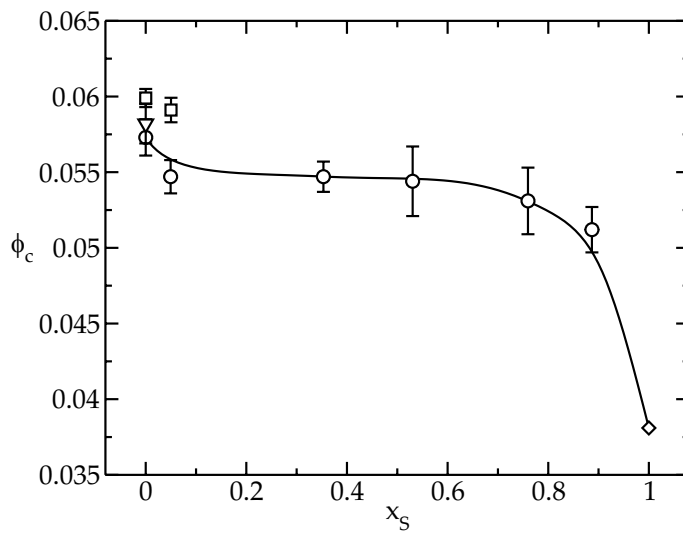


Figure 6.5: Critical volume fraction $\phi_c(x_S)$ of system (a) with charge asymmetry of 2:1 and size asymmetry $\delta = 0.5$, as a function of the salt mole fraction x_S . The points marked with the circles (\circ) are for box size $L = 12\sigma_{MI}$, while those marked with the squares (\square) and the triangles (∇) are for box size $L = 15\sigma_{MI}$. The pure salt critical temperature at $x_S = 1$ (\diamond) is from Ref. [129] and the salt-free critical temperature at $x_S = 0$ (∇) is from Ref. [33]. The line is a guide to the eye.

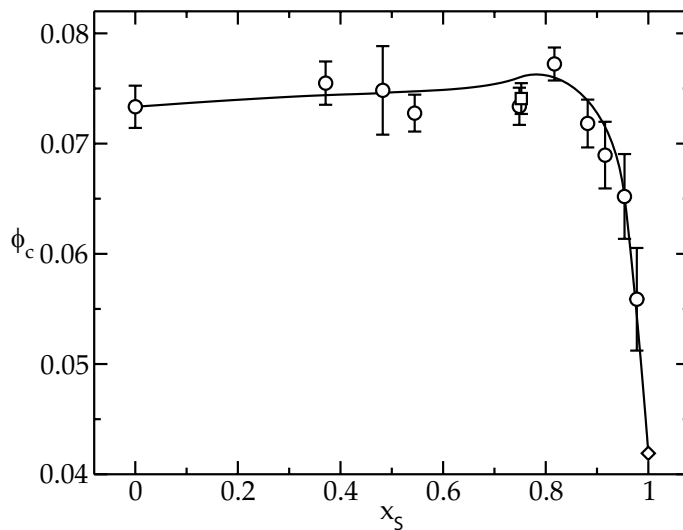


Figure 6.6: Critical volume fraction $\phi_c(x_S)$ of system (b) with charge asymmetry of 3:1 and size asymmetry $\delta = 0.667$, as a function of the salt mole fraction x_S . The points marked with the circles (\circ) are for box size $L = 12\sigma_{MI}$ and the point marked with the square (\square) is for box size $L = 15\sigma_{MI}$. The line is a guide to the eye. The pure salt critical temperature at $x_S = 1$ (\diamond) is from Ref. [129].

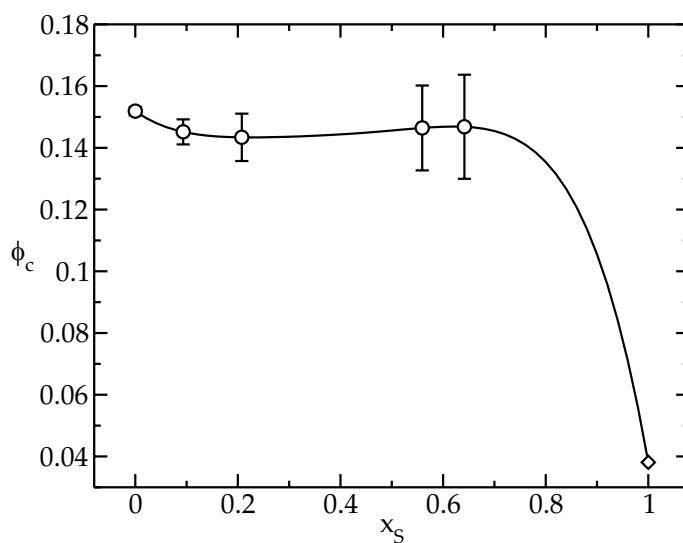


Figure 6.7: Critical volume fraction $\phi_c(x_S)$ of system (c) with charge asymmetry of 10:1 and size asymmetry $\delta = 0.9$ (\circ), as a function of the salt mole fraction x_S . The results are for box size $L = 12\sigma_{MI}$. The line is a guide to the eye. The pure salt critical temperature at $x_S = 1$ (\diamond) is from Ref. [129].

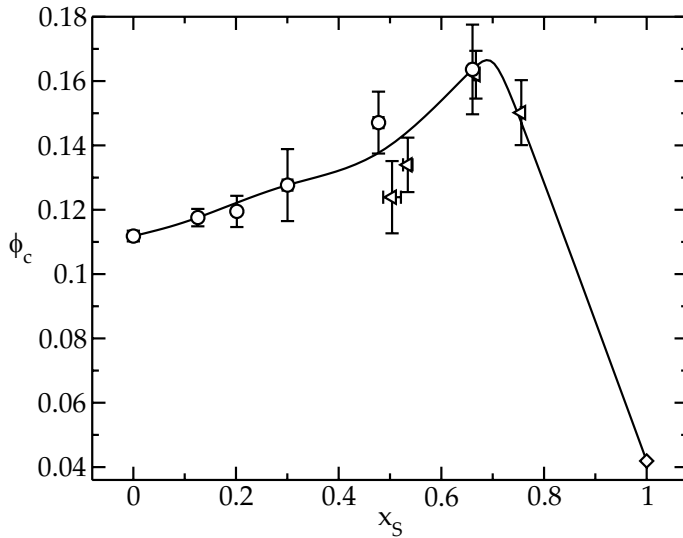


Figure 6.8: Critical volume fraction $\phi_c(x_S)$ of system (d) with charge asymmetry of 10:1 and size asymmetry $\delta = 0.667$, as a function of the salt mole fraction x_S . The points marked with the circles (\circ) are for box size $L = 12\sigma_{MI}$ and those marked with the triangles (\triangleleft) are for box size $L = 10\sigma_{MI}$. The line is a guide to the eye. The pure salt critical temperature at $x_S = 1$ (\diamond) is from Ref. [129].

parameters beyond $x_S \approx 0.66$ for box size $L = 12\sigma_{MI}$, due to sampling problems: the acceptance of macroion insertions in these systems was below 0.1%. However, we were able to calculate critical parameters up to $x_S = 0.76$ for system (d) (10:1 and $\delta = 0.667$) using box size $L = 10\sigma_{MI}$. These results are denoted by the triangles in Fig. 6.8. As the statistical accuracy is poor, it is hard to make any definite conclusions. However, it is tempting to argue that $\phi_c(x_S)$ tends towards the pure salt limit as $x_S \rightarrow 1$.

In order to get an idea of the system size dependence of our results, we recalculated some of the critical points for different box size L . In system (a) (2:1 and $\delta = 0.5$), the two lowest salt critical points were recalculated using $L = 15\sigma_{MI}$, see Figs. 6.1 and 6.5 and Table 6.1. We find considerable system size dependence for this system. This is because, for box size $L = 12\sigma_{MI}$, there are not enough data points at the low-density end of the histogram to fit the Ising curve completely. At higher salt concentration, there are more data points at the low-density part of the histograms and this system size dependence disappears. According to our histogram data, the Ising curve can be fitted completely when $x_S \approx 0.6$. In system (a), our results for box size $L = 15\sigma_{MI}$ agree very well with the earlier results in Ref. [33], that are also for $L = 15\sigma_{MI}$. In system (b) (3:1 and $\delta = 0.667$), the critical point at $\mu_S^* = -1.07$ was recalculated using $L = 15\sigma_{MI}$, and, as can be seen from Table 6.2, the critical parameters are almost within the error bars of the results for $L = 12\sigma_{MI}$. In system (d) (10:1 and $\delta = 0.667$), we recalculated critical points at $\mu_S^* = -1.33$ and at $\mu_S^* = -1.17$ using a box size $L = 10\sigma_{MI}$, see Table 6.4. At $\mu_S^* = -1.17$, all critical parameters (except μ_c^*) are, within the error bars, indistinguishable. However, at $\mu_S^* = -1.33$, we find significant differences between the results for $L = 12\sigma_{MI}$ and for $L = 10\sigma_{MI}$.

Figure 6.9 shows the critical-point loci in the (temperature T^* , pressure P^*) plane. From two independent measurements with box sizes $L = 15\sigma_{MI}$ and $19\sigma_{MI}$, we estimated the pure salt critical pressure $P^* = 0.00297(4)$ using Eq. (6.18) and critical temperature $T^* = 0.0528(2)$. We are not aware of previous work that reports critical pressure of electrolytes. As can be seen from Fig. 6.9, the pure salt

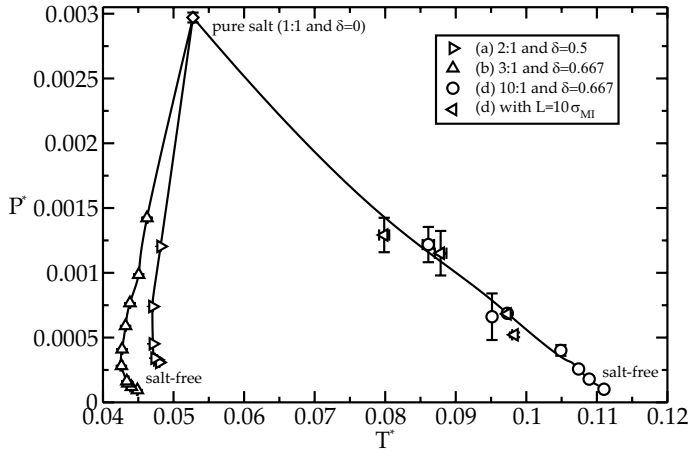


Figure 6.9: Critical-point loci in the (T^*, P^*) plane. The lines are guides to the eye.

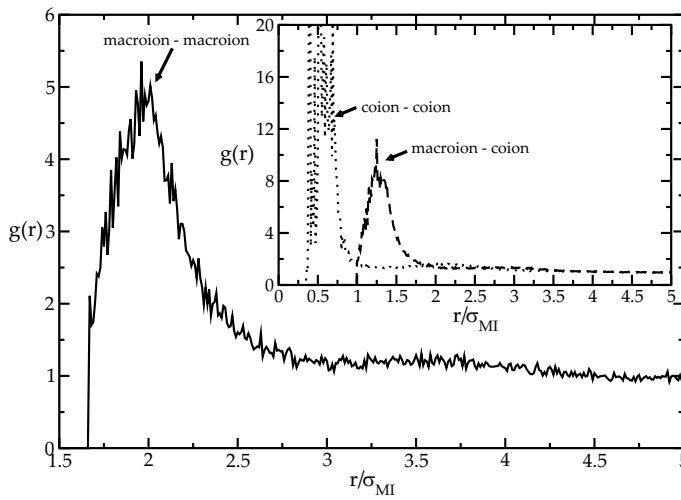


Figure 6.10: Radial distribution functions for system (b) (3:1 and $\delta = 0.667$) at $T^* = 0.045 \approx 1.03T_c^*$, $\mu_S^* = -1.13$, and $\phi = 0.020(2)$.

state has a higher pressure than any of the salt-free states. The reason for this is the ideal gas contribution to the pressure ($P_{id}V = Nk_B T$), which is high for the pure salt state because it has the highest number density of particles than any of the salt-free states (although it has the lowest volume fraction, see Figs. 6.5-6.8). Figure 6.9 also shows that, upon adding salt, the pressure increases very gradually at first, and then in big steps at higher salt concentrations. This is why, even at the highest coion concentration $x_S = 0.977$ [system (c)], where the system consists almost completely of salt, the pressure is well below the pure salt state. Note that the critical-point loci of system (c) (10:1 and $\delta = 0.9$) is missing from Fig. 6.9. In this high size asymmetry case, all pressures are much smaller than in the other systems, see Table 6.3. This is because the length scale in our definition of P^* [see Eq. (6.10)] is the microion diameter and for high size asymmetries, the factor σ_I^3 is very small.

We can conclude that the electrolyte mixtures studied here are type-I mixtures, where the two components mix continuously [166]. Clearly, this conclusion holds less firmly for system (c), where we were not able to reach high enough x_S to see a convergence towards the pure salt limit. However, our data does not give any evidence of a more complicated mixing behavior.

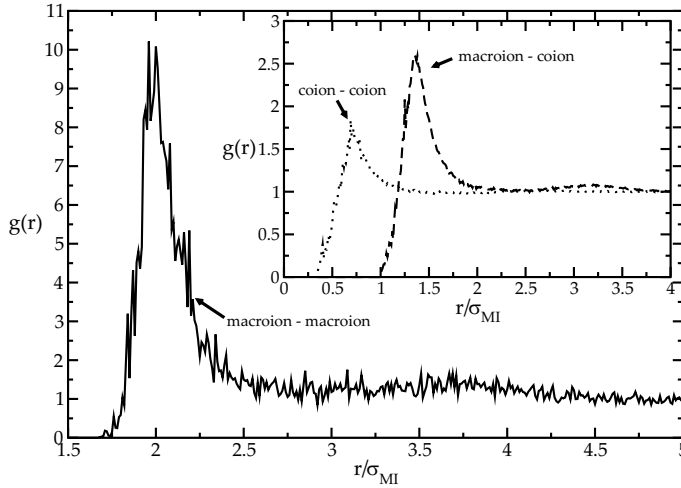


Figure 6.11: Radial distribution functions for system (d) (10:1 and $\delta = 0.667$) at $T^* = 0.1 \approx 1.03T_c^*$, $\mu_S^* = -1.33$, and $\phi = 0.037(2)$.

In all systems, the macroion vapor phase is also the vapor phase for the salt, and the macroion liquid phase is also the liquid phase for the salt. In other words, when the system fluctuates between vapor and liquid phases, macroion and salt densities are coupled. We observed, that for a fixed coion chemical potential μ_S^* , the ratio between macroion and salt number densities is constant to a very good approximation. The coupling between the macroion and the salt densities also explains why the errors in the salt mole fraction x_S are so small. Figures 6.10 and 6.11 show the radial distribution functions of positive like-charged species for the 3:1 (b) and 10:1 (d) systems with $\delta = 0.667$, respectively. The radial distribution functions in Figs. 6.10 and 6.11 are calculated in the vapor phase, close to the $x_S = 0.48$ critical point at $T^* \approx 1.03T_c^*$ (i.e., slightly above the critical temperature). As Figs. 6.10 and 6.11 show, all radial distributions are peaked close to their contact distance. Since, in the low-density vapor phase, the effective interaction potential is, to a good approximation, equal to the negative logarithm of the radial distribution function [$u_{\text{eff}} = -\ln g(r)$], this implies effective attraction between all like-charged species. The effective attraction between macroions and coions explains the coupling between the macroion and salt densities.

The height of the first peaks in the radial distribution functions in Figs. 6.10 and 6.11 is related to the strength of the attraction. As can be seen, the macroion-macroion peak is approximately twice as high for system (d) (Fig. 6.11) than for system (b) (Fig. 6.10), while the coion-coion peak is much higher for system (b) (Fig. 6.10) than for system (d) (Fig. 6.11). A simple explanation for these differences is obtained, when one considers the critical temperature in these systems relative to the salt-free ($x_S = 0$) and pure salt ($x_S = 1$) critical temperatures. Temperature in system (d) (Fig. 6.11) is *below* the critical temperature of the salt-free state, and this is why the macroion-macroion coupling is *high* compared to system (b) (Fig. 6.10), where the temperature is similar to the critical temperature of the salt-free state. Similarly, temperature in system (b) is *below* the critical temperature of pure salt and this is why the coion-coion coupling is *high* compared to system (d), where the temperature is *above* the critical temperature of the pure salt. The difference between the two systems is also well depicted in Figs. 6.12 and 6.13, where snapshots of the vapor phase close to the $x_S = 0.48$ critical point

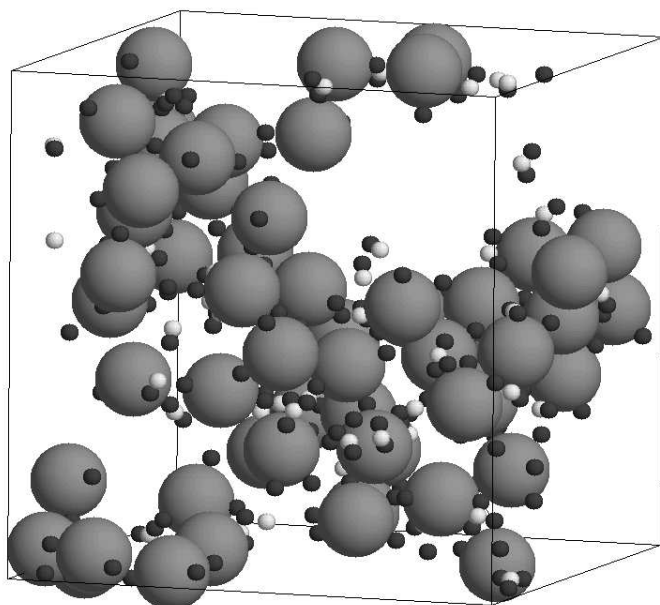


Figure 6.12: Snapshot of system (b) (3:1 and $\delta = 0.667$) at the vapor phase of the $\mu_S^* = -1.13$ [$x_S = 0.482(1)$] critical point with $T^* = 0.044 = T_c^*$, $\mu^* = -2.730$, and $\phi = 0.087$. Big spheres are macroions with charge $+3e$, white small spheres are coions with charge $+e$, and dark small spheres are counterions with charge $-e$.

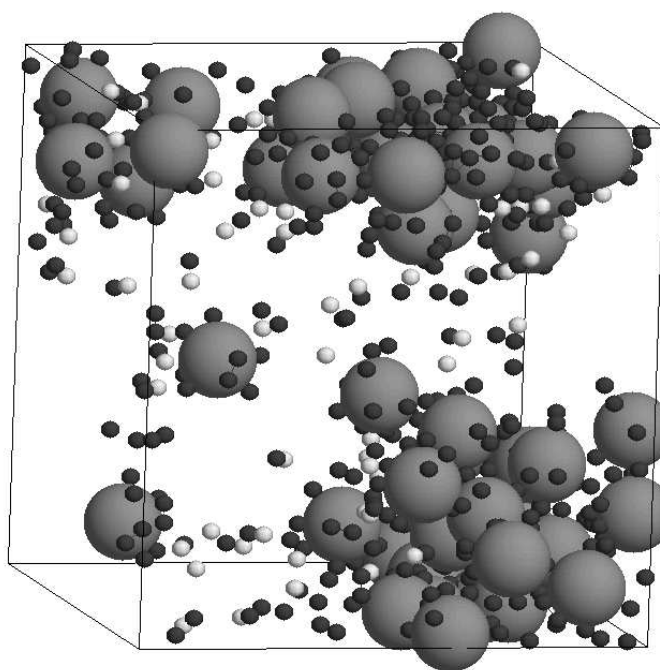


Figure 6.13: Snapshot of system (d) (10:1 and $\delta = 0.667$) close to the $\mu_S^* = -1.33$ [$x_S = 0.48(1)$] critical point with $T^* = 0.0992 = 1.02T_c^*$, $\mu^* = -22.738$, and $\phi = 0.079$. The big spheres are macroions with charge $+10e$, white small spheres are coions with charge $+e$, and dark small spheres are counterions with charge $-e$.

are shown: Macroions in system (d) (Fig. 6.13) form rather dense clusters, while in system (b) (Fig. 6.12) the macroions are more loosely bound to each other. This implies that the macroion-macroion coupling is higher in system (d) than in (b). Co- and counterions in system (b) (Fig. 6.12) form dimers and trimers, while in system (d) (Fig. 6.13) there are free microions, implying that the coion-coion coupling is higher in system (b) than in (d). This agrees with the radial distribution functions in Figs. 6.10 and 6.11. Furthermore, coions in system (b) are bound close to the macroions (see Fig. 6.12), while in system (d) the coions fill the space left empty by the macroions (see Fig. 6.13). This is in agreement with the radial distri-

bution functions in Figs. 6.10 and 6.11, which show a higher macroion-coion peak for system (b) than for (d). The clustering seen in Fig. 6.13 is typical for system (d) with added salt. Clusters were also seen at temperatures above the critical temperature and at densities different from the critical density.

The deepness of the macroion-macroion attraction in system (d) can be estimated from the first peak in Fig. 6.11 to be $\ln(10)k_B T \approx 2.3k_B T$.^{*} This means, that each macroion gains about $2k_B T$ of energy when it comes in contact with another macroion. We observed, that this energy minimum causes considerable sampling problems. Acceptance of the insertion and removal steps drops and simulations tend to get stuck in the high-density state. This is the main reason why we could not reach higher salt concentrations.

6.4 Conclusions

We have studied the critical parameters of asymmetric electrolyte mixtures within the primitive model. The mixtures consist of large multivalent macroions and small monovalent co- and counterions. We view the system as a binary mixture of macroions with their counterions and salt (co- and counterion pair). We calculated the critical-point loci that connect the salt-free state consisting of macroions and counterions with the pure salt state. Critical points were calculated for four systems with charge and size asymmetries of (a) 2:1 and $\delta = 0.5$, (b) 3:1 and $\delta = 0.667$, (c) 10:1 and $\delta = 0.9$, and (d) 10:1 and $\delta = 0.667$.

We used a combination of grand canonical Monte Carlo simulations, histogram reweighting method, and mixed-field finite-scaling method to obtain the critical points. The simulations were done using the fine-lattice discretization method. We implemented a distance biasing method that enhances the efficiency of the grand canonical insertion and removal steps by many orders of magnitude and enables direct simulations of systems with charge asymmetry of 10:1. In systems (c) and (d), at high salt (coion) concentration, we experienced sampling problems that inhibited us from calculating critical points closer to the pure salt limit.

We observed the following nonmonotonic behavior in the critical parameters: (i) in systems (a)-(c), the critical temperature T_c^* as a function of the salt mole fraction x_S goes through a minimum, and (ii) in system (d), the critical volume fraction $\phi_c(x_S)$ goes through a maximum. The binary electrolyte mixtures studied here are type-I mixtures, where the two species mix continuously.

As the salt has nonmonotonic effects on the critical parameters of electrolytes, our results should form a good benchmark for testing theoretical models on electrolytes. In particular, it would be interesting to see if a theory can reproduce the nonmonotonic behavior of $T_c^*(x_S)$ and $\phi_c^*(x_S)$, and predict the type of the mixture correctly.

For future studies, an idea that could help in calculating critical points close to the pure salt limit is to reduce the system size at high salt concentrations. Smaller system size means shorter simulation time and, if done correctly, should not in-

^{*}Here, the validity of the approximation $u_{\text{eff}} = -\ln g(r)$ was checked by calculating the radial distribution at lower densities. At $\phi \approx 0.00479(2)$ the depth of the attraction was estimated to be $\ln(16)k_B T \approx 2.8k_B T$.

troduce considerable finite-size effects because the overall density of the system decreases in the pure salt limit.

Acknowledgements The Monte Carlo code is based on A. Z. Panagiotopoulos' original code.

7

Crystal Structures of Oppositely Charged Colloids with Size Ratio 0.31

ABSTRACT

We study crystal structures in mixtures of large and small oppositely charged spherical colloids with size ratio 0.31 using Monte Carlo simulations, and compare our results with an experimental system that is studied using confocal microscopy. We develop an interactive method based on simulated annealing to predict new binary crystal structures with stoichiometries from 1 to 8. Employing these structures in Madelung energy calculations using a screened Coulomb potential, we construct a ground-state phase diagram, which shows a remarkably rich variety of crystals. Our phase diagram displays colloidal analogs of simple-salt structures and of the doped fullerene C_{60} structures, but also novel structures that do not have an atomic or molecular analog. We find three of the predicted structures experimentally, which provides confidence that our method yields reliable predictions.

7.1 Introduction

Colloids are important model systems for atoms and molecules, as they exhibit the same phase behavior, but are easier to investigate and to manipulate. The possibility to tune colloidal interactions chemically or by an external field has led to a great variety of model systems. Recently, a new model system was presented that consists of oppositely charged colloids that form equilibrium crystals [11, 69]. A profound difference with atomic systems is that ionic colloidal crystal structures are not dictated by charge neutrality as the charge balance is covered by the presence of counterions. This severs the link between charge ratio and stoichiometry, and enlarges the number of possible crystal structures. Predicting these is a computational challenge, not only because of the overwhelming number of possible structures and system parameters (charge, size, solvent, salinity, composition, etc.) but also because of the intricate interplay between attractive and repulsive interactions, entropy, and packing effects. In this chapter, we develop an interactive simulation method to predict binary crystal structures of oppositely charged colloids, based on simulated annealing [167]. Employing this method we are able to predict a whole variety of new binary crystal structures with different stoichiometries, which we used in Madelung energy calculations to map out the ground-state phase diagram. Results are presented for binary mixtures of small and large oppositely charged colloids with size ratio 0.31, corresponding to one of the experimental systems that triggered our theoretical interest [11]. The calculated phase diagram exhibits a plethora of different crystal structures, some of which have atomic and molecular analogs, while others do not. We are able to confirm the stability of three of the crystal structures experimentally.

7.2 Methods

The experimental system consists of spherical, sterically stabilized polymethylmethacrylate (PMMA) particles [168], dispersed in an apolar solvent mixture. The negatively charged larger particles have a radius $a_L = 1.16 \mu\text{m}$ (polydispersity 3%), and the positively charged smaller particles have a radius $a_S = 0.36 \mu\text{m}$ (polydispersity 5%), hence, the size ratio is $a_S/a_L = 0.31$. The two types of particles have two different fluorescent dyes incorporated in their volume. The large spheres are labeled with rhodamine isothiocyanate and the small ones with 7-nitrobenzo-2-oxa-1,3-diazol, by which they can be distinguished using fluorescence microscopy. The colloids are dispersed in a density and refractive index matching mixture of cyclohexylbromide and decalin (80/20 volume ratio). The preparation of the binary mixtures and samples is described in Ref. [11]. Image analysis of xyz data stacks obtained by confocal scanning laser microscopy allows the structures to be studied in real space.

We model this system as N_L large colloids in a volume V with a radius a_L carrying a negative charge $Z_L e$ (where $Z_L < 0$ and e the proton charge) and N_S small colloids with a radius a_S carrying a positive charge $Z_S e$ ($Z_S < |Z_L|$). We assume that the pair potential $u_{ij}(r)$, between colloid i and j at inter-particle separation r , is given by the linear superposition approximation (LSA) [169] of the DLVO

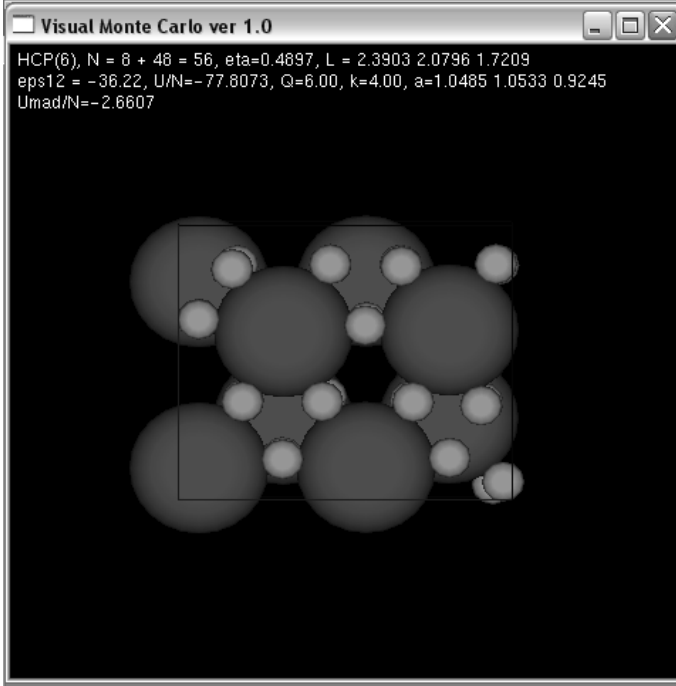


Figure 7.1: A snapshot of the interactive MC simulation program. In the run shown here, the LS_6^{hp} structure was found.

theory [17, 18] as

$$\frac{u_{ij}(r)}{k_B T} = \begin{cases} \frac{Z_i Z_j \lambda_B e^{\kappa(a_i + a_j)}}{(1 + \kappa a_i)(1 + \kappa a_j)} \frac{e^{-\kappa r}}{r} & r \geq a_i + a_j \\ \infty & r < a_i + a_j, \end{cases} \quad (7.1)$$

where Z_i (Z_j) and a_i (a_j) are the charge number and radius of colloid i (j), $\lambda_B = e^2 / \epsilon_s k_B T$ is the Bjerrum length, $\kappa = \sqrt{8\pi\lambda_B \rho_{\text{salt}}}$ is the inverse Debye screening length, ϵ_s is the dielectric constant of the solvent, and ρ_{salt} is the salt concentration. The screened Coulomb potential in Eq. (7.1) has been used to describe oppositely charged colloids before, see Ref. [170]. See also Section 8.2, where the use of screened Coulomb potential for equal size oppositely charged colloids is justified. We denote the composition by $x = N_S / (N_L + N_S)$, the packing fraction of large colloids by $\eta_L = 4\pi a_L^3 N_L / 3V$, the dimensionless large-small colloid contact potential by $\Gamma = |u_{LS}(a_L + a_S)| / k_B T$, and the charge ratio by $Q = |Z_L / Z_S|$. We fix the size ratio to the experimental value $a_S / a_L = 0.31$, and determine the phase diagram of this system for varying Q and κ as these parameters turned out to be hard to measure under crystallization conditions and are likely to vary for different experiments.

7.3 Results

We developed an interactive Monte Carlo (MC) simulation program to predict binary crystal structure candidates. The simulations are performed using periodic boundary conditions. The program has real-time visualization, and allows to change various parameters (Γ , Q , κ , and stoichiometry) during the simulation, to switch between constant pressure (NPT) and canonical (NVT) ensembles

LS_n	fcc	bcc	sc	sh	hcp	bc
1	Zinc blende	Zinc blende	-	-	Wurtzite	-
2	CaF_2	CaF_2	-	-	-	CaF_2
3	LS_3^{fcc}	Cr_3Si	ReO_3	Li_3N	LS_3^{hcp}	ReO_3
4	A_4C_{60}, LS_4^{bct}	A_4C_{60}, SiF_4	-	-	LS_4^{hcp}	-
6	$A_6C_{60}^{bcc}, LS_6^{fcc}$	$A_6C_{60}^{bcc}$	-	-	LS_6^{hcp+hp}	-
8	LS_8^{fcc}	LS_8^{fcc}	-	LS_8^{hcp}	LS_8^{hcp}	-

Table 7.1: The crystal structures found with simulated annealing for each large colloid starting configuration and stoichiometry n . C_{60} stands for the fullerene molecule and line (-) indicates absence of crystal structure.

[93], and to turn on (or off) large-colloid displacement moves. The simulations were started in the NVT -ensemble with the large colloids in a face-centered-cubic (fcc), body-centered-cubic (bcc), hexagonal-close-packed (hcp), simple-cubic (sc), simple hexagonal (sh), or base-centered (bc) crystal, and the small colloids at random (non-overlapping) positions. Next, we used simulated annealing to increase Γ slowly from 0 (high temperatures) to $\Gamma \approx 10 - 20$ (which gives us the ground-state structure), while only the small colloids were allowed to move. At the final Γ we switch to the NPT -ensemble, where volume moves were performed separately for each axis in order to equilibrate the small-colloid positions and the box shape. Finally, the large-colloid moves were turned on and the ideal crystal structures were constructed from snapshots of the final colloid configuration. A snapshot of the interactive MC simulation program is shown in Fig. 7.1, where the LS_6^{hp} structure (defined below) was found.

The search for new stable binary structures was performed by trying all the above mentioned large-colloid crystals as starting configurations, at packing fractions around $\eta_L = 0.3 - 0.56$ and at various initial shapes of the simulation box. This was repeated for small-large stoichiometries $n = 1 - 8$ (denoted by LS_n), where n is related to the composition by $x = n/(n+1)$. The simulations were performed in a box with 4 to 16 large colloids. Such a small simulation box with periodic boundaries facilitates finding structures with crystalline order, as it reduces the probability of stacking faults. Table 7.1 lists the crystal structures found for each stoichiometry and large-colloid starting configuration, for $\kappa a_L = 2$ and $Q = n$. Structures, which have no atomic or molecular analog, are named LS_n^{lat} , where “lat” is the lattice symmetry of the large colloids. In the colloidal analogs of the fullerene structures, A_4C_{60} [171], and the body-centered-cubic A_6C_{60} (or $A_6C_{60}^{bcc}$) [172] the large colloids correspond to C_{60} and the small ones to A (=K, Rb, or Cs). We have not (yet) considered primitive unit cells with more than two large colloids, and have hence excluded $n = 5$ and 7, as well as some other structures (e.g., a colloidal analog of the face-centered-cubic A_6C_{60} structure [173]). This does not mean, of course, that these structures could not form in experiments.

Predicting the phase diagram of a binary mixture often involves a calculation of the Gibbs free energy per particle, since its x -dependence at fixed P and T

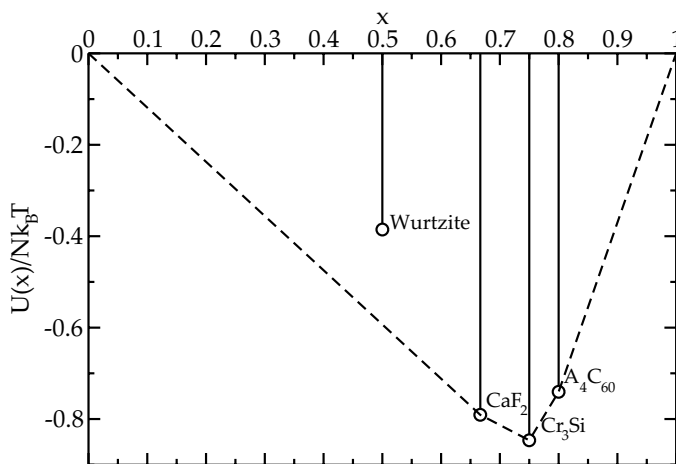


Figure 7.2: The common tangent construction for $Q = 1.8$ and $\kappa a_L = 2.5$. The circles denote the Madelung energies and the dashed line the common tangent construction.

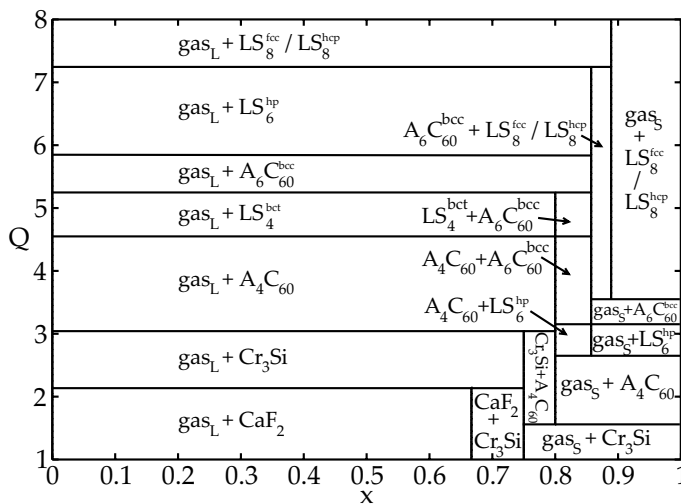


Figure 7.3: x - Q slice of the ground-state phase diagram at $\kappa a_L = 2.5$. “gas_L” and “gas_S” refer to an infinitely dilute gas of large and small colloids, respectively.

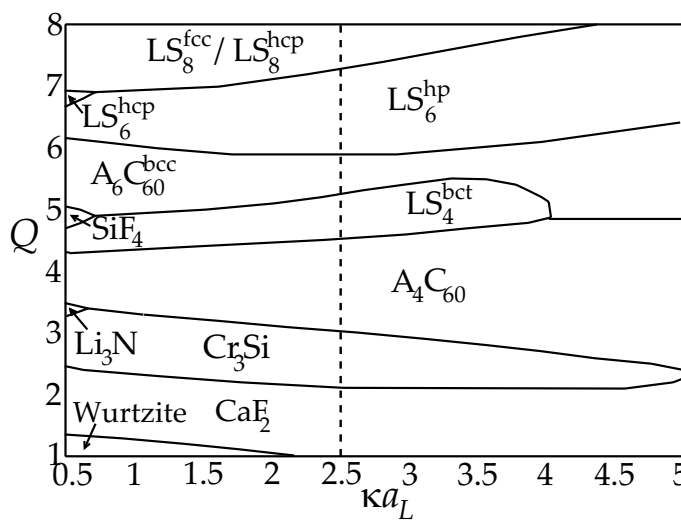


Figure 7.4: κ - Q slice of the ground-state phase diagram at $x = 0$ where the structures coexist with an infinitely dilute gas of large colloids. The dashed line shows the location where the slice in Fig. 7.3 is made.

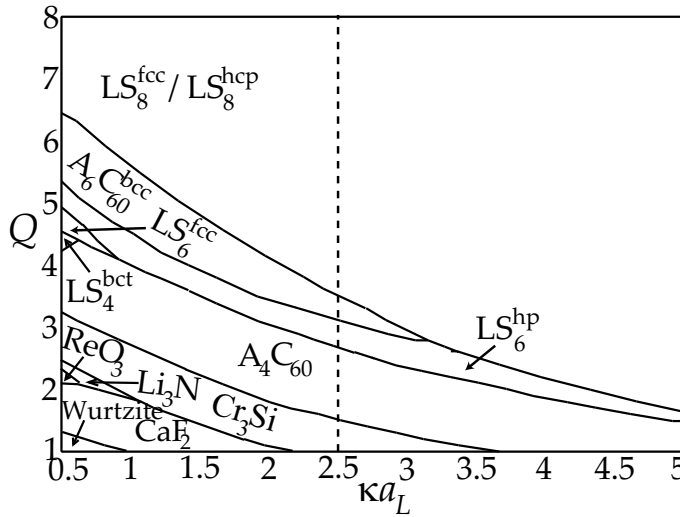


Figure 7.5: κ - Q slice of the ground-state phase diagram at $x = 1$ where the structures coexist with an infinitely dilute gas of small colloids. The dashed line shows the location where the slice in Fig. 7.3 is made.

allows for common tangent constructions. The Gibbs free energy reduces, however, to the enthalpy for the ground state properties of interest here, where entropic effects are ignored. Moreover, since many of our experiments show crystals that are self-supported by their cohesive energy, we restrict attention to the zero-pressure limit. The present phase diagram follows therefore from the internal energy, which for a crystal with all particles at their ideal lattice positions is the composition dependent Madelung energy $U(x)$ [11, 170]. Including entropy and pressure complicates theoretical studies considerably, and will be the subject of future research. In the zero-pressure ground-state approximation, phase stability depends only on the charge ratio Q and the screening parameter κ , and *not* on the absolute values of Z_L , Z_S , and λ_B separately. We calculated $U(x)$ with the MC code for the structures listed in Table 7.1 and for many known structures: NaCl, CsCl, NiAs, CuAu, AlB₂, Cu₃Au, Al₃Ti, CaCu₅, and CaB₆ [174]. In the calculations, the simulation box was repeated periodically such that the relative error in $U(x)$ was smaller than 10^{-7} . The lowest $U(x)$ per colloidal particle was found for given Q and κ by optimizing each possible structure with respect to η_L and the shape of the unit cell. We then performed, for fixed Q and κ , the common tangent construction. Figure 7.2 shows the common tangent construction for $Q = 1.8$ and $\kappa a_L = 2.5$, where the circles denote the Madelung energies $U(x)$ for the Wurtzite, CaF₂, Cr₃Si, and A₄C₆₀ structures, and the dashed line gives the actual common tangent construction. Note that at the two extremes where $x = 0$ or $x = 1$, the Madelung energy is zero ($U(0) = U(1) = 0$) because of the repulsive character of like species. One reads Fig. 7.2 as follows. At $x \in [0, 0.67]$, we have an infinitely dilute gas of large colloids in coexistence with the CaF₂ phase, at $x \in [0.67, 0.75]$ a CaF₂-Cr₃Si coexistence, at $x \in [0.75, 0.8]$ a Cr₃Si-A₄C₆₀ coexistence, and finally at $x \in [0.8, 1]$ a A₄C₆₀ phase in coexistence with an infinitely dilute gas of small colloids. Figure 7.2 also tells us that the phase diagram is three dimensional because all three parameters, x , κ , and Q , affect the phase behavior.

We repeated the common tangent construction for each $Q \in [1, 8]$ and $\kappa a_L \in [0.5, 5]$ to obtain the full phase diagram. Figure 7.3 shows a x - Q slice of the phase diagram at $\kappa a_L = 2.5$. One readily checks from Fig. 7.3 that at $Q = 1.8$, the phase

sequence corresponds to the common tangent construction in Fig. 7.2. Another way of studying the three dimensional phase diagram is to look at the two extremes cases where the crystal coexists with an infinitely dilute gas of pure large colloids ($x = 0$), and pure small colloids ($x = 1$). Figures 7.4 and 7.5 show κ - Q slices of the phase diagram at $x = 0$ and $x = 1$, respectively. The dashed line in Figs. 7.4 and 7.5 at $\kappa a_L = 2.5$ depicts the location where the x - Q slice shown in Fig. 7.3 is made. Figure 7.3 shows an increasing stoichiometry with increasing Q at low x , and Figs. 7.4 and 7.5 show the same at low κa_L . In Fig. 7.3, one has gas-crystal and crystal-crystal coexistence regions, whereas in Figs. 7.4 and 7.5, all crystals are in coexistence with an infinitely dilute gas of large or small colloids. Note that the phase lines in Figs. 7.4 and 7.5 are triple-point lines where a gas and two crystals coexist. From Figs. 7.4 and 7.5 one observes that an excess of small colloids favors structures with high stoichiometry. Moreover, we see that ReO_3 , Li_3N , SiF_4 , LS_6^{fcc} , and LS_6^{hcp} structures are only stable for relatively long-ranged interactions with $\kappa a_L \sim 0.5$. In these structures, shown in Figs. 7.6(a)-(e), the small colloids are in between pairs of neighboring large colloids in the sc (ReO_3), sh (Li_3N), bcc (SiF_4), fcc (LS_6^{fcc}) or hcp (LS_6^{hcp}) structure. Although such structures are electrostatically favorable, they pack inefficiently and thus destabilize at stronger screening. At $Q \approx 1$, we find the Wurtzite structure, which has dimers of large and small colloids stacked in an hcp lattice, see Fig. 7.6(f). The CaF_2 structure, depicted in Fig. 7.6(g), has the large colloids in an fcc lattice and the small colloids in the tetrahedral holes. The Cr_3Si structure has the large colloids in a bcc lattice and the small colloids as shown in Fig. 7.6(h). LS_6^{hp} , shown in Fig. 7.6(i), consists of hexagonal planes of large colloids, which are slightly compressed (6-10%) with respect to an ideal hcp crystal, and of small colloids, which are in two kagome patterns [175] above and below each large-colloid hexagonal layer. In the A_4C_{60} structure [171], the large colloids are in a body-centered-tetragonal (bct) lattice and the small colloids are between two large colloids such that they form a square parallel to the square plane of the tetragonal unit cell, see Fig. 7.6(j). The LS_4^{bct} structure, shown in Fig. 7.6(k), differs from A_4C_{60} in that the small colloids are turned 45 degrees in the square plane.

To verify the theoretical phase diagram, we studied the crystal structures and their formation in our experimental system, with total particle volume fraction 0.2 and added salt (tetrabutylammonium bromide) concentrations in the range 15-35 μM . Interestingly, we experimentally found three of the predicted crystal structures, viz. $\text{A}_6\text{C}_{60}^{\text{bcc}}$, LS_8^{fcc} , and LS_8^{hcp} , which are indeed rather dominant in the phase diagram of Figs. 7.4 and 7.5 at large Q . Typically crystal nuclei appeared within 24 h after preparation of the samples (the earliest were observed after 4-5 h). They had different orientations, which suggests homogeneous nucleation. With time, the crystal domains grew larger and reached sizes of about 100 μm . In the LS_8^{hcp} structure the large colloids form an hcp lattice. In the hexagonal layers, each large colloid is surrounded by a ring of 6 small ones occupying the trigonal interstices. Above and below each layer, there are two planes of small colloids ordered in a kagome pattern, see Fig. 7.7(a). The position of the small colloids in the kagome pattern is the same as in the LS_6^{hp} structure, see Fig. 7.6(i). Figure 7.7(b)

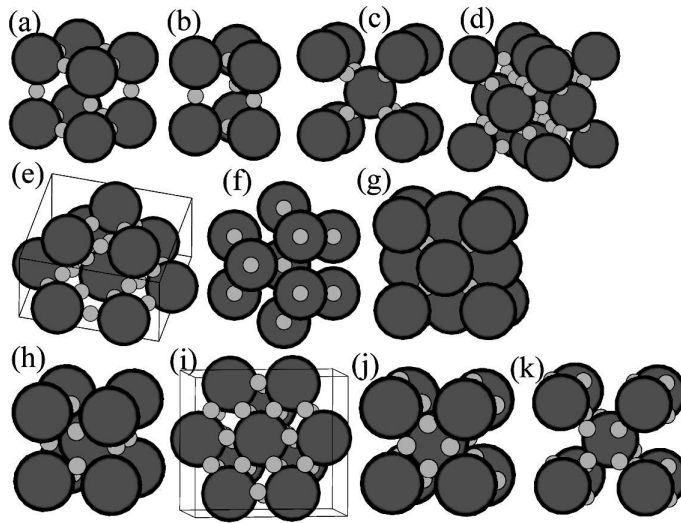


Figure 7.6: Theoretically predicted stable binary crystal structures: (a) ReO_3 , (b) Li_3N , (c) SiF_4 , (d) LS_6^{fcc} , (e) LS_6^{hcp} , (f) Wurtzite, (g) CaF_2 , (h) Cr_3Si , (i) LS_6^{hp} , (j) A_4C_{60} , and (k) LS_4^{bct} .

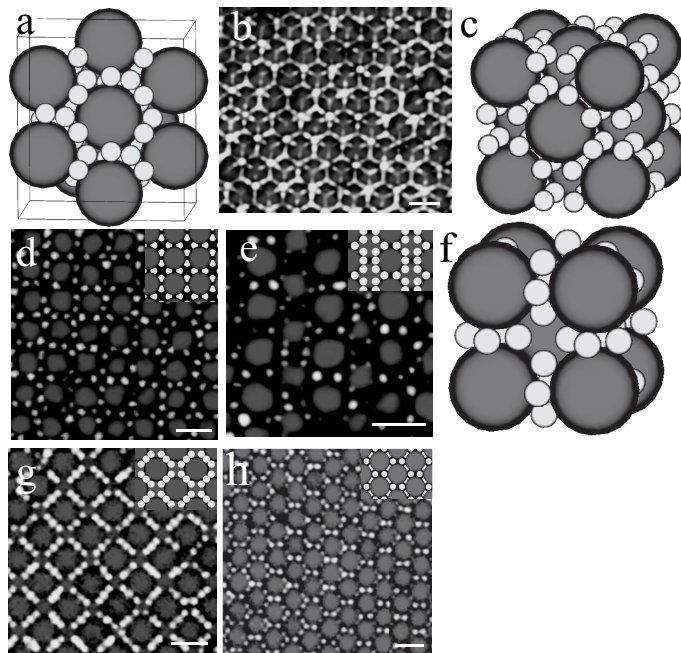


Figure 7.7: Experimental observations and the corresponding theoretical predictions of binary structures. Confocal images of positive (light) and negative (dark) PMMA particles: (b), superposition of several layers of LS_8^{hcp} ; (d), (100) plane of LS_8^{fcc} ; (e), (110) plane of LS_8^{fcc} ; (g), (100) plane of $\text{A}_6\text{C}_{60}^{\text{bcc}}$; (h), (110) plane of $\text{A}_6\text{C}_{60}^{\text{bcc}}$. All scale bars are $3 \mu\text{m}$. The insets in (d, e, g, h) show the corresponding plane in the theoretical predictions. (a, c, f), unit cells of (a) LS_8^{hcp} , (c) LS_8^{fcc} , and (f) $\text{A}_6\text{C}_{60}^{\text{bcc}}$ structures.

shows the LS_8^{hcp} structure as a superposition of 5 layers of large colloids and 15 layers of small colloids. We observe two kagome patterns of small colloids superimposed that are formed because the hcp lattice has two kinds of hexagonal layers of large colloids. The hexagonal structure of the large colloids can be seen below the small colloid kagome patterns. In the other binary structure with stoichiometry 8, the LS_8^{fcc} crystal, the large colloids are ordered in an fcc lattice and in every octahedral hole there are 8 small colloids forming a cube, see Fig. 7.7(c). Figure 7.7(d) shows the (100) plane of the LS_8^{fcc} unit cell, and in Fig. 7.7(e), the (110) plane is shown. The insets in Figs. 7.7(d) and (e) show the corresponding planes of this structure predicted by our simulations, revealing excellent agreement. Experimentally, the LS_8^{hcp} and LS_8^{fcc} structures were found to coexist. This is also in

agreement with our calculations, which predict essentially equal Madelung energies (although LS_8^{fcc} is more stable, but only by 0.005-0.1%). The $A_6C_{60}^{\text{bcc}}$ structure [172] consists of a bcc lattice of the large colloids with 4 small colloids in a square situated in the plane between every large next nearest neighbors, see Fig. 7.7(f). Figures 7.7(g) and (h) show, respectively, the (100) and (110) planes of the $A_6C_{60}^{\text{bcc}}$ structure unit cell together with the corresponding theoretical predictions. Note that this $A_6C_{60}^{\text{bcc}}$ crystal is different from the LS_6 structure observed in Ref. [11]. According to the Madelung energy calculations, $A_6C_{60}^{\text{bcc}}$, which was not considered in Ref.[11], is more stable than LS_6 . It is possible, though, that entropy and pressure can change the relative stability of these two structures.

7.4 Conclusions

We have developed an interactive method based on simulated annealing to predict binary crystal structures of oppositely charged colloids. We used this method for size ratio 0.31 and constructed a ground-state phase diagram based on the binary structures found. Our phase diagram displays novel structures, but also colloidal analogs of simple-salt structures and of doped fullerene C_{60} structures. The latter is not surprising as the size ratios of the two systems are very similar, e.g., $a_{\text{Rb}}/a_{\text{C}_{60}} = 0.3$. Three of the predicted structures, $A_6C_{60}^{\text{bcc}}$, LS_8^{fcc} , and LS_8^{hcp} , were also observed experimentally, thereby providing confidence that the proposed method with the screened Coulomb potential yields reliable predictions, even though the experimentally observed Brownian motion suggests that entropy should not be ignored. We have so far restricted our attention to stoichiometries up to $n = 8$, but expect more structures for larger n , e.g., for $n = 10$ and $Q \approx 10$, we expect a colloidal analog of the $\text{Na}_{10}\text{C}_{60}$ structure [176, 177]. Of course, it is possible that other structures exist that make the current ones metastable. However, introduction of a new structure typically reduces the stability area of the prior ones, but does not completely replace them. It would be interesting to compare our method for finding new structures with genetic algorithms [178, 179]. Finally, it is reasonable to expect even more and different structures for other size ratios, the exploration of which is not only of fundamental but also of practical interest, e.g., for photonic applications.

Acknowledgements The experimental work described in this chapter was done by Christina G. Christova.

8

Phase Behavior of Oppositely Charged Particles

ABSTRACT

We study the phase behavior of oppositely charged equal-size hard spheres using Monte Carlo simulations and compare our results with experimental observations. In the simulations, two systems are considered: the restricted primitive model (RPM) and a system of screened Coulomb particles. The experiments are done using confocal microscopy in a system of oppositely charged colloids, which can be seen as an experimental realization of screened Coulomb particles. The use of screened Coulomb potentials to model oppositely charged colloids is justified by calculating the effective pair interaction from primitive model simulations. We construct the phase diagrams of both the RPM and screened Coulomb particles by computer simulations and predict a novel solid phase that has the CuAu structure. In addition, the CuAu structure is observed experimentally. The qualitative agreement between the RPM, the screened Coulomb system, and the experiments shows that colloids form a suitable model system to study phase behavior in ionic systems. We also study the zero-pressure phase diagram of NaCl and CsCl structures in a system of screened Coulomb particles with charge asymmetry, using zero-temperature Madelung energy calculations, and check the effect of finite temperature by Monte Carlo simulations. We find that the NaCl phase can be stable also in the case of symmetric charges, if the two species are allowed to fractionate.

8.1 Introduction

A basic understanding of phenomena like gas-liquid condensation or freezing of atoms and molecules can be often acquired by studying model systems, in which the interactions between the particles are simplified to the bare minimum. For instance, hard spheres are often used to represent systems with repulsive interactions [91, 92], whereas charged hard spheres are commonly employed to model ionic systems. The simplest and best-known model for the latter is the restricted primitive model (RPM), which consists of a binary mixture of equal-size hard spheres suspended in a uniform continuum solvent, half of which carry a negative and the other half a positive charge of equal magnitude. In the past, the phase behavior of the RPM has been studied extensively [65–68], and the global phase diagram, which includes fluid, CsCl, face-centered-cubic (fcc) disordered, and "tetragonal" phases, has been constructed. Interestingly, all these phases, except the tetragonal phase, have recently also been observed experimentally in a system of oppositely charged colloids [11, 69]. The phase behavior of this system can be understood on the basis of screened Coulomb potentials, in which the screening is due to the presence of co- and counterions in the solvent. First, we justify the use of screened Coulomb potentials to model oppositely charged colloids by calculating the effective pair interaction using primitive model simulations. Then, we calculate the phase diagram of screened Coulomb particles and re-examine the phase behavior of the RPM. We find that the two phase diagrams are qualitatively similar, and, more importantly, that both contain a novel crystal structure where the particles are arranged in a CuAu-type crystal. Remarkably, we are able to observe the CuAu structure also experimentally in a system of oppositely charged colloids.

We also study the zero-pressure phase diagram of NaCl and CsCl structures of screened Coulomb particles with charge asymmetry. In particular, we study the gas-NaCl-CsCl triple point line and the NaCl melting line by Madelung energy calculations that assume zero temperature, and check the effect of finite temperature by Monte Carlo simulations. We find that the NaCl phase can be stable also in the case of symmetric charges, if the two species are allowed to fractionate.

The rest of this chapter is organized as follows. In Section 8.2, we validate the use of screened Coulomb potentials to model oppositely charged colloids by primitive model simulations. In Section 8.3, we present phase diagrams for the RPM and screened Coulomb particles, and discuss the experimental observations of the CuAu structure. In Section 8.4, we study the zero pressure phase diagram of NaCl and CsCl structures for screened Coulomb particles with charge asymmetry. We end with some final remarks in Section 8.5.

8.2 Interactions Between Oppositely Charged Colloids

Our results on the phase behavior of oppositely charged and equal-sized particles presented in this chapter are based on a DLVO-type [17, 18] screened Coulomb

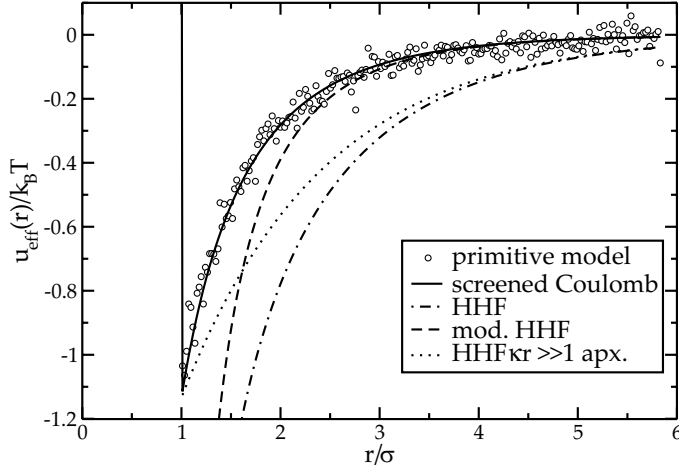


Figure 8.1: Effective potential $u_{\text{eff}}(r)$ between two oppositely charged colloids with charges $Z_{1,2} = \pm 20$, suspended in a solvent with $\lambda_B/\sigma = 0.00517$ and reservoir screening length $\kappa\sigma = 0.7$. The circles denote the primitive model results, the full line is the screened Coulomb potential (8.1), the dot-dashed line is the HHF potential (8.2), the dashed line is the modified HHF potential (8.3), and the dotted line is the approximate HHF potential (8.4).

potential, which is given by

$$\frac{u_{ij}(r)}{k_B T} = \begin{cases} \pm \frac{Z_i Z_j}{(1 + \kappa\sigma/2)^2} \frac{\lambda_B}{\sigma} \frac{e^{-\kappa(r-\sigma)}}{r/\sigma} & r \geq \sigma \\ \infty & r < \sigma, \end{cases} \quad (8.1)$$

where the sign depends on the particle charges Z_i and Z_j , r is the distance between the particles, σ is the diameter of the particles, $\lambda_B = e^2/\epsilon_s k_B T$ is the Bjerrum length, ϵ_s is the dielectric constant of the solvent, $\kappa = \sqrt{8\pi\lambda_B\rho_{\text{salt}}}$ is the inverse Debye screening length, and ρ_{salt} is the salt concentration. In the derivation of the screened Coulomb potential (8.1) for oppositely charged particles, the linear superposition approximation (LSA) has been used, where it is assumed that the electric potential ϕ in the presence of two colloids can be written as a sum of the electric potentials of the individual colloids, ϕ_1 and ϕ_2 , that would be present in the absence of the second colloid [169]. In order to check the validity of this approximation and the potential in Eq. (8.1), we calculated the effective pair interaction between oppositely charged colloids from primitive model simulations that were done using the method described in Section 5. The effective pair potential was extracted by taking the negative logarithm of the colloid-colloid radial distribution function $g(r)$, i.e., $u_{\text{eff}}(r)/k_B T = -\ln[g(r)]$, from a simulation run at low density. The primitive simulations were performed with charges $Z_{1,2} = \pm 20$ at packing fraction $\eta = 0.0018$, suspended in a solvent with Bjerrum length $\lambda_B/\sigma = 0.00517$ and reservoir screening length $\kappa\sigma = 0.7$. We used microns with diameter $\sigma/19$ and lattice discretization $\zeta = 19$. Figure 8.1 shows the effective potential obtained from the simulations (the circles) and the prediction of Eq. (8.1) (the full line). We see that the two results agree very well, thus proving that Eq. (8.1) gives the correct pair potential between oppositely charged colloids, at least for the parameters used here. For comparison, Fig. 8.1 also shows the widely used Hogg, Healy, and Fuerstenau (HHF) potential [180], which for particles with equal size and magnitude of charge reads

$$\frac{u_{\text{HHF}}(r)}{k_B T} = \frac{Z^2}{(1 + \kappa\sigma/2)^2} \frac{\lambda_B}{\sigma} \ln[1 - e^{-\kappa(r-\sigma)}] \quad r > \sigma. \quad (8.2)$$

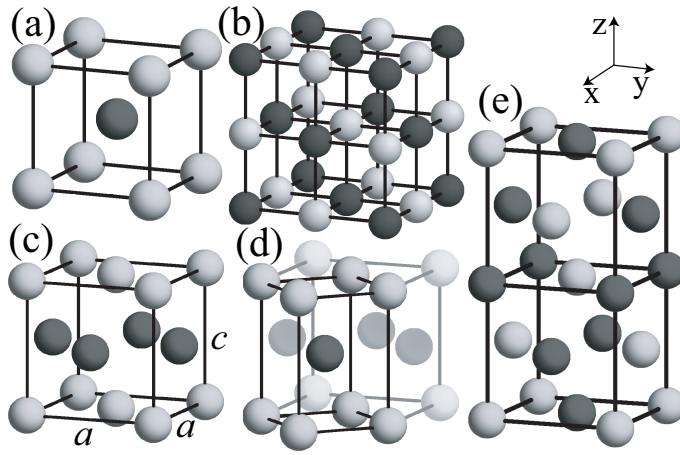


Figure 8.2: Unit cells of (a) CsCl, (b) NaCl, (c)-(d) CuAu, and (e) tetragonal structures, where dark and light spheres have opposite charges. In (d), the tetragonal cell of the CuAu structure is highlighted.

We also plot the modified HHF potential [181] that is Eq. (8.2) with a $1/r$ term,

$$\frac{u_{\text{HHF}}^*(r)}{k_B T} = \frac{Z^2}{(1 + \kappa\sigma/2)^2} \frac{\lambda_B}{\sigma} \frac{\ln[1 - e^{-\kappa(r-\sigma)}]}{r/\sigma} \quad r > \sigma, \quad (8.3)$$

and the large separation, $\kappa r \gg 1$, approximation of the HHF potential,

$$\frac{u_{\text{HHF}}^{\text{apx}}(r)}{k_B T} = \frac{Z^2}{(1 + \kappa\sigma/2)^2} \frac{\lambda_B}{\sigma} e^{-\kappa(r-\sigma)} \quad r > \sigma. \quad (8.4)$$

The potential in Eq. (8.4) is equal to the screened Coulomb potential (8.1) without the $1/r$ term. This potential is sometimes used to describe oppositely charged colloids [182], although the justification for its use is not clear. From Fig. 8.1 we see that the modified HHF potential (8.3) agrees with the screened Coulomb potential at $r \gtrsim 3$, and that both the original HHF potential (8.2) and the approximate version (8.4) do not agree in the range of r that was studied. We note that the agreement between the screened Coulomb potential (8.1) and the HHF potentials (8.2)-(8.4) becomes better at higher $\kappa\sigma$, which justifies their use in highly screened systems.

8.3 Phase Diagrams of Oppositely Charged Particles

In this section, we present the phase diagrams of the RPM and screened Coulomb particles, and show the experimental observations of the CuAu structure. Our simulations consist of N spheres with a diameter σ in a volume V , half of which carry a positive charge Ze and the other half a negative charge $-Ze$. The particles interact via the screened Coulomb potential (8.1), and we define a reduced temperature

$$T^* = \frac{(1 + \kappa\sigma/2)^2 \sigma}{Z^2 \lambda_B} \quad (8.5)$$

that is the inverse of the contact value of the potential in Eq. (8.1). The RPM is achieved by setting $\kappa = 0$, because then the screened Coulomb potential in

Eq. (8.1) reduces to the Coulomb potential and T^* is equal to the dimensionless temperature used in Refs. [67, 68, 183].

The overall (of both the positive and the negative particles) symmetry of a CsCl crystal is body-centered-cubic (bcc) and the substitutional order is shown Fig. 8.2(a). In the NaCl crystal, shown in Fig. 8.2(b), the oppositely charged particles sit in two interpenetrating fcc lattices and the overall lattice has a simple cubic symmetry. The NaCl crystal is only stable when fractionation is allowed (see Section 8.4) and is therefore left out from the calculations presented in this section, where all the phases are restricted to have equal number of positive and negative particles. In the CuAu crystal, the overall crystal symmetry is face-centered-tetragonal (fct), and the oppositely charged particles are arranged in alternating layers, as shown in Fig. 8.2(c). In the tetragonal phase, the overall symmetry is fct, and the substitutional order can be described by two fct cells on top of each other, as shown in Fig. 8.2(e). The fcc disordered phase has no substitutional order, and the two particle species sit in an fcc lattice. We used $N = 250$ for the CsCl phase and $N = 256$ for the CuAu, fcc disordered, and tetragonal phases.

We performed Monte Carlo (MC) simulations using the canonical (NVT) ensemble and periodic boundary conditions. The interactions were truncated at one half of the smallest box side length, L_{\min} . In the case of the RPM, we used the Ewald summation method [93, 128] with k-space cut-off at $k_{\text{cut}} = 10\pi/L_{\min}$. Our Ewald summation method was tested to reproduce the Madelung energies in Ref. [67] for the CsCl, CuAu, and tetragonal crystals. The phase diagrams were determined from the Helmholtz free energies that were calculated for the fluid, CsCl, CuAu, and tetragonal phases using the thermodynamic integration methods presented in Sections 2.3.1 and 2.3.2. The numerical integrations were done using a 10-point Gaussian quadrature and the ensemble averages were calculated from runs with 40 000 MC cycles (attempts to displace each particle once), after first equilibrating the system during 20 000 MC cycles. For the CuAu and tetragonal crystals, a tetragonally shaped simulation box was used. We determined the shape of the simulation box in a separate MC run with additional shape moves that change the side lengths of the box while conserving the volume.

Experimentally, a system of oppositely charged particles was established by preparing salt-containing mixtures of differently labelled fluorescent polymethylmethacrylate (PMMA) colloids in a mixture of cyclohexyl bromide (Fluka) and cis-decalin (27.2 w/w, Sigma-Aldrich), as described in [11]. This solvent mixture nearly matches the density and refractive index of the particles and has a dielectric constant of $\epsilon_s = 5.59$ ($\lambda_B \approx 10$ nm). The particles were made by dispersion polymerization, covalently labelled with the fluorophore 7-nitrobenzo-2-oxa-1,3-diazol (NBD) or rhodamine isothiocyanate (RITC) and sterically stabilized with poly-12-hydroxystearic acid [168]. The NBD- and RITC-labelled particles had diameters of $\sigma = 1.98$ and 2.16 μm , respectively, i.e., the size ratio was close to unity (0.92). The suspensions were 1:1 number density mixtures at an overall packing fraction $\eta \approx 0.30$. The particle charge and the range of the electrostatic interactions were tuned by adding ~ 190 μM of the salt tetrabutylammonium bromide (Sigma-Aldrich). Under these conditions the NBD-labelled particles were negatively charged, whereas the RITC-labelled particles were positive. We estimated $\kappa\sigma \approx 8 \pm 2$ from conductivity measurements on the particle-free solvent mixture

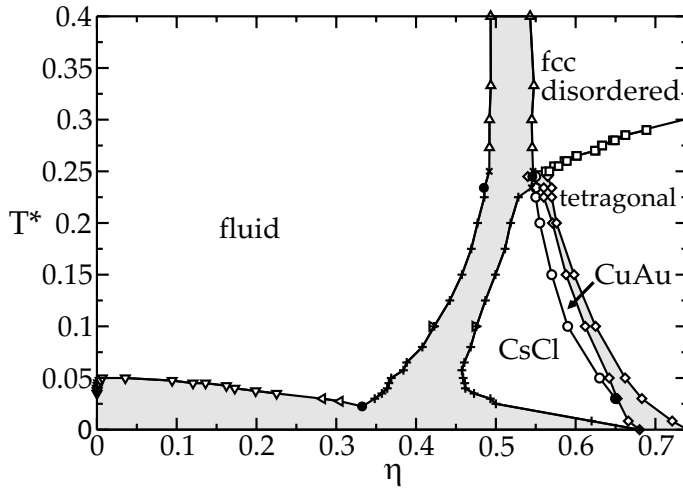


Figure 8.3: Phase diagram of the RPM in the packing fraction η -reduced temperature T^* plane. Phase lines for fluid-CsCl (+), fluid-fcc disordered (Δ), fluid-tetragonal (\times), and fcc disordered-tetragonal (\square) are from Ref. [68]. Gas-liquid phase envelope (∇) is from Ref. [158] and liquid points (\triangleleft) are from Ref. [183]. The circles (\circ) and diamonds (\diamond) mark the CsCl-CuAu and CuAu-tetragonal phase transitions, respectively. The black circles (\bullet) mark the position of the triple points and the gray areas denote the coexistence regions where tie lines are horizontal. The solid lines are guide to the eye.

(with a Scientifica 627 conductivity meter) and applying Walden's rule [108]. Previously, the charges of the same particles were determined, but under conditions at which they formed CsCl-type crystals [11]. Then, charges of +110 e and -75 e were found, i.e., the charge ratio is close to unity (~ 1.5). Although we could not determine the exact particle charges in the suspensions investigated here, semi-quantitative observations indicate that they were likely lower. Therefore, we estimate the reduced temperature to be $T^* \geq 0.6$ in the present experimental system.

We found that the CsCl-CuAu transition is a weakly first-order martensitic phase transition [184] and defined an order parameter a/c , which is the ratio of the CuAu unit cell side lengths, see Fig. 8.2(c). In order to understand this martensitic transition, it is useful to consider the tetragonal cell of the CuAu structure shown in Fig. 8.2(d). In Fig. 8.2(d), the dark particle corresponds to the center particle of the CsCl unit cell in Fig. 8.2(a). The CuAu to CsCl transformation occurs by a continuous isochoric deformation of the tetragonal cell from $a/c = 1$ to $a/c = \sqrt{2}$, where the cell has become cubic. To distinguish between the two structures, we define the threshold value to be in between, i.e., $a/c = (1 + \sqrt{2})/2 \approx 1.2$.

Figures 8.3 and 8.4 show the theoretical phase diagrams of the RPM and the screened Coulomb particles, respectively, in the packing fraction η -reduced temperature T^* representation. The phase coexistence regions were determined from the Helmholtz free energies using a common tangent construction. In Fig. 8.3, we only calculated the CsCl-CuAu and the CuAu-tetragonal phase lines, as the other parts of the phase diagram are known from earlier work [68, 158, 183]. In Fig. 8.4, the weakly first-order tetragonal/CuAu-fcc disordered phase line [185] was obtained from the jump in the internal energy U , that occurs when crossing the phase boundary [67]. The same method was also used for the CsCl-fcc disordered phase transition, although the order of this phase transition has not yet been well characterized. Qualitatively, the two phase diagrams are quite similar.

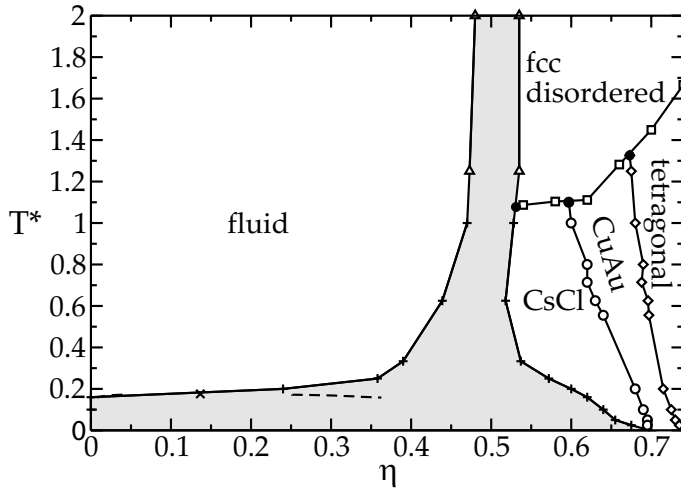


Figure 8.4: Phase diagram of screened Coulomb particles with inverse Debye screening length $\kappa\sigma = 6$ in the packing fraction η -reduced temperature T^* plane. The dashed lines and the cross (\times) show the metastable gas-liquid phase envelope and the critical point, respectively. The rest of the symbols denote the phase lines for fluid-CsCl ($+$), fluid-fcc disordered (Δ), fluid-tetragonal (\times), fcc disordered-tetragonal (\square), CsCl-CuAu (\circ), and CuAu-tetragonal (\diamond). The black circles (\bullet) mark the position of the triple points and the gray areas denote the coexistence regions where tie lines are horizontal. The solid lines are guide to the eye.

Both have a fluid phase in the low packing fraction region, a fluid-fcc disordered phase coexistence in the high temperature-high packing fraction region, a broad gas-CsCl phase coexistence in the low temperature region, and, in the intermediate temperature region, a sequence of CsCl, CuAu, and tetragonal phases with increasing packing fraction. A comparison between the two phase diagrams shows that screening enlarges the CuAu region. In the RPM phase diagram, the CuAu phase forms a narrow pocket that has a low- T^* triple point and seems to close up before reaching the fcc disordered region. In the screened Coulomb phase diagram, however, the CuAu pocket is broad and extends from $T^* = 0$ all the way to the fcc disordered region at $T^* \approx 1.2$. This makes it possible to observe CuAu-fcc disordered phase coexistence, which may explain the experimental observations (see below). We like to point out that the RPM and the screened Coulomb phase diagrams display a slightly different behavior in the $T^* \rightarrow 0$ limit: Although both exhibit a broad gas-CsCl coexistence at $\eta < 0.68$, at higher η the RPM has a stable tetragonal phase, whereas the screened Coulomb system has a stable CuAu phase, only to be followed by the tetragonal phase at $\eta \gtrsim 0.73$. Screening also affects the stability of the gas-liquid critical point. The RPM has a stable gas-liquid critical point at $T^* \approx 0.05$, but in the screened Coulomb phase diagram, the critical point (at $\eta = 0.137$ and $T^* = 0.176$) is metastable with respect to the gas-CsCl phase coexistence, see Fig. 8.4. According to our preliminary results, the gas-liquid critical point of the screened Coulomb system is stable at $\kappa\sigma \lesssim 4$. Our results also indicate that the gas-liquid phase envelope studied in Ref. [182] for $\kappa\sigma = 6$ using the potential in Eq. (8.4), is metastable.

In the following, we compare our theoretical findings with the experimental observations done in the system of oppositely charged colloids. Figure 8.5 shows a selection of representative confocal images, where the packing fraction is $\eta = 0.58 \pm 0.04$. The crystalline structures were observed within 18 days after sample preparation and they remained stable for months. In order to check that they indeed consist of oppositely charged particles, we subjected them to a

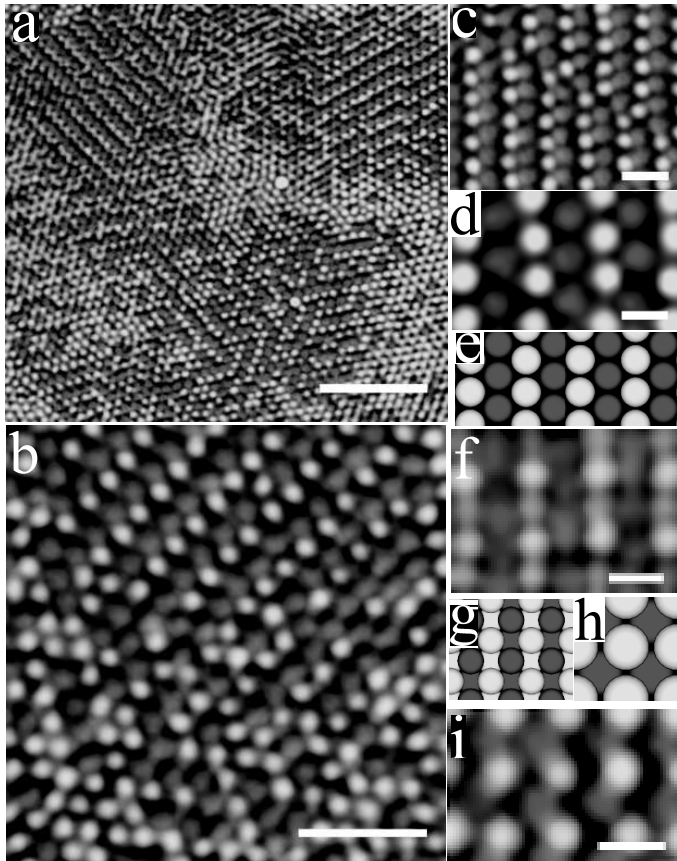


Figure 8.5: Confocal microscope images of CuAu-type crystallites: (a,b) in the presence of an rhcp disordered crystal, (c,d) a (111) plane, (f) a (100) plane, (i) a (001) plane. In (c), one can observe a line defect. Illustrations of CuAu-type crystal planes: (e) the (111) plane, (g) the (100) plane, and (h) the (001) plane. The scale bars are: $25 \mu\text{m}$ in (a), $10 \mu\text{m}$ in (b), $5 \mu\text{m}$ in (c), and $2.5 \mu\text{m}$ in (d), (f), and (i).

static external electric field (7.5 V/mm). This caused the two particle species to move in opposite directions, thereby melting the structures. Figures 8.5(a) and (b) show the CuAu phase in the presence of a random-hexagonal-close-packed (rhcp) disordered phase. The CuAu structure is easily recognized as it has alternating stripes of dark and bright particles that make up the (111) hexagonal plane [with respect to the orientation of the unit cell shown in Fig. 8.2(c)]. Remarkably, whereas the CuAu crystallites were strictly fcc, the substitutionally disordered structures were rhcp. Note that on the basis of hard spheres, one expects to see rhcp because of the small free energy difference between fcc and hexagonal-close-packed (hcp) crystals [186]. The simultaneous observation of the CuAu and fcc disordered phases agrees with the screened Coulomb phase diagram in Fig. 8.4, in which we find the CuAu and fcc disordered phases connected by a weakly first-order phase line. Unfortunately, a more quantitative comparison between the simulations and the experiments is difficult as it is not known whether the experimentally observed structures are in equilibrium, and the experimental values of $\kappa\sigma$ and T^* are not known accurately. However, the relatively low packing fraction ($\eta \approx 0.58$) of the observed CuAu phase and the presence of the rhcp disordered phase point towards the intermediate temperature region of the phase diagram in Fig. 8.4 where $T^* \approx 1$. Thus, the experiments fall in between the energy ($T^* \ll 1$) and entropy ($T^* \gg 1$) dominated limits. Figures 8.5(c) and (d) show close up images of the (111) plane, now with the stripes running vertically. Figure 8.5(e) illustrates the (111) plane in an ideal crystal. Although most of the

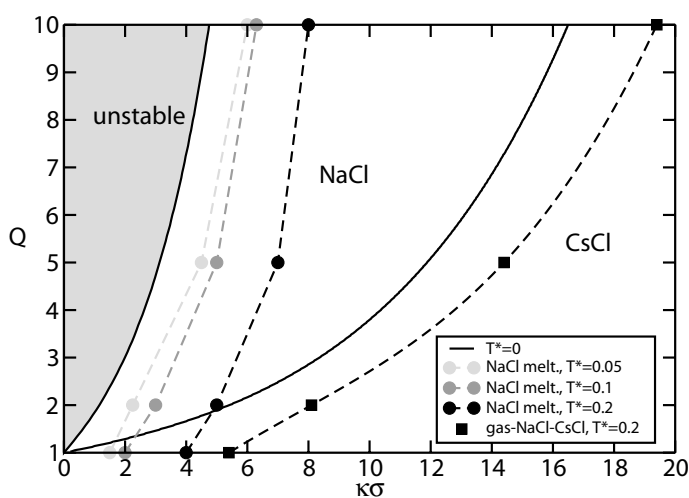


Figure 8.6: NaCl-CsCl zero-pressure phase diagram of screened Coulomb particles in the charge ratio Q -screening length $\kappa\sigma$ representation, where the crystal phases are in coexistence with a zero density gas of the excess species. The solid black lines give the zero-temperature ($T^* = 0$) phase lines obtained from Madelung energy calculations. In the grey area denoted by “unstable”, the NaCl structure is unstable. The circles and squares give the results of finite temperature free energy calculations at the temperatures given in the legend. The dashed lines are guide to the eye.

CuAu-type crystallites were oriented with their (111) plane parallel to the bottom wall of the sample cell, we were able to observe (100) and (001) planes as well. Figure 8.5(f) shows the (100) plane that consists of alternating layers of oppositely charged particles, and Fig. 8.5(g) shows the corresponding plane in an ideal crystal. The (001) plane is shown in Figs. 8.5(h) and (i). Finally, we like to point out that the crystalline structures described above consisted of approximately 10 layers of particles and always formed near the bottom of the sample cell. This means that these structures need a higher osmotic pressure to form.

8.4 NaCl-CsCl Zero-Pressure Phase Diagram

In this section, we present a zero-pressure phase diagram of NaCl and CsCl structures of screened Coulomb particles with charge asymmetry, i.e., with $Q = Z_1/Z_2 \geq 1$, in excess of one of the species. The crystal structures are self-supported and in coexistence with a zero density (i.e., zero pressure) gas of the excess species. In the zero pressure approximation, the Gibbs free energy that determines the phase behavior of binary mixtures is equal to the Helmholtz free energy. If one additionally assumes that the temperature is zero, as was done in Chapter 7, the Gibbs free energy further reduces to the Madelung energy. In this zero temperature-zero pressure approximation, the phase diagram is completely determined by the charge ratio Q and the screening length κ .

Figure 8.6 shows the zero-pressure phase diagram of equal size oppositely charged colloids in the charge ratio Q -screening length $\kappa\sigma$ representation. The zero-temperature phase lines, which were calculated using Madelung energies of ideal NaCl and CsCl structures, are denoted by the black lines. The Madelung energies were calculated assuming contact between neighboring spheres in a structure. The NaCl-CsCl phase transition occurs when the Madelung energies of the two structures are equal. At $Q = 1$, the CsCl phase is stable for all values of $\kappa\sigma$, and at increasing Q , the stability region of the NaCl grows. Note that the phase line separating the NaCl and CsCl structures is in fact a gas-NaCl-CsCl triple

point line, where the gas has zero pressure and density, and consists of the excess species. The grey area denoted by “unstable” is the region where the Madelung energy of the NaCl structure is positive and therefore the structure is unstable at zero pressure.

In order to study the effect of finite temperature, we calculated the gas-NaCl-CsCl triple point line and the NaCl melting line at $T^* > 0$.^{*} The gas-NaCl-CsCl triple points were determined by calculating the Helmholtz free energies of the two crystal phases at different values of $\kappa\sigma$ and finding the point where the NaCl and CsCl phases coexist with a zero pressure gas of the excess species (that has zero density and zero Helmholtz free energy). The NaCl melting points were obtained by performing constant pressure MC simulations at zero pressure. The melting point was defined to be at that $\kappa\sigma$ where the NaCl crystal melted. In Fig. 8.6, the gas-NaCl-CsCl triple points are plotted with the squares, and the NaCl melting points are plotted with the circles. The gas-NaCl-CsCl triple points were calculated at $T^* = 0.2$ and the NaCl melting points at $T^* = 0.2, 0.1,$ and 0.05 . Couple of notions can be made. Finite temperature shifts the gas-NaCl-CsCl triple point line to higher $\kappa\sigma$ compared to the zero temperature result. This means that entropy favors the NaCl phase with respect to the CsCl phase. On the other hand, entropy reduces the stability of the NaCl phase with respect to melting, as can be seen from the NaCl melting line that shifts to higher $\kappa\sigma$ with increasing temperature.

Bartlett et al. [69] observed the NaCl structure in a system of oppositely charged colloids with $Q > 1$. This is in agreement with the phase diagram in Fig. 8.6. One notes that the NaCl phase can be also stable in the case of equally charged colloids where $Q = 1$. This is essentially due to the construction of the phase diagram in Fig. 8.6 that allows the two species to fractionate: The NaCl and CsCl crystals are made out of equal amounts of positive and negative particles, while the gas phase contains only one of the species (the excess species). In the phase diagrams like the ones presented in Section 8.3, where fractionation is not allowed, the NaCl phase is not stable for $Q = 1$. Therefore, it is also possible that other binary crystal structures, different from the ones considered so far, can be stable even for $Q = 1$.

8.5 Conclusions

We have studied the phase behavior of oppositely charged particles described by the RPM and screened Coulomb potentials, and made comparisons with experimental observations in a system of oppositely charged colloids. In Section 8.2, we justified the use of screened Coulomb potentials to model oppositely charged colloids by calculating the effective interaction between two colloids with charges ± 20 using primitive model simulations. We found that the pair interaction is well described with the screened Coulomb potential, and that the HHF potential and variations thereof, give good description of the interactions only at large colloid-colloid separations or at high $\kappa\sigma$.

^{*}For $Q > 1$, the reduced temperature is defined by Eq. (8.5) with Z^2 replaced by $Z_1 Z_2$.

In Section 8.3, we constructed the phase diagram of screened Coulomb particles and re-examined the phase behavior of the RPM for particles with equal size and magnitude of charge. We showed that the two phase diagrams are qualitatively similar, and more importantly, that both contain a novel solid phase, which is analogous to the CuAu structure. We also observed the CuAu structure in our experiments with oppositely charged colloids, which can be seen as an experimental realization of screened Coulomb particles. The fact that the experimental system is in the intermediate temperature region ($T^* \approx 1$), that is, between the energy and entropy dominated limits, makes the observations of the CuAu structure even more interesting. It shows that a novel solid phase, distinct from the previously proposed CsCl, NaCl, and fcc disordered phases [11, 69], can be found in this region. This has important implications for the search for new binary structures, which for oppositely charged colloids has so far only been carried out at zero temperature and zero pressure (see Chapter 7). Furthermore, our results demonstrate that oppositely charged colloids can give insight into the phase behavior of the RPM, and show that colloids can be used for detailed studies, on the single particle level, of ionic phase transitions.

In Section 8.4, we presented a zero pressure phase diagram of NaCl and CsCl structures of screened Coulomb particles with charge asymmetry. The phase diagram was presented in the charge ratio Q -screening length $\kappa\sigma$ representation. We calculated the NaCl melting line and the gas-NaCl-CsCl triple point line in the zero temperature approximation using Madelung energies. The zero temperature approximation was tested by calculating the phase lines at finite temperatures by MC simulations. We found that finite temperature shifts the NaCl melting line, giving rise to less NaCl phase than expected based on the zero-temperature results, while the gas-NaCl-CsCl triple point line shifts such that more NaCl phase is obtained. We noted that the NaCl phase can be stable also in the case of symmetric charges, $Q = 1$, if the two species are allowed to fractionate. This means that it could be possible to find other crystal structures, than the ones found so far, even for $Q = 1$, not to mention for $Q > 1$. The search for these crystal structures would be of great practical and fundamental importance.

Acknowledgements The experimental work described in this chapter was done by Mirjam E. Leunissen, the gas-liquid phase envelope in Fig. 8.4 was calculated by Andrea Fortini, and the Madelung energies for the NaCl and CsCl phases used in Fig. 8.6 were calculated by René van Roij.

9

Phase Behavior of Dipolar Hard and Soft Spheres

ABSTRACT

We study the phase behavior of hard and soft spheres with a fixed dipole moment using Monte Carlo simulations. The spheres interact via a pair potential that is a sum of a hard-core Yukawa (or screened-Coulomb) repulsion and a dipole-dipole interaction. The system can be used to model colloids in an external electric or magnetic field. Two cases are considered: (i) colloids without charge (or dipolar hard spheres) and (ii) colloids with charge (or dipolar soft spheres). The phase diagram of dipolar hard spheres shows fluid, face-centered-cubic (fcc), hexagonal-close-packed (hcp) and body-centered-tetragonal (bct) phases. The phase diagram of dipolar soft spheres shows, in addition to the above mentioned phases, a body-centered-orthorhombic (bco) phase, and is in agreement with the experimental phase diagram. In both cases, the fluid phase is inhomogeneous but we find no evidence of a gas-liquid phase separation. The validity of the dipole approximation is verified by a multipole moment expansion.

9.1 Introduction

Colloidal particles in an external electric or magnetic field whose dielectric constant or magnetic susceptibility is different from that of the solvent, acquire a (electric or magnetic) dipole moment parallel to the field. The behavior of the colloids is governed by the dipole-dipole interaction, whose strength can be tuned by the magnitude of the field. Due to their unique shearing properties, such suspensions are called electrorheological (ER) and magnetorheological (MR) fluids. ER/MR fluids have potential use in industrial applications as hydraulic valves, clutches, brakes [83], and displays [84]. Moreover, the possibility to tune the crystal structure of these suspensions by an external field, makes these suspensions appealing for photonic applications [3, 87, 88].

The equilibrium structure of these fluids has been the subject of many experimental [3, 5, 87, 187, 188], theoretical [85, 86, 189–193] and simulation studies [194–198]. In an early theoretical study, Tao et al. proposed that above a certain critical field strength the system experiences a phase transition to a solid structure [85]. In Ref. [86], Tao and Sun studied the crystal structure of the solid phase and found that, of the structures that they considered, a body-centered-tetragonal (bct) structure was the one with the lowest energy. The bct structure predicted by Tao and Sun has been observed both by computer simulations [194, 196, 197] and by experiments [3, 87, 187, 188].

We determine the phase diagram of two dipolar systems: (i) colloids without charge (or dipolar hard-spheres) and (ii) colloids with a charge $Ze = 300e$ and inverse Debye screening length (in units of the colloid diameter σ) of $\kappa\sigma = 10$ (dipolar soft-spheres). The phase diagram of dipolar hard spheres shows fluid, face-centered-cubic (fcc), hexagonal-close-packed (hcp), and bct phases. The phase diagram of dipolar soft spheres shows, in addition to the above mentioned phases, a body-centered-orthorhombic (bco) phase. As we will show, the phase diagram of dipolar soft spheres is in good agreement with the experimental phase diagram in Ref. [3]. We are able to explain the appearance of a body-centered-orthorhombic (bco) phase based on simple arguments. Furthermore, our calculations propose hexagonal-close-packed (hcp) crystal as the high-density stable phase in systems with dipolar interactions. We also discuss the multipole moment expansion method that is used to verify the energy difference between the fcc and hcp phases. Finally, we briefly study the structure of the fluid phase.

The rest of this chapter is organized as follows. In Section 9.2 we describe the model and the methods used in the simulations, in Section 9.3 we present the results and in Section 9.4 we conclude.

9.2 Model and Methods

We use a dipole approximation to describe the pair potential between two dielectric or magnetic particles. Figure 9.1(a) illustrates the situation and shows two particles with diameter σ that are separated by a vector \mathbf{r} . The vector \mathbf{r} forms an angle θ with the z axis, which is parallel to an external electric (\mathbf{E}) or magnetic (\mathbf{H}) field. In the case of an electric field, the particles and the solvent have a dielec-

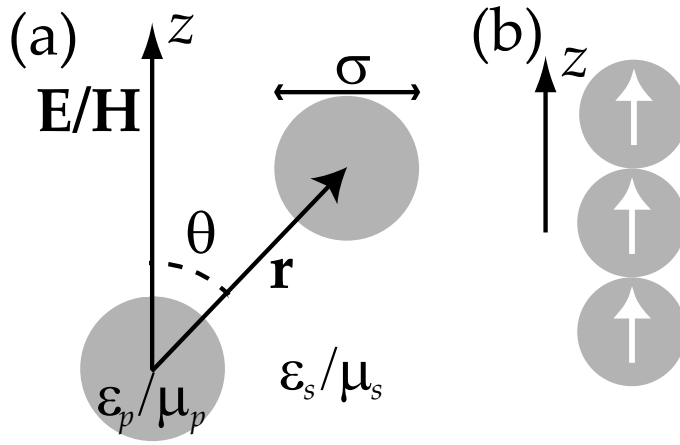


Figure 9.1: Dipole-dipole interactions. (a) Two particles with diameter σ connected by a vector \mathbf{r} . The vector \mathbf{r} forms an angle θ with the z axis. The external electric (\mathbf{E}) or magnetic (\mathbf{H}) field is parallel to the z axis. In the case of an electric field, the particles have a dielectric constant ϵ_p and the solvent ϵ_s . In the case of a magnetic field, the particles have a magnetic susceptibility μ_p and the solvent μ_s . (b) The dipole-dipole interaction favors configurations where the dipoles (denoted by the white arrows) are oriented head-to-toe.

tric constant of ϵ_p and ϵ_s , respectively, whereas in the case of a magnetic field, the particles and the solvent have a magnetic susceptibility of μ_p and μ_s , respectively. The external field induces a (electric or magnetic) dipole moment on the particles, which is parallel to the field direction (the z axis). The dipole-dipole interaction is given by

$$\frac{u_{\text{dip}}(\mathbf{r})}{k_B T} = \frac{\gamma}{2} \left(\frac{\sigma}{r} \right)^3 (1 - 3 \cos^2 \theta), \quad (9.1)$$

where k_B is the Boltzmann constant and T is the temperature. In the case of electric dipoles, the prefactor γ is given by

$$\gamma = \frac{\pi \sigma^3 \alpha^2 \epsilon_s |\mathbf{E}_{\text{loc}}|^2}{8 k_B T}, \quad (9.2)$$

where \mathbf{E}_{loc} is the local electric field, which is a sum of the external field, \mathbf{E} , and the field induced by the other dipoles, \mathbf{E}_{dip} [86, 195, 199], i.e., $\mathbf{E}_{\text{loc}} = \mathbf{E} + \mathbf{E}_{\text{dip}}$. In Eq. (9.2), $\alpha = (\epsilon_p - \epsilon_s)/(\epsilon_p + 2\epsilon_s)$ is the polarizability of the particles. In the case of magnetic dipoles, γ is given entirely symmetrically, and it is written as

$$\gamma = \frac{\pi \sigma^3 \alpha^2 \mu_s |\mathbf{H}_{\text{loc}}|^2}{8 k_B T}, \quad (9.3)$$

where $\alpha = (\mu_p - \mu_s)/(\mu_p + 2\mu_s)$ and $\mathbf{H}_{\text{loc}} = \mathbf{H} + \mathbf{H}_{\text{dip}}$ is the local magnetic field [200].

For charged colloids, we supplement the dipole-dipole interaction in Eq. (9.1) with a soft repulsion caused by like-charge repulsion. According to the DLVO theory [17, 18], the pair interaction between two charged colloids is given by a repulsive Yukawa (or screened Coulombic) plus the hard core potential as

$$\frac{u_Y(r)}{k_B T} = \begin{cases} \epsilon \frac{\exp[-\kappa(r - \sigma)]}{r/\sigma} & r \geq \sigma \\ \infty & r < \sigma, \end{cases} \quad (9.4)$$

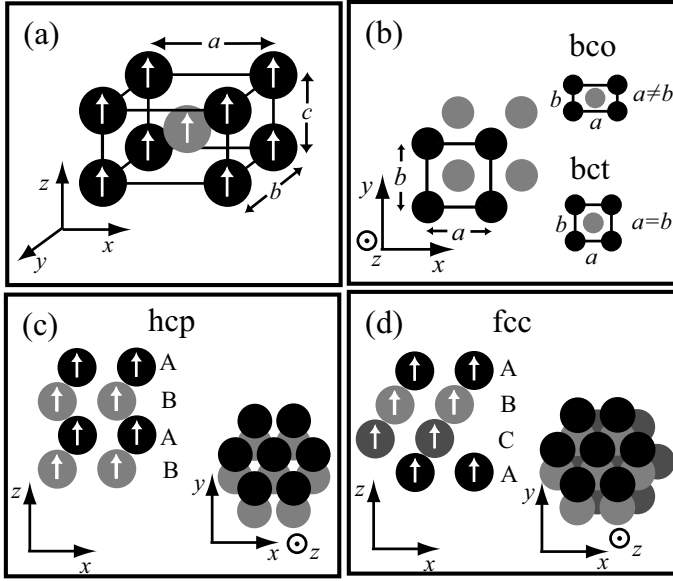


Figure 9.2: (a) Body-centered structure in three dimensions, whose conventional unit cell is $a \times b \times c$. The field is along the z axis. The white arrows show the direction of the field-induced dipole moments. The bct structure corresponds to $a = b \neq c$, and the bco to $a \neq b$, $c \neq a$ and $c \neq b$. (b) Top-view of the body-centered structure that can be constructed by placing strings of particles shifted by $c/2$ into two inter-penetrating rectangular lattices. (c)-(d) The hcp and fcc structures shown in side- and top-views. The hcp structure has AB stacking of the hexagonal planes; the fcc ABC.

where

$$\epsilon = \frac{Z^2}{(1 + \kappa\sigma/2)^2} \frac{\lambda_B}{\sigma} \quad (9.5)$$

is a constant prefactor depending on the colloidal charge number Z , the Debye screening length κ^{-1} , and the Bjerrum length $\lambda_B = e^2/\epsilon_s k_B T$ of the solvent. Since we are interested in modelling systems where the Van der Waals attraction is very small due to refractive index matching, we have neglected it in Eq. (9.4). The phase behavior of repulsive Yukawa particles is well known from earlier work [19, 21, 94, 95] (see also Chapter 2), where it has been shown that, depending on the density, prefactor ϵ , and screening length κ^{-1} , the system exhibits fluid, body-centered-cubic (bcc), and face-centered-cubic (fcc) phases.

Using the pair potentials in Eqs. (9.1) and (9.4), we perform Monte Carlo (MC) simulations in the canonical ensemble (NVT), where we fix the number of particles N , the volume V and the temperature T [93]. The simulation box is periodic in all three directions. Typical number of particles in our simulations is $N = 144 - 288$, and cubic, or nearly cubic, simulation boxes are used. Because of the long-range nature of the dipolar interactions, we use the Ewald summation method to evaluate the potential in Eq. (9.1) [93, 128]. Both the Yukawa and the dipolar potential are truncated at half of the shortest box side length. The width of the Gaussian distribution, the tunable parameter in the Ewald sum, is optimized according to the analytical estimates given in Ref. [201].

In our simulations, we consider the fluid, bcc, bct, bco, fcc and hcp phases. The body-centered (bcc, bct and bco) structures are aligned such that the particles form strings parallel to the z axis (the field direction), see Fig. 9.2(a). The body-centered box side lengths are given in the x , y , and z axis directions by a , b , and c , respectively. Shown in Fig. 9.2(b) are the bco and bct structures viewed along the z axis. As can be seen from Fig. 9.2(b), the bco and bct structures can be constructed by placing strings of particles into two interpenetrating rectangular

($a \times b$) lattices. The particles in the strings are displaced by $c/2$ in the z direction. The bco structure can be thought of as an asymmetric version of the bct structure. The maximum packing of the bct structure is obtained when $a = b = (\sqrt{6}/2)\sigma$ and $c = \sigma$, corresponding to a packing fraction $\eta = \pi\sigma^3 N/6V = 2\pi/9 \approx 0.698$. Note that, the bcc phase has $a = b = c$. The fcc and hcp structures are depicted in Figs. 9.2(c) and (d), respectively. Both fcc and hcp are oriented with the (111) plane perpendicular to the z axis.

The phase behavior was studied by MC simulation runs and by Helmholtz free energy calculations. We used the MC simulation runs to obtain a rough estimate of the phase behavior, after which the more accurate free energy calculations were performed to check the result and to determine the phase boundaries more exactly. Phase coexistence regions were determined by a common tangent construction from Helmholtz free energies that were calculated using thermodynamic integration methods. We used the λ -integration method for the fluid phase and the Frenkel-Ladd method for the solid phase [93, 98]. As a reference state, we used the hard-sphere fluid for the fluid phase and the non-interacting Einstein crystal for the solid phase. The numerical integration was done with a Gaussian quadrature using 10 (or in some cases 20) integration points. The statistical averages needed in the free energy calculations were calculated from MC simulation runs that consisted of 10 000 - 200 000 MC steps (trial moves per particle), and that were first equilibrated with the same (or similar) number of MC steps.

Due to the dipole-dipole interaction, compression along the z axis lowers the energy of all our crystal phases. Therefore, in order to get reliable results, we need to optimize the z axis side length. For the bct, fcc, and hcp phases, we calculated the free energies for various z axis side lengths and used the minimum value to determine the phase boundaries. In the case of soft repulsions, the bco unit box symmetry, given by c and the ratio a/b , was determined by varying a/b and c to find the minimum of the Madelung energy (energy of an ideal crystal per particle). If the minimum state had strings in touching configurations ($c = \sigma$), we set $c = 1.01\sigma$ to ensure that efficient MC sampling of the system is still possible. For some systems, also other choices like $c = 1.04\sigma$ and $c = 1.005\sigma$ were tried, but in general, the results did not depend strongly on the choice of c .

9.3 Results

9.3.1 Phase Diagrams

Our model presented in Section 9.2 can be described by four independent dimensionless parameters: the packing fraction η , the strength of the dipolar interaction γ , the colloidal charge Z , and the inverse screening length $\kappa\sigma$. We fix the colloidal charge Z and study the phase behavior in a constant $\kappa\sigma$ plane, i.e., our phase diagrams are plotted in the (γ, η) representation.

In Fig. 9.3, we show the phase diagram of the dipolar hard-spheres (i.e., $\epsilon = 0$) in the (γ, η) representation. At zero dipole moment strength ($\gamma = 0$), the well-known hard-sphere fluid-fcc coexistence with the coexisting phases at $\eta_{\text{fluid}} =$

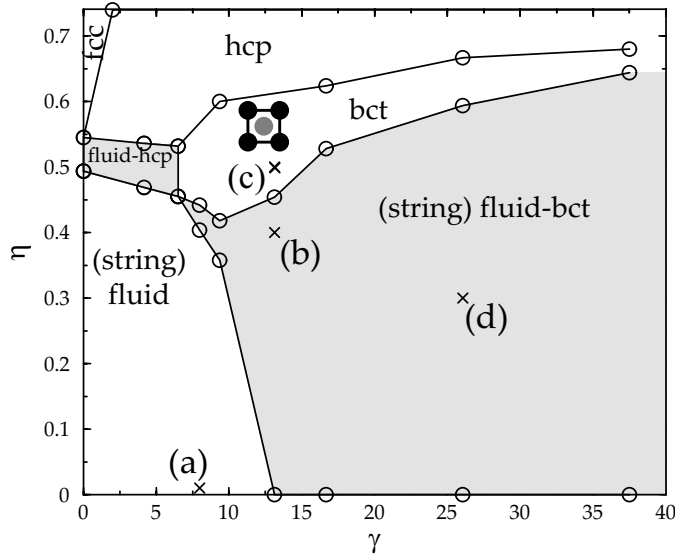


Figure 9.3: The phase diagram of dipolar hard-sphere particles in the (dipole moment strength γ , packing fraction η) representation. The circles denote points where the phase boundary was determined and the grey areas denote coexistence regions (where tie-lines are vertical). The letters (a), (b), (c) and (d) mark the state points where the snapshots shown in Fig. 9.4 are taken.

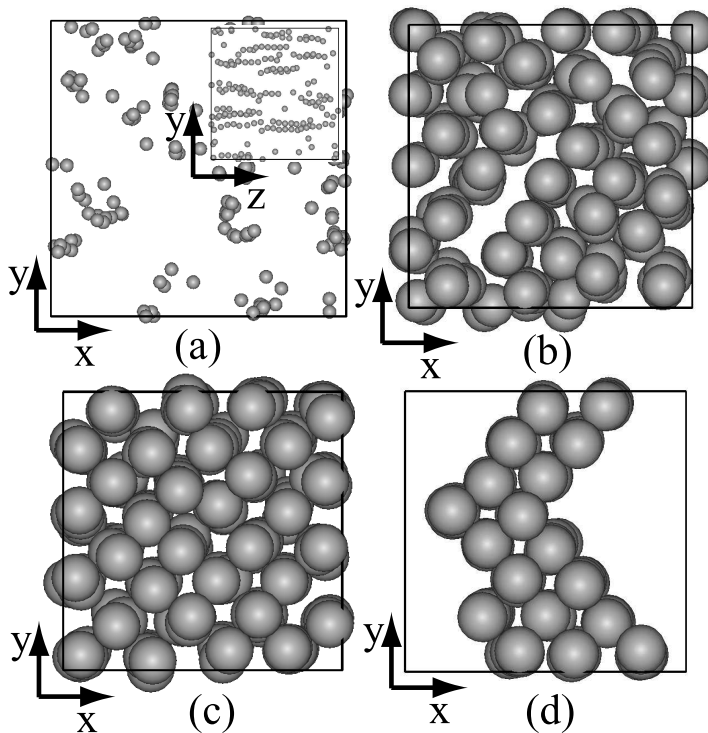


Figure 9.4: Snapshots of the dipolar hard-sphere systems in (a) string fluid phase at ($\gamma = 8.0, \eta = 0.01$), (b) gas-bct coexistence phase at ($\gamma = 13.1, \eta = 0.4$), (c) stable bct phase at ($\gamma = 13.1, \eta = 0.5$), and (d) gas-bct coexistence phase at ($\gamma = 26.1, \eta = 0.3$). See Fig. 9.3 for the locations of the snapshots in the phase diagram.

0.494 and at $\eta_{fcc} = 0.545$ is recovered. At $\gamma > 0$, the fluid-fcc coexistence switches to fluid-hcp coexistence. Increasing the dipole moment strength from $\gamma = 0$ to $\gamma = 6.5$ does not change the fluid-hcp coexistence much. At $\gamma > 6.5$, the bct phase is the stable crystalline phase at low densities, while the hcp phase is, due to more efficient packing, still the stable phase at packing fractions $\eta \gtrsim 0.57$. At the dipole moment strength $\gamma \approx 8.0$, the system phase separates into a (string) fluid phase and a bct phase. Figure 9.4(a) shows a snapshot of the string fluid phase, where the view is along the z axis (i.e., parallel with the field) and we observe strings that look like individual particles or small clusters of particles. The strings can be seen in the inset of Fig. 9.4(a), which shows the same snapshot but viewed such

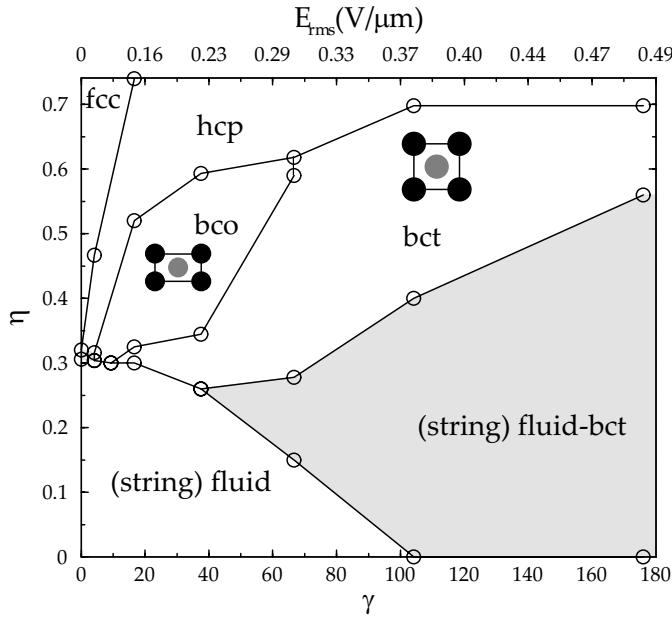


Figure 9.5: The phase diagram of dipolar soft sphere particles with Yukawa parameters $\kappa\sigma = 10.0$ and $Z = 300$ (that with $\lambda_B/\sigma = 0.005$ correspond to a contact value $\epsilon = 12.54$) in the (dipole moment strength γ , packing fraction η) representation. The circles denote points where the phase boundary was determined and the grey area denotes the coexistence region (where tie-lines are vertical). The upper horizontal axis gives an estimate of the root-mean-square external electric field, see text for details.

that the z axis is horizontal. The statepoint of the snapshot in Fig. 9.4(a), and the other snapshots in Fig. 9.4, are denoted by the letters (a), (b), (c) and (d) in Fig. 9.3. The fluid-bct phase coexistence region broadens with increasing dipole moment strength and at $\gamma = 13.1$, the fluid phase has turned into a very low density gas phase (or void). Figure 9.4(b) shows a snapshot of an MC simulation well inside the gas-bct phase coexistence region at ($\gamma = 13.1$, $\eta = 0.4$). For comparison, a snapshot of a stable bct phase with the same γ is shown in Fig. 9.4(c).

At $\gamma > 13.1$, the gas-bct coexistence broadens further and, at $\gamma \approx 38$, the bct phase has packing fraction $\eta_{\text{bct}} = 0.66$ close to the maximum packing. Snapshot Fig. 9.4(d) illustrates the gas-bct phase separation at high dipole moment strength ($\gamma = 26.1$). We expect at higher dipole moment strengths (i.e., $\gamma > 38$), a very broad gas-bct coexistence between a void (low density gas phase) with packing fraction $\eta \approx 0.0$ and a bct phase at the maximum packing $\eta = 0.698$. As can be seen from Fig. 9.3, the stability of the hcp phase is reduced when the dipole moment strength is increased, and beyond $\gamma \approx 25$ the hcp phase is stable only above the maximum bct packing.

The ground-state ($\gamma = \infty$) phase behavior of dipolar hard spheres has been studied in Ref. [198], where the authors found a gas-bct coexistence at $\eta \in [0, 0.698]$, a stable high-density bco phase at $\eta \in [0.698, 0.724]$, a bco-hcp coexistence at $\eta \in [0.698, 0.740]$, and a stable hcp phase at $\eta = 0.740$. This sequence of phases and in particular, the presence of the bco phase, should also be present in our dipolar hard sphere phase diagram at $\gamma \gg 40$, but we did not extend our simulations to high enough γ to observe it. The reason for this is that at very high values of γ , the simulations are hampered by sampling problems as the displacement moves become difficult due to strong dipole-dipole interactions. Note that for dipolar soft spheres (which are discussed next) it is possible to reach higher γ because the soft repulsion compensates partly for the dipolar interaction.

Next, we consider the case where the particles, in addition to the dipole-

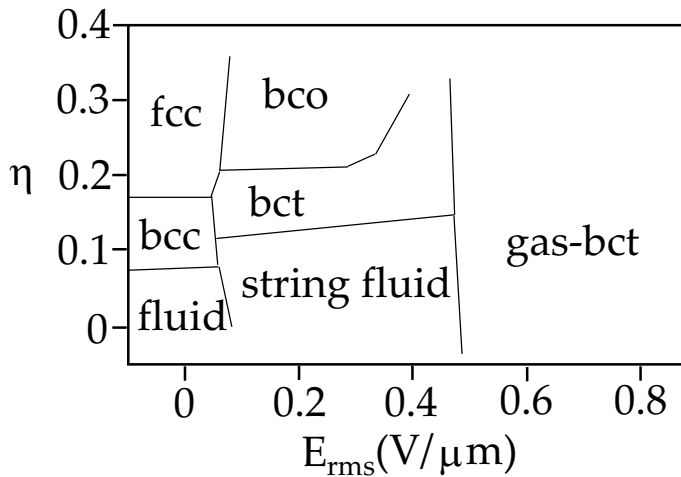


Figure 9.6: A reproduction of the experimental phase diagram in Ref. [3].

dipole interaction, interact via the Yukawa repulsion in Eq. (9.4) with parameters $\kappa\sigma = 10.0$ and $Z = 300$. For a solvent with Bjerrum length $\lambda_B/\sigma = 0.005$, these parameters correspond to a contact value $\epsilon = 12.54$. The phase diagram for this dipolar soft sphere system is shown in Fig. 9.5. At zero electric field, the phase diagram in Fig. 9.5 shows a fluid-fcc phase coexistence with the two phases at packing fractions $\eta_{\text{fluid}} = 0.31$ and $\eta_{\text{fcc}} = 0.32$. At $\gamma > 0$, the fcc phase is replaced by the hcp phase. As is seen from Fig. 9.5, even a small amount of electric field ($\gamma \gtrsim 4$) is sufficient to suppress the stability region of the hcp phase considerably and to replace it by a bco phase, which is stable at low densities for $4 \leq \gamma \leq 10$. In the phase diagram in Fig. 9.5, at $\gamma \approx 17$, the bct phase emerges as the stable low-density crystal. Further increase of the dipole moment strength from $\gamma \approx 17$ reduces the significance of the soft repulsion relative to the dipolar attraction, therefore increasing the region of the stable bct phase. Finally, at $\gamma \approx 67$, the bco phase vanishes completely. Increasing the dipole moment strength reduces the stability region of the hcp phase and, at $\gamma \gtrsim 100$, the hcp phase is only stable at packing fractions higher than the maximum body-centered packing.

The phase diagram in Fig. 9.5 shows that the fluid-bct coexistence region, starting at $\gamma \approx 38$, broadens quickly with increasing dipole moment strength γ . At $\gamma \approx 67$, the fluid phase in coexistence with the bct phase consists of strings of particles (string fluid phase), while the fluid phase is extremely dilute, i.e., $\eta \approx 0$, for $\gamma \gtrsim 100$. At $\gamma > 180$, we expect that the coexisting bct phase reaches the maximum packing $\eta \approx 0.698$.

In Fig. 9.6, we plot a reproduction of the experimental phase diagram of Ref. [3]. We have re-named some of the phases in the experimental phase diagram. Firstly, we call the space-filling tetragonal (sft) phase of Ref. [3] bct. Secondly, the non-space-filling bct phase of Ref. [3], which consist of small bct crystallites with voids, corresponds to our gas-bct coexistence. Experimentally, one observes a micro phase separation instead of a macroscopic phase separation, which depends strongly on the kinetics and dynamics of the phase separation and on how fast the electric field is switched on. For comparison with Fig. 9.6, the upper horizontal axis in Fig. 9.5 gives the (root mean square) electric field strength E_{rms} . The γ

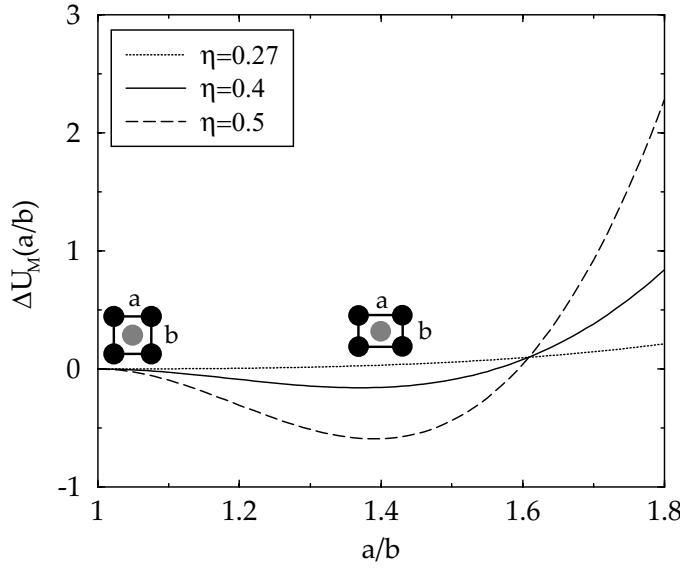


Figure 9.7: The change in the Madelung energy [see Eq. (9.7)] of bco crystals as a function of the asymmetry parameter a/b for dipolar soft spheres with $\kappa\sigma = 10.0$, $Z = 300$ (corresponding to $\epsilon = 12.54$ with $\lambda_B/\sigma = 0.005$) and $\gamma = 37.5$. The dotted line shows the result for packing fraction $\eta = 0.27$, the full line for $\eta = 0.4$, and the dashed line for $\eta = 0.5$.

to E_{rms} conversion is done using

$$E_{\text{rms}} = 2 \frac{|1 - \alpha \frac{\pi}{6}|}{|\alpha|} \sqrt{\frac{k_B T \gamma}{\epsilon_s \sigma^3 \pi'}} \quad (9.6)$$

where we used parameter values that correspond to the experimental system of Ref. [3]: $\alpha = -0.105$, $T = 300\text{K}$, $\epsilon_s = 5.6$ and $\sigma = 2\mu\text{m}$. For the derivation of Eq. (9.6), see e.g. Refs. [86, 195, 199]. We have assumed a cubic lattice, for which the local field is given by $\mathbf{E}_{\text{loc}} = \mathbf{E}/(1 - \alpha\pi/6)$ [86]. As can be checked from Figs. 9.5 and 9.6, the external electric field strength, E_{rms} , has the same order of magnitude in both phase diagrams. Our phase diagram for dipolar soft spheres in Fig. 9.5 shows a remarkable structural agreement with the experimental phase diagram in Fig. 9.6. Both phase diagrams show, at low electric field strength, the same sequence of fluid, bct, and bco phases upon increasing η , and at high electric fields, phase separation between a gas (void) and a bct phase. The main difference between the two phase diagrams is the bcc phase, which is seen experimentally at zero electric field but which is not present in the theoretical phase diagram. This dissimilarity is due to the different Z and κ in the experiments and the simulations. More exact determination of these parameters would require further characterization of the experimental conditions.

9.3.2 Stability of the Bco Phase

In this section, we explain how the soft repulsion give rise to the bco phase. Note that, we mean the bco phase in the phase diagram in Fig. 9.5, not the high-density bco phase discussed earlier, which, according to Ref. [198], appears at very high γ in the dipolar hard sphere phase diagram in Fig. 9.3.

The emergence of the bco phase is most easily explained as follows. Due to dipolar interactions, the particles form strings in the z -direction. If two strings are close to each other, it is favorable to shift one string by $c/2$ in the z direction

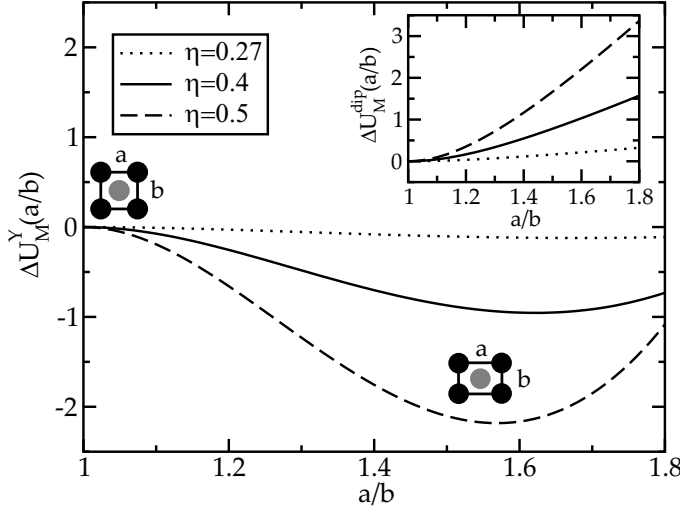


Figure 9.8: Yukawa (i.e., soft repulsive) part of the change in the Madelung energy of bco crystals as a function of the asymmetry parameter a/b . The dotted line shows the result for packing fraction $\eta = 0.27$, the full line for $\eta = 0.4$, and the dashed line for $\eta = 0.5$. In order to enable a comparison, the results have been shifted by $w_Y(1)$ to have the same value at $a/b = 1$. The inset shows the dipolar part of the Madelung energy.

with respect to the other string, as the dipole-dipole interaction favors configurations with small angles θ , see Eq. (9.1). Consequently, two kind of strings, say A and B, are obtained. In Fig. 9.2(b), A strings are black and B strings are grey. The interactions between the strings are such that similar strings (A-A and B-B) repel each other more than dissimilar strings (A-B). This is why the bct is stable: it minimizes the A-B distance. Soft Yukawa repulsion of A-A strings and A-B strings are very similar (A-B being slightly weaker), and it favors configurations where all neighboring strings have almost equal distances. This is achieved by increasing the ratio a/b . Hence, the bco phase. Note that in a hexagonal state (which is the ground state if all strings are similar) all nearest neighbors distances are equal and $a/b = \sqrt{3} \approx 1.73$.

In order to make the above description more quantitative, we calculated the Madelung energies for a bco crystal at a fixed η as a function of a/b . Figure 9.7 shows the change in Madelung energy

$$\Delta U_M(a/b) = U_M(a/b) - U_M(1) \quad (9.7)$$

of a bco crystal (with $c = \sigma$) at packing fractions $\eta = 0.27, 0.4$, and 0.5 . At $\eta = 0.27$, the minimum of the Madelung energy is at $a/b = 1$ and, therefore, the ground state is bct. At $\eta = 0.4$ and 0.5 , the minimum is at $a/b \approx 1.4$, meaning that the ground state is bco. Next, we split the Madelung energy into Yukawa and dipolar parts as

$$\Delta U_M(a/b) = \Delta U_M^Y(a/b) + \Delta U_M^{\text{dip}}(a/b). \quad (9.8)$$

Fig. 9.8 shows the Yukawa [$\Delta U_M^Y(a/b)$] part of the Madelung energy and the inset the dipolar part [$\Delta U_M^{\text{dip}}(a/b)$]. As can be seen from Fig. 9.8, the dipolar part, $\Delta U_M^{\text{dip}}(a/b)$, increases monotonically with a/b , while $\Delta U_M^Y(a/b)$ has a minimum at $a/b > 1.5$. Thus, the bco phase is stabilized by soft repulsion.

9.3.3 Multipole Moment Expansion

The reason why the hcp phase is more stable than the fcc phase is due to the difference between the Madelung energies of the two structures: The hcp structure with the orientation shown in Fig. 9.2(c) has a Madelung energy $U_M(\text{hcp}) = -0.37066 \times 4\gamma$ (as in Refs. [188, 195]), while the fcc structure (whose energy is independent of the orientation) has a Madelung energy $U_M(\text{fcc}) = -0.37024 \times 4\gamma$ (as in Refs. [86, 195]). Although the Madelung energy difference between hcp and fcc is small, $1.7\gamma \times 10^{-3}k_B T$ per particle, so is their zero-field free energy difference: For hard-spheres [186], the free energy per particle of the fcc is about $1 \times 10^{-3}k_B T$ lower than that of the hcp. Therefore, for dipolar hard spheres, the hcp is expected to be stable for $\gamma \gtrsim 1$, which is consistent with Fig. 9.3.

In order to check that the Madelung energy difference between the fcc and hcp crystals is a real effect and not an artifact of the dipole approximation, we calculated the difference using the multipole moment expansion method of Ref. [202]. The total Coulomb energy per particle is given by

$$u = -\frac{2\pi a^3}{3\eta k_B T} |\mathbf{E}|^2 \epsilon_{\text{eff}}, \quad (9.9)$$

where $a = \sigma/2$ is the radius of the particles constituting the structure, η is the volume fraction and \mathbf{E} is the applied electric field. The method in Ref. [202] allows one to calculate the effective dielectric constant ϵ_{eff} with any number of multipoles. In the following we briefly describe the method. For more details we refer the reader to the original article [202]. We consider τ_{max} spheres with a dielectric constant ϵ_p in one unit cell embedded in a solvent with a dielectric constant ϵ_s . According to Ref. [202], The effective dielectric constant ϵ_{eff} is given by

$$\epsilon_{\text{eff}} = \epsilon_s [1 - F(s)], \quad (9.10)$$

where

$$F(s) = \frac{\eta}{\tau_{\text{max}} + 1} \sum_{u=1}^{u_{\text{max}}} \frac{|\sum_{\tau=0}^{\tau_{\text{max}}} U_{u,\tau 10}|^2}{s - s_u}. \quad (9.11)$$

In Eq. (9.11), $U_{u,\tau 10}$ is the $(\tau, l = 1, m = 0)$ component of the u th eigenvector of matrix $\Gamma = \{\Gamma_{\tau l m, \tau' l' m'}\}$, s_u is the corresponding eigenvalue, $s = 1/(1 - \epsilon_p/\epsilon_s)$ is a material parameter, and τ is the index of the sphere in the unit cell. Note that $\tau_{\text{max}} = 1$ for hcp and $\tau_{\text{max}} = 0$ for Bravais lattices like fcc and bct. The index $m = \{-l, \dots, l\}$ and $l = \{1, \dots, l_{\text{max}}\}$. The elements of the matrix Γ are defined as

$$\Gamma_{\tau l m, \tau' l' m'} = \sum_{\tau=0}^{\tau_{\text{max}}} \sum_{\mathbf{R}} \hat{\Gamma}_{l m, l' m'}(\mathbf{R} + \mathbf{R}_{\tau}), \quad (9.12)$$

where the summation goes over all lattice points \mathbf{R} , \mathbf{R}_{τ} is the displacement of the τ th sphere with respect to the origin, and

$$\hat{\Gamma}_{l m, l' m'}(\mathbf{R}) = s_{l'} \int d\mathbf{r}^3 \zeta(\mathbf{r}) \nabla \phi_{l m}^*(\mathbf{r}) \cdot \nabla \phi_{l' m'}(\mathbf{r} + \mathbf{R}). \quad (9.13)$$

In Eq. (9.13), $\zeta(\mathbf{r})$ is the characteristic function of the particles, having value 1 inside the sphere and 0 outside, ϕ_{lm}^* denotes the complex conjugate of ϕ_{lm} , and

$$\phi_{lm}(\mathbf{r}) = f_l(r)Y_l^m(\theta, \phi), \quad (9.14)$$

$$f_l(r) = \begin{cases} \frac{(r/a)^l}{\sqrt{la}} & \text{for } r < a \\ 1 & \text{for } r > a, \\ \frac{1}{(r/a)^{l+1}\sqrt{la}} & \end{cases} \quad (9.15)$$

where $Y_l^m(\theta, \phi)$ are the spherical harmonics and the spherical coordinate system is defined as [203]

$$\begin{aligned} r_x &= r \cos(\phi) \sin(\theta) \\ r_y &= r \sin(\phi) \sin(\theta) \\ r_z &= r \cos(\theta), \end{aligned} \quad (9.16)$$

where $\theta \in [0, \pi]$ and $\phi \in [0, 2\pi)$. We define the relationship between the spherical harmonics and the associated Legendre polynomials as

$$Y_l^m(\theta, \phi) = \sqrt{\frac{2l+1}{4\pi} \frac{(l-m)!}{(l+m)!}} P_l^m(\cos \theta) e^{im\phi}, \quad (9.17)$$

where the Condon-Shortley phase $(-1)^m$ is included in the Legendre polynomials (unlike in Ref. [202]). After evaluating the integrals in Eq. (9.13), we obtain

$$\begin{aligned} \hat{\Gamma}_{lm,l'm'}(0) &= \frac{l}{2l+1} \delta_{ll'} \delta_{mm'}, \\ \hat{\Gamma}_{lm,l'm'}(\mathbf{R}) &= \sqrt{\frac{l!}{(2l+1)(2l'+1)}} B_{lm,l'm'} S(\mathbf{R}), \end{aligned} \quad (9.18)$$

where

$$\begin{aligned} B_{lm,l'm'} &= (-1)^{l'+m} \sqrt{4\pi} \times \\ &\sqrt{\frac{(l+l'+m'-m)!(l+l'+m-m')!}{(2l+2l'+1)(l+m)!(l-m)!(l'+m')!(l'-m')!}} \end{aligned} \quad (9.19)$$

and

$$S(\mathbf{R}) = \frac{Y_{l+l'}^{m'-m}(\theta, \phi)}{R^{l+l'+1}}. \quad (9.20)$$

In Eq. (9.18), $\delta_{ll'}$ and $\delta_{mm'}$ are discrete Kronecker delta functions. As noted in Ref. [202], the summation in Eq. (9.12) is only conditionally convergent for $l+l' \leq 2$ as it involves terms which decay slower than $1/R^3$. Therefore, we used the Ewald method to evaluate the sums with $l+l' \leq 4$ (Note that in Ref. [202], the Ewald method was used for $l+l' \leq 6$). The Ewald sums are given in Section 9.5. Once the matrix elements $\Gamma_{\tau lm, \tau' l' m'}$ are determined from Eq. (9.12), the eigenvectors U_u and the eigenvalues s_u can be solved easily. The calculation was implemented with Mathematica[®]. We tested our program by calculating the dielectric

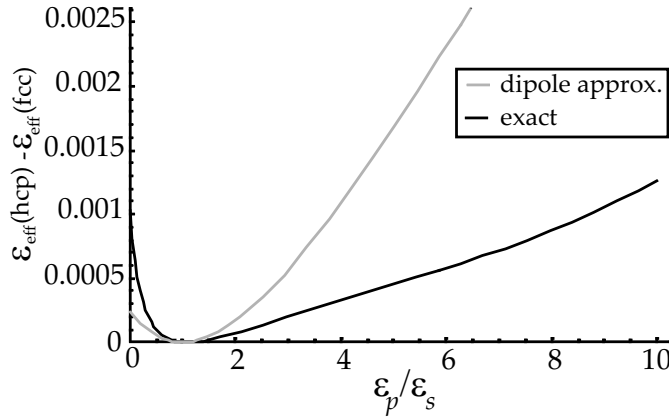


Figure 9.9: The difference in the effective dielectric constants of the hcp and fcc crystals at packing fraction $\eta \approx 0.72948$ as a function of the ratio ϵ_p/ϵ_s . The grey and black lines are the results of the dipole approximation and the exact calculation, respectively.

constants for the bct, fcc, hcp, and bcc crystals, and compared the results with the numerical values given in Ref. [202]. In order to obtain the same accuracy as in Ref. [202], 20-27 multipole contributions (i.e., $l_{\max} = 20 - 27$) were included in the calculation.

In Fig. 9.9, we plot the difference between the effective dielectric constants of the hcp and fcc crystals at packing fraction $\eta \approx 0.72948$ as a function of the ratio ϵ_p/ϵ_s . The grey line plots the result of the dipole approximation where $l_{\max} = 1$, and the black lines plots the result of the exact calculation where $l_{\max} = 27$. As can be seen from Fig. 9.9, the hcp crystal has a higher effective dielectric constant than the fcc crystal for $\epsilon_p/\epsilon_s > 0$, which results, according to Eq. (9.9), in a lower energy than fcc. Figure 9.9 also shows that in the region where $\epsilon_p/\epsilon_s < 1$, the contribution from the multipole moments favors the hcp phase even more than what is expected based on the dipole approximation alone. Note that the experiments in Ref. [3] are in this region as they have $\epsilon_p/\epsilon_s \approx 0.7$. In the region where $\epsilon_p/\epsilon_s > 1$, the multipole moments decrease the energy difference between hcp and fcc crystals.

9.3.4 Dipolar Fluid Phase

In both hard and soft dipolar systems, we observed a highly inhomogeneous fluid phase: The MC simulations showed large local density fluctuations in the fluid phase, reminiscent of a gas-liquid phase separation. However, no spinodal instability was found. An example of a Helmholtz free energy (F) curve is shown in Fig. 9.10, where we plot F/V as a function of η for the dipolar hard sphere fluid at dipole moment strength $\gamma = 8.0$. This system has an inhomogeneous fluid phase at $\eta \leq 0.3$, as can be seen from Fig. 9.4(a) that shows a snapshot of the system at $\eta = 0.01$. However, as Fig. 9.10 shows, the free energy density curve is convex, and therefore, no gas-liquid phase separation is possible. On the other hand, the free energy density F/V is almost linear with η . This means that the compressibility, which is proportional to the second derivative of F/V with respect to η , is very small. The small compressibility explains the appearance of an inhomogeneous fluid phase.

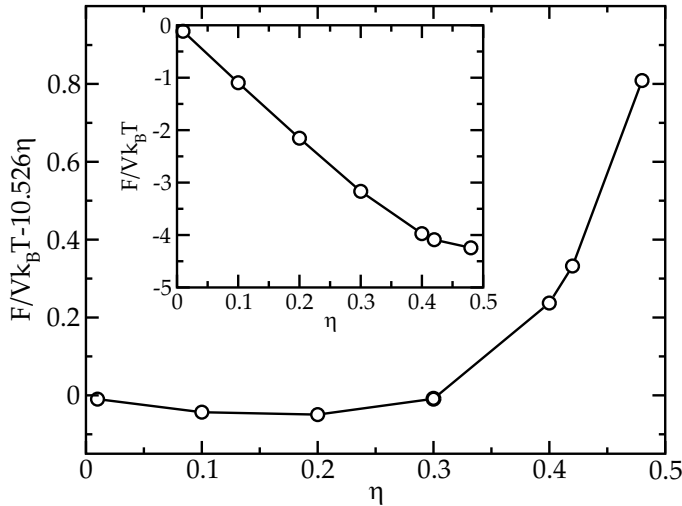


Figure 9.10: The Helmholtz free energy per volume, $F/Vk_B T$, as a function of η for dipolar hard sphere fluid with $\gamma = 8.0$. In the main figure, a linear fit to the first four data points has been subtracted. The inset shows the original free energy data. The lines are guide to the eye.

9.4 Conclusions

We have determined the phase diagrams of dipolar hard and soft spheres using Monte Carlo simulations. Two systems were considered: (i) colloids without charge (or dipolar hard-spheres) and (ii) colloids with charge $Ze = 300e$ and inverse Debye screening length of $\kappa\sigma = 10$ (dipolar soft-spheres). The simulations correspond to dielectric (or magnetic) particles in an external electric (or magnetic) field. The phase diagrams were plotted as a function of the dipole moment strength γ and the packing fraction η . In the phase diagram of dipolar hard spheres, we found stable regions of (string-) fluid, fcc, hcp, and bct phases, and regions of fluid-hcp and fluid-bct coexistence. In the phase diagram of soft spheres, we found all the above phases and also a stable region of the asymmetric bco phase. The stability of the bco phase was explained based on simple Madelung energy considerations. We found the hcp phase as the new stable phase in the high packing fraction region. In this region, the hcp phase is more stable than the fcc phase, because of its lower Madelung energy, and more stable than the bct phase, because of its higher entropy. We showed that the hcp phase has a lower Madelung energy than the fcc phase even when one goes beyond the dipole approximation and performs the full calculation which includes all multipole moments. Our results show that bulk hcp, bct, and bco crystals, can be stabilized and therefore realized experimentally by applying an external electric or magnetic field. It is important to remember that these crystal phases are unstable in the absence of a field. Finally, in both systems, we observed an inhomogeneous fluid phase. However, we did not find any evidence for a gas-liquid phase instability. Our free energy calculations showed that the free energy density vs. packing fraction is close to linear, indicating a small compressibility, which explains why the fluid phase appears inhomogeneous.

9.5 Ewald Sums

In this appendix, we essentially repeat the Appendix D of Ref. [202]. This is done partly because the original article contains some typos. Essentially, the summations in Eq. (9.12) are of the form

$$\sum_{\mathbf{R}} \frac{Y_L^M(\theta, \phi)}{|\mathbf{R} + \mathbf{r}|^{L+1}}, \quad (9.21)$$

where $L = l + l'$ and $M = m' - m$. As noted in Ref. [202], the summation in Eq. (9.21) can be related to summations over the following tensors, which are obtained by successive differentiations with respect to \mathbf{r}

$$T^0 = \frac{1}{|\mathbf{R} + \mathbf{r}|}, \quad (9.22)$$

$$T_i^1 = -\frac{(\mathbf{R} + \mathbf{r})_i}{|\mathbf{R} + \mathbf{r}|^3}, \quad (9.23)$$

$$T_{ij}^2 = \frac{3(\mathbf{R} + \mathbf{r})_i(\mathbf{R} + \mathbf{r})_j}{|\mathbf{R} + \mathbf{r}|^5} - \frac{\delta_{ij}}{|\mathbf{R} + \mathbf{r}|^3}, \quad (9.24)$$

$$T_{ijk}^3 = -\frac{15(\mathbf{R} + \mathbf{r})_i(\mathbf{R} + \mathbf{r})_j(\mathbf{R} + \mathbf{r})_k}{|\mathbf{R} + \mathbf{r}|^7} + \frac{3}{|\mathbf{R} + \mathbf{r}|^5} \left[\delta_{ij}(\mathbf{R} + \mathbf{r})_k + \delta_{ik}(\mathbf{R} + \mathbf{r})_j + \delta_{jk}(\mathbf{R} + \mathbf{r})_i \right], \quad (9.25)$$

and

$$T_{ijkn}^4 = \frac{105(\mathbf{R} + \mathbf{r})_i(\mathbf{R} + \mathbf{r})_j(\mathbf{R} + \mathbf{r})_k(\mathbf{R} + \mathbf{r})_n}{|\mathbf{R} + \mathbf{r}|^9} - \frac{15}{|\mathbf{R} + \mathbf{r}|^7} \left[\delta_{in}(\mathbf{R} + \mathbf{r})_j(\mathbf{R} + \mathbf{r})_k + \delta_{jn}(\mathbf{R} + \mathbf{r})_i(\mathbf{R} + \mathbf{r})_k + \delta_{kn}(\mathbf{R} + \mathbf{r})_i(\mathbf{R} + \mathbf{r})_j \right] - \frac{15(\mathbf{R} + \mathbf{r})_n}{|\mathbf{R} + \mathbf{r}|^7} \left[\delta_{ij}(\mathbf{R} + \mathbf{r})_k + \delta_{ik}(\mathbf{R} + \mathbf{r})_j + \delta_{jk}(\mathbf{R} + \mathbf{r})_i \right] + \frac{3}{|\mathbf{R} + \mathbf{r}|^5} \left[\delta_{ij}\delta_{kn} + \delta_{ik}\delta_{jn} + \delta_{jk}\delta_{in} \right], \quad (9.26)$$

where $(\mathbf{R} + \mathbf{r})_i$ is the i th ($= \{x, y, z\}$) component of the vector $\mathbf{R} + \mathbf{r}$.

The relation between the tensors in (9.24)-(9.26) with the terms $Y_L^M(\theta, \phi)/|\mathbf{R} + \mathbf{r}|^{L+1}$ in the sum (9.21) are given in Table 9.1. Note that, as $L = l + l' \geq 2$, we do not list terms with $L < 2$. Thus, Table 9.1 can be used to convert the sums in Eq. (9.21) to sums over the tensors. The advantage of this is that the tensor sums can be evaluated using the Ewald summation as shown in the following. The zeroth order tensor sum is given by

$$\tilde{T}^0 = \sum_{\mathbf{R}} T^0 = \sum_{\mathbf{R}} \frac{\operatorname{erfc}(\beta|\mathbf{R} + \mathbf{r}|)}{|\mathbf{R} + \mathbf{r}|} + \sum_{\mathbf{G}} \frac{4\pi}{vG^2} \exp(-G^2/4\beta^2) \exp(-i\mathbf{G} \cdot \mathbf{r}), \quad (9.27)$$

L	M	$\frac{1}{ \mathbf{R}+\mathbf{r} ^{L+1}} Y_L^M(\theta, \phi)$
2	2	$\sqrt{\frac{5}{96\pi}} \left(T_{xx}^2 - T_{yy}^2 + 2iT_{xy}^2 \right)$
2	1	$-\sqrt{\frac{5}{24\pi}} \left(T_{xz}^2 + iT_{yz}^2 \right)$
2	0	$\frac{1}{2} \sqrt{\frac{5}{4\pi}} T_{zz}^2$
3	3	$\frac{1}{120} \sqrt{\frac{35}{\pi}} \left[T_{xxx}^3 - 3T_{xyy}^3 + i \left(3T_{xxy}^3 - T_{yyy}^3 \right) \right]$
3	2	$\frac{1}{60} \sqrt{\frac{105}{2\pi}} \left(T_{yyz}^3 - T_{xxz}^3 - 2iT_{xyz}^3 \right)$
3	1	$\frac{1}{24} \sqrt{\frac{21}{\pi}} \left(T_{zzx}^3 + iT_{zzy}^3 \right)$
3	0	$-\frac{1}{12} \sqrt{\frac{7}{\pi}} T_{zzz}^3$
4	4	$\frac{1}{16\sqrt{70\pi}} \left[T_{xxxx}^4 - 6T_{xxyy}^4 + T_{yyyy}^4 + 4i \left(T_{xxxy}^4 - T_{xyyy}^4 \right) \right]$
4	3	$-\frac{1}{8\sqrt{35\pi}} \left[T_{xxxz}^4 - 3T_{xyyz}^4 + i \left(3T_{xxyz}^4 - T_{yyyz}^4 \right) \right]$
4	2	$\frac{1}{8\sqrt{10\pi}} \left(T_{xxzz}^4 - T_{yyzz}^4 + 2iT_{xyzz}^4 \right)$
4	1	$-\frac{1}{8\sqrt{5\pi}} \left(T_{zzzx}^4 + iT_{zzzy}^4 \right)$
4	0	$\frac{1}{16\sqrt{\pi}} T_{zzzz}^4$

Table 9.1: The relation between the tensors (9.24)-(9.26) and the terms in the sum in Eq. (9.21). Here $L = l + l'$ and $M = m' - m$.

where \mathbf{G} is the reciprocal vector of \mathbf{R} , v is the unit cell volume, and β is a free parameter that is chosen to optimize convergence. Separating out the divergent part of Eq. (9.27) and taking successive derivatives with respect to \mathbf{r}_i , we obtain

$$\begin{aligned}
\tilde{T}_{ij}^2 &= - \sum_{\mathbf{G} \neq 0} \frac{4\pi}{vG^2} G_i G_j \exp(-G^2/4\beta^2) \exp(-i\mathbf{G} \cdot \mathbf{r}) \\
&\quad + \sum_{\mathbf{R}} \left[\operatorname{erfc}(\beta|\mathbf{R} + \mathbf{r}|) + \left(\frac{4\beta^3|\mathbf{R} + \mathbf{r}|^3}{3\sqrt{\pi}} + \frac{2\beta|\mathbf{R} + \mathbf{r}|}{\sqrt{\pi}} \right) \exp(-\beta^2|\mathbf{R} + \mathbf{r}|^2) \right] T_{ij}^2 \\
&\quad + \sum_{\mathbf{R}} \frac{4\beta^3}{3\sqrt{\pi}} \delta_{ij} \exp(-\beta^2|\mathbf{R} + \mathbf{r}|^2),
\end{aligned} \tag{9.28}$$

$$\begin{aligned}
\tilde{T}_{ijk}^3 &= i \sum_{\mathbf{G} \neq 0} \frac{4\pi}{vG^2} G_i G_j G_k \exp(-G^2/4\beta^2) \exp(-i\mathbf{G} \cdot \mathbf{r}) \\
&\quad + \sum_{\mathbf{R}} \left[\operatorname{erfc}(\beta|\mathbf{R} + \mathbf{r}|) + \left(\frac{4\beta^3|\mathbf{R} + \mathbf{r}|^3}{3\sqrt{\pi}} + \frac{2\beta|\mathbf{R} + \mathbf{r}|}{\sqrt{\pi}} \right) \exp(-\beta^2|\mathbf{R} + \mathbf{r}|^2) \right] T_{ijk}^3 \\
&\quad - \sum_{\mathbf{R}} \frac{8\beta^5}{\sqrt{\pi}} \frac{(\mathbf{R} + \mathbf{r})_i (\mathbf{R} + \mathbf{r})_j (\mathbf{R} + \mathbf{r})_k}{|\mathbf{R} + \mathbf{r}|^2} \exp(-\beta^2|\mathbf{R} + \mathbf{r}|^2),
\end{aligned} \tag{9.29}$$

and

$$\begin{aligned}
 \tilde{T}_{ijkn}^4 &= \sum_{\mathbf{G} \neq 0} \frac{4\pi}{vG^2} G_i G_j G_k G_n \exp(-G^2/4\beta^2) \exp(-i\mathbf{G} \cdot \mathbf{r}) \\
 &+ \sum_{\mathbf{R}} \left[\operatorname{erfc}(\beta|\mathbf{R} + \mathbf{r}|) + \left(\frac{4\beta^3|\mathbf{R} + \mathbf{r}|^3}{3\sqrt{\pi}} + \frac{2\beta|\mathbf{R} + \mathbf{r}|}{\sqrt{\pi}} \right) \exp(-\beta^2|\mathbf{R} + \mathbf{r}|^2) \right] T_{ijkn}^4 \\
 &- \sum_{\mathbf{R}} \frac{8\beta^5}{3\sqrt{\pi}} (\mathbf{R} + \mathbf{r})_n |\mathbf{R} + \mathbf{r}|^3 T_{ijk}^3 \exp(-\beta^2|\mathbf{R} + \mathbf{r}|^2) \\
 &- \sum_{\mathbf{R}} \frac{8\beta^5}{\sqrt{\pi}} \frac{\exp(-\beta^2|\mathbf{R} + \mathbf{r}|^2)}{|\mathbf{R} + \mathbf{r}|^2} \left[\delta_{in}(\mathbf{R} + \mathbf{r})_j (\mathbf{R} + \mathbf{r})_k + \delta_{jn}(\mathbf{R} + \mathbf{r})_i (\mathbf{R} + \mathbf{r})_k \right. \\
 &\quad \left. + \delta_{kn}(\mathbf{R} + \mathbf{r})_i (\mathbf{R} + \mathbf{r})_j \right. \\
 &\quad \left. - 2(\mathbf{R} + \mathbf{r})_i (\mathbf{R} + \mathbf{r})_j (\mathbf{R} + \mathbf{r})_k (\mathbf{R} + \mathbf{r})_n \left(\beta^2 + \frac{1}{|\mathbf{R} + \mathbf{r}|^2} \right) \right].
 \end{aligned} \tag{9.30}$$

For $\mathbf{r} = 0$, the sums over \mathbf{R} in Eqs. (9.28)-(9.30) should be restricted by the constraint $\mathbf{R} \neq 0$. In this case, the sums over the tensors are given by

$$\sum_{\mathbf{R} \neq 0} T_{ij}^2 = \tilde{T}_{ij}^2(\mathbf{R} \neq 0) + \frac{4\beta^3}{3\sqrt{\pi}} \delta_{ij}, \tag{9.31}$$

$$\sum_{\mathbf{R} \neq 0} T_{ijk}^3 = \tilde{T}_{ijk}^3(\mathbf{R} \neq 0), \tag{9.32}$$

and

$$\sum_{\mathbf{R} \neq 0} T_{ijkn}^4 = \tilde{T}_{ijkn}^4(\mathbf{R} \neq 0) - \frac{8\beta^5}{5\sqrt{\pi}} (\delta_{ij}\delta_{kn} + \delta_{ik}\delta_{jn} + \delta_{jk}\delta_{in}). \tag{9.33}$$

10

Sedimentation of Charged Colloids: Entropic Lift and Charge Separation

ABSTRACT

In this chapter, we present Molecular Dynamics simulations and Poisson-Boltzmann theory of sedimentation equilibrium of suspensions of charged colloids, treated at the level of the primitive model, including the co- and counterions (microions) explicitly. The simulations provide direct confirmation of the theoretical low-salt predictions of (i) a macroscopic separation of colloidal and micro ionic charge, (ii) an almost homogeneous electric field in the suspension, and (iii) a highly non-barometric colloid density distribution. These effects, which cannot be explained within the usual effective one-component picture, have been measured experimentally.

10.1 Introduction

Colloidal suspensions are multi-component fluids that consist of mesoscopic colloidal particles in a molecular solvent, often with additional components such as ions, polymers, etc. Despite this multicomponent character it is common practice to view a colloidal suspension as an effective one-component system of colloidal particles [17, 18]. In this chapter, we study sedimentation of suspensions of charged colloids in the Earth's gravity field, and show that the resulting equilibrium density profile can only be understood in terms of macroscopic charge separation of colloids and salt ions, i.e., the effective one-component description breaks down.

Colloidal suspensions exhibit sedimentation in the Earth's gravity field when the buoyant mass m of the colloidal particles is non-vanishing [72–74, 204]. The equilibrium colloid density $\rho(z)$ at height z follows, within a one-component picture, from the competition between minimal energy (all colloids at $z = 0$, i.e., at the bottom) and maximum entropy (a homogeneous distribution in the available volume). For a dilute suspension at temperature T the equilibrium density profile satisfies the well-known barometric height distribution

$$\rho(z) = \rho_0 \exp\left(-\frac{z}{L}\right), \quad (10.1)$$

with $L = k_B T / mg$ the gravitational length in terms of the Boltzmann constant k_B and the gravitational acceleration g [205]. The normalization constant ρ_0 , which is the number density at $z = 0$, follows from the total number $N = A \int_0^H dz \rho(z)$ of colloids in the system, where A is the planar area and H the height of the sample. Of course the colloidal interactions affect the competition between potential energy and entropy, and hence change the functional form of $\rho(z)$, but one would expect that L sets the length scale for the sedimentation equilibrium in dilute suspensions. Typically, L is of the order of μm – mm for colloids, unless density matching has taken place by special preparation of the sample.

There is, however, both theoretical [78, 206–209] and experimental [75–77, 210] evidence that L is *not* necessarily the relevant length scale in suspensions of highly charged colloids at low ionic strength. The reason is that the usual competition between potential (gravitational) energy and colloid entropy is enriched by two additional free energy contributions in such systems, (i) the entropy of the microions (which favors the co- and counterions to be homogeneously distributed in the sample), and (ii) the electrostatic energy (which favors local charge neutrality). At low enough concentrations of salt these two contributions are in conflict with Eq. (10.1) when $L \ll H$: in order to satisfy local charge neutrality the counterion distribution must, in absence of an appreciable number of coions, also be of the form (10.1), i.e., the counterion distribution will be extremely inhomogeneous on the length scale of the sample size H . (At sufficiently high salt concentrations the relative ion fractionation is much smaller). How does the system resolve this conflict? Theoretical treatments of this problem have so far all been based on Poisson-Boltzmann (mean-field) theory, which predicts that the system sets up an almost homogeneous macroscopic electric field in the suspension (i.e., in a conducting medium!), such that the colloids are lifted to heights of

order ZL , with $Z > 0$ the colloidal charge number that can easily be $10^2 - 10^4$ experimentally. In order to assess the possibility of experimental observation of this intriguing phenomenon, important questions are whether or not the predictions are (i) robust with respect to approximations of the theory (which ignores fluctuations, correlations, and hard-core excluded volume effects), and (ii) quantitatively reliable. In this chapter we present the results of a computer simulation study of this system, and put the mean-field theory, in particular the version of Ref. [78], to the test directly. We briefly present the theory first for completeness. For more details, the reader is referred to Ref. [78].

10.2 Theory

We consider a suspension of N colloidal spheres of charge Ze (with e the proton charge, $Z > 0$) and gravitational length L , in a structureless solvent with dielectric constant ϵ_s at temperature T , in osmotic contact with a salt reservoir with a concentration $2\rho_s$ of monovalent co- and counterions. The ions are massless, and their (yet unknown) average equilibrium density profile in the suspension can be written as a Boltzmann distribution $\rho_{\pm}(z) = \rho_s \exp[\mp\phi(z)]$ [78]. Here $\phi(z)$ is the yet unknown dimensionless electrostatic (Donnan) potential, which follows with the equilibrium colloid density profile $\rho(z)$ from the combined Boltzmann distribution and Poisson-Boltzmann equation,

$$\left. \begin{aligned} \rho(z) &= \rho_0 \exp[-z/L - Z\phi(z)] \\ \phi''(z) &= -4\pi\lambda_B(Z\rho(z) - 2\rho_s \sinh \phi(z)), \end{aligned} \right\} \quad (10.2)$$

subject to the boundary conditions $\phi'(0) = \phi'(H) = 0$. Here $\lambda_B = e^2/\epsilon_s k_B T$ is the Bjerrum length, and a prime denotes differentiation with respect to z [78]. Below we solve this set of equations numerically for the parameters of the simulation. However, this set of equations, or variations thereof, was already studied in Refs. [78, 206, 207, 209], and was found to have solutions $\phi(z)$ linear in z in a macroscopically large volume provided the ion concentration is so low that $2\rho_s \ll Z^2\rho(z)$. In the salt-free case, the resulting electric field is such that the electric force on a colloidal particle is $mgZ/(Z+1)$, which with a gravitational force of $-mg$ yields a net force $-mg/(Z+1)$, i.e., as if the mass were reduced by a factor $Z+1$. Hence the colloidal distribution is much more homogeneous than predicted by the barometric law (10.1), and the typical height of the sediment is now $(Z+1)L$ instead of L [78, 206, 207, 209]. In the limit of high salt, $2\rho_s \gg Z^2\rho(z)$, the barometric law (10.1) is recovered.

We wish to stress that the present theoretical description is entirely of mean-field nature, and disregards *any* of the correlations, i.e., correlations are not even accounted for on the Debye-Hückel level. For a homogeneous system of charged particles (which is obtained here when $m = 0$), this level of approximation leads trivially to an ideal gas mixture in a spatially constant Donnan potential, but in the gravity-induced inhomogeneous system of present interest, nontrivial phenomena already show up within this low-level description.

10.3 Simulation Method

We perform Molecular Dynamics (MD) simulations in a box of dimensions $K \times K \times H$, taken periodic in the horizontal directions $x, y \in [0, K]$ and finite in the vertical direction $z \in [0, H]$. We consider N colloids of positive charge Ze and diameter σ , N_+ coions of charge $+e$, and $N_- = ZN + N_+$ counterions of charge $-e$. The microions have a (small) diameter in order to prevent the system from collapsing. Since a hard-core repulsion is not well-suited for MD simulations we replace it, following Ref. [133], by a softer r^{-9} potential, such that the pair potential between particles of species i and j (i.e., between colloid-colloid, colloid-microion, and microion-microion pairs) is given by

$$U_{ij}(r) = k_B T \frac{Z_i Z_j \lambda_B}{r} + k_B T \frac{|Z_i Z_j| \lambda_B}{9} \left(\frac{\sigma_i + \sigma_j}{2} \right)^8 \frac{1}{r^9}, \quad (10.3)$$

where Z_i and σ_i are the valency and diameter of species i , respectively, while $r = |\mathbf{r}_i - \mathbf{r}_j|$. The prefactor of the soft repulsion was chosen such that the potential well of oppositely charged particles is located at hard-core contact, $r = (\sigma_i + \sigma_j)/2$ [133]. In addition to the pair interaction in Eq. (10.3), the colloids are coupled to the gravitational field that points in the negative z -direction, and the potential is given by $V(z) = k_B T z/L$ with L the gravitational length defined earlier. The microions are considered massless, and do not couple to the gravitational field.

The long range of the Coulomb interaction requires the use of periodic images to account for the electrostatics properly. The standard Ewald summation method [93] cannot be used, since the system is only periodic in the x and y , and *not* in the z -direction. Instead we employed the so-called MMM2D method, which can deal with the slab geometry of present interest properly and efficiently [211, 212]. In order to keep the particles inside the simulation box, repulsive walls are added at $z = 0$ and $z = H$. The wall potential for species j is given by the soft r^{-9} repulsion of Eq. (10.3), now with r equal to the distance from the wall and i equal to the colloid species. This choice mimics, to a good approximation, a hard wall with contact distance given by $(\sigma + \sigma_j)/2$.

It is important to note that the simulated system is *not* osmotically coupled to a salt reservoir; the number of microions is fixed. In principle this complicates the direct comparison with the theory presented earlier [78], where the reservoir salt concentration is fixed and *not* the actual concentration in the suspension. However, we see that the top part of the simulation box contains such a low colloid density that it acts as a reservoir, and the measured total salt concentration in the top can be directly identified with the reservoir salt concentration $2\rho_s$.

The MD simulations are performed for fixed particle numbers, volume, and temperature. Constant temperature is achieved by using the so-called Langevin dynamics [213], where the equation of motion for each particle is a Langevin equation instead of the usual Newton equation (that gives rise to a constant energy). Denoting the potential energy of a configuration by U , the Langevin equation for particle i at position $\mathbf{r}_i(t)$ at time t can be written as [213]

$$m_i \ddot{\mathbf{r}}_i = -\nabla_i U - \nu m_i \dot{\mathbf{r}}_i + \mathbf{F}_i(t), \quad (10.4)$$

where m_i is the inertial mass of the particle, ν a friction coefficient, $\mathbf{F}_i(t)$ a random force, and the dots denote time derivatives. The dissipative term, $-\nu m_i \dot{\mathbf{r}}_i$, damps the motion of the particles, while the fluctuating term, $\mathbf{F}_i(t)$, gives the particles random pushes and therefore, on average, accelerates the motion of the particles. Together these two terms provide a heat bath at constant temperature, provided the fluctuation-dissipation theorem is satisfied by setting $\langle \mathbf{F}_i(t) \rangle = 0$ and $\langle \mathbf{F}_i(0) \cdot \mathbf{F}_i(t) \rangle = 2m_i k_B T \nu \delta(t)$, where the brackets denote the average over a Gaussian distribution. We use the velocity Verlet algorithm to integrate Eq. (10.4) [213], and employ reduced units: the colloid diameter σ and mass m are the units of length and mass, respectively, and $k_B T$ is the unit of energy, resulting in $\sigma \sqrt{m/k_B T}$ for the unit of time.

The density profiles $\rho(z)$, $\rho_+(z)$ and $\rho_-(z)$ for the colloids and microions are calculated from the particle configurations recorded during a simulation run. The electric field $E(z)$ along the z axis inside the simulation box is calculated from the integrated Poisson equation, which in dimensionless form is given by

$$\mathcal{E}(z) = \frac{\sigma e E(z)}{k_B T} = 4\pi \frac{\lambda_B}{\sigma} \sigma^2 \int_0^z q(z') dz', \quad (10.5)$$

where $q(z) = Z\rho(z) + \rho_+(z) - \rho_-(z)$ is the total charge density. One can directly compare the simulated $\mathcal{E}(z)$ with the theoretical prediction $\sigma\phi'(z)$ that follows from the solution of Eq. (10.2).

10.4 Results

We performed four simulations, labelled (a)-(d), which all had $\lambda_B = 4 \times 10^{-3} \sigma$, the inertial mass of the microions $0.01m$, $L = 10\sigma$, the lateral dimension of the box $K \approx 7.24\sigma$, and the total colloidal packing fraction $\eta = (\pi/6)\sigma^3 N/AH = 0.01$. The height of the box is $H = 100\sigma$, except in (d) where $H = 50\sigma$. Simulation (a) and (b) represent salt-free systems ($N_+ = 0$) of $N = 100$ colloids, where $Z = 10$ and $N_- = 1000$ in (a) and $Z = 5$ and $N_- = 500$ in (b). Simulations (c) and (d) have added salt, with (c) having $N = 100$ colloids and $N_+ = 250$ added coions and (d) $N = 50$ colloids and $N_+ = 625$ added coions. In simulations (a)-(c) we use microion diameter $\sigma_{\text{ion}} = 10^{-3}\sigma$ and in (d) we use $\sigma_{\text{ion}} = 0.01\sigma$. The friction coefficient in the Langevin equation (10.4) is chosen to be $\nu = 5 \times 10^{-5}/\Delta t$ for all simulations, and the time step for the velocity Verlet algorithm is chosen to be $\Delta t = 1 \times 10^{-4} \sigma \sqrt{m/k_B T}$ for (a)-(c) and $\Delta t = 5 \times 10^{-5} \sigma \sqrt{m/k_B T}$ for (d). Such a small Δt requires long simulations to sample properly the colloidal degrees of freedom.

The colloidal charges $Z = 5$ and $Z = 10$ that we use are much lower than is typical of realistic colloidal suspensions, where $Z = 10^2 - 10^4$. Such a low colloidal charge is used here for practical reasons: it keeps the total number of particles in the system low enough and the colloid-ion interaction weak enough for fast and efficient simulations [133], while the mechanisms at work can yet be revealed. Note that λ_B/σ and $\sigma_{\text{ion}}/\sigma$ do have values that are typical of colloidal suspensions.

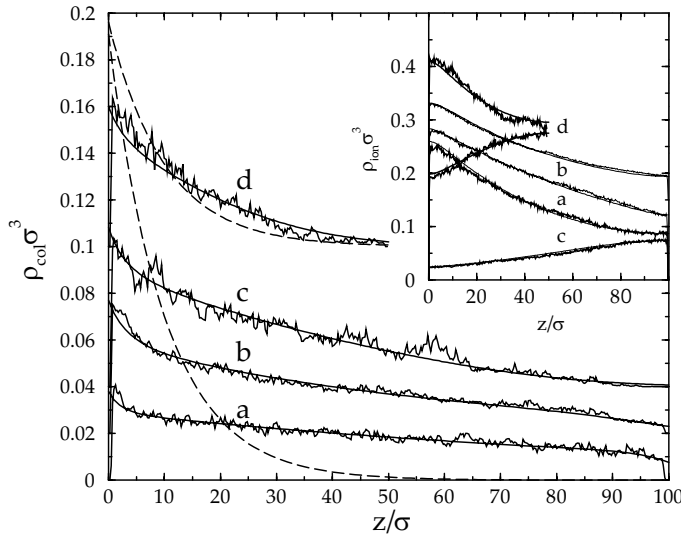


Figure 10.1: Density profiles $\rho(z)$ for a colloidal suspension of height $H = 100\sigma$, total packing fraction $\eta = 0.01$, Bjerrum length $\lambda_B = 4 \times 10^{-3}\sigma$, and gravitational length $L = 10\sigma$, with colloidal charge number Z given by (a) $Z = 10$ without added salt, (b) $Z = 5$ without added salt, and (c) $Z = 5$ with $N_+ = 250$ added coions. The curves labelled (d) correspond to $H = 50\sigma$, $Z = 5$ and $N_+ = 625$ added coions. For clarity, the colloid density profiles for (b), (c), and (d) are shifted upwards by $0.02\sigma^3$, $0.04\sigma^3$, and $0.1\sigma^3$, respectively. The inset shows the corresponding microion density profiles where the density profile for (b) is shifted upwards by $0.15\sigma^3$. The smooth solid curves are the theoretical Poisson-Boltzmann predictions based on Eq. (10.2) and Ref. [78], and the dashed curves give the barometric density distributions with $L = 10\sigma$ for both $H = 100\sigma$ and $H = 50\sigma$.

The salt-free simulations (a) and (b) were started with colloids and ions distributed homogeneously and randomly in the simulation box, while the added salt simulations (c) and (d) had an initial distribution that approximately corresponds to the theoretical prediction [78]. In all cases the density profiles $\rho(z)$ were only acquired after carefully checking that the averaged center of mass of the colloids had reached a plateau, indicating that the sedimentation equilibrium had been reached. In order to check the consistency of our methods, simula-

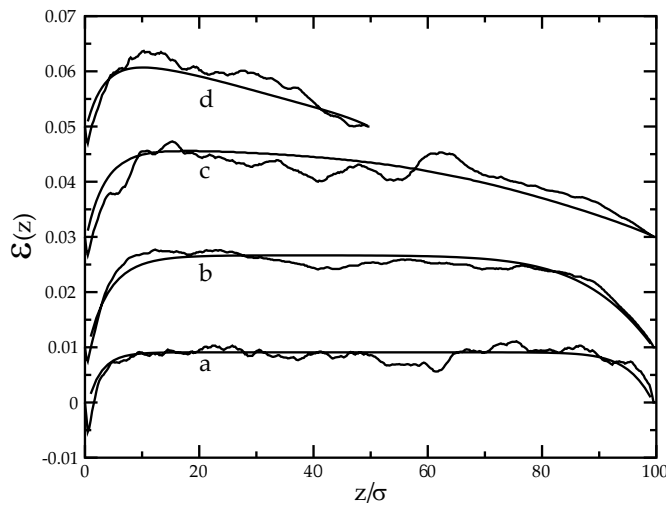


Figure 10.2: Simulated dimensionless electric field $\mathcal{E}(z)$ defined in Eq. (10.5) and its theoretical prediction $\sigma\phi'(z)$ (smooth curve) for the parameter choices (a)-(d) as in Fig.10.1. For clarity, the graphs for (b), (c), and (d) are shifted upwards by $0.01\sigma e/k_B T$, $0.03\sigma e/k_B T$, and $0.05\sigma e/k_B T$, respectively.

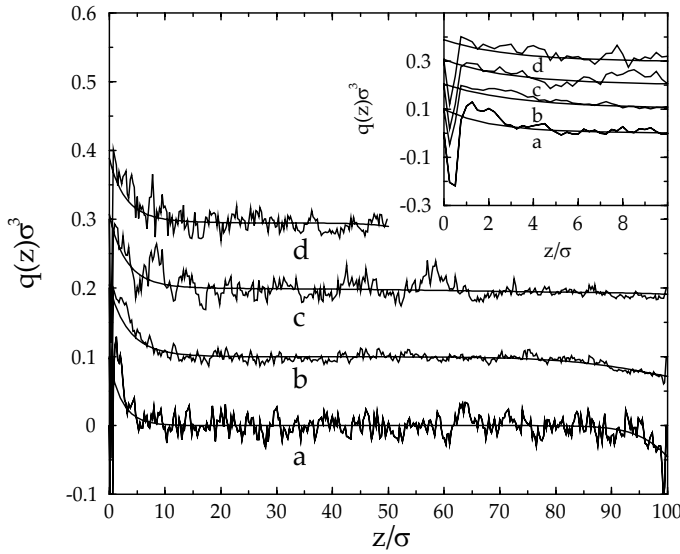


Figure 10.3: Total charge density profile $q(z)$ showing a positive charge at the bottom ($z = 0$) and a negative charge at the top ($z = 100\sigma$ or $z = 50\sigma$), for systems (a)-(d) labelled as in Fig.1. The inset shows a close-up of the bottom region (see text). The smooth curves represent the theoretical predictions. For clarity, the graphs for (b), (c), and (d) are shifted upwards by $0.1\sigma^3$, $0.2\sigma^3$, and $0.3\sigma^3$, respectively.

tions (a) and (b) were first performed without electrostatic interactions and, as expected, the barometric height distribution of Eq. (10.1) was recovered at large enough heights.

Figure 10.1 shows the simulated density profiles $\rho(z)$ together with the corresponding theoretical predictions (the smooth curves) based on numerical solutions of Eq. (10.2). The inset of Fig. 10.1 shows the corresponding microion density profiles. In the theoretical calculation for (c) and (d) we used reservoir salt concentrations $\rho_s = 0.08/\sigma^3$ and $\rho_s = 0.285/\sigma^3$, respectively; these values were obtained from (an extrapolation of) the simulated co- and counterion densities in the top of the container. Figure 10.1 shows that in all four cases the simulation results for both the colloid and ion density profiles agree almost quantitatively with the theoretical estimates. Note that the simulation data for the added salt cases (c) and (d) are noisier than in the salt free cases (a) and (b). The relatively poor statistics in (c) and (d) is due to the larger number of particles in these systems, which require a longer simulation CPU time. The dashed curves in Fig. 10.1 represent the colloidal barometric height distributions of Eq. (10.1) with $L = 10\sigma$. As can be clearly seen, the density profiles (a)-(c) are far from being barometric, while the profile for the high-salt system (d) is close to the barometric distribution.

The non-barometric distributions are due to a spontaneously formed electric field, which we plot in Fig. 10.2. Again, it is seen that the agreement between the simulation results and the theory is remarkable. The nonzero electric field inside the container is caused by charge separation between the colloids and the microions. In other words, there is excess positive charge from the colloids at the bottom of the box and conversely excess negative charge from the microions at the top. The charge separation is readily observed from Fig. 10.3 where we plot the total charge density $q(z)$. In systems (a)-(c) there are clearly two peaks in the total charge density, one at the bottom ($z = 0$) and one at the top ($z = 100\sigma$) of the box. In fact, as is seen from the inset in Fig. 10.3 where we show a close-up of the bottom region of the simulation box, there is also another negative peak at the bottom which is caused by the exclusion of the colloids from the bottom wall due

to their size. This "fine-structure" of the peak is *not* accounted for in the present version of the theory, as it ignores the finite colloidal size. It can, however, be included and explain the exclusion effect.

10.5 Conclusions

We show, for the first time by simulation, that a non-density matched colloidal suspension in a gravitational field gives rise to a macroscopic charge separation of colloids and micro-ions, provided the added salt concentration is low enough (but *not* necessarily unphysically low). The mechanism, which was already identified in earlier work [73, 78, 206–209], is due to the intricate balance between colloidal and ionic entropy, potential energy, and electrostatic energy. The electric field that is generated by the charge separation is shown to be almost constant in the suspension, and is such that it largely compensates the gravitational force on the colloids. Thus, the colloids are lifted to altitudes much larger than their gravitational length. This implies that the system cannot be understood as an effective one-component system of colloids, not even at rather low densities [78].

Our simulations agree quantitatively with the Poisson-Boltzmann theory of Ref. [78], which we briefly repeated here, i.e., the (mean-field) theory is robust with respect to the inclusion of fluctuations, correlations, and hard-core effects present in the simulations. We note that the low Coulomb coupling of the present system is large enough to induce the entropic lift mechanism, but is yet small enough to ignore correlations in the theory. Given that the four systems presented here span the whole interval from the low (zero) salt regime close to the high salt regime, and that the predictions of the theory hold quantitatively for the rather low colloidal charges considered here, it is tempting to conclude that the theoretical prediction of the entropic lift of the colloids due to a macroscopic electric field may also be rather accurate, or at least qualitatively correct, for low-salt suspensions of highly charged colloids.

References

- [1] W. B. Russel, D. A. Saville, and W. R. Schowalter, *Colloidal dispersions*, Cambridge University Press, Cambridge, 1989.
- [2] Z. Q. Chen, X. Y. Wang, J. M. Ko, Y. Q. Ni, B. F. J. Spencer, and G. Yang, *MR damping system on Dongting lake cable-stayed bridge*, Proc. SPIE **5057**, 229 (2003).
- [3] A. Yethiraj and A. van Blaaderen, *A colloidal model system with an interaction tunable from hard sphere to soft and dipolar*, Nature (London) **421**, 513 (2003).
- [4] W. K. Kegel and A. van Blaaderen, *Direct observation of dynamical heterogeneities in colloidal hard-sphere suspensions*, Science **287**, 290 (2000).
- [5] A. Yethiraj, A. Wouterse, B. Groh, and A. van Blaaderen, *Nature of an electric-field-induced colloidal martensitic transition*, Phys. Rev. Lett. **92**, 058301 (2004).
- [6] S. Hachisu, *Phase transition in monodisperse gold sol. Microscopic observation of gas, liquid and solid states*, Croatica Chemica Acta **71**, 975 (1998).
- [7] P. N. Pusey and W. van Megen, *Phase behaviour of concentrated suspensions of nearly hard colloidal spheres*, Nature (London) **320**, 340 (1986).
- [8] Y. Monovoukas and A. P. Gast, *The experimental phase-diagram of charged colloidal suspensions*, J. Colloid Interface Sci. **128**, 533 (1989).
- [9] E. B. Sirota, H. D. Ou-Yang, S. K. Sinha, P. M. Chaikin, J. D. Axe, and Y. Fujii, *Complete phase diagram of a charged colloidal system: A synchrotron x-ray scattering study*, Phys. Rev. Lett. **62**, 1524 (1989).
- [10] H. J. Schöpe, T. Decker, and T. Palberg, *Response of the elastic properties of colloidal crystals to phase transitions and morphological changes*, J. Chem. Phys. **109**, 10068 (1998).
- [11] M. E. Leunissen, C. G. Christova, A.-P. Hynninen, C. P. Royall, A. I. Campbell, A. Imhof, M. Dijkstra, R. van Roij, and A. van Blaaderen, *Ionic colloidal crystals of oppositely charged particles*, Nature (London) **437**, 235 (2005).
- [12] K. N. Pham, A. M. Puertas, J. Bergenholtz, S. U. Egelhaaf, A. Moussaïd, P. N. Pusey, A. B. Schofield, M. E. Cates, M. Fuchs, and W. C. K. Poon, *Multiple glassy states in a simple model system*, Science **296**, 104 (2002).
- [13] D. J. Cebula, S. W. Charles, and J. Popplewell, *Aggregation in ferrofluids studied by neutron small angle scattering*, J. Physique **44**, 207 (1983).
- [14] K. Butter, P. H. H. Bomans, P. M. Frederik, G. J. Vroege, and A. P. Philipse, *Direct observation of dipolar chains in iron ferrofluids by cryogenic electron microscopy*, Nat. Mater. **2**, 88 (2003).
- [15] R. Bubeck, C. Bechinger, S. Naser, and P. Leiderer, *Melting and reentrant freezing of two-dimensional colloidal crystals in confined geometry*, Phys. Rev. Lett. **82**, 3364 (1999).
- [16] J. E. Martin, R. A. Anderson, and R. L. Williamson, *Generating strange magnetic and dielectric interactions: Classical molecules and particle foams*, J. Chem. Phys. **118**, 1557 (2003).
- [17] B. Derjaguin and L. Landau, *Theory of the stability of strongly charged lyophobic sols and of the adhesion of strongly charged particles in solution of electrolytes*, Acta Physicochim. URSS **14**, 633 (1941).
- [18] E. J. W. Verwey and J. T. G. Overbeek, *Theory of the stability of lyotropic colloids*, Elsevier, Amsterdam, 1948.
- [19] M. O. Robbins, K. Kremer, and G. S. Grest, *Phase diagram and dynamics of Yukawa systems*, J. Chem. Phys. **88**, 3286 (1988).
- [20] S. Sengupta and A. K. Sood, *Theory of liquid-bcc-fcc coexistence in charge-stabilized colloidal systems*, Phys. Rev. A **44**, 1233 (1991).
- [21] S. Hamaguchi, R. T. Farouki, and D. H. E. Dubin, *Triple point of Yukawa systems*, Phys. Rev. E **56**, 4671 (1997).
- [22] S. Alexander, P. M. Chaikin, P. Grant, G. J. Morales, and P. Pincus, *Charge renormalization, osmotic pressure, and bulk modulus of colloidal crystals: Theory*, J. Chem. Phys. **80**, 5776 (1984).

- [23] P. Linse, *Structure, phase stability, and thermodynamics in charged colloidal solutions*, J. Chem. Phys. **113**, 4359 (2000).
- [24] A. Khan, K. Fontell, and B. Lindman, *Liquid crystallinity in systems of magnesium and calcium surfactants: Phase diagrams and phase structures in binary aqueous systems of magnesium and calcium di-2-ethylhexylsulfosuccinate*, J. Colloid Interface Sci. **101**, 193 (1984).
- [25] C. Kang and A. Khan, *Self-assembly in systems of didodecyltrimethylammonium surfactants: Binary and ternary phase equilibria and phase structures with sulphate, hydroxide, acetate, and chloride counterions*, J. Colloid Interface Sci. **156**, 218 (1993).
- [26] C. W. Outhwaite and M. Molero, *Effective interaction between colloidal particles using a symmetric Poisson-Boltzmann theory*, Chem. Phys. Lett. **197**, 643 (1992).
- [27] I. Rouzina and V. A. Bloomfield, *Macroion attraction due to electrostatic correlation between screening counterions. 1. Mobile surface-adsorbed ions and diffuse ion cloud*, J. Phys. Chem. **199**, 9977 (1996).
- [28] E. Allahyarov, I. D'Amico, and H. Löwen, *Attraction between Like-Charged Macroions by Coulomb Depletion*, Phys. Rev. Lett. **81**, 1334 (1998).
- [29] N. Gronbech-Jensen, K. M. Beardmore, and P. Pincus, *Interactions between charged spheres in divalent counterion solution*, Physica A **261**, 74 (1998).
- [30] J. Z. Wu, D. Bratko, and J. M. Prausnitz, *Interaction between like-charged colloidal spheres in electrolyte solutions*, Proc. Natl. Acad. Sci. USA **95**, 15169 (1998).
- [31] P. Linse and V. Lobaskin, *Electrostatic attraction and phase separation in solutions of like-charged colloidal particles*, Phys. Rev. Lett. **83**, 4208 (1999).
- [32] P. Linse and V. Lobaskin, *Electrostatic attraction and phase separation in solutions of like-charged colloidal particles*, J. Chem. Phys. **112**, 3917 (2000).
- [33] A. Z. Panagiotopoulos and M. E. Fisher, *Phase transitions in 2:1 and 3:1 hard-core model electrolytes*, Phys. Rev. Lett. **88**, 045701 (2002).
- [34] Q. L. Yan and J. J. de Pablo, *Phase equilibria of charge-, size-, and shape-asymmetric model electrolytes*, Phys. Rev. Lett. **88**, 095504 (2002).
- [35] D. Cheong and A. Z. Panagiotopoulos, *Critical parameters of unrestricted primitive model electrolytes with charge asymmetries up to 10:1*, J. Chem. Phys. **119**, 8526 (2003).
- [36] J. Reščič and P. Linse, *Gas-liquid phase separation in charged colloidal systems*, J. Chem. Phys. **114**, 10131 (2001).
- [37] P. Linse, *Structure and phase separation in solutions of like-charged colloidal particles*, Phil. Trans. R. Soc. Lond. A **359**, 853 (2001).
- [38] N. Ise, T. Okubo, M. Sugimura, K. Ito, and H. J. Nolte, *Ordered structure in dilute solutions of highly charged polymer lattices as studied by microscopy. I. Interparticle distance as a function of latex concentration*, J. Chem. Phys. **78**, 536 (1983).
- [39] N. Ise and M. V. Smalley, *Thermal compression of colloidal crystals: Paradox of the repulsion-only assumption*, Phys. Rev. B **50**, 16722 (1994).
- [40] B. V. R. Tata, M. Rajalakshmi, and A. K. Arora, *Vapor-liquid condensation in charged colloidal suspensions*, Phys. Rev. Lett. **69**, 3778 (1992).
- [41] T. Palberg and M. Würth, *Vapor-liquid condensation in charged colloidal suspensions - Comment*, Phys. Rev. Lett. **72**, 786 (1994).
- [42] K. Ito, H. Yoshida, and N. Ise, *Void structure in colloidal dispersions*, Science **263**, 66 (1994).
- [43] B. V. R. Tata, E. Yamahara, P. V. Rajamani, and N. Ise, *Amorphous clustering in highly charged dilute poly(chlorostyrene-styrene sulfonate) colloids*, Phys. Rev. Lett. **78**, 2660 (1997).
- [44] A. E. Larsen and D. G. Grier, *Like-charge attractions in metastable colloidal crystallites*, Nature (London) **385**, 230 (1997).
- [45] I. Sogami, *Effective potential between charged spherical particles in dilute suspension*, Phys. Lett. A **96**, 199 (1983).
- [46] I. Sogami and N. Ise, *On the electrostatic interaction in macroionic solutions*, J. Chem. Phys. **81**, 6320 (1984).

- [47] R. van Roij and J.-P. Hansen, *Van der Waals-like instability in suspensions of mutually repelling charged colloids*, Phys. Rev. Lett. **79**, 3082 (1997).
- [48] R. van Roij, M. Dijkstra, and J.-P. Hansen, *Phase diagram of charge-stabilized colloidal suspensions: van der Waals instability without attractive forces*, Phys. Rev. E **59**, 2010 (1999).
- [49] P. B. Warren, *A theory of void formation in charge-stabilized colloidal suspensions at low ionic strength*, J. Chem. Phys. **112**, 4683 (2000).
- [50] C. Russ, H. H. von Grünberg, M. Dijkstra, and R. van Roij, *Three-body forces between charged colloidal particles*, Phys. Rev. E **66**, 011402 (2002).
- [51] J. T. G. Overbeek, *Electrostatic interaction in solutions*, J. Chem. Phys. **87**, 4406 (1987).
- [52] H. Löwen and E. Allahyarov, *The role of effective triplet interactions in charged colloidal suspensions*, J. Phys.: Cond. Matt. **10**, 4147 (1998).
- [53] J. Z. Wu, D. Bratko, H. W. Blanch, and J. M. Prausnitz, *Effect of three-body forces on the phase behavior of charged colloids*, J. Chem. Phys. **113**, 3360 (2000).
- [54] M. Brunner, C. Bechinger, C. W. Strepp, V. Lobaskin, and H. H. von Grünberg, *Density-dependent pair interactions in 2D colloidal suspensions*, Europhys. Lett. **58**, 926 (2002).
- [55] R. Klein, H. H. von Grünberg, C. Bechinger, M. Brunner, and V. Lobaskin, *Macroion shielding and state-dependent pair potentials in colloidal suspensions*, J. Phys.: Cond. Matt. **14**, 7631 (2002).
- [56] J. Dobnikar, R. Rzehak, and H. H. von Grünberg, *Effect of many-body interactions on the solid-liquid phase behavior of charge-stabilized colloidal suspensions*, Europhys. Lett. **61**, 695 (2003).
- [57] J. Dobnikar, Y. Chen, R. Rzehak, and H. H. von Grünberg, *Many-body interactions in colloidal suspensions*, J. Phys.: Cond. Matt. **15**, S263 (2003).
- [58] J. Dobnikar, Y. Chen, R. Rzehak, and H. H. von Grünberg, *Many-body interactions and the melting of colloidal crystals*, J. Chem. Phys. **119**, 4971 (2003).
- [59] M. Brunner, J. Dobnikar, H. H. von Grünberg, and C. Bechinger, *Direct measurement of three-body interactions amongst charged colloids*, Phys. Rev. Lett. **92**, 078301 (2004).
- [60] C. Russ, M. Brunner, C. Bechinger, and H. H. von Grünberg, *Three-body forces at work: Three-body potentials derived from triplet correlations in colloidal suspensions*, Europhys. Lett. **69**, 468 (2005).
- [61] J. Dobnikar, M. Brunner, J. Baumgartl, C. Bechinger, and H. H. von Grünberg, *Three- and four-body interactions in colloidal systems*, Proc. SPIE Int. Soc. Opt. Eng. **5514**, 340 (2004).
- [62] R. van Roij, *Attraction or repulsion between charged colloids? A connection with Debye-Hückel theory*, J. Phys.: Cond. Matt. **12**, A263 (2000).
- [63] A. Diehl, M. C. Barbosa, and Y. Levin, *Charge renormalization and phase separation in colloidal suspensions*, Europhys. Lett. **53**, 86 (2001).
- [64] H. H. von Grünberg, R. van Roij, and G. Klein, *Gas-liquid phase coexistence in colloidal suspensions?*, Europhys. Lett. **55**, 580 (2001).
- [65] A. Z. Panagiotopoulos, *Simulations of phase transitions in ionic systems*, J. Phys.: Cond. Matt. , accepted (2005).
- [66] B. Smit, K. Esselink, and D. Frenkel, *Solid-solid and liquid-solid phase equilibria for the restricted primitive model*, Mol. Phys. **87**, 159 (1996).
- [67] F. Bresme, C. Vega, and J. L. F. Abascal, *Order-disorder transition in the solid phase of a charged hard sphere model*, Phys. Rev. Lett. **85**, 3217 (2000).
- [68] C. Vega, J. L. F. Abascal, C. McBride, and F. Bresme, *The fluid-solid equilibrium for a charged hard sphere model revisited*, J. Chem. Phys. **119**, 964 (2003).
- [69] P. Bartlett and A. I. Campbell, *Three-dimensional binary superlattices of oppositely-charged colloids*, Phys. Rev. Lett. **95**, 128302 (2005).
- [70] A. van Blaaderen, *Colloids under external control*, MRS Bulletin, February , 85 (2004).
- [71] J. Zhu, M. Li, W. Meyer, R. H. Ottewill, STS-73 Space Shuttle Crew, W. B. Russel, and P. M. Chaikin, *Crystallization of hard sphere colloids in μ - gravity*, Nature (London) **387**, 883 (1997).

- [72] S. Hachisu and K. Takano, *Pressure of disorder to order transition in monodisperse latex*, Adv. Colloid and Interface Sci. **16**, 233 (1982).
- [73] R. Piazza, T. Bellini, and V. Degiorgio, *Equilibrium sedimentation profiles of screened charged colloids: A test of the hard-sphere equation of state*, Phys. Rev. Lett. **71**, 4267 (1993).
- [74] M. A. Rutgers, J. H. Dunsmuir, J.-Z. Xue, W. B. Russel, and P. M. Chaikin, *Measurement of the hard-sphere equation of state using screened charged polystyrene colloids*, Phys. Rev. B **53**, 5043 (1996).
- [75] M. Raşa and A. P. Philipse, *Evidence for a macroscopic electric field in the sedimentation profiles of charged colloids*, Nature (London) **429**, 857 (2004).
- [76] M. Raşa, B. H. Erne, B. Zoetekouw, R. van Roij, and A. P. Philipse, *Macroscopic electric field and osmotic pressure in ultracentrifugal sedimentation-diffusion equilibria of charged colloids*, J. Phys.: Cond. Matt. **17**, 2293 (2005).
- [77] C. P. Royall, R. van Roij, and A. van Blaaderen, *Extended sedimentation profiles in charged colloids: the gravitational length, entropy, and electrostatics*, J. Phys.: Cond. Matt. **17**, 2315 (2005).
- [78] R. van Roij, *Defying gravity with entropy and electrostatics: sedimentation of charged colloids*, J. Phys.: Cond. Matt. **15**, S3569 (2003).
- [79] D. L. J. Vossen, A. van der Horst, M. Dogterom, and A. van Blaaderen, *Optical tweezers and confocal microscopy for simultaneous three-dimensional manipulation and imaging in concentrated colloidal dispersions*, Rev. Sci. Instrum. **75**, 2960 (2004).
- [80] D. L. J. Vossen and A. van Blaaderen, *Colloidal crystallization induced via single particle control with optical tweezers*, in preparation .
- [81] D. L. J. Vossen, M. A. Plaisier, and A. van Blaaderen, *Colloidal crystallization induced by optical gradient forces exerted by optical tweezers*, Proc. SPIE Int. Soc. Opt. Eng. **5514**, 755 (2004).
- [82] M. Sullivan, K. Zhao, C. Harrison, R. H. Austin, M. Megens, A. Hollingsworth, W. B. Russel, Z. D. Cheng, T. Mason, and P. M. Chaikin, *Control of colloids with gravity, temperature gradients, and electric fields*, J. Phys.: Cond. Matt. **15**, S11 (2003).
- [83] M. Parthasarathy and D. Klingenberg, *Electrorheology: Mechanisms and models*, Mater. Sci. Eng. R. **17**, 57 (1996).
- [84] W. J. Wen, C. Weisbuch, D. M. Phuong, G. Lu, W. Ge, C. T. Chan, and P. Sheng, *Neutral nanoparticle-based display*, Nanotechnology **16**, 598 (2005).
- [85] R. Tao, J. T. Woestman, and N. K. Jaggi, *Electric-Field Induced Solidification*, Appl. Phys. Lett. **55**, 1844 (1989).
- [86] R. Tao and J. M. Sun, *Three-dimensional structure of induced electrorheological solid*, Phys. Rev. Lett. **67**, 398 (1991).
- [87] A. Yethiraj, J. H. J. Thijssen, A. Wouterse, and A. van Blaaderen, *Large-area electric-field-induced colloidal single crystals for photonic applications*, Adv. Mater. **16**, 596 (2004).
- [88] R. Tao and D. Xiao, *Three-dimensional dielectric photonic crystals of body-centered-tetragonal lattice structure*, Appl. Phys. Lett. **80**, 4702 (2002).
- [89] J. D. Bernal, *The Bakerian lecture, 1962: The structure of liquids*, Proc. R. Soc. A **280**, 299 (1964).
- [90] N. Metropolis, A. Rosenbluth, M. Rosenbluth, A. Teller, and E. Teller, *Equations of state calculations by fast computing machines*, J. Chem. Phys. **21**, 1087 (1953).
- [91] B. J. Alder and T. E. Wainwright, *Phase transition for a hard sphere system*, J. Chem. Phys. **27**, 1208 (1957).
- [92] W. W. Wood and J. D. Jacobson, *Preliminary results from a recalculation of the monte carlo equation of state of hard spheres*, J. Chem. Phys. **27**, 1207 (1957).
- [93] D. Frenkel and B. Smit, *Understanding molecular simulations*, Academic Press, London, 2 edition, 2002.

- [94] E. J. Meijer and F. E. Azhar, *Novel procedure to determine coexistence lines by computer simulation. Application to hard-core Yukawa model for charge-stabilized colloids*, J. Chem. Phys. **106**, 4678 (1997).
- [95] F. E. Azhar, M. Baus, J.-P. Ryckaert, and E. J. Meijer, *Line of triple points for the hard-core Yukawa model: A computer simulation study*, J. Chem. Phys. **112**, 5121 (2000).
- [96] G. Salin and J.-M. Caillol, *Ewald sums for Yukawa potentials*, J. Chem. Phys. **113**, 10459 (2000).
- [97] R. T. Farouki and S. Hamaguchi, *Spline approximation of "effective" potentials under periodic boundary conditions*, J. Comp. Phys. **115**, 276 (1994).
- [98] D. Frenkel and A. J. C. Ladd, *New Monte Carlo method to compute the free energy of arbitrary solids. Application to the fcc and hcp phases of hard spheres*, J. Chem. Phys. **81**, 3188 (1984).
- [99] J. M. Polson, E. Trizac, S. Pronk, and D. Frenkel, *Finite-size corrections to the free energies of crystalline solids*, J. Chem. Phys. **112**, 5339 (2000).
- [100] M. Abramowitz and I. Stegun, *Handbook of mathematical functions*, Dover, New York, 1970.
- [101] J. G. Kirkwood, *Statistical mechanics of fluid mixtures*, J. Chem. Phys. **3**, 300 (1935).
- [102] R. J. Speedy, *Pressure of the metastable hard-sphere fluid*, J. Phys.: Cond. Matt. **9**, 8591 (1997).
- [103] N. F. Carnahan and K. E. Starling, *Equation of state for nonattracting rigid spheres*, J. Chem. Phys. **51**, 635 (1969).
- [104] D. A. Kofke, *Gibbs-Duhem integration - A new method for direct evaluation of phase coexistence by molecular simulation*, Mol. Phys. **78**, 1331 (1993).
- [105] D. A. Kofke, *Direct evaluation of phase coexistence by molecular simulation via integration along the saturation line*, J. Chem. Phys. **98**, 4149 (1993).
- [106] E. L. Pollock and J.-P. Hansen, *Statistical mechanics of dense ionized matter. II. Equilibrium properties and melting transition of the crystallized one-component plasma*, Phys. Rev. A **8**, 3110 (1973).
- [107] F. A. Lindemann, Z. Phys. **11**, 609 (1910).
- [108] C. P. Royall, M. E. Leunissen, and A. van Blaaderen, *A new colloidal model system to study long-range interactions quantitatively in real space*, J. Phys.: Cond. Matt. **15**, S3581 (2003).
- [109] L. Belloni, *Colloidal interactions*, J. Phys.: Cond. Matt. **12**, R549 (2000).
- [110] J.-P. Hansen and H. Löwen, *Effective interactions between electric double layers*, Annu. Rev. Phys. Chem. **51**, 209 (2000).
- [111] B. Beresford-Smith, D. Y. C. Chan, and D. J. Mitchell, *The electrostatic interaction in colloidal systems with low added electrolyte*, J. Colloid Interface Sci. **105**, 215 (1985).
- [112] D. Y. C. Chan, *Density functional theory of charged colloidal systems*, Phys. Rev. E **63**, 061806 (2001).
- [113] R. van Roij and R. Evans, *Phase equilibria in a model of low-salt suspensions of charged colloids*, J. Phys.: Cond. Matt. **11**, 10047 (1999).
- [114] M. J. Grimson and M. Silbert, *A self-consistent theory of the effective interactions in charge-stabilized colloidal dispersions*, Mol. Phys. **74**, 397 (1991).
- [115] H. Graf and H. Löwen, *Density jumps across phase transitions in soft-matter systems*, Phys. Rev. E **57**, 5744 (1998).
- [116] J. Dobnikar, M. Brunner, H. H. von Grünberg, and C. Bechinger, *Three-body interactions in colloidal systems*, Phys. Rev. E **69**, 031402 (2004).
- [117] R. Car and M. Parrinello, *Unified approach for Molecular Dynamics and density-functional theory*, Phys. Rev. Lett. **55**, 2471 (1985).
- [118] H. Löwen, P. A. Madden, and J.-P. Hansen, *Ab initio description of counterion screening in colloidal suspensions*, Phys. Rev. Lett. **68**, 1081 (1992).
- [119] H. Löwen, J.-P. Hansen, and P. A. Madden, *Nonlinear counterion screening in colloidal suspensions*, J. Chem. Phys. **98**, 3275 (1993).
- [120] M. Fushiki, *Molecular-dynamics simulations for charged colloidal dispersions*, J. Chem. Phys. **97**, 6700 (1992).

- [121] M. Dijkstra, R. van Roij, and R. Evans, *Phase diagram of highly asymmetric binary hard-sphere mixtures*, Phys. Rev. E **59**, 5744 (1999).
- [122] P. Attard, *Simulation results for a fluid with the Axilrod-Teller triple dipole potential*, Phys. Rev. A **45**, 5649 (1992).
- [123] K. R. Hall, *Another hard-sphere equation of state*, J. Chem. Phys. **57**, 2252 (1972).
- [124] R. P. Sear, *Absence of the liquid phase when the attraction is not pairwise additive*, Phys. Rev. E **61**, 651 (2000).
- [125] F. Bitzer, T. Palberg, H. Löwen, R. Simon, and P. Leiderer, *Dynamical test of interaction potentials for colloidal suspensions*, Phys. Rev. E **50**, 2821 (1994).
- [126] L. Belloni, *Ionic condensation and charge renormalization in colloidal suspensions*, Colloids Surfaces A **140**, 227 (1998).
- [127] H. Löwen and G. Kramposhuber, *Optimal effective pair potential for charged colloids*, Europhys. Lett. **23**, 673 (1993).
- [128] P. P. Ewald, *Die Berechnung optischer und elektrostatischer Gitterpotentiale*, Ann. Phys. **64**, 253 (1921).
- [129] A. Z. Panagiotopoulos and S. K. Kumar, *Large lattice discretization effects on the phase coexistence of ionic fluids*, Phys. Rev. Lett. **83**, 2981 (1999).
- [130] A. Z. Panagiotopoulos, *Thermodynamic properties of lattice hard-sphere models*, J. Chem. Phys. **123**, 104504 (2005).
- [131] J. W. Perram, H. G. Petersen, and S. W. de Leeuw, *An algorithm for the simulation of condensed matter which grows as the 3/2 power of the number of particles*, Mol. Phys. **65**, 875 (1988).
- [132] V. Lobaskin and K. Qamhieh, *Effective macroion charge and stability of highly asymmetric electrolytes at various salt conditions*, J. Phys. Chem. B **107**, 8022 (2003).
- [133] V. Lobaskin and P. Linse, *Simulation of an asymmetric electrolyte with charge asymmetry 60:1 using hard-sphere and soft-sphere models*, J. Chem. Phys. **111**, 4300 (1999).
- [134] P. Linse, *Advanced computer simulation approaches for soft matter sciences II*, volume 185 of *Advances in Polymer Science*, Springer, Berlin, 2005.
- [135] A. R. Denton, *Effective interactions and volume energies in charged colloids: Linear response theory*, Phys. Rev. E **62**, 3855 (2000).
- [136] T. Palberg, W. Mönch, F. Bitzer, R. Piazza, and T. Bellini, *Freezing transition for colloids with adjustable charge: A test of charge renormalization*, Phys. Rev. Lett. **74**, 4555 (1995).
- [137] V. Lobaskin, M. Brunner, C. Bechinger, and H. H. von Grünberg, *On the nature of long-range contributions to pair interactions between charged colloids in two dimensions*, J. Phys.: Cond. Matt. **15**, 6693 (2003).
- [138] L. Belloni, *Electrostatic interactions in colloidal solutions: Comparison between primitive and one-component models*, J. Chem. Phys. **85**, 519 (1986).
- [139] <http://www.csc.fi/gopenmol/>.
- [140] C. P. Royall, M. E. Leunissen, A.-P. Hynninen, M. Dijkstra, and A. van Blaaderen, *Unusual phase behavior in charged colloids: Re-entrant melting and freezing*, submitted .
- [141] M. Kleemeier, S. Wiegand, W. Schröer, and H. Weingärtner, *The liquid-liquid phase transition in ionic solutions: Coexistence curves of tetra-n-butylammonium picrate in alkyl alcohols*, J. Chem. Phys. **110**, 3085 (1999).
- [142] H. L. Bianchi and M. L. Japas, *Phase equilibria of a near-critical ionic system. Critical exponent of the order parameter*, J. Chem. Phys. **115**, 10472 (2001).
- [143] M. E. Fisher and Y. Levin, *Criticality in ionic fluids: Debye-Hückel theory, Bjerrum, and beyond*, Phys. Rev. Lett. **71**, 3826 (1993).
- [144] G. Stell, *Criticality and phase-transitions in ionic fluids*, J. Stat. Phys. **78**, 197 (1995).
- [145] Y. Levin and M. E. Fisher, *Criticality in the hard-sphere ionic fluid*, Physica A **225**, 164 (1996).
- [146] E. González-Tovar, *Critical parameters of asymmetric primitive model electrolytes in the mean spherical approximation*, Mol. Phys. **97**, 1203 (1999).

- [147] D. M. Zuckerman, M. E. Fisher, and S. Bekiranov, *Asymmetric primitive-model electrolytes: Debye-Hückel theory, criticality, and energy bounds*, Phys. Rev. E **64**, 011206 (2001).
- [148] M. N. Artyomov, V. Kobelev, and A. B. Kolomeisky, *Lattice models of ionic systems with charge asymmetry*, J. Chem. Phys. **118**, 6394 (2003).
- [149] J. M. Romero-Enrique, G. Orkoulas, A. Z. Panagiotopoulos, and M. E. Fisher, *Coexistence and criticality in size-asymmetric hard-core electrolytes*, Phys. Rev. Lett. **85**, 4558 (2000).
- [150] E. Luijten, M. E. Fisher, and A. Z. Panagiotopoulos, *Universality class of criticality in the restricted primitive model electrolyte*, Phys. Rev. Lett. **88**, 185701 (2002).
- [151] Y. C. Kim and M. E. Fisher, *Discretization dependence of criticality in model fluids: A hard-core electrolyte*, Phys. Rev. Lett. **92**, 185703 (2004).
- [152] Q. L. Yan and J. J. de Pablo, *Hyper-parallel tempering Monte Carlo: Application to the Lennard-Jones fluid and the restricted primitive model*, J. Chem. Phys. **111**, 9509 (1999).
- [153] Q. L. Yan and J. J. de Pablo, *Phase equilibria and clustering in size-asymmetric primitive model electrolytes*, J. Chem. Phys. **114**, 1727 (2001).
- [154] Q. L. Yan and J. J. de Pablo, *Phase equilibria of size-asymmetric primitive model electrolytes*, Phys. Rev. Lett. **86**, 2054 (2001).
- [155] Y. C. Kim and M. E. Fisher, *The critical locus of a simple fluid with added salt*, J. Phys. Chem. B **105**, 11785 (2001).
- [156] D. G. Angelescu and P. Linse, *Monte Carlo simulation of the mean force between two like-charged macroions with simple 1:3 salt added*, Langmuir **19**, 9661 (2003).
- [157] R. Zhang and B. I. Shklovskii, *Phase diagram of aggregation of oppositely charged colloids in salty water*, Phys. Rev. E **69**, 021909 (2004).
- [158] G. Orkoulas and A. Z. Panagiotopoulos, *Free energy and phase equilibria for the restricted primitive model of ionic fluids from Monte Carlo simulations*, J. Chem. Phys. **101**, 1452 (1994).
- [159] F. H. Stillinger and R. Lovett, *Ion-pair theory of concentrated electrolytes. I. Basic concepts*, J. Chem. Phys. **48**, 3858 (1968).
- [160] A. Z. Panagiotopoulos, *Critical parameters of the restricted primitive model*, J. Chem. Phys. **116**, 3007 (2002).
- [161] N. B. Wilding and A. D. Bruce, *Density-fluctuations and field mixing in the critical fluid*, J. Phys.: Cond. Matt. **4**, 3087 (1992).
- [162] Y. C. Kim and M. E. Fisher, *Fluid critical points from simulations: The Bruce-Wilding method and Yang-Yang anomalies*, J. Phys. Chem. B **108**, 6750 (2004).
- [163] A. M. Ferrenberg and R. H. Swendsen, *New Monte Carlo technique for studying phase transitions*, Phys. Rev. Lett. **61**, 2635 (1988).
- [164] A. M. Ferrenberg and R. H. Swendsen, *Optimized Monte Carlo data analysis*, Phys. Rev. Lett. **63**, 1195 (1989).
- [165] R. Evans, U. M. B. Marconi, and P. Tarazona, *Fluids in narrow pores: Adsorption, capillary condensation, and critical points*, J. Chem. Phys. **84**, 2376 (1986).
- [166] J. S. Rowlinson and F. L. Swinton, *Liquids and liquid mixtures*, Butterworth, London, 1982.
- [167] S. Kirkpatrick, C. D. Gelatt, and M. P. Vecchi, *Optimization by simulated Annealing*, Science **220**, 671 (1983).
- [168] G. Bosma, *Preparation of monodisperse, fluorescent PMMA-latex colloids by dispersion polymerization*, J. Colloid Interf. Sci. **245**, 292 (2002).
- [169] G. M. Bell, S. Levine, and L. N. McCartney, *Approximate methods of determining the double-layer free energy of interaction between two charged colloidal spheres*, J. Colloid Interface Sci. **33**, 335 (1970).
- [170] G. R. Maskaly, PhD thesis, MIT, Boston, 2005.
- [171] R. M. Fleming, M. J. Rosseinsky, A. P. Ramirez, D. W. Murphy, J. C. Tully, R. C. Haddon, T. Siegrist, R. Tycko, S. H. Glarum, P. Marsh, G. Dabbagh, S. M. Zahurak, A. V. Makhija, and C. Hampton, *Preparation and structure of the alkali-metal fulleride A4C60*, Nature (London) **352**, 701 (1991).

- [172] O. Zhou, J. E. Fischer, N. Coustel, S. Kycia, Q. Zhu, A. R. McGhie, W. J. Romanow, J. P. McCauley, A. B. Smith, and D. E. Cox, *Structure and bonding in alkali-metal-doped C60*, Nature (London) **351**, 462 (1991).
- [173] M. J. Rosseinsky, D. W. Murphy, R. M. F. R. Tycko, A. P. Ramirez, T. Siegrist, G. Dabbagh, and S. E. Barrett, *Structural and electronic-properties of sodium-intercalated C-60*, Nature (London) **356**, 416 (1992).
- [174] L. Pauling, *The nature of the chemical bond*, Cornell University Press, Ithaca, New York, 1960.
- [175] K. Husimi and I. Syôzi, Prog. Theor. Phys. **5**, 177 (1950).
- [176] T. Yildirim, O. Zhou, J. E. Fischer, N. Bykovetz, R. A. Strongin, M. A. Cichy, A. B. Smith, C. L. Lin, and R. Jelinek, *Intercalation of sodium heteroclusters into the C-60 lattice*, Nature (London) **360**, 568 (1992).
- [177] L. Forró and L. Mihály, *Electronic properties of doped fullerenes*, Rep. Prog. Phys. **64**, 649 (2001).
- [178] D. M. Deaven and K. M. Ho, *Molecular-geometry optimization with a genetic algorithm*, Phys. Rev. Lett. **75**, 288 (1995).
- [179] D. Gottwald, G. Kahl, and C. N. Likos, *Predicting equilibrium structures in freezing processes*, J. Chem. Phys. **122**, 204503 (2005).
- [180] R. Hogg, T. W. Healy, and D. W. Fuerstenau, *Mutual coagulation of colloidal dispersions*, Trans. Faraday Soc. **62**, 1638 (1966).
- [181] J. E. Sader, S. L. Carnie, and D. Y. C. Chan, *Accurate analytic formulas for the double-layer interaction between spheres*, J. Colloid Interface Sci. **171**, 46 (1995).
- [182] J. B. Caballero, A. M. Puertas, A. Fernández-Barbero, and F. J. de las Nieves, *Oppositely charged colloidal binary mixtures: A colloidal analog of the restricted primitive model*, J. Chem. Phys. **121**, 2428 (2004).
- [183] C. Vega, F. Bresme, and J. L. F. Abascal, *Fluid-solid equilibrium of a charged hard-sphere model*, Phys. Rev. E **54**, 2746 (1996).
- [184] A. G. Khachatryan, *Theory of structural transformations in solids*, John Wiley & Sons, New York, 1983.
- [185] J. L. F. Abascal, C. Vega, C. McBride, and F. Bresme, *Characterization of the order-disorder transition of a charged hard-sphere model*, Phys. Rev. E **68**, 052501 (2003).
- [186] A. D. Bruce, N. B. Wilding, and G. J. Ackland, *Free energy of crystalline solids: A lattice-switch Monte Carlo method*, Phys. Rev. Lett. **79**, 3002 (1997).
- [187] T. Chen, R. N. Zitter, and R. Tao, *Laser diffraction determination of the crystalline structure of an electrorheological fluid*, Phys. Rev. Lett. **68**, 2555 (1992).
- [188] U. Dassanayake, S. Fraden, and A. van Blaaderen, *Structure of electrorheological fluids*, J. Chem. Phys. **112**, 3851 (2000).
- [189] T. C. Halsey and W. Toor, *Structure of electrorheological fluids*, Phys. Rev. Lett. **65**, 2820 (1990).
- [190] W. R. Toor and T. C. Halsey, *Surface and bulk energies of dipolar lattices*, Phys. Rev. A **45**, 8617 (1992).
- [191] R. Friedberg and Y.-K. Yu, *Energy of an electrorheological solid calculated with inclusion of higher multipoles*, Phys. Rev. B **46**, 6582 (1992).
- [192] B. Khusid and A. Acrivos, *Phase diagrams of electric-field-induced aggregation in conducting colloidal suspensions*, Phys. Rev. E **60**, 3015 (1999).
- [193] S. Klapp and F. Forstmann, *Phase behavior of aligned dipolar hard spheres: Integral equations and density functional results*, Phys. Rev. E **60**, 3183 (1999).
- [194] R. Tao and J. M. Sun, *Ground state of electrorheological fluids from Monte Carlo simulations*, Phys. Rev. A **44**, R6181 (1991).
- [195] J. E. Martin, R. A. Anderson, and C. P. Tigges, *Simulation of the athermal coarsening of composites structured by a uniaxial field*, J. Chem. Phys. **108**, 3765 (1998).
- [196] J. E. Martin, R. A. Anderson, and C. P. Tigges, *Thermal coarsening of uniaxial and biaxial field-structured composites*, J. Chem. Phys. **110**, 4854 (1999).

- [197] M. Gross and C. Wei, *Ground state of a dipolar crystal*, Phys. Rev. E **61**, 2099 (2000).
- [198] B. Groh and S. Dietrich, *Crystal structures and freezing of dipolar fluids*, Phys. Rev. E **63**, 021203 (2001).
- [199] R. Tao, *Electric-field-induced phase transition in electrorheological fluids*, Phys. Rev. E **47**, 423 (1993).
- [200] R. Tao, *Super-strong magnetorheological fluids*, J. Phys.: Cond. Matt. **13**, R979 (2001).
- [201] Z. Wang and C. Holm, *Estimate of the cutoff errors in the Ewald summation for dipolar systems*, J. Chem. Phys. **115**, 6351 (2001).
- [202] H. Ma, W. Wen, W. Y. Tam, and P. Sheng, *Dielectric electrorheological fluids: Theory and experiment*, Adv. Phys. **52**, 343 (2003).
- [203] G. Arfken, *Mathematical methods for physicists*, Academic Press, New York, 1970.
- [204] A. Vrij, *Sedimentation equilibrium in concentrated, multicomponent particle dispersions. Hard spheres in the Percus-Yevick approximation*, J. Chem. Phys. **72**, 3735 (1980).
- [205] T. Biben, J.-P. Hansen, and J.-L. Barrat, *Density profiles of concentrated colloidal suspensions in sedimentation equilibrium*, J. Chem. Phys. **98**, 7330 (1993).
- [206] T. Biben and J.-P. Hansen, *Sedimentation equilibrium in concentrated charge-stabilized colloidal suspensions*, J. Phys.: Cond. Matt. **6**, A345 (1994).
- [207] J.-P. Simonin, *Calculation of equilibrium sedimentation profiles of screened charged colloids*, J. Phys. Chem. **99**, 1577 (1995).
- [208] H. Löwen, *The apparent mass in sedimentation profiles of charged suspensions*, J. Phys.: Cond. Matt. **10**, L479 (1998).
- [209] G. Téllez and T. Biben, *Equilibrium sedimentation profiles of charged colloidal suspensions*, Eur. Phys. J. E **2**, 137 (2000).
- [210] A. P. Philipse and G. H. Koenderink, *Sedimentation-diffusion profiles and layered sedimentation of charged colloids at low ionic strength*, Adv. Colloid and Interface Sci. **100**, 613 (2003).
- [211] A. Arnold and C. Holm, *A novel method for calculating electrostatic interactions in 2D periodic slab geometries*, Chem. Phys. Lett. **354**, 324 (2002).
- [212] A. Arnold and C. Holm, *MMM2D: A fast and accurate summation method for electrostatic interactions in 2D slab geometries*, Comput. Phys. Comm. **148**, 327 (2002).
- [213] M. P. Allen and D. J. Tildesley, *Computer simulation of liquids*, Clarendon Press, Oxford, 2002.

Summary

In this thesis, we have presented results of computer simulations on the phase behavior of charged colloidal suspensions using various levels of description (DLVO, DLVO with effective many-body interactions, and the primitive model) at both weak and strong electrostatic coupling. We have also looked at the effect of external electric or magnetic fields on the phase behavior and studied charged colloids in gravity. The content of this thesis can be divided into four parts.

Part I, consisting of Chapters 2, 3, 4, and 5, deals with the phase diagram of charged colloids in bulk. In Chapter 2, we studied the phase diagram of hard-core Yukawa (i.e. DLVO) particles. Special interest was paid on the effect of the hard core on the phase behavior by making a comparison with results for point Yukawa particles. We showed that the phase behavior of hard-core Yukawa particles can be understood based on the phase diagram of point Yukawa particles, as long as the contact values are sufficiently high. Additionally, one has to bear in mind that the hard-core repulsion favors the face-centered-cubic (fcc) over the body-centered-cubic (bcc) phase for $\eta > 0.5$. In Chapter 3, we studied the effect of density-dependent truncation on the phase diagram of hard-core Yukawa particles. The most important observations were (i) a radical reduction of the stability of the bcc phase with respect to the fcc phase, (ii) more fluid phase due to instability of the fcc phase, and (iii) a re-entrant fluid phase. The effect of three-body interactions on the phase behavior was studied in Chapter 4. The main effect is a reduction of the stability of the bcc phase in favor of the fluid and fcc phase or coexistence of the latter two. Furthermore, the three-body attractions induce, at sufficiently low salt concentration, a very broad coexistence regime of a dilute fluid with an extremely dense fcc phase, while at intermediate salinity a broad bcc-fcc coexistence regime appears. In Chapter 5, we used the primitive model to study the melting line of charged colloids using the same parameters as in Chapter 4. However, we did not find any broad coexistence regions or any other manifestations of three-body interactions. In fact, we found reasonable agreement with the phase diagram of hard-core Yukawa particles. This suggests that the four- and higher-body terms play an essential role in the parameter range considered here; they seem to cancel the effective three-body attraction. Thus, the effective Hamiltonian of charged colloids seems to be better described by the standard pairwise DLVO potential, than by a Hamiltonian including a density-dependent truncation or many-body interactions. In Chapter 5, we also discussed the difficulties in mapping between the primitive model and the Yukawa model descriptions at concentrated colloidal dispersions ($\eta > 0.2$).

In Part II, given in Chapter 6, we studied the gas-liquid critical point of asymmetric electrolyte mixtures consisting of large multivalent ($Z = 3$ and 10) macroions and small monovalent co- and counterions. The system can be seen as a binary mixture of colloids with their counterions and salt at strong electrostatic coupling. We calculated the critical point loci that connects the salt-free state consisting of macroions and counterions with the pure salt state. We found that the binary electrolyte mixtures studied here are type-I mixtures, where the two species mix continuously. Non-monotonic behavior of the critical parameters was observed.

Part III, consisting of Chapters 7 and 8, deals with oppositely charged colloids. In Chapter 7, we calculated the ground-state phase diagram of a mixture of large and small (size ratio 0.31) oppositely charged colloids. The phase diagram displays novel structures, but also colloidal analogs of simple-salt structures and of doped fullerene C_{60} structures. Three of the predicted structures called, $A_6C_{60}^{bcc}$, LS_8^{fcc} , and LS_8^{hcp} , were also observed experimentally. In Chapter 8, we calculated the phase diagrams of (i) the restricted primitive model (RPM) and (ii) screened Coulomb particles. We showed that the two phase diagrams are qualitatively similar, and more importantly that both contain a new solid phase, which is a colloidal analogue of the CuAu structure. Remarkably, the CuAu structure was also observed experimentally in a system of oppositely charged colloids.

In Part IV, which consists of Chapters 9 and 10, we studied charged colloids in external fields. In Chapter 9, we calculated the phase diagram of colloids in an external electric or magnetic field, where the field induces a fixed dipole moment on the particles giving rise to a dipole-dipole interaction. Two cases were considered: (i) colloids without charge (or dipolar hard spheres) and (ii) colloids with charge (or dipolar soft spheres). The phase diagram of dipolar hard spheres showed fluid, fcc, hexagonal-close-packed (hcp), and body-centered-tetragonal (bct) phases. The phase diagram of dipolar soft spheres showed, in addition to the above mentioned phases, a body-centered-orthorhombic (bco) phase, and is in agreement with the experimental phase diagram. In both cases, the fluid phase is inhomogeneous but we found no evidence of a gas-liquid phase separation. The validity of the dipole approximation was verified by a multipole moment expansion method. In Chapter 10, we used the primitive model and Molecular Dynamics simulations to study charged colloids in gravity. We showed that gravity gives rise to a macroscopic charge separation of colloids and microions, provided the added salt concentration is low enough. The mechanism is due to the intricate balance between colloidal and ionic entropy, potential energy, and electrostatic energy. The electric field that is generated by the charge separation is shown to be almost constant in the suspension, and is such that it largely compensates the gravitational force on the colloids. Therefore, the colloids are lifted to altitudes much larger than their gravitational length and one observes highly non-barometric sedimentation profiles. This implies that the system cannot be understood as an effective one-component system of colloids, not even at rather low densities. Our results agree quantitatively with the Poisson-Boltzmann theory, showing that the theory is robust with respect to the inclusion of fluctuations, correlations, and hard-core effects present in the simulations.

Samenvatting

In dit proefschrift bestuderen we met behulp van computer simulaties het fasegedrag van suspensies van geladen colloïden. In de simulaties maken we gebruik van verschillende benaderingsniveaus (effectieve paar potentialen (DLVO), effectieve “veel-deeltjes” interacties en het zogenaamde primitieve model, waarin de co- and tegenionen expliciet worden mee genomen), zowel met zwakke als sterke elektrostatische koppeling. Daarnaast bestuderen we het effect van extern aangelegde elektrische of magnetische velden op het fasegedrag en hebben we geladen colloïden onder invloed van zwaartekracht bestudeerd. De inhoud van dit proefschrift kan in vier stukken verdeeld worden.

Deel I, bestaande uit de hoofdstukken 2, 3, 4 en 5, behandelt het fasegedrag van geladen colloïden in de bulktoestand. In hoofdstuk 2 bestuderen we het fasegedrag van zogeheten “hard-core” Yukawa (ofwel DLVO) deeltjes. Hierbij richten we ons in het bijzonder op het effect van de harde kern op het fasegedrag door een vergelijking te maken met de resultaten voor “punt” Yukawa deeltjes. We hebben laten zien dat het fasegedrag van hard-core Yukawa deeltjes begrepen kan worden op basis van het fasegedrag voor punt Yukawa deeltjes zolang de contactwaarde hoog genoeg is. Bovendien moet men in gedachten houden dat voor $\eta > 0.5$ de harde-kern repulsie een voorkeur voor de vlakgecentreerde kubische (fcc) fase in plaats van de lichaamsgecentreerde kubische (bcc) fase met zich meebrengt. In hoofdstuk 3 bestuderen we de gevolgen van een dichtheids-afhankelijk afgekapte paar interactie op het fasegedrag van hard-core Yukawa deeltjes. De belangrijkste waarnemingen waren (i) een destabilisatie van de bcc-fase ten opzichte van de fcc-fase, (ii) een groter gebied met een stabiele vloeistoffase door een destabilisatie van de fcc-fase en (iii) een wederkerende, ofwel “re-entrant”, vloeistoffase. Het effect van effectieve “drie-deeltjes” interacties op het fasegedrag is bestudeerd in hoofdstuk 4. Het belangrijkste effect is een destabilisatie van de bcc-fase ten gunste van de vloeistof- en de fcc-fase of een coexistentie van deze twee. Daarnaast induceren de drie-deeltjes attracties bij voldoende lage zoutconcentraties een zeer breed coexistentie gebied van een verdunde vloeistof en een dichte fcc-fase, terwijl bij intermediaire saliniteit een uitgebreide bcc-fcc coexistentie optreedt. In hoofdstuk 5 gebruiken we het primitieve model, met dezelfde parameters als in hoofdstuk 4, om de smeltlijn van geladen colloïden te bestuderen. Op deze wijze vonden we echter geen brede coexistentie-gebieden of andere manifestaties van de drie-deeltjes interacties. In feite vinden we een redelijke overeenstemming met het fasegedrag van hard-core Yukawa deeltjes. Dit suggereert dat de “vier-deeltjes” en “meer-deeltjes” interacties een essentiële rol spelen binnen het hier beschouwde parametergebied; ze lijken de effectieve drie-deeltjes attracties op te heffen. De effectieve Hamiltoniaan van geladen colloïden lijkt dus beter benaderd te worden door de standaard paarsgewijze DLVO-potential dan door een Hamiltoniaan die veel-deeltjes interacties of een dichtheids-afhankelijk afgekapte potential omvat. Tenslotte bespreken we in hoofdstuk 5 de moeilijkheden bij het kwantitatief vergelijken van de primitieve- en Yukawa-model beschrijvingen voor geconcentreerde colloïdale dispersies ($\eta > 0.2$).

In deel II, te weten hoofdstuk 6, bestuderen we het gas-vloeistof kritisch punt van asymmetrische elektrolyt mengsels, bestaande uit grote meerwaardige ($Z = 3$ en 10) macro-ionen en kleine eenwaardige co- en tegenionen. Dit systeem kan beschouwd worden als een binair mengsel van colloïden met hun tegenionen en zout, met sterke elektrostatische koppeling. We berekenen de lijn van kritische punten dat de zout-vrije toestand, bestaande uit macro-ionen en tegenionen, verbindt met de toestand van puur zout. We vinden dat de hier bestudeerde binaire elektrolyt mengsels zogenaamde type-I mengsels zijn. De twee componenten mengen zich op een continue wijze. Bovendien vinden we niet-monotoon gedrag van de kritische parameters.

Deel III, bestaande uit de hoofdstukken 7 en 8, behandelt colloïden die tegengesteld geladen zijn. In hoofdstuk 7 berekenen we het fase-diagram voor de grondtoestand van een mengsel van grote en kleine (grootteverhouding 0.31) colloïden met tegengestelde lading. Naast volledig nieuwe structuren vertoont het fase-diagram ook colloïdale analogons van eenvoudige-zout structuren en van gedoteerde fullereen- C_{60} structuren. Drie van de door ons voorspelde structuren, $A_6C_60^{bcc}$, LS_8^{fcc} en LS_8^{hcp} genaamd, zijn ook experimenteel waargenomen. In hoofdstuk 8 berekenen we de fase-diagrammen van (i) het beperkte primitieve model ("restricted primitive model", RPM) en (ii) afgeschermd Coulomb of hard-core Yukawa deeltjes. We hebben laten zien dat de twee fase-diagrammen kwalitatief vergelijkbaar zijn en, wat nog belangrijker is, dat ze beiden een nieuwe vaste fase bevatten, die het colloïdale analogon van de CuAu-structuur vormt. Deze CuAu-structuur is opmerkelijk genoeg ook experimenteel waargenomen in een systeem van tegengesteld geladen colloïden.

In deel IV, gevormd door de hoofdstukken 9 en 10, bestuderen we geladen colloïden in externe velden. In hoofdstuk 9 berekenen we het fase-diagram van colloïden in een extern elektrisch of magnetisch veld. Het veld induceert een gefixeerd dipoolmoment in de deeltjes, met een dipool-dipool interactie als gevolg. Twee afzonderlijke gevallen worden beschouwd: (i) colloïden zonder lading (ofwel dipolaire harde bollen) en (ii) colloïden met lading (ofwel dipolaire zachte bollen). Het fase-diagram van de dipolaire harde bollen vertoont vloeistof-, fcc-, hexagonaal dichtstgepakte (hcp) en lichaamsgecentreerd tetragonale (bct) fasen. Het fase-diagram van de dipolaire zachte bollen vertoont naast deze fasen ook een lichaamsgecentreerd -orthorhombische (bco) fase en is in overeenstemming met het experimentele fase-diagram. De vloeistoffase is in beide gevallen inhomogeen, maar we vinden geen aanwijzingen voor een gas-vloeistof fasescheiding. De validiteit van de dipool-benadering hebben we gecontroleerd met behulp van een multipool-expansiemethode. In hoofdstuk 10 gebruiken we het primitieve model in moleculaire dynamica simulaties om geladen colloïden onder invloed van zwaartekracht te bestuderen. We laten zien dat de aanwezigheid van zwaartekracht leidt tot een macroscopische ladingsscheiding van colloïden en micro-ionen, mits de concentratie toegevoegd zout laag genoeg is. Dit mechanisme is het gevolg van een complex evenwicht van entropie van de colloïden en de ionen, de potentiële energie en de elektrostatische energie. Het elektrisch veld dat door de ladingsscheiding gegenereerd wordt, is nagenoeg constant in de suspensie en is zodanig dat het de zwaartekracht die op de colloïden werkt grotendeels compenseert. Hierdoor worden de colloïden opgetild tot veel grotere hoogten dan hun gravitationele

lengte en neemt men sedimentatieprofielen waar die sterk niet-barometrisch zijn. Onze resultaten komen kwantitatief overeen met de Poisson-Boltzmann theorie, wat aantoont dat de theorie robuust is voor wat betreft het meenemen van fluctuaties, correlaties en “hard-core” effecten, zoals aanwezig in de simulaties.

Acknowledgements

First and foremost I would like to thank my supervisor Marjolein Dijkstra. Marjolein, the past four years have been a great learning experience for me and I could not have wished for a better supervisor for myself. Your intelligent, kindness, and patience has made a great impact on me. It has always been very pleasant to work with you, and only with your help have I gotten this far. Secondly, I want to thank René van Roij for providing the theoretical backing and many good ideas needed in my projects. Both you and Marjolein never seemed to be too busy to answer my questions. I value the discussions with both of you very much. Thank you.

I would like to thank my promotor Alfons van Blaaderen for giving me the opportunity to work in one of the leading soft condensed matter groups in the world, and for many valuable comments and suggestions that you have given me over the years. I think the combination of experiments, simulations, and theory, which you value, is certainly very beneficial, and has made me understand the importance of collaboration with experimentalists. I thank Arnout Imhof for numerous interesting discussions and for lending me many useful books.

I thank Hennig von Grünberg for the opportunity to visit Konstanz University and for many interesting discussions with him and with his group members, Jure Dobnikar and Carsten Russ. I would like to thank Athanassios Panagiotopoulos for the opportunity to visit his group at Princeton University. My visit to Princeton and many discussions with you and the members of your group, Daniel Cheong, Owen Hehmeyer, and Gaurav Arya, certainly gave a great impulse for my research and many new ideas. I also thank you for the opportunity to continue my research career at Princeton.

During my years in the Soft Condensed Matter group I have had the privilege to collaborate with some very intelligent people. Job Thijssen and Anand Yethiraj helped me to understand experimental aspects of colloids in external fields and provided important critical comments on my manuscript. Mirjam Leunissen's and Christina Christova's experiments on oppositely charged colloids were absolutely crucial for the research described in Chapters 7 and 8, and it has been very pleasant and instructive to work with both Mirjam and Christina. Discussions with Paddy Royall taught me many things about experimental colloidal suspensions. Dirk Vossen's crash course in colloid synthesis, which me and Marjolein took, was both educating and fun. I am grateful to Bas Zoetekouw for providing the Poisson-Boltzmann code used in Chapter 5. It is a pleasure to thank Svytoslav "Slava" Savenko and Andrea Fortini for many good talks, and especially Andrea his help with the gas-liquid critical phase envelope calculations in Chapter 8. I thank Esther Vermolen who helped me to classify the binary crystal structures in Chapter 7. I would also like to mention people with whom I have had fruitful discussions or who have in some other way contributed to my research: Dirk Aarts, Andrew Campbell, Alejandro Cuetos, Daan Frenkel, Jacob Hoogenboom, Astrid van der Horst, Patrick Johnson, Christos Likos, Alexander Moroz, Peter Pusey, Matthias Schmidt, Emmanuel Trizac, Chantal Valeriani, Krassimir Velikov, and Yu Ling Wu. I also thank the whole Soft Condensed Matter group for an inspir-

ing working atmosphere.

I am grateful to Per Linse for critical comments on many of my manuscripts that clearly made them stronger, and for the nice chats we had. Vladimir Lobaskin is thanked for long talks on charged systems, particularly related to the critical point of electrolyte mixtures (Chapter 6) and for his comments on my manuscripts.

Computer simulations are not possible without powerful computer resources. I would like to thank the Dutch National Computer Facilities foundation for access to the SGI Origin 3800 and the High Performance Computing group of Utrecht University for ample computer time. I would also like to acknowledge the financial support from the Finnish Cultural Foundation during the first year of my research. I thank Henk Moss for maintaining our computer systems and María Delgado Flores for her help with paperwork. I am grateful to Teemu Heinilehto for designing the cover and the invitation, and for his help with the layout of the thesis.

Finally, I thank Farah, my family, and my friends for their support.

Curriculum vitae

Antti-Pekka Hynninen was born on the 21st of December 1977 in Oulu, Finland. After finishing high school in 1996, he completed a one year civil service as a computer helpdesk at Merikoski Vocational Training Center in Oulu.

In 1997, he started studies at Helsinki University of Technology (HUT) in the Department of Engineering Physics and Mathematics. At HUT, he studied physics and mathematics with strong emphasis on numerical methods. During the summer breaks from HUT, he worked as a Java programmer in an advertising agency, and as a research assistant in the Laboratory of Biomedical Engineering (HUT) and in the Laboratory of Physics (HUT). In September 2001, he earned a Master of Science in Engineering from HUT with distinction. His master's thesis was on path integral calculation of jump rates and surface diffusion coefficients, and it was supervised by Prof. Tapio Ala-Nissilä at the Laboratory of Physics (HUT). Part of the thesis work was done at Brown University (Rhode Island, USA) under the supervision of Prof. See-Chen Ying.

In January 2002, he joined Alfons van Blaaderen's Soft Condensed Matter group at Utrecht University as a graduate student. His research at Utrecht was on computer simulations studies of the phase behavior of charged colloidal suspensions, and was carried out under the supervision of Dr. Marjolein Dijkstra. Specific research topics include, the effect of many-body interactions on the phase behavior of charged colloids, oppositely charged colloids, and colloids in external fields. The results of his research are described in this thesis and published in international peer-reviewed journals. He has attended numerous schools and workshops, and presented his results at conferences. During his time in Utrecht, he collaborated with Dr. René van Roij from the Institute of Theoretical Physics (Utrecht), with many experimentalists from the Soft Condensed Matter group, and with Prof. Athanassios Panagiotopoulos from Princeton University (New Jersey, USA), whom he visited during 2003.

In January 2006, he will start as a Fellow at the Princeton Center for Complex Materials, where he will work with Prof. Panagiotopoulos.

List of publications

This thesis is based on the following publications

1. A.-P. Hynninen and M. Dijkstra, *Phase diagrams of hard-core repulsive Yukawa particles*, Phys. Rev. E **68**, 021407 (2003). (Chapter 2)
2. A.-P. Hynninen and M. Dijkstra, *Phase diagram of hard-core repulsive Yukawa particles with a density-dependent truncation: a simple model for charged colloids*, J. Phys.: Cond. Matt. **15**, S3557 (2003). (Chapter 3)
3. A.-P. Hynninen, M. Dijkstra, and R. van Roij, *Effect of three-body interactions on the phase behavior of charge-stabilized colloidal suspensions*, Phys. Rev. E **69**, 061407 (2004). (Chapter 4)
4. A.-P. Hynninen, M. Dijkstra, and R. van Roij, *Effect of triplet attractions on the phase diagram of suspensions of charged colloids*, J. Phys.: Cond. Matt. **15**, S3549 (2003). (Chapter 4)
5. A.-P. Hynninen and M. Dijkstra, *Melting line of charged colloids from primitive model simulations*, submitted. (Chapter 5)
6. A.-P. Hynninen, M. Dijkstra, and A. Z. Panagiotopoulos, *Critical Point of Electrolyte Mixtures*, J. Chem. Phys. **123**, 084903 (2005). (Chapter 6)
7. A.-P. Hynninen, C. G. Christova, R. van Roij, A. van Blaaderen, and M. Dijkstra, *Prediction and Observation of Crystal Structures of Oppositely Charged Colloids*, submitted. (Chapter 7)
8. A.-P. Hynninen, M. E. Leunissen, A. van Blaaderen, and M. Dijkstra, *CuAu structure in the restricted primitive model and oppositely charged colloids*, submitted. (Chapter 8)
9. A.-P. Hynninen and M. Dijkstra, *Phase diagram of dipolar hard and soft spheres: Manipulation of colloidal crystal structures by an external field*, Phys. Rev. Lett. **94**, 138303 (2005). (Chapter 9)
10. A.-P. Hynninen and M. Dijkstra, *Phase Behavior of Dipolar Hard and Soft Spheres*, Phys. Rev. E accepted. (Chapter 9)
11. A.-P. Hynninen, R. van Roij, and M. Dijkstra, *Sedimentation profiles of charged colloids: Entropic lift and charge separation*, Europhys. Lett. **65**, 719 (2004). (Chapter 10).

The author has also contributed to the following publications.

1. C. P. Royall, M. E. Leunissen, A.-P. Hynninen, M. Dijkstra, and A. van Blaaderen, *Unusual phase behavior in charged colloids: Re-entrant melting and freezing*, submitted.
2. M. E. Leunissen, C. G. Christova, A.-P. Hynninen, C. P. Royall, A. I. Campbell, A. Imhof, M. Dijkstra, R. van Roij, and A. van Blaaderen, *Ionic colloidal crystals of oppositely charged particles*, *Nature (London)* **437**, 235 (2005)
3. A. Cuetos, A.-P. Hynninen, M. Dijkstra, J. Zwanikken, and R. van Roij, *Layering in sedimentation of multicomponent suspensions of charged colloids: simulation and theory*, submitted.